Control of the Electron Energy Distribution Function (EEDF) in a Hall Thruster Plasma

by

Kimberly R. Trent

A dissertation submitted in partial fulfillment
of the requirements for the degree of
Doctor of Philosophy
(Applied Physics)
in The University of Michigan
2016

Doctoral Committee:

Professor Alec D. Gallimore, Chair
Professor John E. Foster
Professor Brian E. Gilchrist
Professor Yue Ying Lau
Professor Duncan G. Steel

To My Father

ACKNOWLEDGEMENTS

Firstly, I'd like to thank God for putting me safely on this earth and for giving me a passion for scientific inquiry. In addition, I would like to thank him for giving me the courage and the resources to face and overcome each and every challenge I was faced with throughout my graduate school experience.

Secondly, I'd like to thank my family for their words of wisdom and encouragement, which sustained me and helped me to keep pushing forward. Specifically, I'd like to thank my Dad for his support, his prayers, and for making himself available so that whenever I called with a concern or issue that I was facing— even if it was in the middle of the night, he was there to listen, give perspective and offer advice. I'd like to thank my Mom for her support, prayers, motivation and instruction, and for talking on the phone with me for long periods of time, even when she was really busy, which helped me to feel still connected to the family and grounded since I wasn't able to get back home as often as I would have liked.

My sister, Tiffany, thank you for being so loving and caring, for always wanting the best for me, and for being there for me during those times when I needed you the most. I'd like to thank my sister and her boyfriend Matt for offering to fly to Michigan, and helping me pack all my belongings into a U-Haul and then helping me move back to NYC on their days off between busy work weeks. For me this was another demonstration of what it meant to have a loving family, and I will never forget this act of kindness and support. Tiffany & Matt, I'd also like to thank you for your encouragement, and the protective spirit you have towards me. I would also like

to thank my father, my mother and my sister for coming out to visit me in Michigan on separate occasions while I was doing experimental work to spend time with me, to help me to stay encouraged, and to keep me company. My Uncle Randall, thank you for your nurturing words and prayers, especially during the time I was writing my dissertation.

I'd like to thank my Uncle Keith for his support and prayers, and everyone else in my family and extended family who kept me in their prayers throughout my time in graduate school, and who I was able to fellowship with while visiting at home. I'd also like to thank my Uncle Gordy, and my Godfather, Uncle Walter, for their presence and support in my life. I was so happy that they wanted and had planned to come to Michigan to be there for my defense, and I was devastated by their passing in 2015. They mean a lot to me, and I still feel and see the impression they have left on my life everyday.

Alec, my advisor, thank you for taking me on as a graduate student, for believing in my potential to carry out experimental electric propulsion work, for mentoring and guiding me throughout my graduate school journey, and for allowing me the freedom to explore my ideas, while also providing structure and direction when needed. Your leadership and mentoring skills are truly unparalleled, which speaks to the state-of-the-art lab you have created, which continues to stay at the forefront of the field while creating additional leaders in the field. I feel completely blessed that you led me through the graduate school process. Any limits I may have subconsciously placed on how many challenges I could handle at the same time were completely obliterated through what I encountered in carrying out this research project, and I would not have been able to get through it all without the right level of push and flexibility through the guidance of a research advisor. You provided the right balance of the two for me in each situation. I'm still in awe of how you do it, and I will forever be grateful to you for helping me get through this journey successfully.

I'd also like to thank my PEPL peers. Adam, Mike M., and Robbie, thank you for showing me the ropes in the lab, and dedicating the time that you did to answering the myriad of questions I had about the various concepts and pieces of equipment I was working with. I'd like to thank the graduate students who came in after me for helping to continue the PEPL tradition of graduate student symbiosis where the newer graduate students pitch in to help out those who are in the process of finishing up their experiments, and in return receive hands on experience in helping to set up and run experiments at PEPL and learn the ins and outs and quirks of the process. Given the relatively unique twist to my time in LVTF, coming in right after the X3 took the chamber for a spin, which left several matters that had to be addressed, I am even more thankful to the recent PEPL students than they may realize for how they all stepped up to help out at every step of the way in this process:

Marcel and Ethan, words can not express how much the diligence and thoroughness you demonstrated time and again with each task you were presented with was appreciated. Thinking back on just how much there was to do, and that even with me working 12 - 22 hour days during much of the time I was prepping for carrying out experiments in LVTF, especially during the last few months, there was still so much more that needed to be addressed, so I could not have gotten through it without you.

Sarah, I wanted you to know that I will never forget the time when I was in the lab coming up to another H6 test with the thrust stand, and I was going to be testing throughout the night. You told me to just let you know when I was ready to test and you would come back to the lab. (For those who don't know, we need a testing buddy for safety reasons whenever we run experiments.) Even though I didn't start until 2 or 4 am, you were still by your phone waiting for the call and came back to the lab when I called. You have no idea how much that support at that key time, when I was really stressed about how that test was going to go and about all that I still had left to do, meant to me and how it helped to keep me going. In addition,

thank you for all of the other times you lent a hand when needed.

Scott and Tim, I will never forget the fact that you were two of the first people to volunteer to come in on the weekend before I had to be out of the chamber for good to help with all of the graphoil taping for protecting the probes and other general pump down prep items that needed to be completed in order for me to be able to pump down and test starting that Monday. In addition, thank you for all the other help you provided when it was needed. I recognize the fact that you had defined projects at that point, and had to find a way to weave that help into the tasks you had to do for moving your own projects forward.

Frans, thank you for lending a helping hand as well. I greatly appreciated the fact that even though you were mainly doing computational work and were not going to be using LVTF, you still volunteered to help me out with equipment prep for pumpdown. In addition, from my perspective, your spirit and kindness formed a large part of the camaraderie of the lab.

Roland, you are a unique one! Thank you for making the laboratory experience such an adventure, from the creation of the PEPL garden, to PEPL gym, to the war against various rodents (rats and groundhogs) that unfortunately decided to wander into PEPL or PEPL garden and the creative tools with Italian names that you were planning to show them who was boss with— there was never a dull moment when you were around. Thank you for always finding the humor in a situation and for always making me laugh.

Chris, we have been through all the major aspects of graduate school together, from first year classes, to carrying out our graduate research at PEPL. I admire your calm demeanor and the fact that even when things got stressful, you never let it rattle you. Our adventures with traveling to and within Japan for IEPC 2015 with Gbenga and Horatiu are memories I will always cherish.

In looking back on my time in graduate school, I realize that my time in CTF was

preparation for what I was going to deal with during my time in LVTF in more ways than just carrying out experiments for my thesis. While running experiments in this smaller chamber, I learned through talking with the senior grad students at the time the amount of money and resources that were involved in every single pump down for running experiments in LVTF; and in addition, just how much money it was per hour to have the cryopumps running. So, I decided that I would start to prep for my time in LVTF by running very carefully planned out and executed experiments in CTF so I could make the most of each time I pumped down when I got to LVTF. While this practice ended up being even more valuable than I realized during my time in LVTF, given the additional fact of the limits the chamber placed on how long I could stay pumped down during my tests, many of the issues that had to be addressed with the chamber itself also were issues I was able to preview and practice addressing in CTF.

Iverson, it was fun working with you while you were piggybacking on my experiments in CTF. When we started, I don't think we realized just how involved addressing the issues the chamber had would be, so I'd like to thank you for being a trouper and staying committed to helping with those adventures. I watched with pride as you took the things you had learned about getting a chamber into testing shape and the experience you had obtained with running experiments in CTF back to your lab to be able to do the same there. Also, I'm thankful that our friendship survived a work situation, and I know that in you I have a true friend.

Ray, thank you for your advice, troubleshooting help and your kindness throughout the years. Your resourcefulness, organization and skillfulness as an engineer always shined, and it was always very clear when I would come across something in the lab that you had built. For example, in looking over the thrust stand electrical box in preparation for using it, it was clear there was a very high level of planning, care and execution there that made the equipment robust and practical enough to last a long time and be useful for multiple scenarios and hence to other people in the

lab that came after you. Thank you for this as well.

Laura, thank you for being an excellent mentor. I am so happy that Applied Physics assigned you to that role for me. Thank you for helping me prep for quals, settle into PEPL, and for all the advice you gave me. I want you to know that when I think back on some of the decisions I made that put me in a very good position for success in various aspects of my life I remember: Oh yeah, it was Laura who advised me to do that.

Mike S., thank you for your words of wisdom, advice and encouragement as I started conducting experiments in LVTF, and thank you for showing us the ropes for using LVTF. Rohit and David, thank you for your advice and kindness. Ricky, Christopher Bellant and Ingrid, all of you are awesome, and I enjoyed the time I shared with all of you in the lab. J.P. and Tim Smith, thank you for listening to our updates during the PEPL meetings with an attentive ear and for offering advice, support and guidance.

I'd like to thank the undergrads who worked with me over a semester/summer or multiple semesters. Specifically Gregorio Lopez and Bakari Hassan whose dedication to the projects I assigned them went above and beyond what was expected. I'd also like to thank the summer student Samuel Majors, who at the time was in high school, for his assistance with searching for and ordering parts, experiment prep, and building small electronic circuits.

I'd like to give a special thanks to the PEPL alumni and individuals in the electric propulsion community whom I contacted over the years or ran into at conferences and research related events, who answered questions about using various pieces of experimental equipment, running some aspect of an experiment, or gave general grad school/career advice, such as Rich Hofer, Tom Liu, Sonca Nguyen, Dan Brown, Kristina Lemmer, Kevin Diamant, Valery Godyak, Pete Peterson, and Professor Mitchell Walker. Dan Goebel, thank you for replying to my emails with detailed

advice about cathode troubleshooting. Your words of wisdom helped me immensely. Professor Foster, thank you for your advice, support and encouragement throughout the years, for checking up on me through email, and for answering my many questions about cathodes. Eric from EDA, your help with building probes and probe support structures during my time in LVTF is extremely appreciated. I don't know what I would have done without you there. I'd also like to thank my dissertation committee for their advice, support, and thoughtful comments on my dissertation work.

I'd like to thank all the other graduate students I came across over the years, some from Applied Physics and some from other programs, who gave support, advice and encouragement in various ways throughout the years. When I look back on my graduate student experience, I will fondly think about all the times I met up with other grad students at coffee shops, libraries or the Trotter Multicultural Center on campus to do work, and the events we attended together when we took a break from studying. I have made some life long friends among you.

I also thank all those who are a part of the University of Michigan staff (including Kathleen Grimes, Lauren Segall, Cynthia McNabb, Colleen Root, Bonnie Bryant, Julie Power, Kristin Parrish, Cynthia Enoch, Tom Griffin, Martin Stenzel (RIP), Aaron Borgman, Terry Larrow, and David McLean) for their hard work, dedication to their jobs and kindness. I thank the Applied Physics Program Leadership past and present (including Professor Cagliyan Kurdak, Professor Roy Clarke, and Professor Bradford Orr) for their advice, support and encouragement.

I'd like to thank Rev. Yolanda Whiten for her prayers, warm spirit and fellowship throughout the years. In closing, I would also like to thank the many others from the Ann Arbor community whom I met over the years during my time in Michigan for their welcoming demeanor and for providing a home-away-from-home environment.

TABLE OF CONTENTS

LIST OF FIGURES

Figure

LIST OF TABLES

Table

LIST OF VIDEOS

Video

LIST OF APPENDICES

Appendix

LIST OF ABBREVIATIONS

Constants

ϵ_0 vacuum permittivity, 8.85×10^{-12} F/m

π ratio of a circle's diameter to its circumference, 3.14

e elementary charge, 1.6×10^{-19} C

g acceleration due to gravity on Earth, 9.81 m/s^2

h Planck's constant, 4.14×10^{-15} eV-s

k_B Boltzmann constant, 1.38×10^{-23} J/K

M_e mass of an electron, 9.11×10^{-31} kg

M_{Xe} mass of a xenon atom or ion, 2.2×10^{-25} kg

Variables

Δv sum of all the instantaneous changes in speed over the course of the trip needed to complete the mission, m/s

ϵ_B total effective ionization cost per beam ion, eV

$\epsilon_{B_{min}}$ smallest possible ionization cost per beam ion, eV

ϵ_i ionization potential for the ith ion species, eV

η_a anode efficiency

η_B current utilization efficiency

η_c cathode efficiency

η_{Div} divergence efficiency, or beam utilization efficiency

η_m mass utilization efficiency

η_{mag} electromagnet efficiency

η_q charge utilization efficiency

η_{tot} total thruster efficiency

η_V voltage utilization efficiency

θ_B plume divergence half angle, $^\circ$

Θ_{ion_T} thruster's ionization fraction

λ_D Debye length, m

λ_{MFP} mean free path, m

ν_c collision frequency, s^{-1}

σ standard deviation

χ^2 the reduced chi-squared value (chi-squared/degrees of freedom (dof)), a statistical measure of the goodness-of-fit along with R^2

Ω_i current fraction of the ith ion species

a acceleration, m/s^2

B magnetic field, T or G

d_{gap} distance between the parallel plates in the ExB probe, mm

D_T thruster diameter

E electric field, V/m

F force, N or mN

F_{tot} total force, N or mN

F_x force along the x direction

F_y force along the y direction

F_z force along the z direction

I current, A

I_D thruster's discharge current, A

I_e electron current, A

I_i total current collected by the ExB probe for the ith ion species, A

I_{ion_i} ion current of the ith ion species, A

I_{ion_T} ion current, A

I_s specific impulse, s

m mass, kg

m_0 initial total mass (rocket plus propellant), kg or lb

$\dot{m}$ mass flow rate of the propellant, mg/s

$\dot{m}_A$ propellant mass flow rate through the anode, mg/s

$\dot{m}_C$ propellant mass flow rate through the cathode, mg/s

$\dot{m}_{ion_i}$ mass flow rate of the ith ion species out of the thruster, mg/s

$\dot{m}_{ion_T}$ total ion mass flow rate out of the thruster, mg/s

$\dot{m}_N$ neutral gas mass flow rate out of the thruster, mg/s

$\dot{m}_T$ total mass flow rate ($\dot{m}_A + \dot{m}_C$), mg/s

m_f final total mass (rocket without propellant), kg or lb

N total number

N_e electron number density, m^{-3}

n_{ion_T} total ion particle number density, m^{-3}

n_n neutral number density, m^{-3}

n_T total number density (neutral and ion particles), m^{-3}

p linear momentum, kg m/s

P_{base} base pressure of the vacuum chamber, Torr

$P_{corrected}$ corrected pressure, Torr

P_D thruster's discharge power, kW

P_{jet} thruster's jet power, kW

P_{loss} thruster's discharge power not used for jet power, and not part of the minimum needed for ionization (loss power), kW

P_{min} minimum thruster power needed for ionization, kW

$P_{reading}$ pressure read from the gauge, Torr

P_{tot} total thruster power (discharge and magnet powers), kW

r electron recycle current fraction

R^2 the R-squared value, a statistical assessment of how close the data are to the fit

R_c thruster channel radius

T temperature, K

t time, s

T_e electron temperature, eV

$T_{e(K)}$ electron temperature, K

T_{eV} temperature, eV

T thrust, mN

V voltage, V

v velocity, m/s

V_o initial voltage, V

v_0 initial velocity, m/s

V_{accel} ion acceleration voltage, V

V_{c-g} cathode-to-ground voltage, V

V_D discharge voltage, V

v_e effective exhaust velocity, m/s

v_{e_i} effective exhaust velocity of the ith ion species, m/s

v_f final velocity, m/s

V_{mp} most probable voltage, V

V_p plasma potential, V

V_{probe} voltage applied to the probe, V

V_{shift} voltage shift corresp. to the velocity shift of a drifting Maxwellian EEDF, V

$\hat{y}$ unit vector in the y-axis direction

Z ion species charge

Z_i charge of the ith ion species

Units

A Amps

C Celsius

cm Centimeter

eV Electron Volts

G Gauss

K Kelvin

kg Kilogram

kg/s Kilograms per Second

kHz Kilohertz

km Kilometers

km/s Kilometers per Second

kN Kilonewton

kW Kilowatt

m Meter

mg/s Milligrams per Second

MHz Megahertz

mm Millimeter

MN Meganewton

mN Millinewton

m/s Meters per Second

mT Millitesla

mTorr Millitorr

MW Megawatt

N Newton

s Second

sccm Standard Cubic Centimeters per Minute

T Tesla

Torr A unit of pressure. 1 Torr = $\frac{1}{760}$ atm

V Volts

W Watt

Acronyms

AC Alternating Current

AFRL Air Force Research Laboratory

BaO-W Barium-Oxide Impregnated Tungsten

B-field Magnetic Field

BN Boron Nitride

CEX Charge Exchange Collision

CFF Cathode Flow Fraction

CFT Cross-field Transport

CTF Cathode Test Facility

DAQ Data Acquisition

DC Direct Current

EDA ElectroDynamic Applications Inc.

EEDF Electron Energy Distribution Function

EEPF Electron Energy Probability Function

E-field Electric Field

EP Electric Propulsion

EVA Extravehicular Activity

FP Faraday Probe

FWHM Full-Width at Half-Maximum

GRC Glenn Research Center

HDLP High-speed Dual Langmuir Probe

HET Hall-effect Thruster

HHT Helicon Hall Thruster

HWHM Half-Width at Half-Maximum

ICP Inductively Coupled Plasma

Isp Specific Impulse

I-V Current-Voltage

IVD Ion Voltage Distribution

JLVTF Junior Test Facility

JPL Jet Propulsion Laboratory

LaB_6 Lanthanum Hexaboride

LEO Lower Earth Orbit

LP Langmuir Probe

LTP Low Temperature Plasma

LVDT Linear Voltage Differential Transducer

LVTF Large Vacuum Test Facility

NASA National Aeronautics and Space Administration

NHT Nested Hall Thruster

OML Orbital Motion Limited

PEPL Plasmadynamics & Electric Propulsion Laboratory

PID proportional-integral-derivative

RF Radio Frequency

RPA Retarding Potential Analyzer

SD Standard Deviation

SEE Secondary Electron Emission

SEP Solar Electric Propulsion

SPT Stationary Plasma Thruster

SRS Stanford Research Systems

TRL Technology Readiness Level

TVS Transient Voltage Suppression

ABSTRACT

Control of the Electron Energy Distribution Function (EEDF) in a Hall Thruster Plasma

by

Kimberly R. Trent

Professor Alec D. Gallimore

Further improvements to Hall-effect thruster (HET) efficiency in the high thrust-to-power regime (i.e, low voltage regime) will help enable more extensive, cost-capped robotic and manned space missions involving round-trip, sample-returns from Mars and near-Earth asteroids and will translate into larger fuel reserves for future manned space missions. HET efficiency depends on its ability to ionize and accelerate neutral propellant, which can be further improved when electrons with energies and trajectories that contribute to ionization are increased in the right locations. Therefore, tailoring of the EEDF is needed. However, predictive control of the EEDFs in plasma devices is a challenging problem in plasma physics due to complex electromagnetic interactions that take place in the actual system that lead to the turbulent nature of these plasmas.

In an effort to control the EEDF in an HET for the immediate benefit of boosting thruster efficiency, and to also uncover further insights into the operation and dynamics of these devices, various analyses were carried out. These were a neutral gas injection method to indirectly influence electron mean free path and therefore in-

crease ionization, a gas mixing scheme to introduce particles with electrons in excited metastable states that have enough energy to ionize the thruster's propellant, and a reverse-orientation cathode technique to control the EEDF by placing the cathode downstream and pointing towards the thruster to redirect high-energy electrons to a less circuitous path to the thruster channel where ionization takes place.

The results from the experiment carried out to test the gas injection method using an inductively coupled plasma as the test-bed showed that the change in the EEDF and the change in the ion number density were not significant enough to be a promising approach to improving efficiency in the Hall thruster. From this the idea followed that in order to increase ionization, the EEDF would have to be manipulated to increase a select energy population of electrons. Hence, the next scheme was developed and tested that involved incorporating an auxiliary inert gas into the plasma device's gas feed, which was characterized by metastable states with enough energy to ionize the main propellant gas.

The calculations and experiment carried out to test the feasibility of this strategy used a hollow cathode as the test-bed. Neon was used as the auxiliary gas in the calculations. The outcome revealed that using a heavy particle as the delivery method for the high energy electron is not ideal for increasing the ionization rate because although the cross section for atom-atom collisions is much higher than electron-atom collisions, the speed of the particle, which also factors into the collision frequency, counteracts gains associated with the larger cross section. When using this to calculate the propellant ion production rate for this interaction, the small fraction of regularly present metastable atoms in the auxiliary gas for this plasma condition does not make up for this particle speed deficit. Therefore the ion production rate for metastable neon atom-xenon atom collisions ends up being several orders of magnitude lower than that of electron-atom ionization.

This drove the realization that in order to control the EEDF to improve thruster

efficiency, the energy of the electrons alone needed to be directly altered, which led to the EEDF tailoring method that involved positioning the hollow cathode, the thruster's source of ionizing and neutralizing electrons, so it was downstream from the thruster with the cathode orifice pointing towards the thruster exit plane, and was positioned so that the cathode was outside the densest part of the thruster plume, instead of current orientations that place it pointing away from the discharge channel. The intention behind this orientation was to establish more control on the path for the electrons (especially the high-energy electrons) to the channel exit plane where the Hall current, responsible for ionizing gas propellant, is formed.

The two operating conditions tested were 300 V and 150 V with a 20 mg/s anode flow rate using the H6 Hall thruster. All results with the downstream reverse-flow cathode were compared to identical measurements taken with the standard, centrally mounted cathode. Performance parameters were obtained from thrust stand data and the breakdown of utilization efficiencies was found using a suite of thruster diagnostics (Faraday probe (FP), Langmuir probe (LP), retarding potential analyzer (RPA), and ExB probe). These tests were conducted with the thruster body floating instead of grounded, which more closely simulates thruster conditions when operated in space. For the 300 V 20 mg/s nominal H6 thruster condition, the total thruster efficiency increased by a few percentage points with the external, downstream cathode as compared to the central cathode configuration; however, for the 150 V off-nominal condition, thruster efficiency decreased by one percentage point for the same downstream cathode positioning.

For both operating conditions, RPA measurements showed an increase in voltage utilization efficiency of at least a few percentage points for the external cathode over the central cathode, and ExB probe measurements showed that the charge utilization remained about the same. For both cathode orientations, the EEDFs were calculated and characterized from LP data at locations behind and to the side of where the

reverse-flow cathode was placed. For the external cathode positioning, the electron temperatures from these drifting Maxwellian distributions were on average about half the value of the corresponding central cathode values at the locations where data was taken. In addition, the electron number densities were 30-70% larger for the external cathode outside of the central peak region, and the densities were comparable near thruster centerline. These trends are applicable to the ion number densities through quasi-neutrality.

The results implied that in both operating conditions, the reverse-orientation cathode placed more control on directing high-energy electrons into the thruster channel since less were in the downstream locations, and no additional energy was added or removed from the system. The reason why these EEDF changes only correlated with an increase in efficiency for the nominal condition is most likely due to a larger ion beam divergence in the off-nominal condition. However, to confirm these inferences, internal ion current density and divergence measurements where thrust is produced are needed.

Therefore, this quest for EEDF control made clear the need for non-invasive, performance diagnostic measurements inside the thruster channel near the exit plane where thrust is produced for being able to draw more direct conclusions not only about the results from the methods considered but also about thruster operation, performance and dynamics in general.

CHAPTER I

Introduction, Background & Motivation

1.1 What is Space Propulsion

While the first person to come up with the equation that describes the velocity increment of a rocket that is propelled forward by the expulsion of some of its mass, was Scientist Konstantin E. Tsiolkovsky in 1897 motivated by the possibility of space travel, equations that describe the velocity of the rocket at points along its trajectory and the velocity and altitude of the rocket once all the propellant is used up were first written down by the Mathematician William Moore in 1813. Moore came up with these equations for application to weapons research and was led to develop these relations by a competition set up by the Copenhagen Scientific Society in 1809. The challenge questions asked for a description of the trajectory a rocket travels along in vacuum and in air, and asked how to characterize and eliminate trajectory disturbances caused by the fuel not being expelled in parallel layers, perpendicular to the axis of motion. Rocket use in warfare had been around for a while when this inquiry challenge was published; however, these questions were driven by the desire to improve the reliability of these devices during wartime use. Moore published his findings in a collection of papers (titled 'On the Motion of Rockets', 1810, 1811) and in a book (*A Treatise on the Motion of Rockets*, 1813).[1, 2]

On the other hand, Tsiolkovsky, born in 1857, was inspired by his passion for the

possibility of human space travel and he derived what is now called the rocket equation for this specific application. He described the velocity of the rocket in relation to its changing mass specifically, instead of a constant thrust term under the assumption of a constant fuel burnout rate as Moore had used. During his scientific career, Tsiolkovsky also made several other contributions that brought us closer to making spaceflight a reality. These included being the first to work out such details as using liquid oxygen and hydrogen fuel for a rocket, describing how to carry out soft landings on planets and moons that do not have an atmosphere, developing detailed plans for what he called spacestations and space colonies, designing spacesuits that would allow people to leave a spacecraft and have maneuverability while completing tasks in space, and sketching out various extravehicular activity (EVA) techniques. He recorded these ideas in many publications such as a series of articles called 'Exploration of Cosmic Space by Means of Reaction Devices' in 1903, 1911, 1914 & 1926 and the book *Space Rocket Trains* in 1929. His detailed contributions are why he is considered a pioneer in astronautics and rocket dynamics, and called the father of spaceflight.[3–5]

We can motivate the derivation of the Tsiolkovsky rocket equation by considering the ensuing drawing of a rocket in motion vertical to the earth's surface. This diagram, Fig. 1.1, shows the forces at work on the rocket, which are the force of the propellant and the force of gravity. Air resistance is neglected in this abbreviated derivation. In order to correctly write down the equations of motion that describes this system that leads to the rocket equation, we must, as Tsiolkovsky did, apply certain axioms in physics.

First we know from Newton's first law that any object either stays at rest or in motion at a constant speed unless acted upon by a force. In other words, only a force can change the velocity of an object. If there are no forces acting on an object, then its linear momentum is conserved throughout time. An object's linear momentum is defined as its mass times its velocity ($\vec{p} = m\vec{v}$). If there is a force acting on the

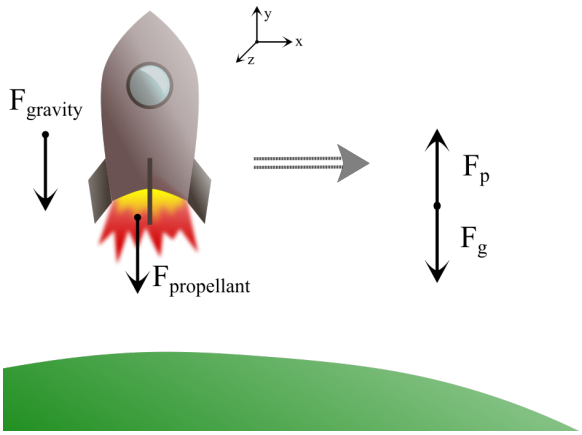

Figure 1.1: A diagram showing the forces acting on a rocket while moving away from earth's surface (neglecting air resistance) and the free body diagram for the rocket, which is obtained using Newton's third law.

object, then this leads to Newton's second law, which is that the rate of change (in time) of an object's momentum is equal to and is in the same direction as the total force acting on that object:

$$\vec{F}_{tot} = \frac{d\vec{p}}{dt} = \frac{d(m\vec{v})}{dt} = m\frac{d\vec{v}}{dt} = m\vec{a}. \tag{1.1}$$

Newton's second law can also be used to describe the thrust of a rocket, which is the product of the rate at which the fuel is being used and the speed at which the fuel is leaving the rocket:

$$\vec{T} = \vec{F} = \frac{d(m\vec{v})}{dt} = \vec{v}\frac{d(m)}{dt} = \vec{v_e}\dot{m} \tag{1.2}$$

where v_e is the velocity of the propellant relative to the rocket, and is termed the effective exhaust velocity. It is taken as a constant in this simplified derivation.

Tsiolkovsky perceived that these relations along with Newton's third law, which states that for every action, there is an equal and opposite reaction, could lead to an equation describing the change in velocity of the rocket, which will be depicted in

this derivation. From Fig. 1.1, the forces seen to be acting on the rocket (shown on the left) lead to the free-body diagram (on the right) through understanding that the action of the propellant being expelled downward from the rocket creates an equal but opposite reaction on the rocket ship propelling it upward. This free-body diagram leads to the following equation of motion from Newton's second law:

$$\sum \vec{F} = \cancelto{0}{\sum \vec{F}_x} + \sum \vec{F}_y + \cancelto{0}{\sum \vec{F}_z} = \sum \vec{F}_y \tag{1.2a}$$

$$= \sum F_y \hat{\boldsymbol{y}} = (F_{propellant} + F_{gravity})\hat{\boldsymbol{y}} \tag{1.2b}$$

$$= m\frac{d(v)}{dt}\hat{\boldsymbol{y}} = (v_e\dot{m} - mg)\,\hat{\boldsymbol{y}} \tag{1.2c}$$

$$m\frac{dv}{dt} = -v_e\dot{m} - mg. \tag{1.3}$$

Going from Eqn. 1.2c to 1.3, we have also switched the frame of reference from that of the spaceship to that of a stationary observer, so the negative sign in front of v_e represents the fact that the exhaust velocity is opposite the direction of motion of the rocket.

When gravity is neglected and we integrate both sides of the equation, this leads to Tsiolkovsky's rocket equation:

$$m\frac{dv}{dt} = -v_e\frac{d(m)}{dt} \tag{1.4a}$$

$$dv = -v_e\frac{dm}{m} \tag{1.4b}$$

$$\Delta v = v_f - v_0 = -v_e ln\left(\frac{m_f}{m_0}\right) \tag{1.4c}$$

where m_0 is the initial mass of the entire rocket (including the propellant) and m_f is the mass of the rocket at the point in time later on when all of the fuel has been used.

The Δv calculated in Eqn. 1.4c does not represent the total change in the spacecraft's velocity over the course of the trip, but describes the sum of all of the instantaneous changes in speed (or the sum of the total instantaneous thrust per unit mass) over the course of the trip needed to complete the mission and is called the velocity increment or the delta-v. This is different from the total change in velocity from the beginning to the end of the mission because in the event of deceleration to zero velocity at the end of a mission in order to land on a celestial body, the Δv for that trip would still be a non-zero value. The Δv takes into account all changes in speed needed for acceleration of the spaceship at the beginning of the trip, deceleration at the end to enter an orbit or land, and includes all other maneuvers that occur in between. The equation for Δv given in Eqn. 1.4c can be manipulated to give

$$m_f = m_0 e^{-\Delta v / v_e} \tag{1.5}$$

which shows the relationship between the final mass of the rocket, and the initial mass, the effective propellant velocity, v_e, and the Δv. From this equation it can be seen that for small v_e relative to Δv, m_f is small relative to m_0. This form of the rocket equation demonstrates the power of this relation to the initial phases of planning a space expedition in terms of determining what propulsion exhaust velocities would be needed for the trip's Δv and desired delivered payload weight.

Another relation that is used in mission planning when gauging the effectiveness of a propulsion system's v_e for a given mission is the specific impulse (Isp) which is

$$I_s = \frac{\dot{m} v_e}{\dot{m} g} = \frac{v_e}{g}. \tag{1.6}$$

The Isp describes the thrust provided by the fuel relative to the weight-use-rate of the fuel. For a higher specific impulse, the fuel flow rate required to obtain a certain Δv is smaller; however, a smaller fuel flow rate means the thrust will be lower, which

leads to the spacecraft taking longer to reach that Δv. This relationship between Δv, I_s, and $\dot{m}$ will be further explored in the next three sections.[6–8]

1.2 Chemical Propulsion

Chemical propulsion systems are characterized by having low specific impulse (Isp) and very high thrust. The first rockets for wartime use and space applications employed this kind of propulsion. The basic principle behind chemical propulsion is that thrust is produced by the expulsion of the bi-products heated by the chemical reaction that created them. The chemical reaction was the result of mixing two or more materials. In modern rockets, a nozzle at the end of the rocket is used. The nozzle is designed to optimize the thrust produced by the expansion of the heated bi-products, and to maintain a certain pressure inside the rocket chamber where the chemical reaction is taking place. Many combinations of chemicals and their resultant reactions can be exploited to create thrust for a rocket. Some of the earliest versions of rockets, employed by Chinese militaries for war in the 13th century (that were actually propelled by their constituents and not by an arrow from a bow-shot) used black powder (gunpowder), which is a combination of sulfur (the fuel), charcoal or meal powder (the binder) and saltpetre (potassium nitrate $KN0_3$, the oxidizer) in a slow burn to create thrust.[1, 9] This mixture is classified as a type of solid fuel.

Currently, there are many types of chemical propulsion systems that are used for space applications, and they can be broken down into various categories including solid fuel and liquid fuel rockets. Solid fuels do not produce the largest thrust values out of all the chemical propulsion fuel subcategories; however, they can be stored in the rocket for long periods of time, and then still perform as expected. Due to this benefit, they are used for applications such as military missiles, and as auxiliary propulsion for increasing the speed or changing the attitude of a spacecraft or launch vehicle. An example of solid propellant used in a modern space application is a

combination of atomized aluminum powder (the fuel), ammonium perchlorate (the oxidizer), iron oxide powder (the catalyst), polybutadiene acrylic acid acrylonite (the binder) and an epoxy curing agent. This solid fuel mixture is used for the NASA Space Shuttle Solid Rocket Boosters (SRBs).[10] Solid propellant rocket motors can have vacuum exhaust velocities up to about 3,000 m/s.[7, 11]

In chemical propulsion systems that employ liquid fuel, the liquids are fed into a combustion chamber where they vaporize, mix, combust and expand. One subset of liquid propellant engines are bipropellant rockets such as the NASA Space Shuttle main engines that used liquid hydrogen as the fuel and liquid oxygen as the oxidizer. Examples of other spacecrafts that currently use various types of liquid fuel motors are the United Launch Alliance (ULA) Delta IV, SpaceX's Falcon 9, and the Russian Soyuz rockets. These engines can have effective exhaust velocities up to 5,000 m/s.[7, 11]

The high thrust that chemical propulsion can supply, is what allows them to be useful for escaping earth's gravitational field where a thrust to vehicle weight ratio of more than one is required. The thrust each of these propulsion units can provide is up to several hundreds of kNs. [11] However, some missions that are characterized by a high Δv are best carried out with a propulsion system that has a comparably high exhaust velocity. Given what was shown in Section 1.1 with Eqn. 1.5, which is that in order to keep the amount of propellant required for a mission to a reasonable fraction of the total mass of the spacecraft, in order to deliver an adequately sized payload to the final destination, as the Δv increases, the propulsion system's exhaust velocity needs to be similar to this value.

The exhaust velocities to vacuum that chemical propulsion systems can produce are up to values of around 6,000 m/s.[7] Chemical propulsion exhaust velocities are limited by the energy produced by the chemical reaction and the amount of additional increase in speed that nozzle expansion can produce. However, missions such as

a round trip expedition between Earth and Mars' surface, or the same for other destinations such as Mercury, Jupiter's moons and Saturn's moons all have a Δv on the order of 10^4 to 10^5 m/s.[7, 11] For missions such as these, a propulsion system that can produce exhaust velocities orders of magnitude higher than what chemical propulsion is limited to is needed.

1.3 Electric Propulsion (EP)

Electric propulsion refers to any spacecraft engine that uses electric and magnetic fields to confine and accelerate charged propellant particles to produce thrust (electrostatic propulsion and electromagnetic propulsion), or that heats a propellant gas by electrical means (electrothermal propulsion). In electrostatic propulsion systems, the energy that translates into directed acceleration of the propellant is supplied by an external power supply, and applied directly to the propellant particles. This means that the exhaust velocities attainable by these propulsion engines are not limited by an internal energy release as it is with chemical propulsion. Instead it is limited by how much external power can be supplied. Due to this feature, electric propulsion engines can reach much higher v_e values than chemical rockets.[7]

1.3.1 Hall-effect Thrusters (HETs)

A Hall-effect thruster (HET) is a type of electrostatic propulsion system. In a Hall thruster, Fig. 1.2, the voltage applied between the anode (at the beginning of the thruster channel) and the cathode (just outside the exit plane) sets up an axial electric field (E-field). In addition, a semi-radial magnetic field (B-field) is applied towards the end of the thruster channel using anti-parallel, coaxial solenoids (electromagnets) of different lengths. The B-field magnitude is scaled so that the electrons are magnetized and the ions are not. This means that the Larmor radius of the electrons is much smaller than the length scale of the thruster channel so that

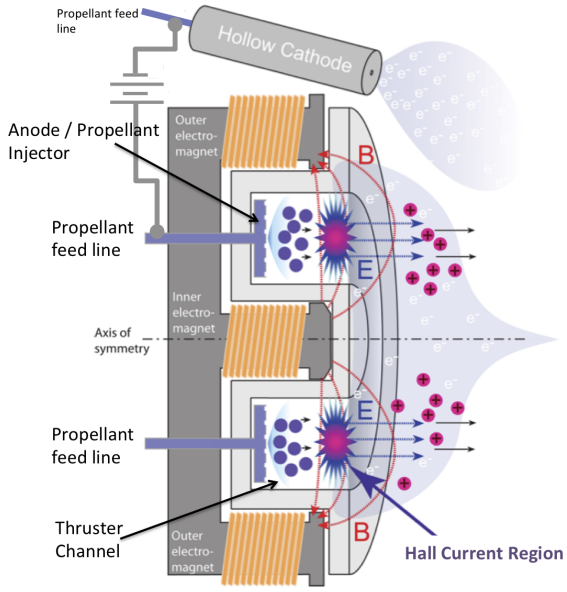

Figure 1.2: Schematic of a Hall Thruster. From Ref. [14] and modified slightly.

the established semi-radial B-field and axial E-field (crossed electric and magnetic fields, or ExB fields) impede the flow of the electrons to the anode by causing the electrons from the cathode to circulate azimuthally near the exit plane, establishing the "Hall current." This Hall current maintains the electric field along the channel. (See Section 1.9 for more details about Hall thruster operation.) A constant stream of neutral gas propellant (usually xenon), which is injected into the channel through the anode, collides with this energetic (on the order of 10 eV) electron Hall current. The resultant ions, which have a large Larmor radius with respect to the thruster channel are therefore accelerated out of the thruster by the electric field.[11–13]

The cathode is also used as a neutralizer. Some of the electrons from the cathode are drawn into the plume where the accelerated ions are, which maintains an overall quasi-neutral plasma plume. This aids in thrust production by preventing a positively charged plume, which would be attracted to the negatively charged Hall current, which would place a charge separation limit on the amount of thrust this system could provide.[11, 13]

The exhaust velocity of the accelerated ions can be calculated using the following equation:

$$v_e = \sqrt{\frac{2Ze\eta_V V_D}{M_{Xe}}}. \tag{1.7}$$

This equation, which was derived using equations from the following references: [8, 13, 15], gives v_e in terms of the mass, M_{Xe}, and charge state, Z, of the xenon ion and the thruster's discharge voltage, V_D. V_D is the voltage applied between the anode and cathode. The parameter η_V is used to account for the actual voltage utilization efficiency of these systems, otherwise Eqn. 1.7 would imply that all the applied voltage translates to particle acceleration, or an efficiency of 100%. The deviation from 100% efficiency is due to a) some of that voltage drop being used to accelerate electrons from the cathode into the thruster and the plume, b) some of the ions being created further down stream and therefore not exposed to the full potential drop, c) ionization costs, and d) other losses. For state-of-the-art Hall thrusters, the efficiency of the applied voltage being used for accelerating the ions is about 90%. [16] More detail about this and other HET efficiency parameters will be discussed in Section 1.5 and Chapter III of this thesis. Eqn. 1.7 can be used to show why HET exhaust velocity is so high. For a typical range of Hall-effect thruster discharge voltages of 50-500 V and assuming 90% efficiency, v_e ranges from 9 x 10^3 to 3 x 10^4 m/s.

These exhaust velocities translate into specific impulse values of around 8 x 10^2 to 2 x 10^3 s. However, the flow rates for these systems are small, around 5-50 mg/s, giving thrust values of ∼40 mN to 1 N for a typical, single HET unit.

1.4 Hall-effect Thruster Space Flight Applications

1.4.1 HETs For Earth Orbiting Satellite Stationkeeping

Currently, one of the main space applications of HETs is stationkeeping of earth orbiting satellites. Station-keeping refers to the maintaining of a spacecraft's intended orbit. It can be perturbed from its orbit by various forces including a) non-uniform gravitational forces from the Earth that come from whether the satellite is over a mountain range or a valley or over the poles, which are slightly flatter, b) gravitational forces from the Sun and Moon, c) atmospheric drag if the orbit is low enough, and d) radiation pressure from the sun. Stationkeeping is accomplished using a combination of a propulsion system, control electronics, sensors, gyros, and other components that together are used to determine how far off course the satellite is, and to correct its motion. [17] Typically for geostationary orbits that are at an altitude of 35,786 km, where the satellite is able to stay over a fixed position relative to the Earth's surface, a Δv of around 50 m/s is needed per year for station-keeping. The use of electric propulsion for this duty has been growing in popularity due to the savings in propellant weight that it allows, which can reduce launch costs or make room for a heavier payload.

For example, a satellite may carry enough propellant to enable it to maintain orbit for 10 years which amounts to a total Δv of $\sim$500 m/s. If a chemical propulsion engine such as a hydrazine thruster is employed, where v_e is equal to 1,000 m/s, then using Eqn. 1.5, the ratio of the payload and spacecraft without propellant (the dry mass) to the spacecraft mass including the propellant (wet mass) is 60%. This means about 40% of the spacecraft's initial weight would have to be propellant. If instead a Hall thruster with an exhaust velocity of 15 km/s is used, then only about 3% of the spacecraft wet mass is propellant. Since it costs more than $20,000 to launch a kilogram of mass into space, this can lead to a significant cost savings or a larger

payload can be delivered to orbit at the same price.[11]

1.4.2 HETs and Lunar Missions

Both electric propulsion systems and chemical rockets have been used to deliver payloads from Earth's orbit to an orbit around the moon (a travel distance of about 380,000 km) where the required Δv is $\sim$5 km/s which translates to an exhaust velocity that is within the range of both of these propulsion systems. In the Apollo missions to the moon in the 1960s and 1970s, the 2nd and 3rd stages of the Saturn V rocket consisted of J-2 engines, each with a thrust of 1.05 MN and an exhaust velocity of 4,210 m/s. These engines allowed the rocket to enter an orbit around the Earth that would prepare for trans-lunar injection and subsequently were also used for trans-lunar injection by being fired in order to break away from this orbit and head towards the moon. These manned journeys to the moon with these chemical propulsion engines took a few days. An unmanned mission to the moon using Hall thrusters takes about a year and a half. For example, SMART-1 was a European Space Agency (ESA) satellite launched in 2003 with various instruments on board to carry out lunar surface measurements while in orbit. The spacecraft used a Hall thruster called the PPS 1350 that operated at 1.35 kW with a v_e of 15 km/s, a 55% efficiency, and a thrust of 70 mN to get to the moon. It took the spacecraft, which had a wet mass of about 370 kg, 84 kg of which was propellant, about 17 months to travel from a geostationary orbit to a lunar orbit. The trip from this geosynchronous Earth orbit to the lunar orbit it decelerated into had a total Δv of around 4 km/s.[11, 18]

For the sake of further understanding the benefits and the limits of electric propulsion as compared to chemical rockets, consider the following thought experiment. If one were to use electric propulsion for a manned mission to the moon and wanted to get there within a few days, then assuming a v_e of 5 km/s and using Eqn. 1.2, a mass flow rate of around 210 kg/s would be needed to match the thrust of a J-

2 engine. This flow rate would require a thruster size that is vastly outside that which can currently be constructed or a current density that is outside of the levels that can currently be withstood by the thruster channel even using present day advanced B-field configurations and wall materials, and would require a power supply that could handle a current that is outside of current capabilities, let alone one that would have a high enough power to mass ratio to fit within mission constraints. However, the prevailing near-term and long-term Hall thruster goals do not involve reaching chemical propulsion level thrust values. In manned missions, Hall thrusters have the potential to shine when dealing with longer distance missions in terms of the propellant savings, which means a larger payload could be delivered as compared to carrying out the same mission with chemical propulsion, or if the additional payload is not needed, flight times could be decreased. However, there are issues that remain that would further increase the benefit of using electric propulsion system for these long-haul manned missions.

1.4.3 A Brief History of EP & HETs In Space

The first suggestions of electric propulsion systems were in the 1900s when both Goddard and Tsiolkovsky independently wrote about them. [19] The first electric thruster was demonstrated by Valentin Petrovich Glushko at the Gas Dynamics Laboratory in Lenningrad (Saint Petersburg), U.S.S.R. around 1930. This electric thruster was an electrothermal rocket, whereas Hall thrusters are categorized as electrostatic propulsion systems. [19, 20] Hall thrusters were first devised in both the U.S.S.R. and in the US at around the same time in the late 1950s. While working systems were reported in the US during the first part of the 1960s, they were only fully developed to flight status in the U.S.S.R. initially. The US did not do this until these systems were reintroduced to them by the Russians a few decades later. [13]

A certain type of HET called an anode layer (TAL) Hall thruster was first proposed

and the concept demonstrated by Askold Zharinov at the Institute of Atomic Energy (IAE), in the suburbs of Moscow, in the late 1950s to the early 1960s. Then, at the Tsentral Research Institute of Machinebuilding (TsNIIMASH), also in the Moscow region, Zharinov led a group that built and carried out initial laboratory testing of these systems by the end of the 1960. Alexey Morozov, another scientist at IAE, led a team in the development of another type of Hall-effect thruster called E-accelerators or stationary plasma thrusters (SPT), which is the type of HET used in this dissertation. Morozov and his team's work was conducted in the early 1960s and the first laboratory models of these SPT Hall-effect thrusters were tested by the mid 1960s. [20] In the US at the NASA Lewis Research Center (now NASA Glenn), the first ion thruster (another type of electrostatic thruster) was operated in 1960. [7]

The first space flight demonstrations of electrostatic propulsion devices by both the US and the U.S.S.R. were in 1964. [7, 20] In 1964, the U.S.S.R. tested a half dozen Pulsed Plasma Thrusters (PPTs) on the space probe Zond-2 for maintaining spacecraft stabilization during 70 minutes of the probe's interplanetary trip to Mars. PPTs were developed in the U.S.S.R. in the early 1960s. [21] Earlier in 1964, the U.S. tested two ion propulsion systems in suborbital space onboard the SERT-1 (Space Electric Rocket Test) spacecraft. [7].

The SPT Hall-effect thrusters have been flown in space since 1972 by the Russians on board geostationary satellites for the purpose of fine satellite orbit correction, complete station keeping and orbit transfer. [20, 22] After Hall-effect thrusters were reintroduced to the US in the early 1990s by the Russians, the first HET to fly on an American spacecraft was the Russian D-55 built by TsNIIMASH. It was flown on the National Reconnaissance Office's Space Technology Experiment Satellite (STEX) in 1998. Since their reintroduction, the US has been designing, building and testing their own HETs once again, and the first US Hall thruster to be flown on a US spacecraft was the Busek BHT-200 on the US Air Force TacSat-2 in 2006. [20, 23–25]

Since the first satellite, Sputnik 1, was launched into orbit by the U.S.S.R. in 1957, more than 8,000 spacecrafts, from various countries with various purposes have been launched into space. Their objectives include deep space science missions to explore and further our knowledge of our solar system, and earth orbiting science, telecommunications, weather, and surveillance satellites. Private companies and governments utilize these spacecrafts. However, fewer than an order of magnitude less than that number have made use of electric thrusters as their primary propulsion. [26] In the 1980s, electric propulsion (EP) started to be used more frequently for orbit station-keeping. The benefits of this device over chemical propulsion for this application were discussed in Section 1.4.1. Since the 1980s, the number of satellites using EP has grown at a steady rate as the cost of the system itself started to decrease due to the maturation of the commercial product lines of these devices. This allowed the cost savings from the smaller total propellant weight possible when using EP as compared to chemical propulsion to be realized. [27] In 2013, there were ∼1,100 operational satellites in orbit around the earth. Of those 437 were in geostationary orbit and about half of those were using electric propulsion for station-keeping. [28, 29]

More recently electric propulsion (EP) has slowly started to be utilized more frequently for deep space missions as well. The Deep Space-1 spacecraft, which launched in 1998, was the first US deep space satellite to use electric propulsion instead of chemical propulsion. The purpose of the mission was to validate new space technology for interplanetary missions. It rendezvoused with the comet Borrelly, and later performed a fly by of the Mars-crossing asteroid 9969 Braille. [30] The successful use of solar power and an ion thruster in this mission laid the foundation for the use of solar EP on future US deep space and interplanetary missions. [31]

Unfortunately, at the beginning of the Deep Space-1 mission, the ion thruster grids shorted together causing the thruster to cut off. Efforts to relight the thruster did not work. It was not until after two weeks of thermally cycling the grids (which

had the effect of varying the size of the grids) that the contamination between the grids, which was causing the shorting, was eventually dislodged. This issue has also been experienced with other ion thrusters that were used on spacecraft. [32] Due to a) the complexity of ion thrusters relative to Hall thrusters, which can lead to issues of this nature, in addition to b) the growing commercial use of Hall thrusters for stationkeeping, which reduces the cost of their production, and c) the lighter weight of Hall thrusters relative to ion engines and chemical propulsion, NASA, through the In-Space Propulsion Technology Program, is heavily investing in Hall-effect thrusters to further improve their specific impulse, throttle-ability, and lifetime so they can meet the specifications needed in order to be used in NASA's near-term and mid-term deep space New Frontiers and Discovery class, cost-capped, science missions. [33, 34]

1.4.4 HETs For Manned Missions

One of NASA's current long-term goals is a manned, round-trip missions to Mars to be carried out with a combination of solar powered 100-Kilowatt class EP systems and chemical propulsion during the 2030s. [35, 36]. Solar energy panels with a beginning of life (BOL) specific power >200 W/kg (<5kg/kW) and an efficiency of ∼33% [37] are being tested and moved through the TRLs to be used as the power source for these missions that will require power levels up to the hundreds of kW. [29] The development of a couple other electric propulsion systems in addition to a Nested Channel HET (NHT) [38] are being supported with the potential to be used for these manned interplanetary missions. If history can be used as a predictor of overall decisions that are made regarding the incorporation of new technology on space missions, given the successful flight heritage of the Hall thruster, which means it poses a lower risk for use on missions of this type, if the NHT is able to meet mission demands, there is a good chance it will be the first EP system to bring people to Mars. [29, 39]

In order to prepare for this interplanetary, crewed mission, NASA is planning to

carry out a number of 'proving ground' missions that will use the technology currently under development to carry out this mission and that will be available within the next 5-10 years. The purpose of these missions will be to demonstrate the performance of this technology and to allow those involved to practice the skills and techniques needed, such as effective responses to the unique situations that will be encountered in this next phase of space travel. The proving ground missions will involve a progression in the complexity of the missions with a corresponding step up in the power rating of the propulsion and power systems used. [29]

To date, the 4.5 kW BPT-4000 Hall thruster, initially used on the AEHF-1 (Advanced Extremely High Frequency) U.S. Air Force satellite for orbit raising in 2010 has been the highest power rated thruster used in space to date. [40, 41] The first missions will demonstrate solar electric propulsion at the 50-Kilowatt power level (specifically 40 kW). One of these missions will be the Asteroid Redirect Robotic Mission (ARRM). This mission, depicted in Fig. 1.3, will be an unmanned mission that will encounter and bring back a small asteroid or a boulder from the surface of a larger asteroid and place it in orbit around the moon. It will utilize three and have one spare 12.5 kW magnetically shielded (long life) HERMeS Hall Thrusters that have an Isp of 3,000 s and a 50,000 hour ($\sim$6 year) lifetime. With the experience gained in this mission, and using components of the spacecraft modules that were proven through carrying out this mission in order to save costs, subsequent proving ground missions will ensue until the technologies and experience necessary to carry out a peopled interplanetary mission have formed and matured. [29, 42, 43]

One possible (simplified) scenario for the Mars mission would involve sending a cargo vehicle ahead of the manned vehicle to deliver the Mars descent and ascent vehicle(s), Mars habitation module, and in-situ resource utilization plant that would make propellant for the ascent vehicle. This cargo mission would most likely use multiple spacecraft modules initially built for the ARRM mission to save costs. These

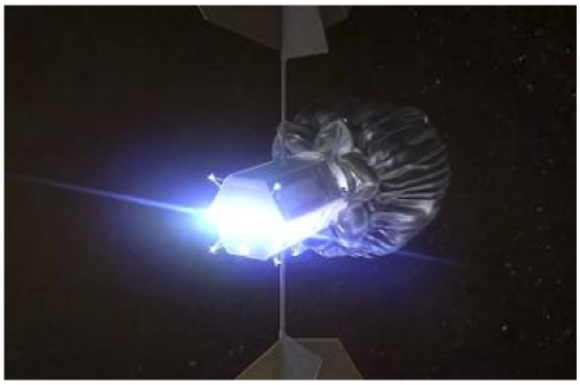

Figure 1.3: A concept drawing of the Asteroid Redirect Robotic Mission's spacecraft reproduced from Figure 12 of Ref. [29].

modules, called blocks, include the solar electric propulsion (SEP), propellant storage, and other systems that would be developed and used throughout the proving ground missions. This mission could be completed with 300 kW of SEP. These blocks would be launched into Earth orbit, assembled, and then would wait for a departure window to make an approximately 300-400 day transit to Mars. [42] (see Ref. [42] for a more detailed possible mission scenario.) Once the cargo was delivered to the planet and the in-situ propellant was finished being produced, the components of the manned spacecraft would be launched into Earth orbit, and assembled for deployment. [44]

The chemical/electric hybrid propulsion system option for these manned and cargo spacecrafts would allow them to take advantage of the benefits of each propulsion system during the portions of the trajectory where they would be most effective. Electric propulsion would be used during the transfer of the cargo and manned spaceships from Earth-Moon orbit to Mars orbit and back, which would bring a significant fuel savings allowing a larger delivered payload— a mission enabler. EP would also be used for slowly spiraling the components of the cargo and manned vehicles from LEO to cislunar space (most likely the Earth-Moon L2 point) (this would take 120-200 days). Chemical propulsion would be used to transfer the crew itself between LEO and L2 (which would only take 8-10 days) to decrease their exposure to the radiation in the Van Allen belts surrounding the earth. Chemical propulsion would also be used to

reduce the manned spacecraft's velocity after transit to Mars to allow quick insertion into Mars orbit leading to a shorter overall trip time for the crew. (An approach to the large elliptical 5-sol parking orbit to allow cargo deployment that is captured into a closer Mars orbit by aerobreaking or chemical propulsion would most likely be used for the preceding cargo vehicle.) [36, 37, 42]

A likely propulsion system for this crewed vehicle would have a MW power level, with 6 operating NHTs running at 125 kW each. The spacecraft would carry enough solar arrays to produce 1 MW of power at beginning-of-life (BOL) and 800 kW of power at end-of-life (EOL) so that a constant 500 V of power could be supplied to the EP engines throughout the mission. The electric propulsion systems would run at an Isp of 2400 s on a direct-drive voltage of 500. This would produce trip times of 330-440 days each way with a delivered payload of 30-50 tons of cargo/payload.

Switching to a variable Isp mode, so that the thrusters could operate between 300 V and 700 V, instead of direct drive, reduces the flight times slightly despite the increase in weight that comes with including the power processing units that would allow these changes in voltage. It accomplishes this by providing more mission flexibility to switch between high thrust and high Isp performance for the various segments of the mission trajectory where one of these options would be more effective. In addition it also allows for a greater margin of safety by providing more options for aborting the mission in the event that terminating the mission becomes necessary. However, currently, there would not be a more drastic decrease in trip length because of the trade off in efficiency that comes with changing the input voltage. [36, 42]

1.4.5 Issues associated with HET Low Voltage Operation

Unfortunately, HET efficiency is not consistently high across the range of Isps that it is capable of operating over. Efficiency is usually much lower in the low voltage range, which is the high thrust-to-power range. For example, with the H6 thruster

used in this research, these trends have been observed during the characterization of this thruster, see Fig. 1.4. From this figure, it can be seen that the high thrust-to-power range refers to low power and low voltage operation and that in this range, the efficiency tends to be lower than in the low thrust-to-power (high power/high voltage) range. [16] Also see [34] and [43] for other examples of this trend that is seen in Hall thrusters.

The Δv for the trip from Earth-Moon orbit to Mars orbit discussed in subsection 1.4.4 is about 6-7 km/s with a travel distance of about 460 million km. [7, 11, 45] With a chemical rocket, a manned vehicle can be propelled to Mars in 180 days. [46, 47]. The longer the crew is in space, the more opportunities there are for equipment to malfunction, and the greater the health risks are for the crew in terms of exposure to harmful levels of high-energy protons and high-energy (E) and charge (Z) (HZE) nuclei contained in the galactic cosmic rays (GCRs), and to solar particle events (SPEs) even with present shielding methods. Current estimates for the total number of "safe days" in deep space for astronauts to be under the career limit or even under a given mission limit still have large uncertainties. As new data and understanding of the risk factors are obtained, which constantly updates these exposure limits, and while even more advanced shielding methods are being investigated, working to shorten flight times through improving thruster efficiency can only help matters, especially for a cost-capped mission, where additional fuel savings may allow extra weight margins for additional or improved shielding that is developed. [48–52] Further fuel savings can still make a significant impact since the total amount of xenon propellant required for a manned, hybrid chemical/electric spacecraft carrying out a round trip to Mars, like the one discussed in subsection 1.4.4, is $\sim$45% of the total spacecraft mass. [36]

Another motivation for added thruster efficiency is the following: With the details given in the previous subsection, an entire manned trip to Mars between the initial cargo delivery, in-situ fuel generation, and crew round trip would take more than 1,750

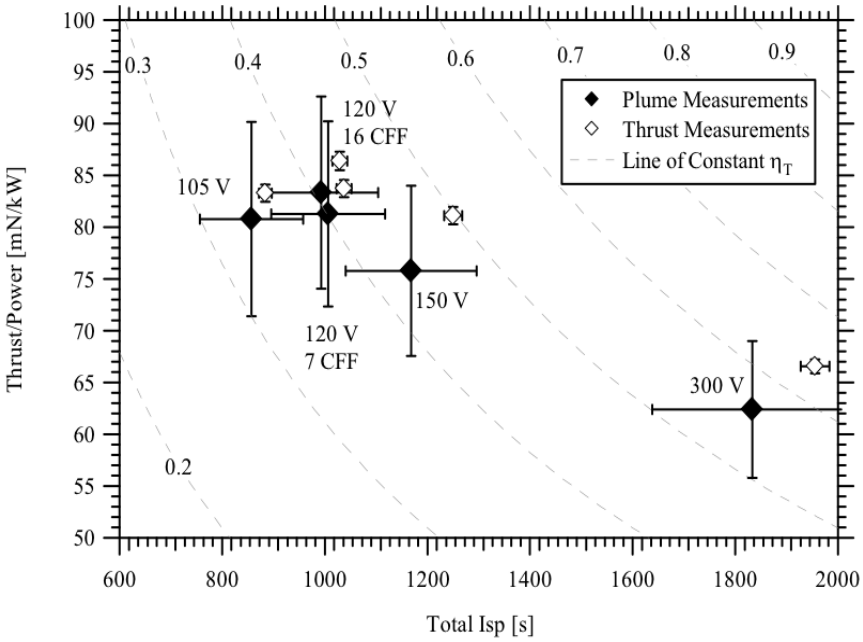

(a)

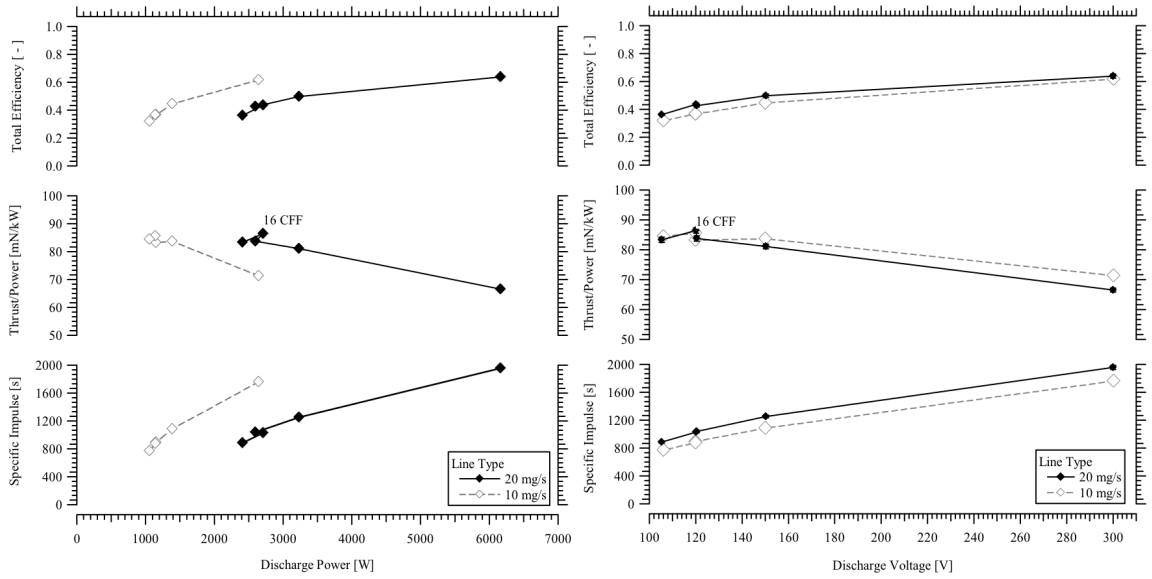

(b) (c)

Figure 1.4: A series of graphs showing performance parameters for the H6 Hall thruster from Ref. [16]. They are Figures 5-25, 5-14, and 5-13 respectively in that document. Unless otherwise stated, the cathode flow fraction is 7%. (a) Thrust-to-power (T/P) vs. Specific Impulse with total efficiency (η_T) for each operating point shown through lines of constant η_T. The anode flow rate ($\dot{m}_A$) for each point in this particular plot is 20 mg/s. As the discharge voltage increases (which directly correlates to an increase in discharge power since $\dot{m}_A$ is the same for all operating points) so does η_T. (b)&(c) These charts show the specific impulse, T/P & η_T vs. discharge power (P_D) and discharge voltage (V_D) respectively at both 10 & 20 mg/s. T/P increases with decreasing P_D or V_D (with $\dot{m}_A$ kept constant) while η_T decreases with decreasing P_D or V_D (with $\dot{m}_A$ constant).

days, assuming a 300 day stay on Mars, which is a total of about 5 years. NASA is hoping for routine trips where the spacecraft can be reused once refueled, without needing complex refurbishing, where instead predictable repairs can be carried out through automation and remotely controlled robots in order to reduce overall costs and permit an ongoing and advancing effort that continues to build on itself for greater and greater goals to be accomplished at the planetary destination. [42, 53]

While the research to develop these capabilities for all the relevant spacecraft stages and modules is underway, it will still be challenging to complete even 2 trips per decade given how long the trip times are currently and given any unforeseen issues that may arise. Due to these initial estimates, it can clearly be seen that it would be prudent to aim to decrease the transit times while still holding onto the cost benefits Hall thrusters provide, and doing so without relying heavily on the possibility of further increases in mission power level, which would also increase spacecraft complexity. Decreasing transit times by increasing efficiency would leave a greater margin of error in case of the unexpected especially while the transition from expendable, to limited reusability, to fully reusable systems is underway.

Improvements in thruster efficiency in the high thrust-to-power (low voltage, low Isp) range, which for these missions would be 300 V, to allow more efficient use of a variable Isp HET propulsion system for interplanetary missions would enable even shorter trip times through greater flexibility for trajectory optimization and through using even less total propellant. This would give greater time and/or weight margins in order to a) meet crew safety needs (once these become more resolved) and b) meet NASA timetable requirements for making these trips frequent enough to be cost effective. In addition, Hall thrusters used for station-keeping, which operate in the lower power regime of around 150 V, would benefit from an increase in efficiency in the high thrust-to-power regime as well.

1.5 Overview of HET Performance and Efficiency Analysis

As discussed in the previous subsection, additional improvements in Hall-effect thruster efficiency, especially in the high thrust-to-power regime, have the potential to provide significant advantages to present-day manned space endeavors that would positively impact crew safety, and trip costs. In order to determine the efficiency of a particular HET, and to measure differences in that efficiency with the various adjustments that are made to aspects of their design, a performance architecture was developed. In this thesis, this framework will be used to analyze the changes made in order to measure progress towards efficiency enhancement.

Thruster efficiency is a measure of the propulsion system's ability to use inputted power to turn neutral gas propellant into charged particles that are then accelerated through as much of the established electric field as possible in directed trajectories that optimize thrust and thrust per unit weight of propellant (or the specific impulse).

As discussed in Section 1.1 the thrust and Isp are defined in Eqns. 1.2 & 1.6 respectively. These equations are restated here:

$$T = v_e \dot{m}$$
$$I_s = \frac{\dot{m} v_e}{\dot{m} g} = \frac{v_e}{g}.$$

HET anode efficiency can be broken down into five different utilization components—charge, voltage, beam, current and mass utilization efficiencies. Voltage utilization, also known as acceleration efficiency, is a measure of how much of the established discharge voltage the ions are accelerated over:

$$\eta_V = \frac{V_{accel}}{V_D}, \tag{1.8}$$

where V_{accel} is the ion acceleration voltage and V_D is the discharge voltage.

Current utilization describes how much of the discharge current is ion current:

$$\eta_B = \frac{I_{ion_T}}{I_D} = 1 - \frac{I_e}{I_D}, \tag{1.9}$$

where I_{ion_T} is the total ion current, I_e is the backstreaming electron current, and I_D is the discharge current. Together voltage utilization and current utilization are the components of the thruster's energy efficiency.

Beam efficiency signifies the effective component of the ions' velocity that is parallel to thruster centerline, and therefore producing useful momentum compared to the ideal case where the velocity of all the ions in the plume is fully parallel to thruster centerline. This is a measure of plume divergence.

$$\eta_{Div} = \left(\cos\theta_B\right)^2, \tag{1.10}$$

where η_{Div} is the divergence efficiency, or beam utilization efficiency and θ_B is the plume divergence half angle. This value can be calculated as the angle from thruster centerline that encompasses 90% (or 95% depending on how it is defined) of the total thruster current, or it can be computed as the ratio of the sum of the axial components of the current to the total current. This second approach can be carried out using the following equation:

$$\cos\theta_B = \frac{2\pi R^2 \int_0^{\pi/2} j(\theta)\cos(\theta)\sin(\theta)d\theta}{I_{ion_T}} \tag{1.11}$$

where I_{ion_T} can be found using the following equation:

$$I_{ion_T} = 2\pi R^2 \int_0^{\pi/2} j(\theta)\sin(\theta)d\theta. \tag{1.12}$$

Here, R is the radial distance between the probe and thruster centerline at the

thruster's exit plane as the probe traverses in a circular arc along a plane that intercepts channel centerline through the hemisphere in front of the thruster to sample the current density, $j(\theta)$.

As for the components of propellant efficiency, charge utilization delineates the ion species fractions and the mass utilization efficiency is a measure of the flux of ions to the total incoming flux of neutrals from the anode.

The charge utilization efficiency is found using:

$$\eta_q = \frac{\left(\sum_{i=1}^{N} \Omega_i/\sqrt{Z_i}\right)^2}{\sum_{i=1}^{N} \Omega_i/Z_i}, \tag{1.13}$$

where the current fractions, Ω_i, are

$$\Omega_i = \frac{I_i}{\sum_{i=1}^{N} I_i}. \tag{1.14}$$

In Eqn. 1.13, Z_i is the charge of the ith ion species, and N is the total number of ion charge states used in the calculation. In Eqn. 1.14, I_i is the current collected by the ExB probe for the ith ion species (see Section 2.7 for details about this probe, which was used to obtain the measurements needed to calculate this value).

The mass utilization efficiency is

$$\eta_m = \frac{\dot{m}_{ion_T}}{\dot{m}_A}, \tag{1.15}$$

where $\dot{m}_A$ is the neutral gas propellant mass flow rate through the anode. $\dot{m}_A$ can be defined as

$$\dot{m}_A = \dot{m}_{ion_T} + \dot{m}_N, \tag{1.16}$$

where $\dot{m}_N$ is the neutral gas mass flow rate out of the thruster, and the total ion mass flow rate out of the thruster, $\dot{m}_{ion_T}$, can be calculated using the following reasoning:

$$\dot{m}_{ion_i} = \frac{M_{Xe} I_{ion_i}}{Z_i e} \tag{1.17a}$$

$$\dot{m}_{ion_T} = \sum_{i=1}^{N} \dot{m}_{ion_i} = \frac{M_{Xe} I_{ion_T}}{e} \sum_{i=1}^{N} \frac{\Omega_i}{Z_i}. \tag{1.17b}$$

Here, $\dot{m}_{ion_i}$ is the mass flow rate of the ith ion species out of the thruster, I_{ion_i} is the ion current of the ith ion species, I_{ion_T} is the total ion current, M_{Xe} is the mass of a xenon ion, and Ω_i is defined in Eqn. 1.14.

As mentioned earlier, an E×B probe is used to measure the parameters needed to calculate the charge utilization. A retarding potential analyzer (RPA) and a Langmuir probe (LP) are used to find voltage utilization, the measurements from an E×B probe and Faraday probe (FP) are used to determine mass utilization, and a FP is used for beam and current utilization. Using these measurements and the utilization efficiency equations, the total thruster efficiency can be found using Eqn. 1.18a:

$$\eta_{tot} = \eta_V \eta_B \eta_{Div} \eta_q \eta_m \eta_{mag} \eta_c \tag{1.18a}$$

$$= \eta_a \eta_{mag} \eta_c = \left(\frac{T^2}{2\dot{m}_A P_D}\right)\left(\frac{P_D}{P_{tot}}\right)\left(\frac{\dot{m}_A}{\dot{m}_T}\right) = \frac{T^2}{2P_{tot}\dot{m}_T}. \tag{1.18b}$$

Notice that η_a, the anode efficiency, is equal to $(\eta_V \eta_B \eta_{Div} \eta_q \eta_m)$. η_{mag} is the electromagnet efficiency, and the cathode efficiency is η_c. The total neutral gas mass flow rate is equal to the anode plus the cathode neutral gas mass flow rates, $\dot{m}_T = \dot{m}_A + \dot{m}_C$. Anode power is equal to $\frac{T^2}{2\dot{m}_A}$, the total thruster power, P_{tot}, is the discharge power plus the magnet power, and P_D represents the discharge power. In summary, this equation for the total thruster efficiency is a measure of the conversion of applied discharge power to jet kinetic power. This total efficiency parameter does not take into account the efficiency of the electrical units that provide power to a Hall thruster.

The total efficiency obtained using the diagnostics mentioned (RPA, LP, E×B probe and FP) can be checked against the total efficiency deduced using thrust stand measurements and Eqn. 1.18b. Checking that these two approaches give comparable efficiency values provides a means to establish additional confidence in the results. Another check for consistency can be done through calculating the current utilization efficiency, η_B, which in Eqn. 1.9 was expanded into an expression that would use FP measurements, and can also be calculated using thrust stand, RPA, and ExB probe measurements using the following equation for I_{ion_T} from expanding the equation for thrust:

$$\begin{aligned}\vec{T} = \sum_{i=1}^{N} \vec{v_{e_i}} \dot{m}_{ion_i} &= \sum_{i=1}^{N} (v_{e_i} cos\theta_B) \dot{m}_{ion_i} \\ &= \sum_{i=1}^{N} \left(\sqrt{\frac{2\, e \eta_V V_D Z_i}{M_{Xe}}} cos\theta_B \right) \left(\frac{M_{Xe} I_{ion_T}}{e} \frac{\Omega_i}{Z_i} \right) \\ &= \sqrt{\frac{2\, M_{Xe} \eta_V V_D}{e}} cos\theta_B I_{ion_T} \sum_{i=1}^{N} \frac{\Omega_i}{\sqrt{Z_i}}\end{aligned} \tag{1.19a}$$

$$I_{ion_T} = \frac{T}{cos\theta_B} \left(\frac{1}{\sum_{i=1}^{N} \frac{\Omega_i}{\sqrt{Z_i}}} \right) \left(\sqrt{\frac{e}{2\, M_{Xe} \eta_V V_D}} \right) \tag{1.19b}$$

The expression for v_e comes from Eqn. 1.7, and the expression for $\dot{m}_{ion_T}$ comes from Eqn. 1.17b. The $cos\theta_B$ term is added in to account for the divergence in the ion trajectories from thruster centerline. [16, 54–57] For more details about these equations, and how they are used, see Section 3.2 of this dissertation and Refs. [16, 54–57].

A high efficiency Hall thruster such as the H6, a 6-kW thruster, has component utilization efficiencies around 80-90%. However, there is still room for improvement, as the product of these constituent efficiencies puts the total thruster efficiency at 50-60% at nominal operating condition [16, 58]. Therefore, in addition to these com-

ponent utilization efficiencies, there are other parameters and elements of these utilization efficiencies that are looked at to further reveal the aspects of the HET that can benefit from further improvements. For example, from the equation for current utilization efficiency, Eqn. 1.9, the backstreaming electron current over the discharge current is called the electron current recycle fraction:

$$r = \frac{I_e}{I_D}. \tag{1.20}$$

This value represents the portion of the measured discharge current that is not ion current but instead electrons migrating upstream within the thruster channel and being collected by the positively biased anode. This current has opposite charge and flow direction to the ion current, and is therefore registered as positive discharge current, but does not contribute to thrust. For the Hall thruster, typical values for this parameter are much larger than what classical collision theory (between neutrals and electrons) predicts for the plasma conditions present in the channel of the thruster. This transport is an issue because HET efficiency depends on its ability to ionize and accelerate neutral propellant, and the ExB fields that establish the Hall current are supposed to prevent the electrons from reaching the anode until a number of ionization collisions with neutrals have occurred. [59, 60]

Since these electrons are reaching the beginning of the thruster channel more quickly than classical collision theory predicts, which decreases their residence time and therefore reduces the total amount of ionization they can accomplish, this uses up power and reduces thruster efficiency. [60] However, it is also stated that this leakage current or some of this leakage current may be necessary for thruster operation by completing the circuit. [61] For the H6 Hall thruster operating at 300 or 150 V and 20 mg/s, the electron leakage current is around 20% of the total discharge current.[16]

Another parameter related to the electron leakage current is the proposed mini-

mum power needed for ionization for steady-state thruster operation. This value can be approximated using Eqn. 1.21a, which was obtained from equations (2-53), (2-19), (2-23) and (2-21) from Ref. [16]. As seen in this equation, the sum of the ionization potential for each ion species weighted by its corresponding ion current fraction and then multiplied by the total ion current produces the minimum ionization power estimate. Using this relation, the minimum total effective ionization cost per beam ion is found with Eqn. 1.21b by dividing the minimum ionization power by the sum of the the ion current divided by the charge state for each ion species. This weighting by the charge of the ion species translates into there being a higher cost for each multiply charged ion created.

$$P_{min} = I_{ion_T} \sum_{i=1}^{N} \Omega_i \, \epsilon_i = \sum_{i=1}^{N} I_{ion_i} \, \epsilon_i \tag{1.21a}$$

$$\epsilon_{B_{min}} = P_{min} \frac{1}{\sum_{i=1}^{N} I_{ion_i} {Z_i}^{-1}} \tag{1.21b}$$

In operation, the difference between P_{jet} ($= I_{ion_T} V_{accel}$) and the discharge power, P_D is larger than P_{min}, and that amount, P_{loss}, defined in Eqn. 1.22a. P_{loss} is usually attributed to Joule heating— specifically energy deposition to the anode and channel walls (ohmic heating), and to plasma interactions within the discharge such as excitation, ionization creating multiply-charged particles, and radiation. Associated with this parameter is the actual ionization cost per beam ion, which can be found using Eqn. 1.22b. [16]

$$P_{loss} = P_D - P_{jet} - P_{min} \tag{1.22a}$$

$$\epsilon_B = (P_D - P_{jet}) \frac{1}{\sum_{i=1}^{N} I_{ion_i} {Z_i}^{-1}} \tag{1.22b}$$

Figure 1.5 shows the values for these variables for the H6 HET for discharge powers corresponding to anode flow rates ($\dot{m}_A$) of 10 and 20 mg/s, and discharge voltages ranging from 105 to 300 V. As seen in Fig. 1.5(a), for constant anode flow rate, P_{min} is relatively constant (compared to the change in jet power). This is because P_{min} is only dependent on the fraction of the discharge current that is ion current, I_{ion_T}, the ion species composition of this ion current,Ω_i, and the ionization potentials for the gas being used,ϵ_i (Eqn. 1.21a); and Ω_i and I_{ion_T} tend to stay relatively unchanged with increasing discharge voltage and constant anode flow rate. Similarly, P_{loss} is relatively constant compared to P_{jet} (Fig. 1.5(a)). P_{loss} depends on P_{min} and the difference between the discharge power, P_D, and the jet power, P_{jet} (Eqn. 1.22a). This means that as P_D decreases with decreasing V_D (while anode flow rate is held constant), a smaller and smaller fraction of the total power is going to jet power.

For example, with $\dot{m}_A$ equal to 20 mg/s, at 300 V, I_{ion_T} = 16.4 A, $P_D \approx$ 6,000 W, $P_{min} \approx$ 300 W, $P_{loss} \approx$ 1,500 W, and $P_{jet} \approx$ 4,400 W, whereas at 150 V, I_{ion_T} = 15.5 A, $P_D \approx$ 3,000 W, $P_{min} \approx$ 240 W, $P_{loss} \approx$ 1,100 W (which is about the same as in the 300 V condition), and P_{jet} is only about $\approx$ 2,000 W. These values are found using the fact that the first, second and third ionization energies of xenon are around 12 eV, 21 eV and 31 eV respectively which means ϵ_{Xe_1} = 12 eV, ϵ_{Xe_2} = 33 eV, and ϵ_{Xe_3} = 64 eV. [16, 54, 62–65]

In Fig. 1.5(b), $\epsilon_{B_{min}}$ is seen to be relatively constant for constant anode flow rate for similar reasons to why P_{min} is in Fig. 1.5(a) and explained above. ϵ_B scales with the difference between P_D and P_{jet}. While a smaller and smaller portion of the total discharge power goes to jet power as V_D decreases with constant anode flow rate, there is still a slight decrease in P_D - P_{jet} since V_D is also decreasing. This is the reason for the trend of ϵ_B decreasing with decreasing P_D. Still, ϵ_B remains significantly larger than $\epsilon_{B_{min}}$ across the range shown. For example, for 300 V and 20 mg/s, $\epsilon_{B_{min}}$ is $\approx$ 20 eV while ϵ_B is $\approx$ 120 eV. At the same flow rate and 150 V, $\epsilon_{B_{min}}$ is $\approx$ 17 eV while

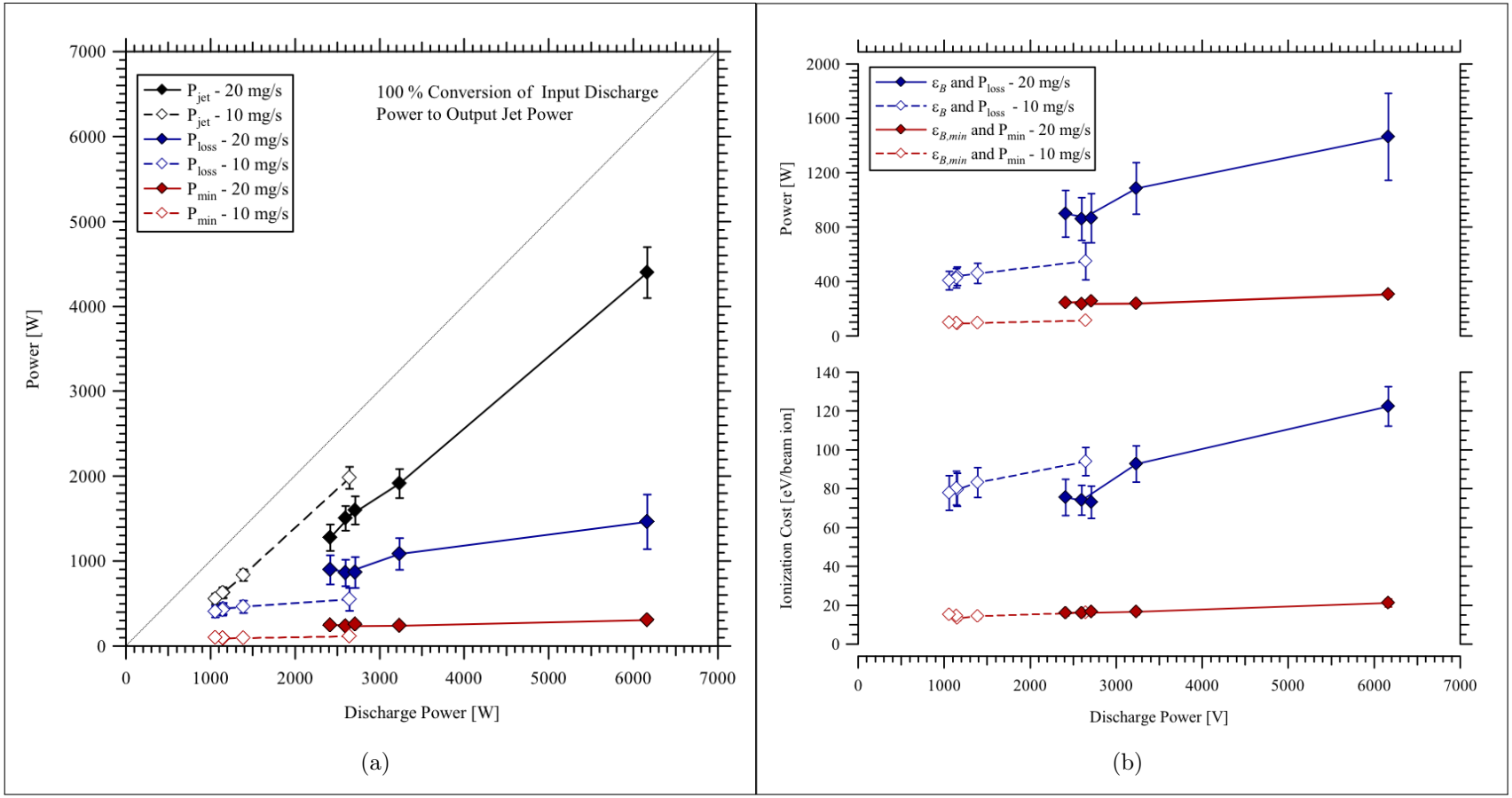

Figure 1.5: A series of graphs showing performance parameters for the H6 Hall thruster from Ref. [16]. They are Figures 5-34 and 5-35 respectively in the reference document. The cathode flow fraction is 7%. (a) This figure shows the how the discharge power (P_D) is utilized for ion acceleration (P_{jet}), and how the rest of the power can be broken down into a classical estimate of the minimum power needed for ionization (P_{min}) and the remaining power (P_{loss}) using Eqns. 1.21a & 1.22a. These values are shown for P_D corresponding to anode flow rates ($\dot{m}_A$) of 10 and 20 mg/s, and discharge voltages (V_D) ranging from 105 to 300 V. (b) For the same operating conditions, this chart shows P_{min}, the minimum ionization cost per beam ion ($\epsilon_{B_{min}}$), and the actual ionization cost per beam ion (ϵ_B) vs. P_D. $\epsilon_{B_{min}}$ & ϵ_B can be calculated using Eqns. 1.21b & 1.22b.

ϵ_B is $\approx$ 93 eV. [16]

Another parameter of interest is the ionization fraction. This parameter is usually compared to the mass utilization efficiency. However, the mass utilization is a measure of the flux of ions to the total incoming flux of neutrals from the anode, see Eqn. 1.15, so it is a number density times a velocity, while the ionization fraction compares the number density of ions to the number density of neutrals. This parameter is measured downstream of the ionization region of the thruster, and it assumes that the neutrals and ions flow over equal areas. See Eqn. 1.23. The ionization fraction in Hall thrusters is around 10%. However, the velocity of neutrals in a thruster is around 100 m/s, while that of the ions is around 10 km/s— 2 orders of magnitude higher. So even though the density of ions is a tenth of that of the total flow, because their velocity is so much higher, the mass utilization efficiency is very high, usually $\sim$90%. In addition, since the mass utilization efficiency is relative to the anode mass flow rate, this ratio can be higher than 100% if a substantial portion of the cathode flow is ionized. [16, 54] For these reasons, the cost per beam ion and the ionization fraction more clearly point to loss mechanisms that can be targeted to create significant HET efficiency improvements.

$$\Theta_{ion_T} = \frac{n_{ion_T}}{n_T} \tag{1.23}$$

In addition, the cathode-to-ground voltage, V_{c-g}, has significance when gauging thruster performance. Consider Fig. 1.6 which shows the beam voltage, V_b or V_{accel}, the plasma potential, V_p, and V_{c-g} and how these voltages add up to the discharge voltage, V_D. This figure also shows how these voltages are distributed around the reference potential, which is ground. The ions are accelerated between the anode potential and the plume's plasma potential. Along with V_p, V_{c-g} is one of the voltages that takes away from the potential that can be used for V_{accel}. The cathode-to-ground

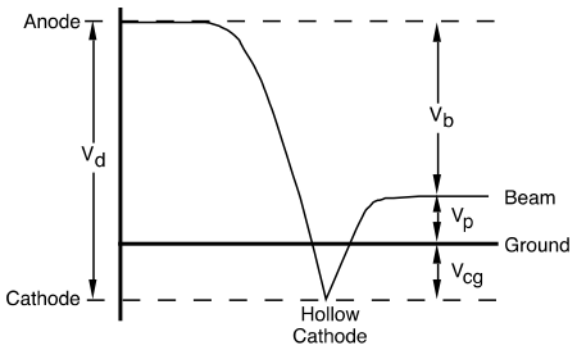

Figure 1.6: A diagram, taken from Ref. [66], showing how the applied discharge voltage is distributed within the HET electrical system.

voltage represents the potential needed to accelerate the electrons out of the cathode and into the plume and Hall current. The less potential drop needed for this task, and the smaller the V_p means that the portion of V_D that can go towards accelerating ions would be larger. Typically for Hall thrusters, the V_{c-g} is around 10 V below ground. [13, 16, 58]

1.6 Overall Problem Statement

Previous investigations of state-of-the-art Hall thrusters have observed lower total efficiency operation in the high thrust-to-power, low discharge voltage regime when compared with high power, high Isp operating modes. Higher total thruster efficiencies are needed in the high-thrust-to-power regime (around 300 V) for trajectory optimization, mission flexibility and safety of high delta-v missions, whether the mission is powered with solar arrays or nuclear reactors. The more efficient the propulsion system is the fewer improvements and breakthroughs in nuclear energy systems will be needed in order to decrease the travel time to Mars. In addition, station-keeping Hall thrusters, which operate in high thrust-to-power mode, at around 150 V, would benefit from efficiency increases as well. Therefore, all high power interplanetary missions and earth orbiting satellites employing Hall thrusters can benefit from finding a way to make further increases in thruster efficiency in the low power range.

NASA desires the full propulsion system to have efficiencies greater than 60% across the range of operating Isps for long haul missions. This means the efficiency of the thruster itself needs to be larger than this amount. [67]

For low Isp HET firing, the efficiency gap between this goal and actual performance numbers is the highest. When the performance loss mechanisms behind the polarity between low and high discharge voltage operation were examined, it was discovered that increased electron leakage current to the anode and increased ion beam divergence in this high thrust-to-power regime are the main contributors. This references the current utilization, η_B, and the electron current recycle fraction, r in addition to divergence efficiency, η_{Div}, and the the plume divergence half angle θ_B, which were discussed in Section 1.5. The near-term goal of finding a way to improve Hall thruster efficiency during low Isp operation will require seeking a deeper understanding of the complex interactions and form of these magnetized discharges and specifically of thruster plasma and electron dynamics that contribute to a larger electron current to the anode and greater beam divergence in the high-thrust-to-power regime.

1.7 Prior HET Efficiency Improvement Research

Within the last decades, efforts to increase thruster efficiency have explored various methods including adding in an upstream initial and additional ionization stage and nesting multiple thruster channels. The helicon Hall thruster (HHT) is a two stage HET that investigated the use of an opening radiofrequency ionization stage in increasing thruster efficiency in the high thrust-to-power range [68]. Dual and triple channel nested Hall thrusters (NHTs) were also developed and a number of performance characterization studies have been carried out for the dual channel NHT, the X2. Since at present, single channel HETs tend to have a narrow band of operating conditions at which their efficiency peaks given the channel dimensions chosen, NHTs

are being developed for complex and long-range space missions to planets further out in our solar system. For these types of applications, high-power thrusters (10s to 100s of kW) will be needed, which can also operate efficiently at low power for solar powered missions when the spacecraft is further away from the sun. NHTs can achieve this in a multi-channel mode so that a higher total current can be obtained while maintaining standard operating voltages. In addition, each channel is designed for optimized performance in a particular operating regime so that with various combinations of channel operation, peak thruster efficiencies can be maintained over a wide power throttling range.[69–72]

The X2 has demonstrated high-power operation up to 10 kW (250 V 40 A) with comparable efficiencies to state-of-the-art thrusters. In addition, in the high thrust-to-power range of the H6, at operating conditions of 300 V 20 A and 150 V 40 A with the X2 operating in dual-channel mode, it achieves comparable thrusts and efficiencies. With nesting channels, inter-channel neutral ingestion was observed, given the fact that in dual channel mode, the thrust increased to 4-9% greater than the superposition of the performances of each channel, controlled for background xenon pressure. It was discovered that this increase in thrust was due to the neutral ingestion resulting in a higher beam current. Given this and the lessons learned from this iteration of NHT design, specifically the lower overall performance of the outer channel compared to the inner one, it is hoped that the X3 will have even better efficiency at these operating conditions. Still, since a single channel HET is the building block of the NHT, further improvements to HETs can lead directly to further improvements in these more complex systems as well [16, 55, 69–73].

Looking at the issue of improving thruster efficiency in the high thrust-to-power range from a different angle opens up the possibility of approaching this problem from different paths. Past and current efforts have focused on improving thruster efficiency by adding additional components and complexity to the thruster. Another

approach considers the electrons, a key element in the ionization process, and asks if there is a way to tailor their energies to decrease the ionization cost per beam ion and increase ionization. This course is of interest because on average, 90% of the propellant remains neutral, which means there is more than enough un-ionized propellant currently in the channel of a single-channel thruster during operation to provide room for significant improvements in efficiency.

1.8 The Hollow Cathode

The hollow cathode is the thruster's source of ionizing and neutralizing electrons. It is a type of plasma source that features a special material that has the property of emitting electrons when it reaches a certain temperature. This insert material, that is shaped into a hollow cylinder, makes the hollow cathode a useful tool in various plasma applications such as to provide the charge species needed to study various physical properties of matter, to power or regulate another plasma source, or to aid in a myriad of manufacturing practices. In a hollow cathode, once the insert material reaches emission temperatures (which is usually accomplished with a concentric heater around the insert) a high voltage is applied to the keeper, which is the anode of this plasma source, and is shown in Fig. 1.7(a). This voltage accelerates the electrons and draws them out of the insert region. As the electrons travel down the center of the hollow cathode, they collide with the neutral gas that is fed into this area, creating ions in the process. This starts the cathode's plasma discharge (Fig. 1.7(b)).

Once the discharge is established, the keeper voltage will decrease and level out to a value that will maintain the insert temperature, allowing the discharge to be self-sustaining. This is because the voltage drop between the keeper and insert that pulls electrons from the cathode also causes ions to flow in the opposite direction. These ions accelerate through the insert's sheath and collide with the insert. This heats the insert causing more electrons to be emitted, which collide with the flowing

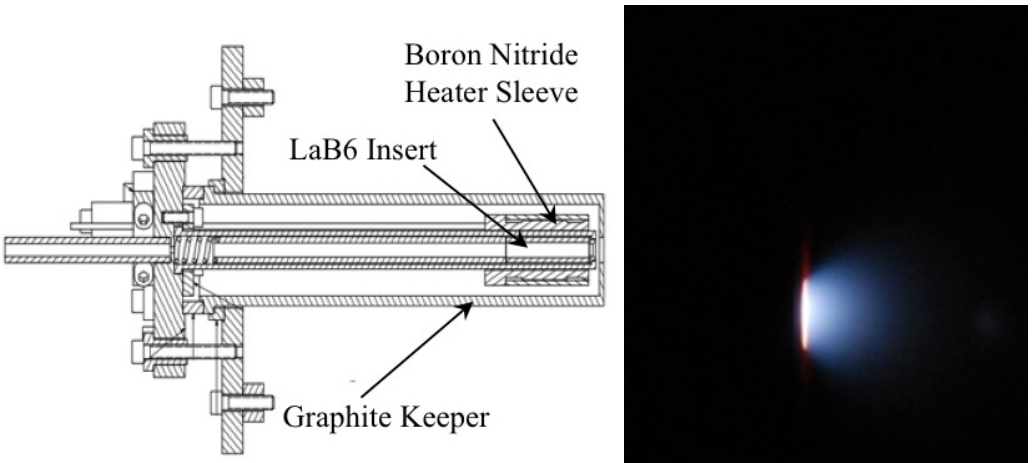

(a) (b)

Figure 1.7: (a) Cutaway cross section of the lab-built hollow cathode showing the ceramic sleeve used as a heat spreader for the heating filament, the insert, and the keeper. (b) Operation of the LaB6 cathode without an anode.

gas causing more ions to be formed. The insert region of the cathode is characterized by a high density yet neutral plasma with a low electron energy and therefore a low plasma potential. The low plasma potential and high collision rates mean the energy of ions that accelerate through the sheath to the insert have energies less than 20 eV, which reduces insert material sputtering, and the quasi-neutral plasma means that the electron emission is not space charge limited. [13]

A new laboratory model lanthanum hexaboride (LaB_6) hollow cathode sized for a 20 A HET discharge was developed at PEPL. This development was led by McDonald and reported in the literature.[74] The cathode's design was based on previous high-current LaB_6 [75] cathodes with a modified heating element, which is discussed in Ref. [74] and also in Section 2.5. This cathode was developed to be used as the plasma source for initial experiments to study electron dynamics in Hall-effect thrusters at PEPL. Since the cathode is the main source of electrons for the thruster, and can be operated using a relatively smaller scale production than the thruster, it serves as an ideal platform for testing electron dynamics experimental procedures and diagnostic

tools that will be used on the thruster.

One of these projects involved using this cathode as a test cell in a triode configuration with an external annular anode to permit operation in plume mode for extended periods in order to test a potential gas-mixing EEDF tailoring method for HETs and to practice LP measurement techniques in preparation for EEDF tailoring experiments on the HET itself (Chapter III). These applications are discussed in Section A.2.

The hollow cathode was first discussed by Paschen in 1916. His setup, which created a low pressure discharge, featured a rectangular hollow cathode made of a metal-like material and a cylindrical anode. It was used as the excitation source to analyze the spectral lines of helium. The hollow cathodes used today have a wide variety of applications, and their designs are all versions of Paschen's initial cathode yet modified for the particular implementation. [76] Over the years, the applications of hollow cathodes have included use as the excitation source in analytical spectroscopy, as done by Paschen, the ion source for industrial thin film application, the electron source in scanning electron microscopes, and the electron source for plasma volume neutralization in electric thrusters.

LaB_6 was first investigated for use as an electron emitter by Lafferty in the late 1940s. [77] The Russians have used LaB_6 hollow cathodes in Hall thrusters from the first flight of a SPT in 1972. [78] In the United States, barium-oxide impregnated tungsten (BaO-W) dispenser hollow cathodes were used initially, starting in the 1960s. [75] These cathodes make use of a tungsten-based insert that is gridded with holes, and filled with a barium, calcium oxide, and alumina mix. When heated to temperatures around 1000 °C, this mixture dispenses electrons from these openings in the tungsten.

Lanthanum hexaboride is made by press-sintering LaB_6 powder into a solid, polycrystalline (i.e., multiple crystal orientation) form. [79] It requires a higher operating temperature than BaO-W, and the US did not begin to consider LaB_6 for hollow cath-

odes for space-application until the 1970s. Compact high current cathodes became of interest at this time for future applications that would require high current densities such as high-power electric thrusters that are able to deliver a higher thrust. Experimental data for BaO-W and LaB_6 calculations using Richardson and evaporation coefficients ascertained by Lafferty show that BaO-W has a maximum emission current density of 12 A/cm^2 at an operation temperature of $\sim$1100 °C, whereas LaB_6 can provide 40 A/cm^2 at a temperature of 1800 °C. [80] For comparison, LaB_6 provides $\sim$12 A/cm^2 at around 1510 °C. [81]

In addition to their high current density, LaB_6 has a longer calculated insert lifetime than a BaO-W insert, by almost an order of magnitude for discharge currents from 10 A to 60 A. These calculations take into account the evaporation rate of these materials, which is lower for LaB_6, despite its substantially higher operating temperature, up to an emission current density of 15 A/cm^2. The slightly lower evaporation rate and the fact that there is more bulk emitting material in LaB_6 than in the impregnated holes of the tungsten matrix in BaO-W dispenser material are what account for the longer LaB_6 lifetime. These calculations do not take into account impurity build-up, which reduces lifetime and re-deposition of some insert material after evaporation, which increases lifetime. [79]

Another advantage of LaB_6 is that special conditioning and storage procedures do not have to be followed, because this material is not susceptible to contamination from oxygen and water vapor, which can raise the work function of BaO-W, decreases its life, and often times cease emission from the material altogether rendering the dispenser cathode completely useless. The reason for this is that in BaO-W, a chemical reaction needs to take place in the barium, calcium oxide, and alumina mixture at the 1000 °C operating temperature in order for a barium-oxide dipole to form to reduce the work function of the surface to $\sim$2 eV. This is what allows this material to be an abundant source of electrons. In comparison, the formation of a low work function

on the surface of LaB_6 material does not involve a chemical reaction. The lanthanum hexaboride itself is the electron emitter and has a work function of ∼2.7 eV at a temperature of 1650 °C. Therefore, a LaB_6 insert's emission capability is relatively unaffected by impurities that can hinder the chemical reactions necessary in BaO-W cathodes. [82]

However, in addition to the higher temperatures required for lanthanum hexaboride to emit electrons, another disadvantage is that at high temperatures, some frequently used refractory metals such as tungsten and molybdenum are susceptible to boron diffusion if they are in contact with the LaB_6 material. Boron diffusion into these metals leads to their embrittlement, jeopardizing their structural integrity. In addition, this diffusion of the boron atoms (from the hexaboride crystal structures that surround the large lanthanum metal atom) releases the lanthanum atoms, causing the insert to become depleted of its emitting material.[77] Therefore, when constructing the hollow cathode, care needs to be taken in making sure that metals susceptible to boron diffusion are not used for parts that will be in contact with the insert.

1.9 HET Plasma Oscillations

The basic operation of a Hall-effect thruster was described in Section 1.3.1. While these thrusters are characterized as electrostatic devices due to the constant voltage applied between the anode and cathode that works with the magnetic field to set up an electric field along the channel that accelerates the ions[13], interactions between the plasma and the applied electromagnetic field give rise to a dynamic exhaust plasma plume, which has a broad spectrum of fluctuations and is carried by waves of ionized propellant with the largest oscillations occurring at frequencies less than 1-MHz. [83] These oscillations are not only seen in the discharge current, but also in the plasma parameters. Therefore, it is important to note that the efficiency parameters

discussed in Section 1.5 are average parameters.[54, 83] Still, since the AC components of this system's functioning contribute to its steady state behavior, for preliminary investigations into new techniques, time-averaged values of the thruster's parameters can still be very insightful, and can help point out areas for further study.

A basic explanation of the reason for these oscillations can be obtained from considering the process by which neutrals fill the discharge channel and ions leave the ionization zone, which naturally settles into a distinctive "predator-prey" cycle. First, some of the neutrals that fill the channel are ionized, producing a comparable portion of electrons. Many of these electrons join the Hall current. This increase in Hall current enhances the electric potential between this region and the anode, which increases the ExB velocity of the electrons. This in turn causes more collisions with neutrals, and the ensuing ionization depletes most of the neutrals in the channel. This burst of collisions also decreases the Hall current. The cycle then starts again as neutrals from the steady flow of propellant continue to fill the channel. These oscillations, which are usually measured from the discharge current, are termed the "breathing mode." [84]

The complexity of HETs which is in large part due to these oscillations has led to these characteristics being the focus of many research investigations in the hopes of understanding the processes that cause some of the behaviors that are being observed. The literature contains many works dedicated to describing and characterizing these oscillations and higher modes, of which some are listed here. [14, 59, 61, 85] One of the unanticipated behaviors of these systems which is related to their oscillatory, turbulent nature is the anomalously high transport of electrons across the magnetic field and the impact of this lack of full control on the confinement of these electrons in the Hall current on ionization and thruster efficiency [57, 85–90].

In addition, controlling the electron energy distribution function (EEDF) in low temperature plasmas (LTPs) has been the subject of many experimental, theoretical

and computer generated investigations. There is great interest in this pursuit because electron processes directly influence certain reaction rates in the discharge, plasma parameters, and the efficiency of the process or device that utilizes these plasmas [91–98]. The complex dynamics of these systems and our lack of a full understanding of their intricacies makes the pursuit of EEDF tailoring in HETs an interesting and challenging task. Perhaps looking for ways to change the EEDF to increase efficiency (and therefore increase confinement) is another path towards understanding the anomalous electron cross-field transport. Hence the question was posed as to whether there is a way to tailor the energies of the electrons to increase HET efficiency, specifically by improving ionization.

1.10 Statement of Dissertation Goals

This work was an investigation to see if electron energies can be manipulated to accomplish a decrease in the ionization cost per beam ion in the low voltage Hall thruster operating regime where thrust is maximized. This would translate into an increase in ionization fraction, and therefore also in thrust and efficiency.

1.11 Thesis Organization

Chapter II gives an overview of the facilities, equipment, and diagnostics used over the course of this research. Appendix A addresses the early work, detailing the first two methods of EEDF control that were explored. These two methods were neutral gas injection and inert gas mixing. The sections on these methods conclude with how the results from these investigations influenced the development of the EEDF control scheme for HETs that was investigated using an H6 HET. Chapter III presents this particular method, which is the reverse-flow cathode method of EEDF control, its performance results and its EEDFs. These results are compared to the control

case, which is the same thruster run with the standard, centrally mounted cathode configuration. Additional EEDF plotted results from this method are found in Appendix D, and Appendix C shows video of the thruster being ignited and run with the centrally mounted and the externally mounted cathode. Appendix B contains the detailed procedures used to carry out the research in this thesis. Chapter IV gives an overarching summary of the studies discussed in the thesis, lists the main takeaways from this work, and mentions suggestions for future research on EEDF control towards increasing thruster efficiency.

CHAPTER II

Experimental Equipment and Diagnostics

2.1 Junior Test Facility (JLVTF)

Junior is a cylindrically shaped vacuum chamber at PEPL with a diameter of about 1.2 m, and a center region length of about 1.5 m where an experimental setup can be placed (See Fig. A.2(a)). It is attached at one end to the Large Vacuum Test Facility (LVTF), which is the largest vacuum chamber in the lab and is discussed in Section 2.3. JLVTF can be isolated from this chamber using a large gate valve that connects them. The chamber is roughed down to ∼100 mTorr with a mechanical pump and blower. Then a turbopump, set to a rotational frequency of 500 Hz, is used to bring the chamber down to its base pressure, which is on the order of 10^{-6} Torr. Junior was isolated from LVTF during the test cell experiment discussed in Appendix A.1.

2.2 Cathode Test Facility (CTF)

A cylindrical vacuum chamber that is ∼2 m long and ∼0.6 m in diameter was used for the experiment described in Appendix A.2. This chamber, called CTF, which stands for the Cathode Test Facility, operates with a dry scroll mechanical pump and a TM450 cryopump. The cryopump has a stated argon pumping speed of

6,400 liters per second (l/s). CTF reaches a base pressure of 1×10^{-7} Torr. Further details about the operation of this chamber can be found in Appendix B.9.

2.3 Large Vacuum Test Facility (LVTF)

The experiments discussed in Chapter III were carried out in the Large Vacuum Test Facility (LVTF) at PEPL. This vacuum chamber, measuring 9 m long and 6 m in diameter is roughed down to 100 mTorr by two roots-type blowers each with a pumping speed of 2,000 ft^3/min and four rotary gas ballast mechanical pumps each capable of 400 ft^3/min. The chamber is then brought to high vacuum using seven PHPK TM-1200s with a total pumping speed of 500,000 l/s on air and 240,000 l/s on xenon.

In these experiments, which used flow rates of 20 mg/s in all the operating conditions tested, with a 7% cathode flow fraction (CFF), for total flow rates of 214 sccm, the chamber pressure was on the order of 10^{-5} Torr. This measurement was taken with an Agilent UHV-24 nude ionization gauge mounted on top of the chamber and corrected for xenon flow using Equation 2.1 [99].

$$P_{corrected} = \frac{(P_{reading} - P_{base})}{2.87} + P_{base} \tag{2.1}$$

The base pressures measured with this gauge were around 1×10^{-6} Torr during the tests conducted in this study. Pressure measurements were also taken with an internally mounted ion gauge as described in the next subsection.

2.3.1 Internal Pressure Measurements

In addition to the ionization gauge measuring the pressure at the edge of the chamber, an Agilent 571 external ionization gauge was set up inside the chamber near the thruster to get a better idea of what the pressure was there during thruster

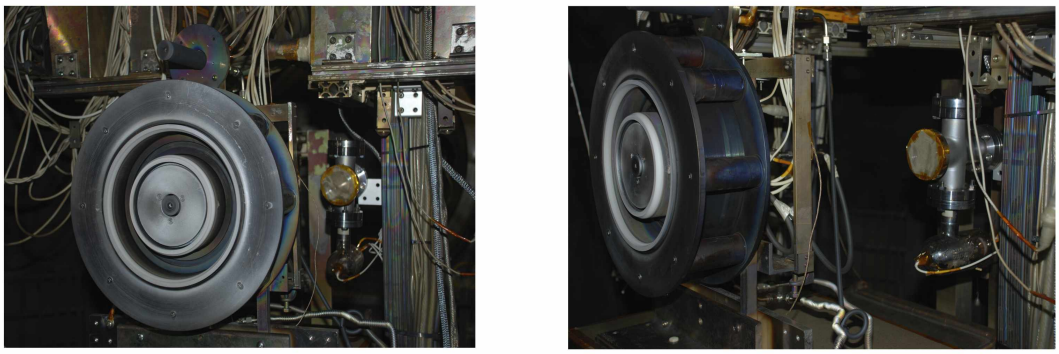

(a) (b)

Figure 2.1: (a) A picture of the H6 6-kW thruster installed inside LVTF with a centrally mounted cathode (plus a cathode mounted in a standard external position). (a) & (b) In addition, the internally installed ion gauge was placed several centimeters behind the thruster and slightly to the side of the edge of the thruster. It was also lined up to be roughly along thruster centerline. The gauge was mounted on a conflat 'tee.' The opening of the tee that was facing forward towards the thruster was covered in a fine mesh. The other openings of this adapter flange were capped off.

operation. The location of the gauge was comparable to the setup described by Diamant with adjustments made for differences in the size of this thruster compared to theirs (Fig. 2.1). The opening of the tee facing the thruster was covered in a fine mesh with a 25 micron aperture size, and an open area fraction of 38%. This aperture size was chosen since it was smaller than the estimated Debye length. [100] The other openings on this adapter flange were capped off, and the tee and mesh were isolated from chamber ground. In the experiments that utilized this setup (discussed in Chapter III), flow rates of 20 mg/s and a 7% cathode flow fraction (CFF) were used in all the operating conditions tested. For this ~214 sccm total flow rate, the chamber pressure, measured with this internal gauge, was around 1.3×10^{-5} Torr, corrected for xenon flow.

2.4 6-kW Hall Thruster (H6)

The Hall-effect thruster used in these tests was a 6-kW Hall thruster, the H6, which is shown in Fig. 2.1(a) mounted inside LVTF. This laboratory model thruster is one of three identical thrusters built in 2007 through a collaboration between the Air Force Research Laboratory (AFRL), the Plasmadynamics & Electric Propulsion Laboratory (PEPL), and the Jet Propulsion Laboratory (JPL). It serves as a common test bed for Hall thruster physics research, which makes it easier for the three facilities to corroborate research findings, and to coordinate research efforts. This thruster was designed to allow a cathode to be mounted along the center of the thruster. The nominal operating condition for this thruster is 300 V and 20 mg/s. [101]

2.4.1 Floating the Thruster

All testing was done with the thruster body floating instead of grounded. This more closely simulates thruster conditions when it is operated in space. Following a setup used by McDonald to isolate the thruster body, first, a few sheets of 0.1 mm thick mica were placed between the thruster's mount and the thrust stand's mounting plate, and the thruster was screwed into the mounting plate using fiberglass screws to isolate it from the grounded thrust stand. Also, an electrical line was run from the thruster body to the outside of the chamber, and was used to control the grounding of the thruster. [85]

In addition, cryogenic ceramic breaks were connected in line with the thruster's flexible metal gas lines so the thruster would not have an alternate path to ground through these grounded metal gas lines. A cryogenic break is made up of two segments of metal tube with a ceramic middle section where the ceramic-to-metal interfaces are hermetically sealed using high-temperature, vacuum tube-grade braze alloys. The cryogenic break provides up to 6 kV of electrical isolation. Lastly, the front of the thrust stand, which extended out beyond the thruster's exit plane, and was the closest

grounded surface to the downstream region of the thruster, was covered with a sheet of boron nitride sprayed graphoil to decrease the possibility of the thruster arcing to ground through the plume. All of these additions are shown in Fig. 2.2.

On the air side of the chamber, two circuit options were set up to allow the safe lighting and floating of the thruster. The cable running from the thruster body could be connected to either one. The first circuit grounded the thruster body, and allowed the current to ground to be read into an Agilent data acquisition (DAQ) unit, using an F.W. Bell current sensor. Usually the thruster was grounded during lighting since the thruster's start up transients could increase the chance of arcing to ground. The second circuit isolated the thruster body from ground, and allowed the thruster's floating voltage relative to ground to be read into the DAQ.

As an added precaution, a bi-directional clamping diode, also known as a transient voltage suppression (TVS) diode, was connected in parallel between the floating line and ground so that if there were any transients too far above or below ground, the diode would short to ground to prevent arcing within the chamber. The particular TVS used has a breakdown voltage of around 68 V and a clamping voltage of 121 V. The breakdown voltage was picked to be about twice the expected thruster body floating potential. Also of note is the fact that on a few occasions, the thruster was started while the thruster body was floating, and with this particular set up no arcing between the thruster and ground or cathode spots along the poles were seen.

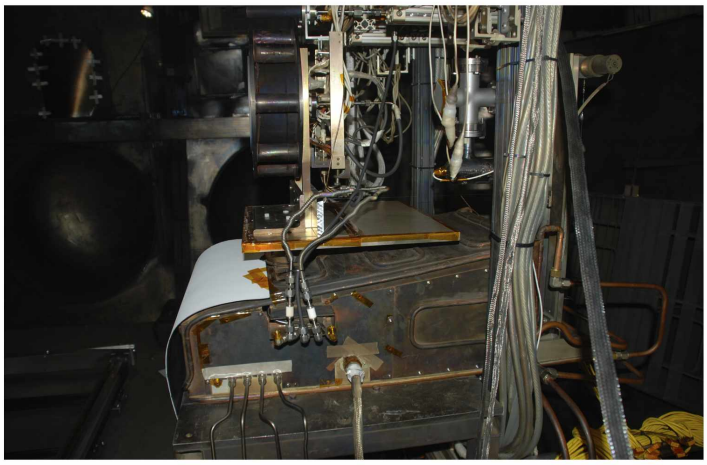

Figure 2.2: The thruster shown with the various components used to float the thruster body including cryogenic breaks in the metal gas lines, mica sheets between the thruster and thrust stand, fiberglass screws for securing the thruster to the thrust stand mount, and a boron nitride sprayed graphoil flap over the exposed and grounded thrust stand that had a line of sight to the thruster's plume.

2.5 PEPL-designed/built Hollow Cathode

As mentioned in Section 1.8, the two cathodes used in the experiments in this thesis were lab-built lanthanum hexaboride (LaB_6) hollow cathodes based on a JPL design that was devised, constructed, and evaluated for use with the H6, and has a nominal operating current of 20 A. [75] The two cathodes featured a graphite insert retaining tube (also called the cathode tube) and a graphite keeper with an outer diameter of less than 25.4 mm. These parts were made out of graphite because this material is easily machinable, has a high melting point, and unlike refractory metals such as tungsten and molybdenum, is not susceptible to boron diffusion from the LaB_6 insert or the boron nitride heater sleeve. Boron diffusion leads to the embrittlement of those materials, which would jeopardize the structural integrity of the cathode. [77]

Similar to previous cathodes, the LaB_6 insert has a 6.35 mm outer diameter, a thickness of 1.27 mm, and is 25.4 mm in length. Since this length is approximately

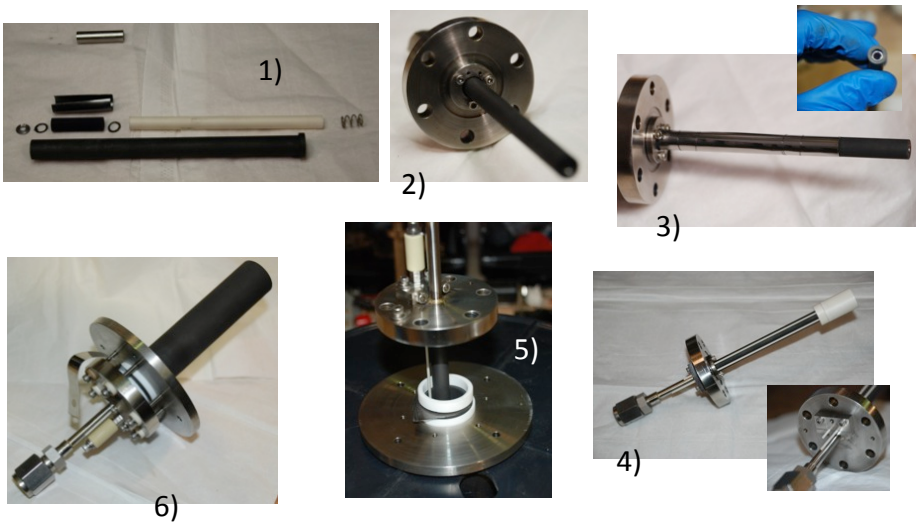

Figure 2.3: A visual summary of the hollow cathode assembly. 1) Components for the first part of the build process including the cathode tube, insert, alumina insert spacer, tungsten spring, and graphoil and graphite gaskets for around the insert. 2) & 3) Cathode tube secured to the stainless steel gas adapter flange 4) Cathode with BN heater sleeve and alumina lead tubes 5) After the radiation shielding is wrapped around the heater sleeve, the entire assembly is lowered into the keeper tube, which is hanging down inside of the stainless steel thruster interface flange. 6) The full hollow cathode assembly.

one-fifth the length of the graphite cathode tube, the insert is held against the orifice by an insert spacer and a 12.7 mm tungsten spring (Fig. 2.3). The insert's 3 cm^2 interior surface area is the insert's emission area. According to the Richardson-Dushman equation, the LaB_6 insert material can emit 20 A/cm^2 at a temperature of 1700 °C. [80, 81] Therefore, this cathode has an upper emission current of around 60 A.

LaB_6 cathode inserts have an area that is too large for direct heating because the resistance of the material is too low, so the insert must be heated indirectly to bring it to thermionic emission temperatures in the range of 1500-2000 K. [80] Unfortunately, the most failure-prone component of LaB_6 cathodes is generally the heating element. The gradual but inevitable failure of the heating element and occasional, irreversible fusion of the heating element to other critical parts of the cathodes previously used in the 6 kW Hall thruster motivated the construction of a low-cost, robust cathode with an alternative heater that has a more graceful failure mode. This development

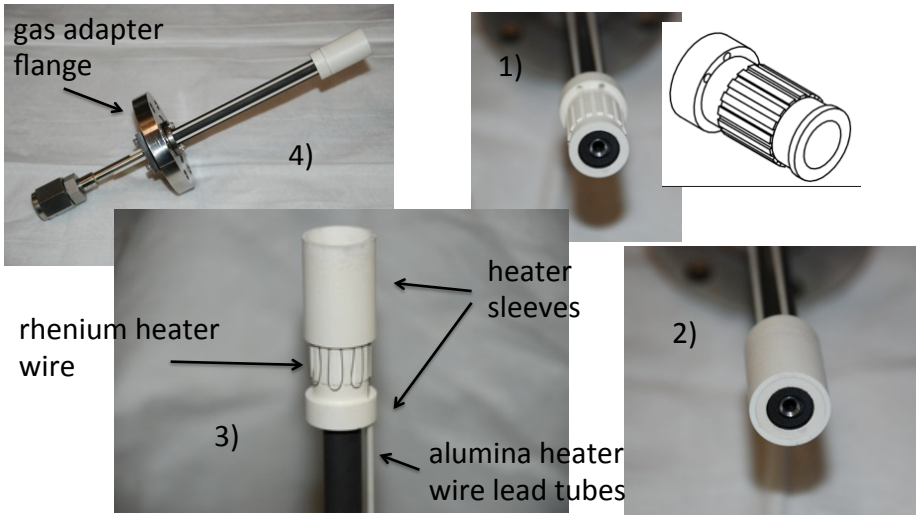

Figure 2.4: A visual summary of the cathode heater assembly. 1) Inner heater sleeve in place over the cathode tube around the area where the insert is placed inside the cathode tube. The inner sleeve has axial grooves machined into it to guide the heater wire. 2) Outer heater sleeve placed over the inner heater sleeve. 3) Outer heater sleeve pushed up to show the heater wire wound around the area where the insert is in a serpentine pattern. 4) Cathode with heater sleeves and alumina lead tubes. (Same picture as 4) in Fig. 2.3.)

was led by McDonald and reported in the literature.[74]

The new heater design is composed of an HP grade boron nitride (BN) ceramic heat spreader/sleeve and a pure rhenium filament with a diameter of ∼0.381 mm (Fig. 2.4). The heat spreader is electrically isolating but very thermally conductive. It completely encloses the heater wire to reduce the possibility of a heater-keeper short. One of the cathodes built features a double helix wire path in the ceramic heat spreader and the other, shown in Fig. 2.4, has an axial pattern so that the wire has a serpentine path through the heater sleeve. The axial pattern is easier to machine; however, the double helix allows a longer length of heater wire to be wound around the area directly above the insert, which means the wire has a larger total resistance leading to a lower current being needed to reach the deposited power required to ignite the cathode without sparking (see Section B.13, the LaB_6 Cathode Startup Procedure for more details about this). The more current that is run through this thin wire, the greater chance there is of the wire failing somewhere along its length.

Two alumina tubes provide an outbound and return path for the rhenium heater wire, eliminating the need to spot-weld the wire to the cathode tube itself, and permitting easy mechanical attachment, assembly, and disassembly (See Fig. 2.3). The alumina tubes guide the wires up to the gas adapter flange. To make sure the leads have less resistance than the heater wire so that most of the power is deposited there, the tubes are friction fit with thin pieces of tungsten wire. See Ref. [74] for details about the design and heat retention optimization process that led to the cathode construction and lighting procedure used in this thesis. Note that in the most recent designs, the cost of the pure rhenium wire for the length (0.9 m for the helical heater spreader design) and thickness used was about $87 US. Also, the tantalum heat shielding (10 layers of 0.025 mm thick tantalum foil) is only used around the heater sleeve, not along the entire length of the cathode tube.

2.6 Thrust Stand

Thrust measurements were taken using an inverted pendulum thrust stand that was built at PEPL, and based on a NASA Glenn Research Center (GRC) design. The thrust stand was operated in null mode meaning that a closed feedback loop between the tuned PID controller and the null coil work together to keep the thrust stand's pendulum in a fixed position so that the thruster does not move during the test. The PID controller uses displacement information received from a linear voltage differential transducer (LVDT) to determine the amount of movement that needs to be compensated for and the null coil produces a counterforce on a centrally suspended metal plunger that is used to correct for any shifts in position. The analog Stanford Research Systems (SRS) SIM960 PID controller was tuned using a Ziegler-Nichols procedure using the method described in its operation manual. The thrust stand's platform where the thruster was mounted was kept level during the test manually by using a stepper motor and a readout from an inclinometer. Additional details on the

design of this thrust stand can be found in the literature. [16, 72, 102]

A correlation between thrust and the PID controller's voltage output signal was determined using a set of calibration weights that were hooked up to the back of the thruster. Before the thruster was turned on, and while the chamber was at vacuum, a thrust stand calibration was performed by adding calibration weights one at a time to the thrust stand, and recording the PID response after the signal's oscillations damped out and reached steady state. Each calibration weight was weighed beforehand with a sensitive scale, and these values along with the measurement uncertainty published by the company that made the scale were recorded. In between each thrust stand calibration measurement, all of the weights were taken off to obtain a zero measurement which was then subtracted from the previous measurement with the weight to obtain a zero-drift corrected measurement value.

Recommendations for best thrust stand practices outlined by Polk [103] were incorporated into the procedure to obtain high quality thrust stand measurements so that differences in thruster performance between the downstream, reverse-orientation cathode and the internally mounted cathode could be determined with confidence. The detailed, step-by-step procedure used to obtain data with the thrust stand can be found in Appendix B.8.

2.7 ExB Probe

The ExB probe, shown in Fig. 3.8(b), which was designed by the NASA Glenn Research Center (GRC), is a velocity selector that uses a balance between the forces of perpendicular electric and magnetic fields on the incoming ion beam to discern the various velocity distributions. The ExB probe consists of three sections which are the entrance collimator, the ExB test section, and the exit collimator. Both the entrance and exit collimators are about 75 mm long. The orifices on both ends of the entrance collimator and at the front end of the exit collimator are all 1.6 mm in

diameter. Once the ions pass through the entrance collimator, the beam enters the test section, which is 150 mm long and consists of two metal parallel plates with a 9.41 mm separation gap to which a bias voltage is applied to establish the electric field, and two permanent magnets, which established a magnetic field. The total voltage bias is split around facility ground so that during sweeping of the bias voltage, the center of the test section stays around facility ground to minimize perturbations to the plasma external to the probe. As an ion in the collimated beam passes through the test section, its motion is explained by the Lorentz equation, which describes the forces on a charged particle due to electric and magnetic fields:

$$\vec{F} = eZ\left(\vec{E} + \vec{v} \times \vec{B}\right). \tag{2.2}$$

Ions with velocities that allow a balancing of these forces, so that $\vec{F} = 0$ in Equation 2.2, will pass through the test section undeflected allowing them to continue through the 1.6 mm exit collimator orifice and be collected by the conically shaped collector at the base of the exit collimator section. This high aspect ratio collector, whose shape makes certain that any secondary electron emission (SEE) can be recollected for a net zero current from SEE, is also spray coated with tungsten, which has a relatively low SEE yield under xenon bombardment.

Given this design, and the fact that in the Hall thruster, most of the singly and multiply charged ions are created over a short axial distance— meaning their acceleration voltages are about the same, and the voltage applied to the plates is swept across a range suitable for the thruster and operating conditions being tested, the current collected will form peaked distributions. The probe voltage bias at the peak of each of these distributions can roughly be related back to the ion acceleration

potential times its charge state using the following equations [7, 15]:

$$v = -\frac{E}{B} \tag{2.3a}$$

$$E = -\frac{V_{probe}}{d_{gap}} \tag{2.3b}$$

$$< v > = \sqrt{\frac{2ZeV_{accel}}{M_{Xe}}} \tag{2.3c}$$

to solve for ZV_{accel} :

$$ZV_{accel} = \left(\frac{V_{probe}}{Bd_{gap}}\right)^2 \frac{M_{Xe}}{2e}. \tag{2.4}$$

However, this can only be used to get a rough correlation for this particular probe design because along the 150 mm length of the test section, the magnetic field ranges from 0.097 T at the entrance to a peak value of 0.16 T in the middle. To use Equation 2.4 most accurately to determine ZV_{accel} from V_{probe}, the probe would need to be calibrated with an ion source over a range of discharge voltages. Further details on the design and setup of this probe can found in the literature. [55, 72, 104] For the ExB measurements taken for this thesis, the sweep voltage was 0 V to 80 V, 241 points per trace were taken, and 3 traces were averaged together for the data point obtained at each operating condition. The procedure used to obtain ExB probe data can be found in Appendix B.6.

2.8 Retarding Potential Analyzer (RPA)

A retarding potential analyzer designed and built by ElectroDynamic Applications Inc. (EDA) was used to obtain the most probable voltage (V_{mp}). This value was plasma potential corrected using measurements from a Langmuir probe that was mounted 10 mm from the edge of the RPA (see Fig. 3.9(a)). This RPA features two electron repelling grids one right before the sweeping grid to repel electrons from the plume and a second one right before the collector to repel secondary electron emission

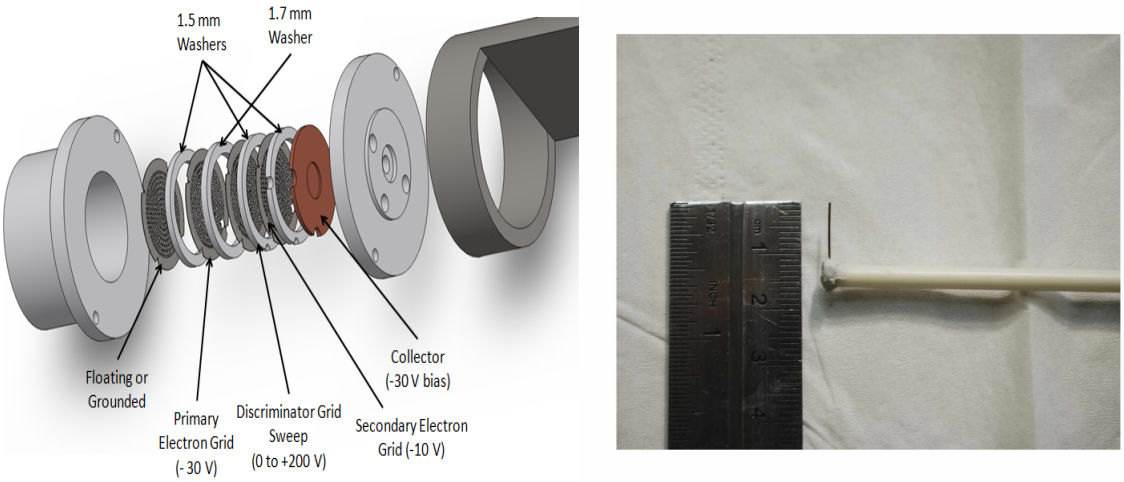

(a) (b)

Figure 2.5: (a) The schematic of the RPA showing the spacing of the grids. This photo is courtesy of EDA (b) A close up photograph of the tip of the LP showing its length.

(SEE) from the collector in order to send this current back to the collector to cancel out its effect on the measured current. Figure 2.5(a) shows the arrangement of these grids and their spacing. Further details such as the theory of operation of RPAs and considerations for choosing grid spacing can be found in other references. [105, 106] For these experiments, the first grid was left floating to shield the ambient plasma from the biased grids within the RPA. The electron repelling grids were biased to ~ -35 V, the sweeping grid was swept from 0 V to two times the V_D, and no bias voltage was applied to the collector. Measurements were taken at 11° from thruster centerline and a radial distance of $\sim$3 D_T. These measurements were taken on the opposite side to where the external cathode was located (see Figs. 3.6, 3.7, 3.9(b)). The procedure used to obtain RPA data can be found in Appendix B.5.

2.9 Faraday Probe (FP)

A Faraday probe was used to measure the ion current in the thruster plume for the experiments in Chapter III. Faraday probes are used to calculate the total ion current, I_{ion_T}, and the current utilization efficiency, η_B, shown in Eqn. 1.9. In addition,

they are used to calculate the plume divergence half angle, θ_B, and the divergence efficiency, η_{Div}, in Eqn. 1.10. There are many different types of Faraday probes including magnetically-filtered, collimated, nude, gridded and reduced acceptance angle FPs. [55] A nude probe design was used here. This type of Faraday probe has a flat, circular collecting surface, and is biased to a negative voltage to repel electron current.

The probe's design and a picture of the completed probe, which is shown in Fig. 2.6 was based on Reid and Shastry's FP designs, but with some modifications. [55, 107, 108] The probe surface was made of grade 365 molybdenum and was machined to have a finish of 32 μ" AA as done by Brown for the collectors in his nested Faraday probes. [16] The probe surface measured 4.7 mm in diameter, and the sides were covered in ceramabond so that current was only collected by the top surface (Fig. 2.6). The probe was enclosed in a long alumina tube, which insulated the rest of the probe body and acted as an electrically isolated support structure for positioning and mounting the probe within the experimental setup.

See Fig. 3.9(a) for a picture of this probe incorporated into the experimental setup. For the testing carried out in this thesis, the probe was biased to a voltage of -60 V, and a 56 Ω metal foil resistor was used. This type of resistor was chosen for taking FP measurements due to its low thermal drift. The procedure used to obtain FP data, along with the probe's electric circuit, and a block diagram of the equipment and electrical connections used for data collection can be found in Appendix B.7. Additional details about various FP designs can be found in the literature. [16, 55, 72, 107]

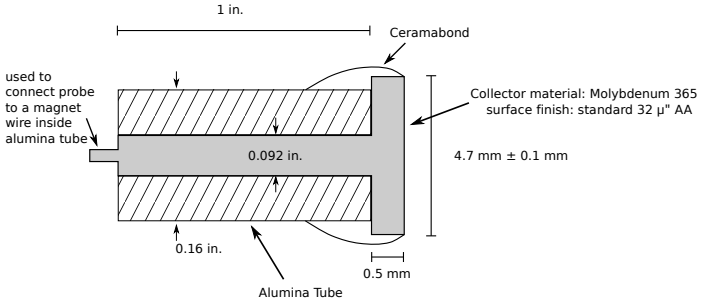

(a)

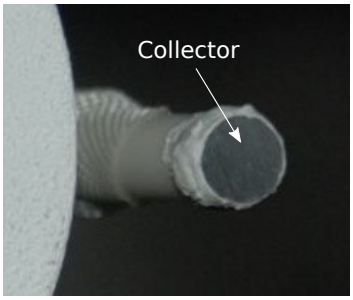

(b)

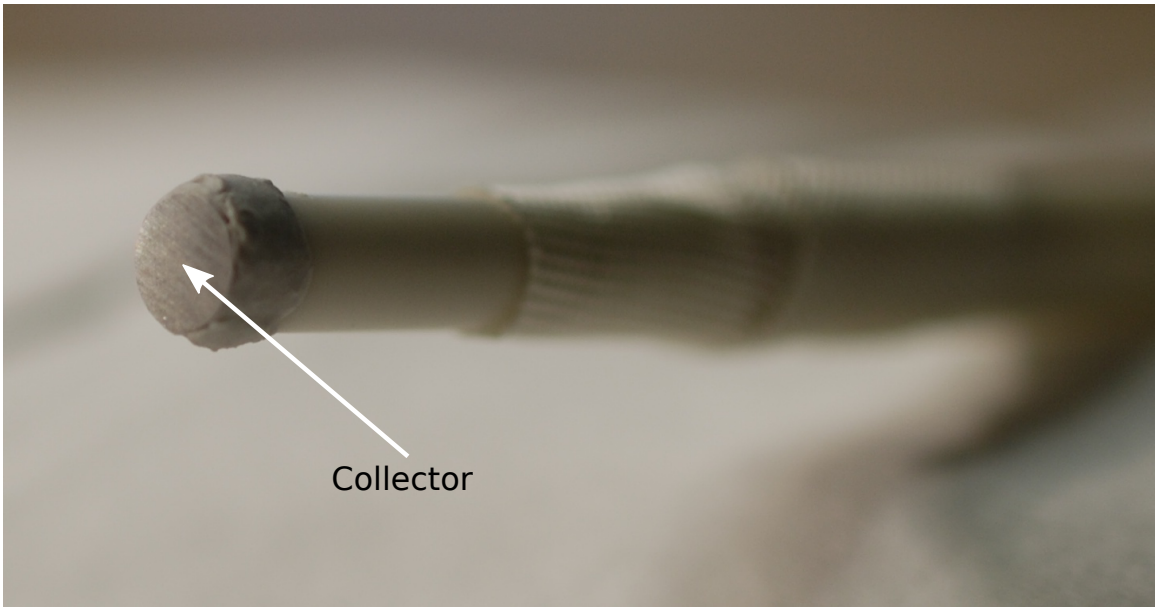

(c)

Figure 2.6: (a) The schematic of the Faraday probe. Once this portion of the probe was built, it was fit inside a larger alumina tube in a telescoping manner and fiberglass tape was used to cover the seam to prevent plasma from entering. The magnet wire was attached to the probe using the narrowed section at the back of the probe shown in this diagram and a butt wire splice connector. This connection and the wire were insulated by the telescoping alumina tube. See Fig. 3.9(a) for a picture of the full FP installed in the chamber. (b) A close up photograph of the Faraday probe tip while it was in the chamber. (c) Another zoomed in photograph of the tip of the FP after assembly was completed.

2.10 High-speed Dual Langmuir Probe (HDLP)

A lab-built, high-speed dual Langmuir probe (HDLP) system was used to obtain time-averaged LP measurements in this thesis. This HDLP system was built by Lobbia for obtaining Langmuir probe (LP) traces at frequencies high enough to be time-resolved with respect to the breathing mode oscillations characteristic of Hall-effect thrusters. The system uses a custom-built, high bandwidth, high-voltage amplifier. It also has a current sensing circuit that features thin-film metal oxide, ultra-low inductance shunts, and high-bandwidth, ultra-high input impedance voltage and current JFET (junction field-effect transistor) buffers. [14] More details about this system, and its use for time-resolved measurements can be found in the literature. [14, 59]

For the experiments in Chapter III and Appendix subsection A.2.1, this system was used to obtain time-averaged measurements of electron density, electron temperature, plasma potential, and the EEDF since time-resolved measurements were not necessary for these initial, proof-of-concept tests. For the experiments in Chapter III, an LP sweep rate of 10 Hz along with a 100 kHz sampling rate were used. The type of LP used was a cylindrical probe that had a diameter of 0.5 mm (0.02 in.) and a length of 10 mm (see Fig. 2.5(b)). Measurements were taken at 11° from thruster centerline and a radial distance of $\sim$3 D_T, and also at 30° and 58° with a radial distance of $\sim$2 D_T. These measurements were taken on the opposite side to where the external cathode was located (see Figs. 3.6, 3.7, 3.9(b) & 3.29). The detailed, step-by-step procedures used to build the dual LPs, calibrate the measurement circuitry, and obtain Langmuir probe data can be found in Appendices B.2, B.3, and B.4 respectively.

2.10.1 The Langmuir Probe Trace

When the tip of a thin metal wire, forming a cylindrical LP, is placed in a low temperature plasma (LTP), and a series of incrementally increasing voltages, with

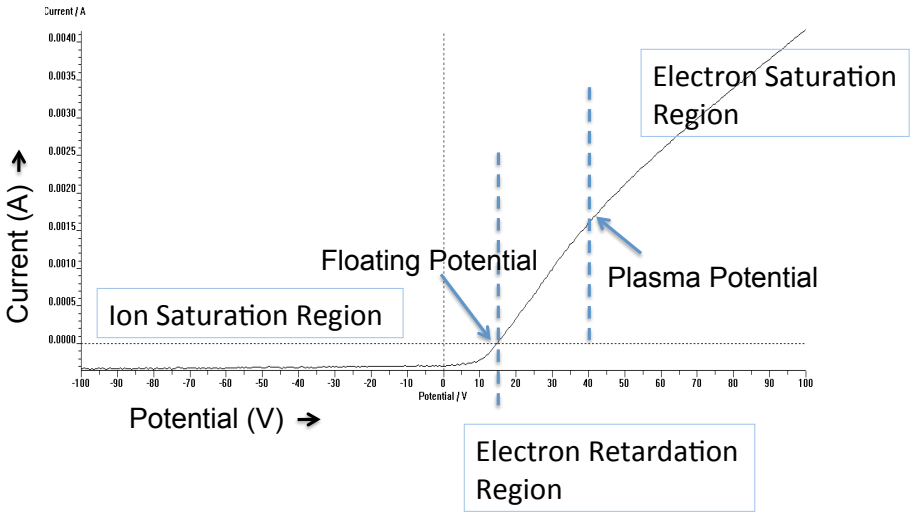

Figure 2.7: An example of a typical current-voltage (I-V) trace obtained from the plasma sources used in this thesis with the various regions and important features of the characteristic indicated.

respect to reference ground potential, is applied to the wire in succession through a shunt (or resistor), the current the wire draws at each voltage value forms a current vs. voltage plot. When this I-V curve is analyzed by applying the appropriate theory, given the plasma regime and probe dimensions, the value of various key plasma parameters can be revealed. To understand what these plasma parameters say about the plasma, the first step is to understand the three regions of the probe trace. As seen in Fig. 2.7, when a large negative voltage is applied to the probe wire, almost all of the electrons are repelled, so mainly ion current is collected. This is called the ion saturation region. According to convention, LP I-V characteristics are plotted with the current signs reversed, hence this ion current is shown as a negative value, and it can be thought of as a negative current flowing into the plasma from the probe. [109–111]

As the probe potential increases from negative values, more and more electrons in the plasma will have a kinetic energy that allows them to overcome the repelling potential and reach the probe. In addition, a relatively constant ion current continues to be collected by the probe, since at these negative potentials the probe is not

repelling the ions. Hence the probe current increases more rapidly within the electron retardation region. This region and the ion saturation region are separated by the voltage where an equal amount of electron and ion current are collected by the probe totaling zero current. This voltage is called the floating potential. The end of the electron retardation region is marked by the plasma potential, where electrons are no longer decelerated by the probe and ions are no longer accelerated towards the probe, so both reach the probe at their respective thermal velocities. Since the electrons have a higher thermal velocity than the ions due to their smaller mass, more electron current is collected than ion current. The plasma potential is a positive value, and this parameter can be understood through the concept of ambipolar diffusion. [109, 111]

Ambipolar diffusion describes the fact that both electrons and ions diffuse from the plasma at the same rate. This is because as the electrons, which have a higher thermal velocity than the ions, diffuse, it creates a potential difference between the electrons and the ions that are left behind. This slows down the electron diffusion rate and draws the ions out of the plasma more quickly, thus increasing the diffusion rate of the ions until a balance is reached where both charge species are diffusing from the plasma at the same rate. This also enforces the quasi-neutral assumption about the plasma. Therefore, the plasma has a positive potential relative to its surroundings—which in this case are the grounded chamber walls, and the negative sloping potential profile between the two forms a region of charge imbalance called the sheath.

The sheath, depicted in Fig. 2.8 is a region that forms between any surface that is exposed to plasma and the bulk plasma. The sheath phases out the impact the potential of that surface has on the plasma. Therefore, in the bulk plasma (and in areas of negligible B-field), it can be assumed that on scales larger than the sheath thickness, the influence of that potential is not seen, meaning electric fields are negligible. This veiling of electric fields as a result of the behavior of the charges in a plasma is called Debye shielding, and the sheath thickness is usually on the order of

a few to several Debye lengths. [109, 110] The Debye length is defined as

$$\lambda_D = \sqrt{\frac{\epsilon_0 k_B T_{e(K)}}{N_e e^2}}, \tag{2.5}$$

where $T_{e(K)}$ is the electron temperature in Kelvin, and N_e is the electron number density in m^{-3}.

The more energetic the electrons are, the higher the plasma potential is to keep the electrons from diffusing too quickly. In addition, the more energetic the electrons are, the lower the floating potential, because a lower potential is needed to repel more of the electrons to keep the total current equal to zero. A surface has no sheath when it is biased to the plasma potential, where neither electrons nor ions are being repelled or attracted.

If the potential of a metal surface within the plasma is much higher than the plasma potential, electrons are accelerated towards the surface and ions are repelled, leaving a sheath with more ions than electrons, since the electrons are less massive and therefore more mobile than the ions. In theory, the electron current collected by the surface would level off to a maximum value; however, for a cylindrical metal probe in a low-temperature plasma, as seen from the probe characteristic (Fig. 2.7), this does not happen. This is because as the probe potential increases, the size of the sheath increases as the electrons are collected by the probe at an even faster rate, leaving behind an ion sheath with an even larger radius, which increases the effective collecting surface area of the probe, thus increasing the collection of electron current even more.

For metal surfaces at voltages much lower than the plasma potential, such as the chamber walls, or a negatively biased probe tip, since the surface repels most of the electrons, this also creates a sheath with more ions than electrons. Within this sheath, ions are accelerated towards the surface, and electrons migrate more slowly. As the

potential is further decreased, the collected ion current tends towards a saturation value, since the collected current is a function of the ion momentum flux, which, assuming a collisionless sheath, is a conserved quantity. This means that even as the ion velocity increases with more negative probe voltages, the density of ions that reach the probe decreases to keep the flux constant. Still, there is also a slight dependence of the collected ion current on probe voltage, since the size of the sheath, and hence the effective probe collecting area, grows as the applied potential decreases. It is of importance to note that since none of the ions are repelled by the probe in the region of the trace where dominantly ion current is being collected, Langmuir probes do not measure the distribution of ion temperatures. [109–111]

However, since the electrons are repelled from the probe, according to their energies, as the probe potential is decreased to values lower than the plasma potential, the electron energy distribution function (EEDF) can be calculated from the trace. Then, the EEDF can be integrated to find the electron number density and the mean electron temperature. Usually, the EEDF is assumed to be Maxwellian. When the electrons' energy distribution is Maxwellian, the electron retardation region in the initial I-V trace is exponential. The form of a Maxwellian distribution function along with the plasma characteristics that are implied by this assumption are discussed in the next subsection, Section 2.10.1.1.

For a more detailed overview of Langmuir probe theory, including the various plasma regimes that may be encountered and the special considerations that are needed for them, the literature can be consulted. [59, 109–117] The Langmuir probe analysis procedure used to interpret the data in each experiment in this thesis is outlined. For the experiments conducted for the neutral gas injection method and the gas mixing method (discussed in Appendix A), the LP analysis procedure is in Section A.1.2. For the reverse-flow cathode EEDF control method discussed in Chapter III, the LP analysis steps are detailed in Section 3.3.1.

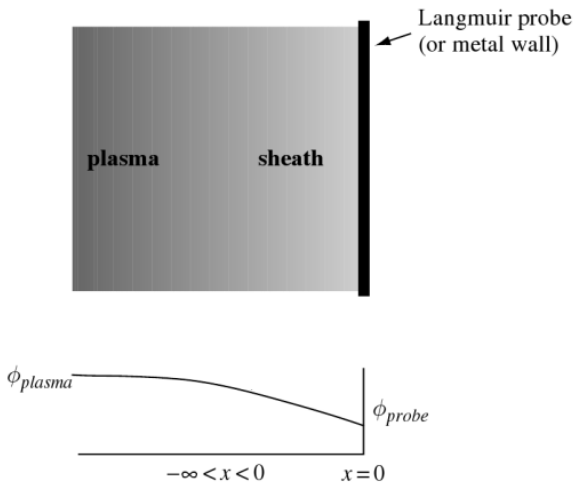

Figure 2.8: A simple 1-D diagram of the sheath showing the potential between the surface and the plasma. From Ref. [109] and modified slightly.

2.10.1.1 The Form of the EEDF

The Maxwellian velocity distribution, also called the Maxwell-Boltzmann velocity distribution that describes the motion of a species of particles in a classical ideal gas in thermodynamic equilibrium is defined as follows:

$$g_{\vec{v}}(v_x, v_y, v_z) = \left(\frac{m}{2\pi k_B T}\right)^{3/2} e^{\frac{-m(v_x^2+v_y^2+v_z^2)}{2k_B T}}, \tag{2.6}$$

where v_x, v_y & v_z are the velocity components. [118] This equation shows that the distribution depends only on the magnitude of the velocity vector and not on the direction, meaning that overall, all of the particles' motion averages out to be of equal magnitude in all directions, which is to say this is an isotropic distribution. For this reason, another convenient way to express this distribution is in spherical coordinates, where each particle's velocity is described with a distance from a fixed origin, and polar and azimuthal angles to define the inclination and direction of that

magnitude:

$$g_{\vec{v}}(v_x, v_y, v_z)dv_x dv_y dv_z = \left(\frac{m}{2\pi k_B T}\right)^{3/2} e^{\frac{-m(v_x^2+v_y^2+v_z^2)}{2k_B T}} dv_x dv_y dv_z$$
$$g_{\vec{v}}(v, \theta, \phi)d^3v = \left(\frac{m}{2\pi k_B T}\right)^{3/2} e^{\frac{-mv^2}{2k_B T}} v^2 sin\theta dv d\theta d\phi \,. \tag{2.7}$$

Here, θ is the polar angle, ϕ is the azimuthal angle, and v is the magnitude of the velocity vector, and hence the speed. Integrating over the angles leads to Eqn. 2.8, which is also called the Maxwellian velocity distribution or the Maxwell-Boltzmann distribution function, where here, the word 'velocity' is used when 'speed' is meant, out of tradition. [119]

$$g_v(v)dv = \sqrt{\frac{2}{\pi}} \left(\frac{m}{k_B T}\right)^{3/2} e^{\frac{-mv^2}{2k_B T}} v^2 dv \tag{2.8}$$

Another way to explain this distribution function is that $g(v)dv$ is the probability one of these particles has a speed within dv at v. Therefore when these probability distributions for a particle's velocity are integrated over all velocities, or speeds, it should come out to 1. The normalization constants in front of Eqns. 2.6 & 2.8 ensure that this is the case. The speed distribution function can be transformed to be in terms of energy using the fact that $E = \frac{1}{2}mv^2$. This leads to:

$$g_v(E)dE = \frac{2}{\sqrt{\pi}} \left(\frac{1}{T_{eV}}\right)^{3/2} e^{\frac{-E}{T_{eV}}} \sqrt{E} dE. \tag{2.9}$$

This Maxwellian energy distribution function (EDF)[111] is the form of the normalized distribution that will be used in this research.

As stated previously, a Maxwellian distribution assumes thermodynamic equilibrium of the gas. This is only possible if there is a significantly sizable number of large-energy-loss, inelastic collisional processes involving the electrons and propellant particles (such as ionization), which deplete the higher energy electron population,

and increase ion density and hence the electron density as well. This increase in electron number density and decrease in electron temperature creates an increase in elastic collisions such as electron-electron collisions, which help establish equilibrium due to the efficient energy transfer that is possible with a collision of two particles of equal masses. This creates the EEDF form that is characteristic of the Maxwellian distribution where the function decreases steeply with increasing energy. [7, 120, 121] If in one direction, the electrons experience a shift or drift in velocity due to their motion in an electric field balanced by collisions, or due to crossed electric and magnetic fields, or due to some other type of drift that affects electron guiding center motion, such as those that result from non-uniform fields, then the distribution will be anisotropic, and will appear stretched towards higher energies.[104] This is a Maxwellian EEDF with a velocity shift, and is the second type of EEDF used in this thesis since both hollow cathode [74] and HET EEDFs [122] have been known to fit this type of distribution:

$$g_v(E) = \frac{1}{\sqrt{\pi}}(T_{eV}\Delta E)^{-1/2} e^{-\frac{E+\Delta E}{T_{eV}}} sinh\left\{\frac{2\sqrt{E\Delta E}}{T_{eV}}\right\}. \tag{2.10}$$

The units of Eqn. 2.10 are 1/eV, where $\Delta v = \sqrt{(2q\Delta V)/m_e}$ can be used to find the velocity shift from the corresponding voltage shift. [122]

The derivation of this Maxwellian + velocity shift (or drifting Maxwellian) EEDF starts with Eqn. 2.6 where a velocity drift is added to one component of the electron's velocity. Choosing for this alteration to occur in the z-direction, this drift is of the form

$$v_z = v_{z_o} - \Delta v \tag{2.11}$$

where v_{z_o} is the initial velocity before the velocity shift is applied. Then Eqn. 2.6

becomes

$$g_{\vec{v}}(v_x, v_y, v_z) = \left(\frac{m}{2\pi k_B T}\right)^{3/2} e^{\frac{-m(v_x^2+v_y^2+(v_z+\Delta v)^2)}{2k_B T}}. \tag{2.12}$$

Expanding and then simplifying the squared shifted velocity component term, switching to spherical coordinates, integrating over the angles, and then using the fact that $E = \frac{1}{2}mv^2$ & $\Delta E = \frac{1}{2}m(\Delta v)^2$ to transform the speed distribution to an energy distribution leads to Eqn. 2.10, and Eqn. 2.13 is the form of this equation used in the fitting of the EEDFs calculated from the LP traces. These distributions are normalized. This can be checked by integrating this or the velocity (i.e. speed) form of the distribution using various calculus tools such as 1. integration by parts, 2. u-substitutions, 3. hyperbolic functions in the 'exponentials form', 4. completing the square, and 5. rules for even and odd functions in order to manipulate the terms into forms that are more easily integrated and/or evaluated.

$$g_{M+v}(V_b) = \frac{1}{\sqrt{\pi}}(T_e \Delta V)^{-\frac{1}{2}} e^{-\frac{(V_s - V_b)+\Delta V}{T_e}} sinh\left\{\frac{2\sqrt{(V_s - V_b)(\Delta V)}}{T_e}\right\} \tag{2.13}$$

CHAPTER III

The Reverse-Flow Cathode EEDF Control Method

The previously stated goal of this dissertation is to improve HET efficiency by targeting the ionization cost per beam ion and the plasma's ionization fraction through electron energy distribution function (EEDF) control. The first EEDF control method that was attempted was neutral gas injection to indirectly influence electron mean free path and therefore increase ionization (see Section A.1 for details). This experiment, which used an inductively coupled plasma as the test-bed, revealed that the addition of this flow did not change the shape of the EEDF or increase ion number density significantly enough. There was only a 10% increase in ion number density accompanied by a 10% decrease in electron temperature.

This led to the idea that in order to increase ionization, the EEDF would have to be manipulated in such a way as to target and increase narrow energy populations of electrons that could ionize the propellant gas. From this hypothesis, it was decided to target these populations with a gas mixing scheme where gas particles with electrons in naturally occurring metastable states with enough energy to ionize the thruster's main propellant would be used to transport electrons with the energies needed to increase ionization (see Section A.2 for details). The calculations and experiment carried out to test the feasibility of this method used a hollow cathode as the test-bed. Neon was used as the auxiliary gas in the calculations. The results disclosed

that another atom is not a good energy delivery method for increasing the ionization rate, because although the cross section for atom-atom collisions is much higher than electron-atom collisions, the speed of the particle, which also factors into the collision frequency, takes away gains associated with the larger cross section. In addition, this particle speed deficit is not made up for by the small fraction of regularly present metastable atoms in the gas being mixed in for this plasma condition when calculating the propellant ion production rate for the metastable neon atom-xenon atom collision. Therefore, the ion production rate for this scheme was several orders of magnitude lower than that of electron-xenon atom ionization.

A metastable neon number density that is two orders of magnitude larger than that of the electrons would be needed to compensate for its lower collision frequency to allow metastable neon-propellant atom ionization to even be comparable to electron-propellant atom ionization in the insert plasma environment. This would require a neon to xenon gas density ratio of 2×10^5 to 1 (i.e., a neon gas mixing ratio of $2\times10^7\%$). In the Hall thruster channel's ionization/acceleration zone (see. Table A.7 for the plasma parameters in these areas) the trends would most likely be similar, and this would flood the channel with neon neutrals, which would completely change the plasma conditions there, creating a negative affect on thruster efficiency in other ways. For example, it would greatly reduce the Hall current which aids in setting up the spatial electric field responsible for accelerating the ions to produce thrust.

This motivated the realization that in order to control the EEDF to improve thruster efficiency, the energy of the electrons alone needed to be directly altered in a way that took advantage of features that occur naturally within the Hall thruster environment. This led to proposing an EEDF tailoring method that involved positioning the hollow cathode, which is the thruster's source of ionizing and neutralizing electrons, so it is downstream of the thruster, and at an angle that is pointing back towards the discharge channel, and outside the densest part of the thruster plume,

instead of current orientations that place it pointing away from the discharge channel. Continuing in pursuing techniques that would not require additional power sources or additional thruster components for ease of implementation and so that gains would directly translate into increased efficiency, the intention behind this cathode placement was to allow a more direct path for the electrons to the channel's exit plane where the Hall current, responsible for ionizing gas propellant, is formed. The logic behind this scheme was that doing this would decrease the amount of energy the system used to get the electrons to the channel so that a larger portion of the available energy would be used in ionizing collisions. This approach translates into manipulating the EEDF by trajectory redirection in order to shift the entire distribution to higher energies in the location where ionization occurs.

The next section discusses how knowledge of various aspects of the thruster system were applied to determine the best downstream cathode placement, and also further expounds on why this reverse-orientation cathode modification was expected to increase thruster efficiency.

3.1 Testing Matrix

3.1.1 MCHall Simulations

An electron trajectory model for Hall thrusters called MCHall [85], written by Dr. Michael McDonald, was used in this thesis to model trajectories for an array of downstream cathode positions with various angles of orientation towards the thruster and at different radial locations from thruster centerline. The MCHall code calculates electron trajectories in three dimensional space using the DC electric and magnetic fields from the thruster. These fields are two-dimensional maps through thruster centerline that are assumed to have no azimuthal dependence given the annular design of the thruster. The B-field is imported from MagNet simulations and the E-field is

calculated from plasma potential maps generated from time-averaged emissive probe measurements within the plume and thruster pole-mounted Langmuir probes. The simulation domain is about 0.7 thruster diameters in the direction perpendicular to the thruster exit plane with the domain starting approximately at the thruster's exit plane and centered on thruster centerline. The width of the simulation domain is about 0.9 thruster diameters.

MCHall was used by McDonald to investigate how electrons made their way from a centrally mounted cathode to the channel. With this and other standard cathode mounting positions, the electrons are ejected with all of their velocity components directed perpendicular to or going in the complete opposite direction of the thruster channel. The results from the set of simulations he carried out showed that none of the electrons made their way to the channel or the thruster poles due to the DC electric and magnetic fields considered in the simulation for the centrally mounted cathode. [85] Therefore, it is most likely due to the AC components of the E and B fields and through the coupling of the electrons to the plasma that a significant fraction of the electrons arrive at the channel when the cathode is in this type of standard orientation. Further details about the MCHall code, McDonald's simulations, and a background on various Hall thruster models can be found in his thesis. [85] Instructions on how to run the model itself can be found in the Appendix of this thesis, see Section B.1.

The purpose of the simulations carried out with MCHall in this thesis was to determine from a DC standpoint what types of electrons would enter the channel of the thruster or would hit a thruster pole piece for the reverse-flow cathode as compared to the centrally mounted cathode in order to establish a sense for how the electrons from this type of cathode positioning would behave in the applied thruster fields. The MCHall methodology described in Section B.1 was used to design the test cases that were run in this simulated experiment. Instead of seeding full energy

and angular distributions of electrons, it was decided to consider single seed test cases with an origin angle and initial energy. One thing to note is that since the experimental data used to obtain the E-field was obtained with a centrally mounted cathode, the influence of the cathode position on the local plasma potential in the areas electrons were seeded from, that would allow these electrons to gain kinetic energy (or a "kick" as it is referred to in [85]) from their surroundings as they traveled out of the cathode, would not be realized. Therefore, in this first order approximation, this kick was introduced for some of the electron test cases by using an initial energy equivalent to the energy gain it was estimated the electrons would obtain upon exiting the cathode from the difference between the cathode and the local plasma potentials. In addition, these simulations did not take into account collisions with neutrals and the implications of this will be discussed in the results.

First, control simulations of electrons seeded from a centrally mounted cathode, and then other control simulations with an electron seeded over the channel and 0.1 m downstream were carried out. The results were compared to McDonald's baseline simulations to make sure the code was being used correctly here. See Fig.3.1 for results from a few of the control tests that were carried out. In image 1 in this figure, which is for a central cathode electron seeding location, an electron ejected along thruster centerline with zero initial energy heads straight and exits to the far field, building up energy as it goes from lower to higher potential and travelling parallel to the B-field lines. This matches the results obtained by McDonald in Ref. [85] Figure 4.12.

Images 2 and 3 in Fig. 3.1 are the result of an electron trajectory started 0.1 m downstream in front of the channel with no initial energy to simulate a secondary electron produced in the near-field by an inelastic electron-neutral collision, so that the results could be compared to the second image in Ref. [85] Figure 4.12. Results are similar with the electron's motion dominated by the influence of the crossed

electric and magnetic fields in this region, which is causing its azimuthal traversal. However, in this simulation, which did not include collisions with neutrals, as the electron gains more and more energy from the electric field and is directed further into the high-B-field region between the cathode and channel as its path stays for the most part aligned with the B-field, it continues to oscillate back and forth even more due to magnetic mirroring from this B-field gradient and the particle's kinetic energy is converted into potential energy as the electron is reflected downstream into a plasma potential hill.

After the control simulations were run and it was established that the model was working as expected, electrons ejected from potential downstream cathode locations were simulated. This was done using energies from 20 eV to around 84 eV at 0.05 to 0.2 m downstream, radial positions of either R_c or $1.4R_c$ (which is over the outer pole), and at seeding angles (relative to thruster centerline) from 0 to $\sim$90 degrees. An energy of 30 eV was chosen as a typical electron energy after experiencing an acceleration due to the potential difference between the cathode insert and the bulk plasma, using values obtained from Ref. [58]. Energies up to 84 eV were chosen to represent electrons in the high energy tail of the electron distribution. Fig. 3.2 shows some of the initial test cases that were carried out. With a seeding energy of 20 eV, an electron directed towards the channel from approximately channel centerline and 0.1 m downstream did not have enough energy to cross the B-field and enter the channel; however, at 83.5 eV it did.

These results led to the next set of test cases shown in Fig. 3.3, where simulations 1-4 show that at low energy (0 eV) and various downstream distances, the electron is eventually lost to the far field after a trajectory similar to that shown in Fig. 3.1 images 2 & 3, where the total time the electron is oscillating in the near-field decreases with increasing axial distance. When comparing results 5-7 in this figure with results 4-6 in Fig. 3.5, it shows that at similar high energy values (65 -75 eV), electrons

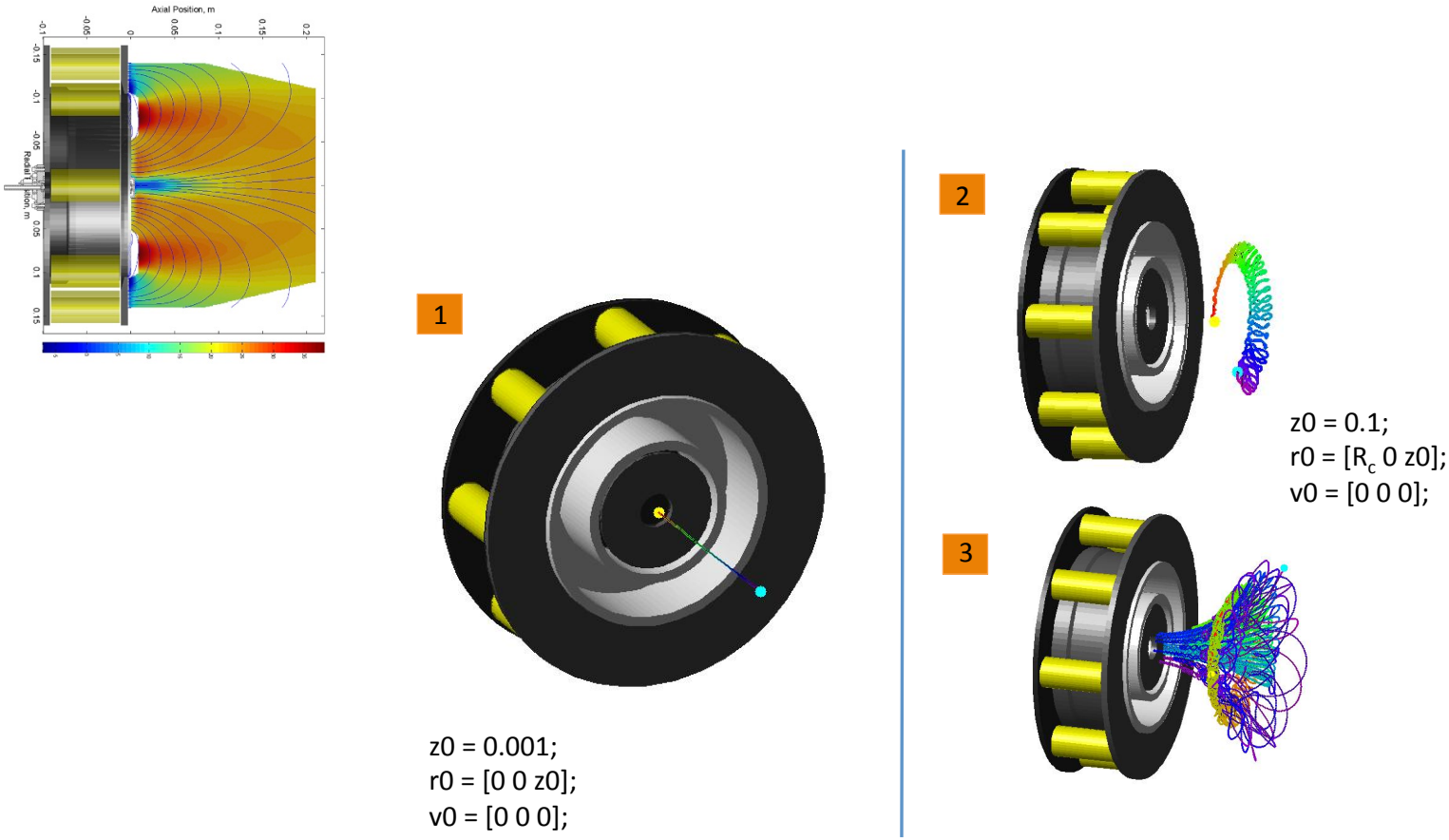

Figure 3.1: This figure shows a few of the MCHall control simulations that were carried out. The image in the upper left hand corner, shows the H6 plasma potential map used in the MCHall simulations (from Ref. [85] via [58]), with the addition of the cathode location for the simulation results shown in 1. In 2 and 3, the results are shown for seeding an electron 0.1 m downstream in front of the channel with no initial energy. In 2, the simulation was run for 1×10^5 timesteps and 3 is the same simulation run until the electron exited the simulation domain. In all of these images, the yellow dot is the electron's starting position, and the blue dot shows its position at the end of the simulation. In addition, the trajectory is indicated from beginning to end in rainbow color order starting from red and ending with violet.

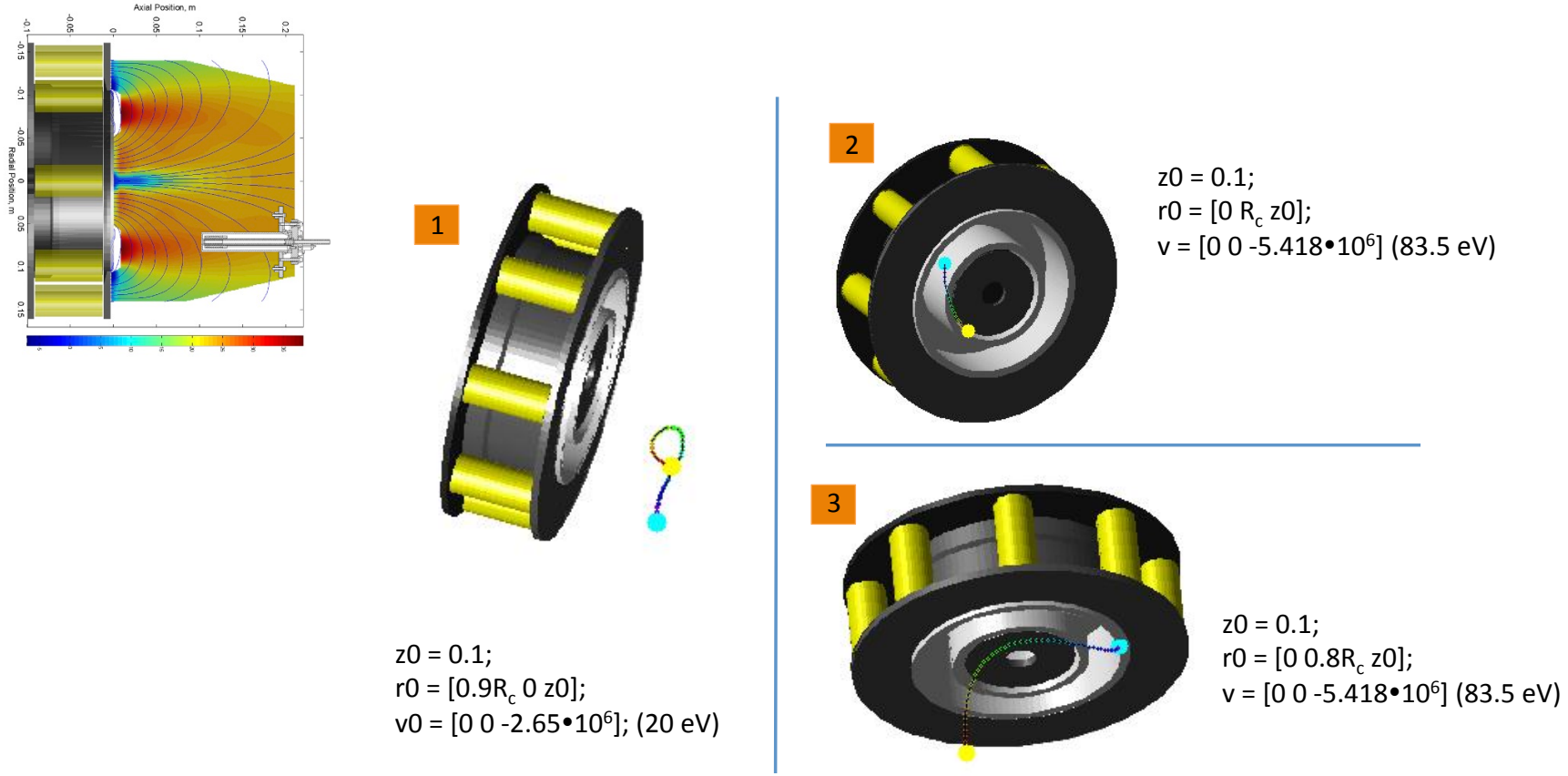

Figure 3.2: This figure shows a few of the initial MCHall simulations for a downstream cathode that were carried out. The image in the upper left hand corner, shows the H6 plasma potential map used in the MCHall simulations (from Ref. [85] via [58]), with the addition of the cathode location for the simulation results shown in 1, 2 and 3. In all of these images, the yellow dot is the electron's starting position, and the blue dot shows its position at the end of the simulation. In addition, the trajectory is indicated from beginning to end in rainbow color order starting from red and ending in violet. As seen from these results, a low energy electron (20 eV) is lost to the far field; however, high energy electrons enter the channel (in 2) and hit the outer channel wall (in 3) in these simulations.

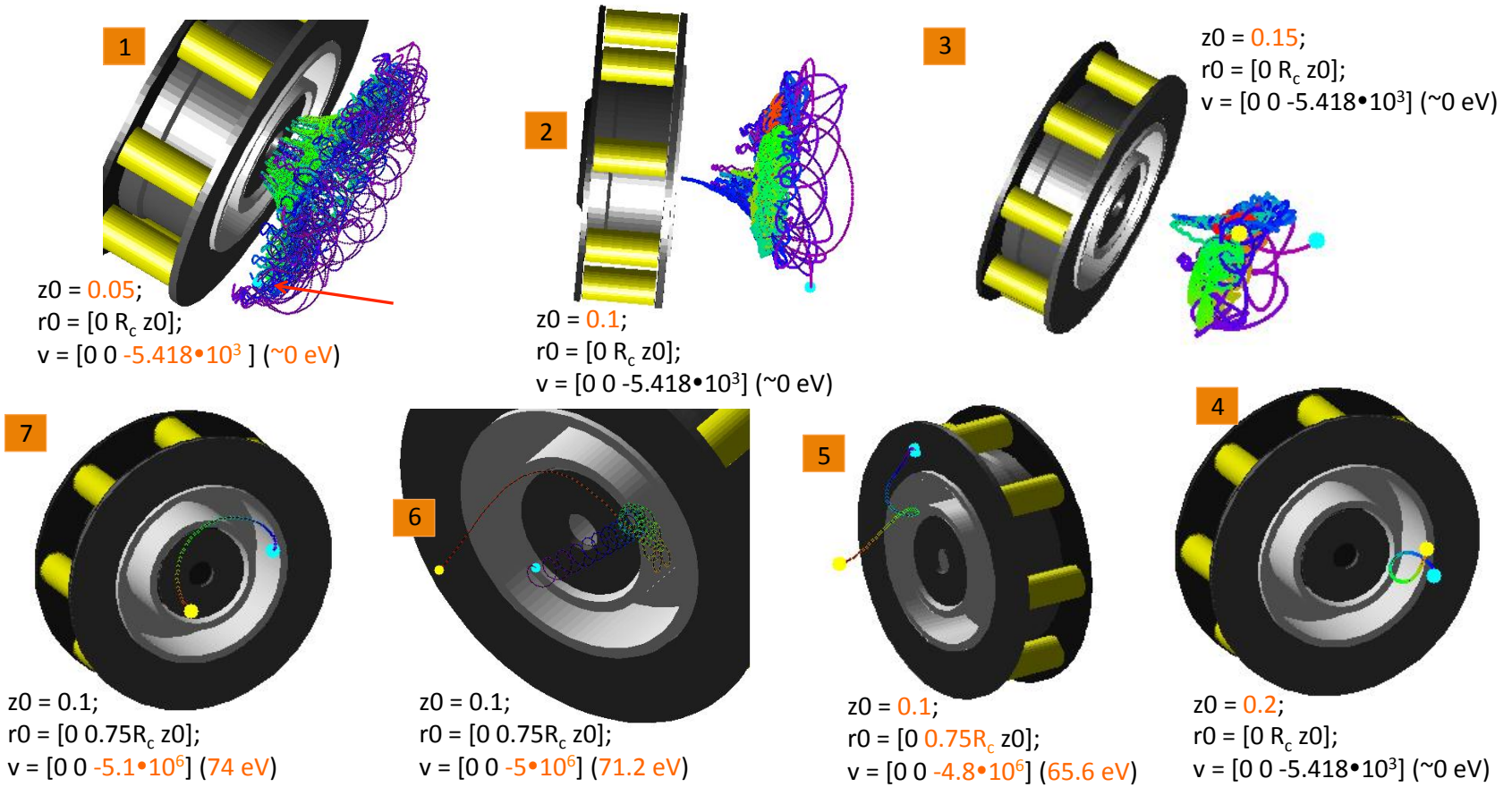

Figure 3.3: This figure shows additional MCHall simulations carried out for a downstream cathode. The image in the upper left hand corner of Fig. 3.2 shows the cathode location for these simulations. The differences between these simulated scenarios from one number to the next are indicated with orange text. Results 1-4 show that at low energy (0 eV) and various downstream distances, the electron is eventually lost to the far field after a trajectory similar to that shown in Fig. 3.1 images 2 & 3. These electrons are caught in a near-field oscillation that decreases in length-of-time with increasing axial distance. However, results 5-7 show that at high energy (65 -74 eV) and 0.1 m downstream, the electrons can impact the outer pole (as in 5), hit the inner channel wall (6) or enter the channel (7) when seeded close to channel centerline.

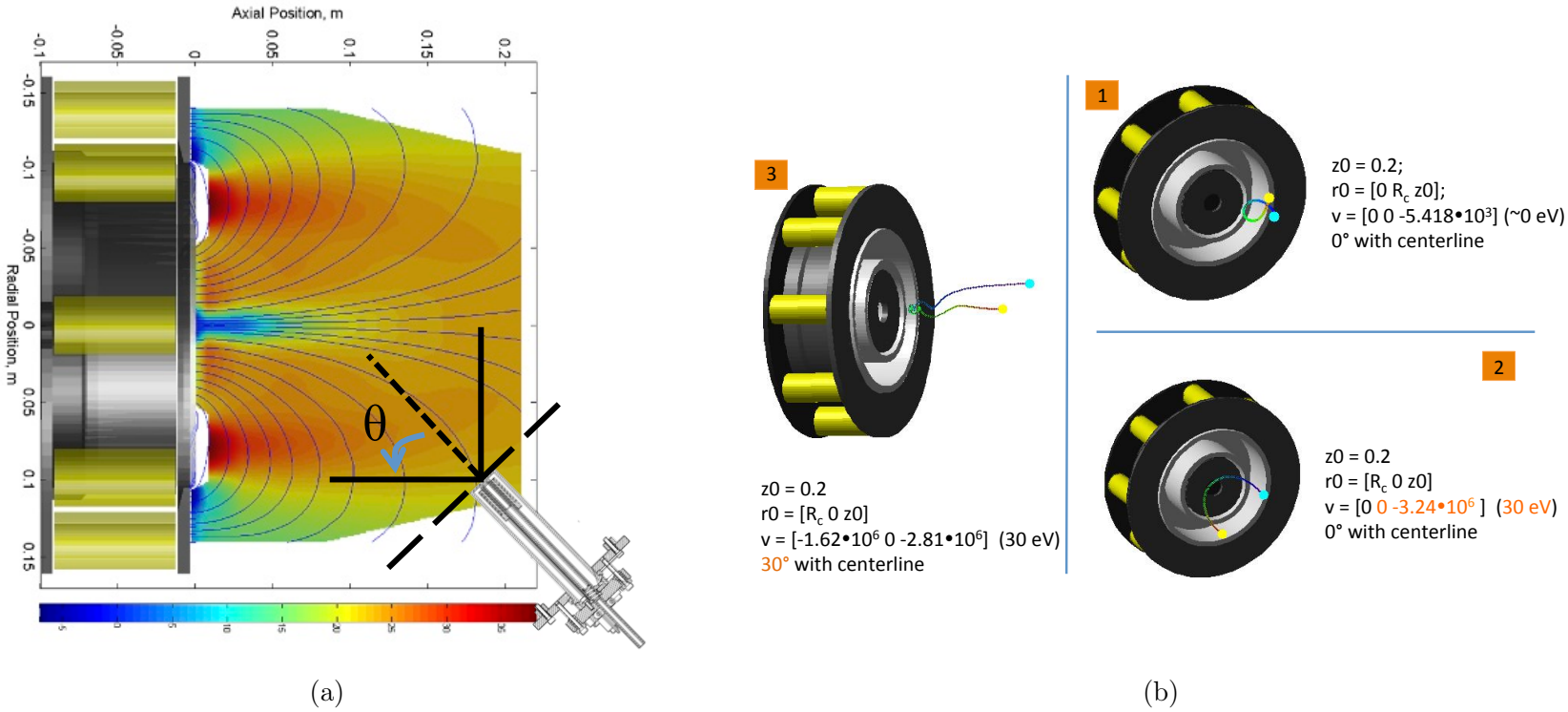

(a) (b)

Figure 3.4: This figure shows some of the last set of MCHall simulations carried out for a downstream cathode. The differences between these simulated scenarios from one number to the next are indicated with orange text. (a) A picture showing the H6 plasma potential map used in the MCHall simulations (from Ref. [85] via [58]), with the addition of the cathode location for the simulation results in this figure. The cathode is placed at various angles relative to thruster centerline. (b) At 0.2 m downstream with energies less than 30 eV and at various angles, the electron is lost to the far field. The results continue in Fig. 3.5.

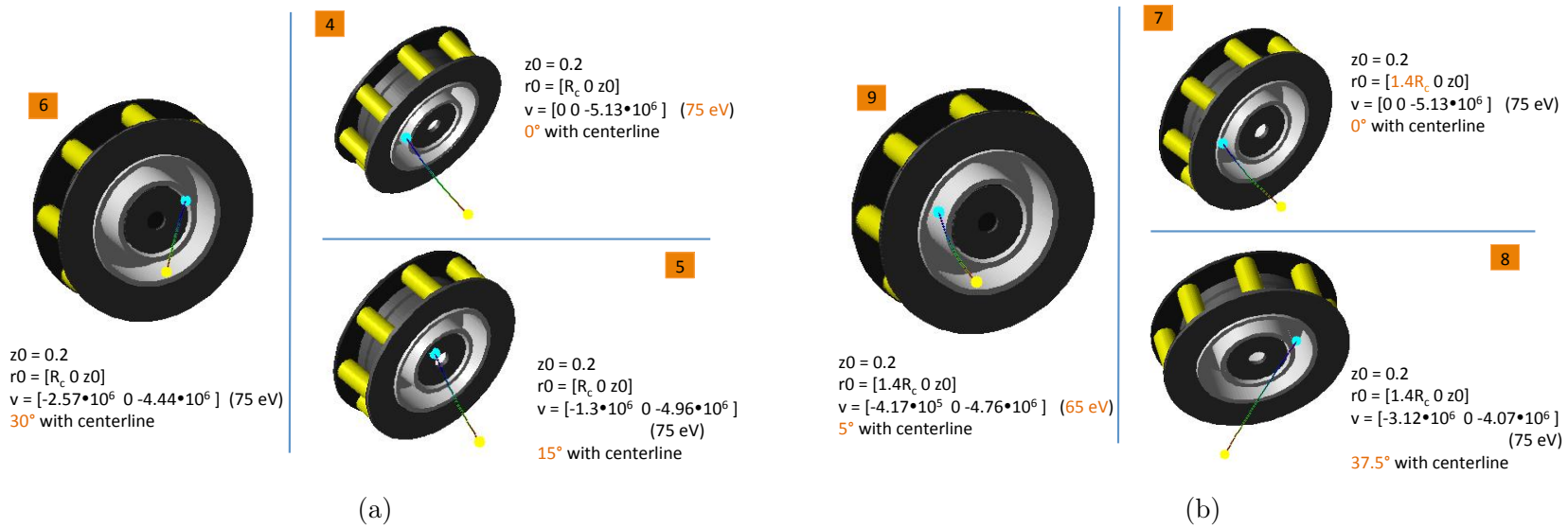

Figure 3.5: This figure is a continuation of Fig. 3.4. Together, these figures show the final set of MCHall simulations carried out for a downstream cathode. The differences between these simulated scenarios from one number to the next are indicated with orange text. (a) At a higher energy (75 eV) the electron's trajectory is straight and can be controlled to impact different parts of the thruster by changing the seeding angle. (b) Similarly, at a seeding location over the outer pole, at high energies, the electron can be made to impact the channel in various locations.

that are further downstream (0.2 m as compared to 0.1 m) can impact the poles and enter the channel with a straight line trajectory as opposed to looping around in the near-field crossed electric and magnetic fields before impact.

Figure 3.4 also shows that changing the angle of the trajectory at a lower energy of 30 eV causes the electron to come closer to impacting the channel, but it still does not actually make contact. For example, image 3 shows the results for a 30° angle with centerline, and the results are similar for other angles between 0 and 90°. Images 4 through 9 in Fig. 3.5 show that with a combination of high electron energies (65 -75 eV), ejection positions in front of the channel or the outer pole, and 0.2 m downstream, the electrons impact various locations on the front face of the thruster and enter the channel in various locations when changing the start angle. The electrons can even cross over the center of the thruster to impact the thruster on the opposite side to the seeding location.

The MCHall reverse-flow cathode test case simulations were run to gain an understanding of how these electrons might behave in the static component of the near, crossed electric and magnetic fields of the thruster to first order in order to help make predictions about the effectiveness of this method, and to help narrow down the downstream locations and angles that should be considered during empirical testing. What can be inferred from these experiments is that electrons in the high energy tail of the EEDF should have little issue getting to the thruster channel when it comes to the DC electric and magnetic fields. Secondly, the bulk electrons, which were predicted to obtain ∼30 eV of directed kinetic energy from the cathode to ambient plasma potential difference, will most likely be aided by non-classical transport mechanisms that also enable electrons from the standard cathode positions to enter the channel. The first point about higher energy electrons being able to head straight to the channel implies that they will not collide with neutrals, and neutral collisions were neglected during these simulations. This was a valid assumption because for

straight-line trajectories in this vicinity, the electron mean free path is greater than the distance between the seeding location and the thruster. The electron mean free path in the first 0.2 m of the thruster can be calculated using xenon neutral number densities from [58] of 0.5 to 1×10^{19} m^{-3} and total (excitation, elastic and ionization) neutral xenon-electron collision cross sections for electrons with energies of 30 eV and higher from [123] which states values of around $10\text{-}20\times10^{-20}$ m^2. These numbers give electron mean free paths of $\sim$0.5 to 2 m.

From the results of these simulations, it was decided to focus on cathode locations that would be further downstream than 0.1 m, so there is less chance of electrons getting caught bouncing around in the crossed near-fields of the thruster before entering the channel like in Fig. 3.3 images 5-7, and would instead have a straighter trajectory, as shown in shown in Fig. 3.5. This difference is most likely due to the electrons having time to build up even more kinetic energy as they travel towards the higher plasma potentials in front of the channel, which allows its trajectory to not be as affected by the magnetic field, (see the plasma potential field between the downstream cathode and the channel shown in Fig. 3.4(a)). It is preferable for the electrons to go straight towards the channel, so there is less chance of them colliding with neutrals in the near field before entering the channel. If ionization occurs in the near field instead of in the thruster channel, these ions would experience less of the full potential drop established by the applied fields and the plasma, which would decrease voltage utilization efficiency. Also, having the cathode further downstream would help with keeping the cathode out of the main part of the ion beam, which is another criteria used in determining the cathode's downstream position, and is discussed in further detail in the next subsection.

3.1.2 Cathode's Downstream Positioning & Experimental Setup

The downstream placement of the cathode was governed by two criteria. The first was to keep the cathode outside of the main part of the ion beam. This was accomplished by using an analysis done by Reid [55]. A notable portion of the ions in the very near-field region of the thruster have a radial component to their velocity vector, which leads to what he calls "ion beam crossover," meaning that this causes the ions to be focused towards thruster centerline. The radial velocities necessary for the ions to reach centerline by about 1 thruster diameter (D_T) downstream is in keeping with the difference in potential seen between the region in front of the channel and thruster centerline within the first 0.5 D_T downstream of the H6's exit plane through plasma potential measurements that were made. This plasma potential difference establishes a radially inward pointing electric field whose aggregate effect on the ions would be strong enough to cause the observed ion beam focusing at about 1 D_T downstream. Because of this, and the results from the MCHall simulations discussed in subsection 3.1.1, the search for the best downstream cathode placement centered around an axial location of 1 D_T from the thruster's exit plane during the empirical experiment phase for this EEDF control method.

The second specification for downstream cathode placement was keeping the cathode inside the separatrix. For the thruster's B-field, the separatrix is the surface where this vector field switches from open to closed field lines. In past cathode placement experiments, carried out by Sommerville et al., [124] with the cathode placed at a 90° angle relative to thruster centerline, the cathode to ground voltage (V_{c-g}) increased significantly (became less negative) when the electrons were sourced from inside the separatrix of the thruster's magnetic field relative to when it was outside the separatrix. This larger V_{c-g} signifies a smaller potential difference between the cathode and the ambient plasma. Also since Sommerville saw an increase in discharge current along with this increase in V_{c-g} as the cathode was moved inside of the separatrix,

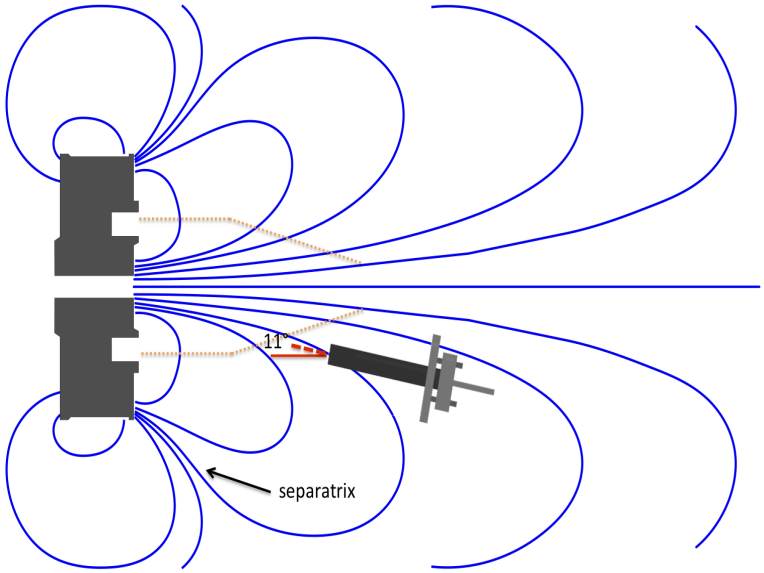

Figure 3.6: This is a rough sketch of the H6's magnetic field lines showing the placement of the downstream reverse-orientation cathode relative to the separatrix and the thruster. The drawing is based on a Magnet simulation of the H6's B-field. **Note: The field lines in this sketch are not exact, nor is the picture to scale with actual H6 dimensions.**

this meant the amount of work needed to send the electrons from the cathode to the locations where they were needed in the plume to establish charge neutrality and to complete the circuit was reduced. Figure 3.6 gives a rough sketch of the H6 B-field lines relative to the general placement of the cathode.

The testing matrix also included angles between 0 and 90° for the cathode relative to thruster centerline (see Fig. 3.6) and radial locations that would place the tip of the cathode around channel centerline. In order to move the cathode around during the test, the cathode was mounted on a theta stage that was then mounted on X-Y tables. The tip of the cathode was centered on the theta stage's axis so that rotating the theta stage would not change the radial and axial location of the point from which electrons were sourced, only the angle. See Fig. 3.7 for a diagram and Figs. 3.8(a) & 3.9(b) for pictures of the cathode's downstream positioning system. The X and Y linear stages were long enough to allow the cathode to be moved well outside the range of the thruster during thruster operation with the centrally mounted cathode.

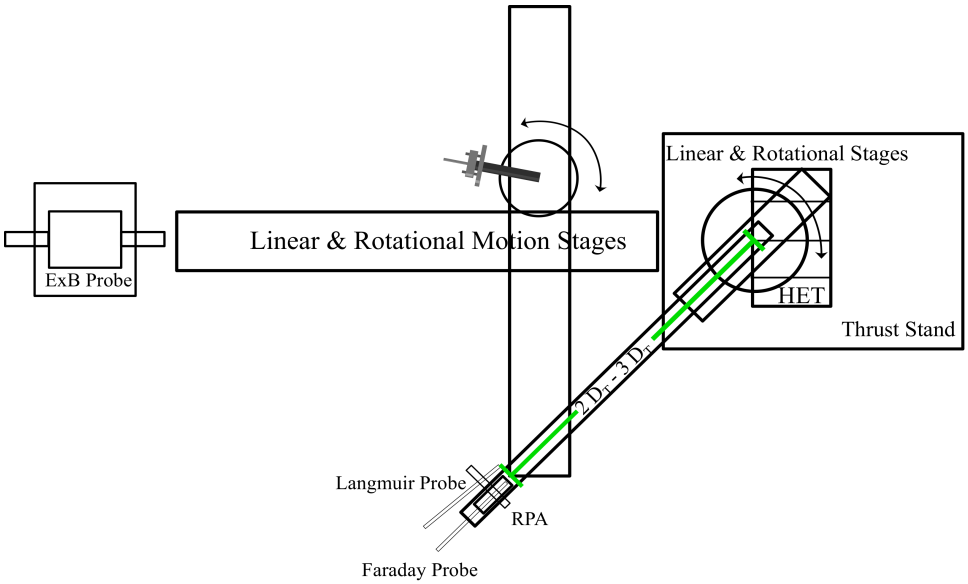

Figure 3.7: A schematic showing the experimental setup. The cathode was mounted on a rotational stage, which was then mounted on linear stages that could move the cathode in two dimensions. A Faraday probe, RPA and LP were mounted on an arm that was secured to a rotational and linear stage so that the angle and radius could be adjusted during the tests. Data was also taken with a thrust stand and ExB probe.

In the initial chamber experiments with the downstream cathode, first the thruster was lit with the centrally mounted cathode with the downstream cathode out of range. Next the external cathode was lit at a 10 sccm flow rate and then slowly moved into position. Then the plume was handed off to the external cathode by slowly decreasing the flow of the central cathode and increasing the flow to the external cathode to a 7% CFF, which was 14 sccm. This process was not ideal since the cathodes dealt with being in such close proximity and nearly facing each other by driving their V_{c-g} well below ground, to around -36 V until the switch off occurred. Therefore, starting the thruster with the external cathode was practiced and perfected.

With a center mounted cathode, the thruster is started while the B-field coil currents are about $^2/_3$ of their nominal value. With the external cathode, this caused sparking on startup to create the initial electrical connection between the cathode and the thruster, however when the coil currents were decreased to $^1/_3$ nominal during start up, igniting the thruster with the external cathode was as smooth as igniting with the

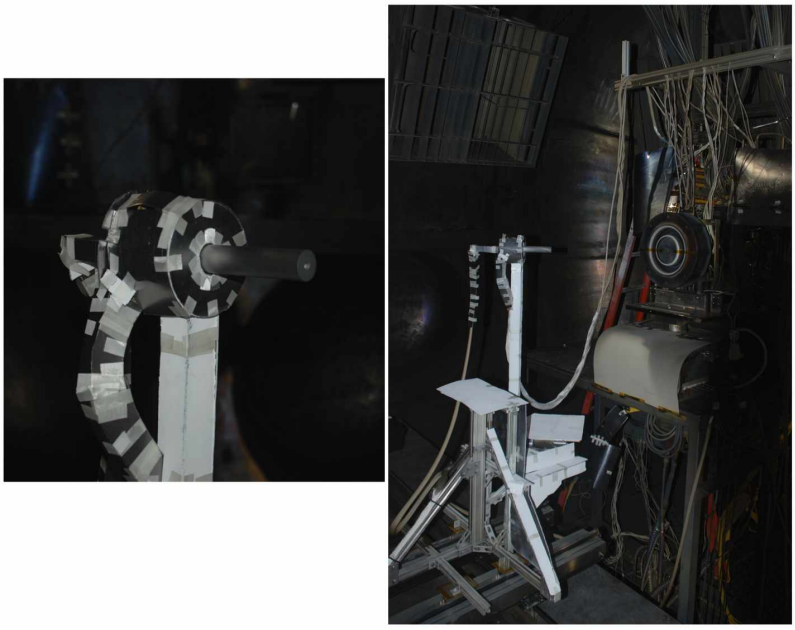

(a)

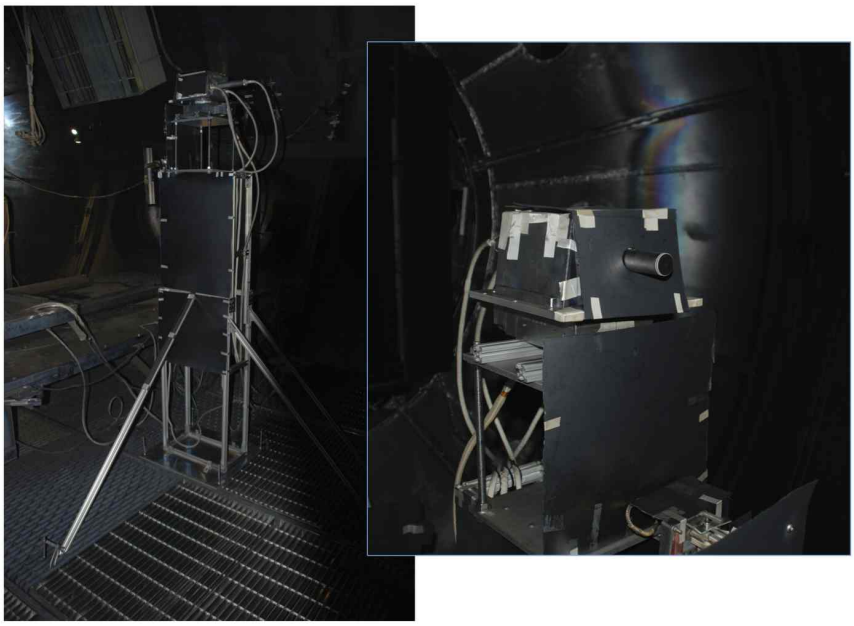

(b)

Figure 3.8: (a) A picture of the external cathode mounted on the X-Y and θ stages, and a close up showing how the cathode and its mount were protected from the plume using graphoil secured with fiberglass tape. Some of the graphoil is white because it was sprayed with boron nitride. (b) Close up pictures of the ExB probe and its mounting structure.

(a)

(b)

Figure 3.9: (a) Close up pictures of the RPA, FP and LP. (b) The full view of the experimental setup, which shows the cathode and the rotational arm that held the RPA, FP and LP.

internal cathode. (See the videos of firing the thruster with the internal and external cathodes in Appendix C.) After start up, the B-field was then increased to the desired operating condition, which was the nominal value for the H6 thruster where $^{B_r}/_{B_r^*} = 1$, and is described in more detail elsewhere [59]. During external cathode operation, the central cathode (and its keeper) were left floating so that its interaction with the plasma would be minimal.

3.1.3 Operating Conditions

The operating conditions that were tested are shown in Tables 3.1 & 3.2 and Figs. 3.10 & 3.11. A 150 V and a 300 V condition were explored for a flow rate of 20 mg/s. These tables and figures also show the position of the external cathode that was used to explore the effect of a downstream cathode on thruster efficiency. This location was settled on by moving the cathode around and watching the cathode-to-ground voltage, the discharge current, and changes in the null coil current on the thrust stand to get an idea of the overall change in thruster efficiency. Changes in null coil current did not give a definite idea of the thrust value, as the null current's zero value drifts throughout operation. Therefore, the actual thrust values were not obtained until the thruster was turned off and the thrust value was adjusted with the zero value. This exploration was performed for both the 300 V and the 150 V conditions, so it was not assumed the same position would optimize a change in efficiency for both conditions.

Thruster discharge current oscillations were monitored throughout testing using a Tektronix TCPA current probe. The same peak-to-peak values and oscillatory behavior were observed between operation with an external and an internal cathode. Residual Gas Analyzer (RGA) traces of partial pressure vs. atomic number (from 0 to 150 a.m.u.) with the thruster on were taken for the internal and external cathode operating conditions and compared to determine if there were detectable differences

Table 3.1: 300 V 20 mg/s Operating Conditions

$\dot{m}_T$	Cathode orientation	Cathode position	V_D	I_D	V_{keeper}	$V_{f,thruster}$	V_{c-g}
21.4 mg/s	Internal	$\theta = 180^\circ$ $R = 0$ $Z = 0$	300.1 V	17.7 A	2 V	-35 V	-11.1 V
	External	$\theta = 11^\circ$ $R = 1\ R_{channel}$ $Z = (15 \setminus 16)\ D_T$	300.7 V	18.4 A	6 V	-39 V	-8.3 V

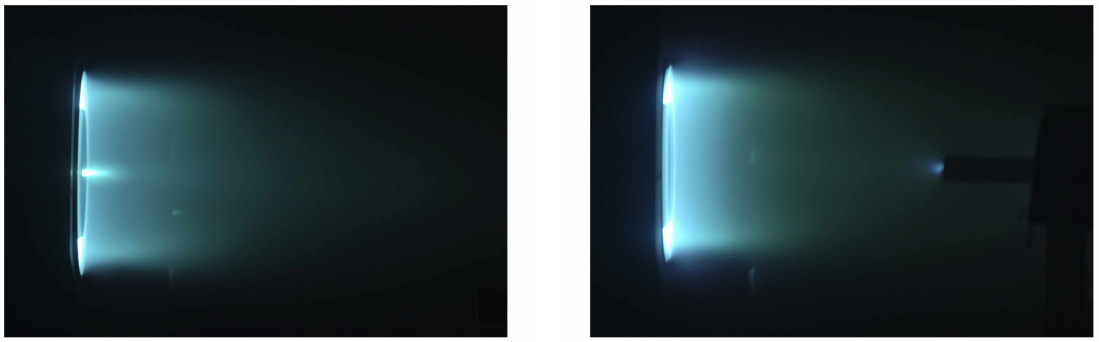

(a) Thruster Operating with Internal Cathode (b) Thruster Operating with External Cathode

Figure 3.10: 300 V 20 mg/s Operating Conditions

Table 3.2: 150 V 20 mg/s Operating Conditions

$\dot{m}_T$	Cathode orientation	Cathode position	V_D	I_D	V_{keeper}	$V_{f,thruster}$	V_{c-g}
21.4 mg/s	Internal	$\theta = 180^\circ$ $R = 0$ $Z = 0$	150.4 V	18.9 A	3 V	-24 V	-8.9 V
	External	$\theta = 11^\circ$ $R = 1\ R_{channel}$ $Z = (15 \setminus 16)\ D_T$	150.1 V	19.7 A	5.6 V	-29.5 V	-8.7 V

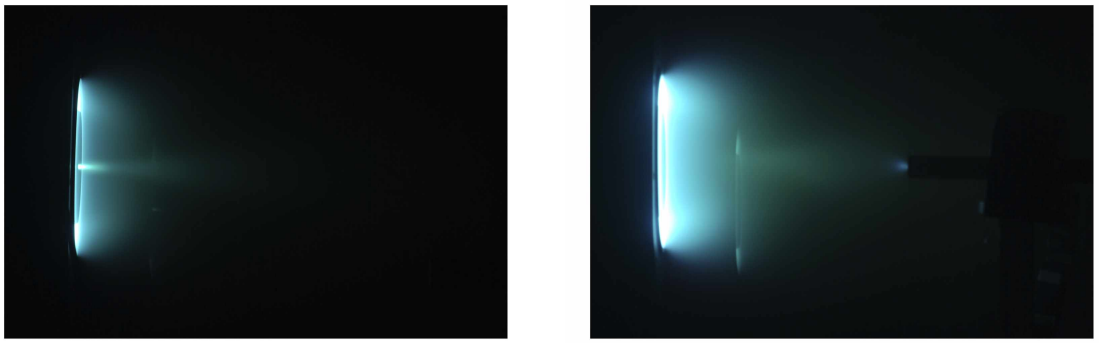

(a) Thruster Operating with Internal Cathode (b) Thruster Operating with External Cathode

Figure 3.11: 150 V 20 mg/s Operating Conditions

in the plume composition to ensure that cathode and cathode mount materials were not contributing to the measured thrust. The mass spectrometer used, the Kurt J. Lesker AccuQuad model SRS RGA-200 with a minimum detectable partial pressure of $\sim 5 \times 10^{-11}$ Torr, showed no significant differences between the traces for the two operating configurations. Changing the B-field strength, and using the trim coil to explore the possibility of further improvements in efficiency with cathode location were outside the scope of these tests.

3.2 Performance

In the ensuing subsections that show the results from the probes and thrust stand for analyzing the performance of the reverse-flow cathode EEDF control method, efforts were taken to minimize systematic bias that would affect the data, and random error was also reduced as much as possible. For instance, one way this was done was by calibrating the instruments used. The error considered in this work included uncertainty in the instrument's readings after calibration, and error in measurements made by hand with a ruler given the geometry of the object being measured and the number of increments on the ruler. Hand measurements were made twice to reduce systematic error from a mismeasurement. Systematic error from errors in the theory applied to analyzing a measurement are corrected where possible and where it will make a difference in the final terms that are being corrected such as CEX in some instances. At other times, when this error would be more complicated to account for, it is just mentioned as another source of error in the text or in the references cited.

3.2.1 Thrust Stand Results

As described and demonstrated in the experimental equipment description chapter (specifically Section 2.6) and the thrust stand data collection procedures (Appendix B.8), the calibration of the thrust stand is a key component of taking precise thrust

data. This calibration was carried out prior to taking measurements, and checked immediately after measurements were complete while the chamber was at vacuum on each day of thrust stand testing.

To aid this process, a MATLAB chi-squared fitting routine was used to fit a function to the calibration data. This routine used the measured values and their x & y error bars and returned the model fit parameters and their uncertainties. The reduced chi-squared value ($\sim\chi^2$, and also sometimes denoted in this thesis as simply χ^2) and the residuals plots were examined to determine the goodness-of-fit. Two residual plots were used. First, the residuals were plotted against the weight applied (the x-value in the calibration graphs) as discussed by Polk.[103] In addition, the residuals were plotted in the order data was taken to more easily observe certain types of systematic biases that may have been introduced while taking the data.

Initially, the PID response from the four weights was gone through several times as Polk recommends in order to construct the calibration curve from a large number of measurements. However, given the fact that each calibration set (with the four weights) took about 45 minutes to perform and it was not automated, and the fact that after the first two data sets, the calibration parameters changed by negligible amounts, four calibration sets were done. To check for hysteresis, every other calibration was performed in the opposite direction, meaning that initially, the calibration weights were added in sequence to increase the total weight, and then the next calibration set started with all of the weights added, and then one at a time each weight was removed to decrease the total weight. This sequence was repeated once more to total four calibration sets. In between each measurement in each set of calibrations, all the weights were removed to obtain a zero-drift correction. The zero-drift correction was also obtained for each thrust measurement taken during testing by turning off the thruster after each thrust measurement and subtracting this thrust measurement from the measurement with the thruster on.

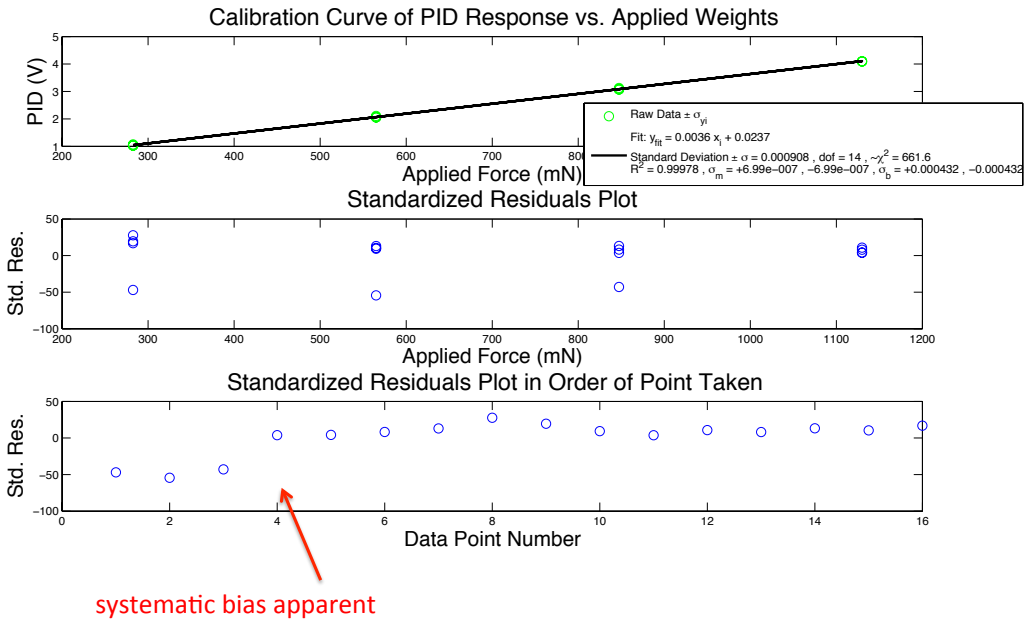

(a)

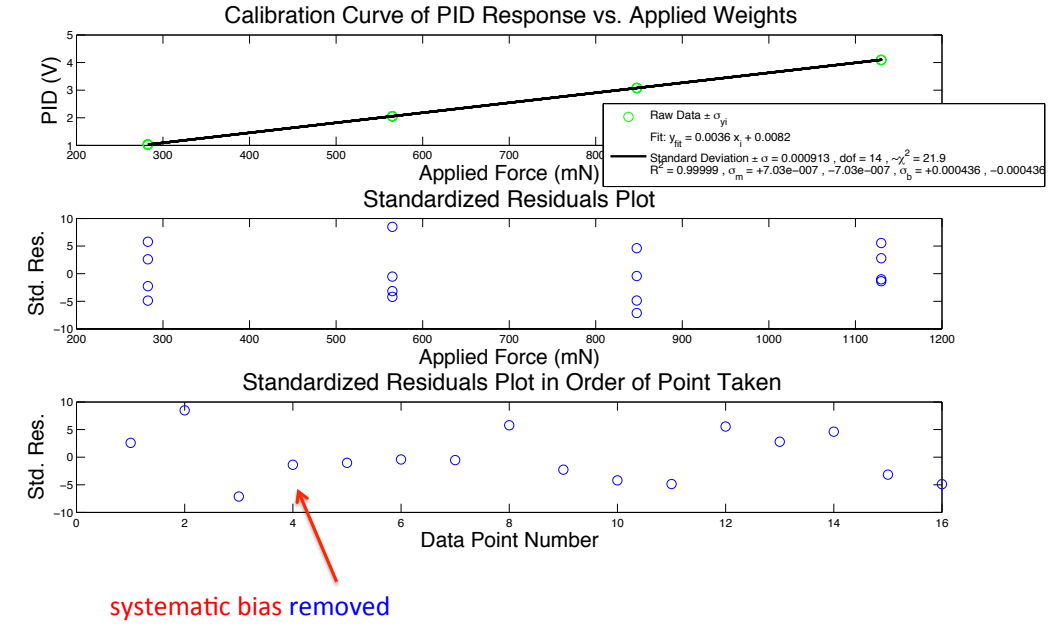

(b)

Figure 3.12: A chi-squared fitting routine was used to fit the function to the data. Residuals were observed plotted against the weight applied and also against the order in which the points were taken to see if any systematic bias was being introduced with the method used to take the data. (a) A calibration curve where the systematic bias imposed by not keeping the thrust stand platform inclination constant throughout the calibration was apparent from the residuals plots. (b) A calibration curve that was obtained when the inclination was kept constant. This is an example of the calibration curves used to calculate thrust.

During calibration, any hysteresis from the way each weight was applied to the thrust stand was easily observed in the residuals when plotted against the order in which the points were taken. For example, Fig. 3.12 shows what happened during a preliminary calibration when the thrust stand platform's inclination was not being regulated, which needed to be done manually. In the first set of charts in that figure (Fig. 3.12(a)), after the first three data points, the platform was placed back at its set inclination value, and was kept close to this value for the rest of the calibration. This adjustment is most clearly seen in the last of that set of plots, which is of the residuals versus the order in which the data points were taken and in the χ^2 value. In the second set of plots, Fig. 3.12(b), the inclination was kept constant throughout the entire calibration, resulting in a lower χ^2 value, a random and more narrowed distribution of residuals, and a shift in the y-intercept value of the fit.

After the calibration was verified following the completion of the testing with the thrust stand for that day, these fit functions were then used to calculate the thrust and the uncertainty seen in the thrust stand results shown in Tables 3.3- 3.6. Figure 3.12(b), is an example of the calibration curves used in calculating thrust.

Another way that precise thrust stand measurements were promoted was by placing thermocouples on various components throughout the thrust stand to make sure that the chiller was in fact keeping the thrust stand at a steady temperature that was within the operating ranges for the hardware within it. Thermocouples were placed on 1. the base of the thruster, which was attached to the thrust stand mounting platform 2. under the mounting platform, which was the roof of the internal portion of the thrust stand that housed many of its mechanical and electronic devices 3. the LVDT core mount 4. the LVDT coil mount 5. the null plunger mount 6. the null coil mount. As seen in Fig. 3.13, which was taken during one of the days of testing, all the thermocouples in the thrust stand's interior read temperatures that stayed between $\sim$292 K - 294 K even while the base of the thruster rose to around 400 K as the

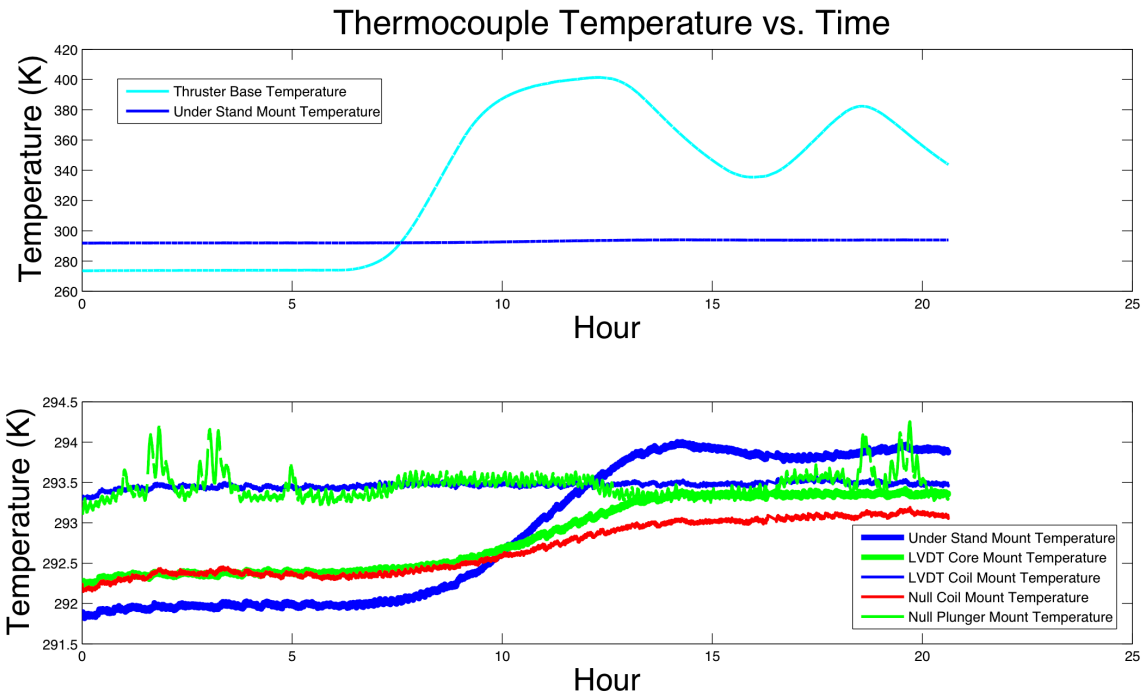

Figure 3.13: This figure shows the thermocouple data for the thrust stand before and while running the thruster.

thruster heated up during operation. After the thruster was turned on around hour 7, the thruster mount reached a steady state temperature after about three hours. The dip in temperature, starting around hour 13, was when the thruster was turned off for a period of time until around hour 16.

Due to the fact that in the literature thrust results have usually been taken with the thruster body grounded, thrust measurements were first taken for the operating conditions tested with a grounded thruster body, and they were compared to the literature (see Table 3.3). These thrust and thrust-to-total power (T/P_{tot}) values that were all obtained with the standard cathode configuration are comparable to the literature. The differences in the thrust-to-total power values here, which are slightly higher than those in the literature [16, 58], may be due to changes in the discharge channel wall and other portions of the device over time as the thruster was run for many hours, and due to slight differences in how the thrust data was taken.

Thrust measurements with the thruster body grounded were also compared to

Person (Location)	V_D	I_D	$\dot{m}_A$	P_D	$T(mN)$	$uncer.\pm$	Notes
Hofer (JPL)	300 V	20 A	19.7 mg/s	6 kW	401 mN	4 mN	Hofer AIAA 2012 [125]
Reid (PEPL)	300 V	19.94 A	20 mg/s	6 kW	398 mN	2 mN	Reid thesis 2009 [55]
Jameson (UCLA)	300.3 V	20 A	21 mg/s	6 kW	392 mN	2 mN	Jameson thesis 2008 [58], used trim coil
Trent (PEPL)	300.1 V	18.00 A	20 mg/s	5.4 kW	393.3 mN	0.3 mN	
Brown (PEPL)	150 V	21.53 A	20 mg/s	3.2 kW	260 mN	5 mN	Brown thesis 2009 [16], different magnet settings
Trent (PEPL)	150.5 V	18.66 A	20 mg/s	2.8 kW	249.2 mN	0.2 mN	

Table 3.3: Thrust Results Compared to Previous H6 Thrust Measurements

Thruster Isolation	V_D $uncer.\pm$	I_D $uncer.\pm$	$\dot{m}_A$ $uncer.\pm$	P_{tot} $uncer.\pm$	T $uncer.\pm$	T/P_{tot} $uncer.\pm$
Grounded	300.1 V ± 0.1	18.00 A ± 0.03	20.0 mg/s ± 0.2	5.439 kW ± 0.008	393.3 mN ± 0.3	72.3 mN/kW ± 0.1
Floating	300.1 V ± 0.1	17.70 A ± 0.03	20.0 mg/s ± 0.2	5.350 kW ± 0.008	385.8 mN ± 0.3	72.1 mN/kW ± 0.1
Grounded	150.48 V ± 0.07	18.66 A ± 0.03	20.0 mg/s ± 0.2	2.850 kW ± 0.004	249.2 mN ± 0.2	87.5 mN/kW ± 0.2
Floating	150.48 V ± 0.07	18.79 A ± 0.03	20.0 mg/s ± 0.2	2.868 kW ± 0.004	252.0 mN ± 0.2	87.9 mN/kW ± 0.2

Table 3.4: Thrust Results - Thruster Body Floating vs. Grounded, both with Internal Cathode

those with a floating thruster body for both the 150 V and the 300 V operating conditions used in this thesis. An internal cathode was used for these operating conditions as well (see Table 3.4). The thrust measurements shown are from an average of measurements taken over about a two minute span of time while the thrust stand inclination was steady. The corresponding discharge current, voltage, and total power shown for each of these measurements were averaged over the same time period while data was being taken.

As seen in Table 3.4, since the total power between the two cases is slightly different, the best way to compare these thrust values to determine if there is a significant difference is to look at the thrust-to-total power (T/P_{tot}). For both the

Cathode Location	V_D $uncer.\pm$	I_D $uncer.\pm$	$\dot{m}_A$ $uncer.\pm$	P_{tot} $uncer.\pm$	T $uncer.\pm$	T/P_{tot} $uncer.\pm$
External	300.7 V ± 0.1	18.44 A ± 0.03	20.0 mg/s ± 0.2	5.588 kW ± 0.008	404.4 mN ± 0.2	72.4 mN/kW ± 0.1
Internal	300.1 V ± 0.1	17.70 A ± 0.03	20.0 mg/s ± 0.2	5.350 kW ± 0.008	385.8 mN ± 0.3	72.1 mN/kW ± 0.1
External	150.07 V ± 0.07	19.71 A ± 0.03	20.0 mg/s ± 0.2	2.994 kW ± 0.004	253.9 mN ± 0.2	84.8 mN/kW ± 0.2
Internal	150.48 V ± 0.07	18.79 A ± 0.03	20.0 mg/s ± 0.2	2.868 kW ± 0.004	252.0 mN ± 0.2	87.9 mN/kW ± 0.2

Table 3.5: Thrust Results - Cathode Location Internal vs. External

150 V and the 300 V conditions, there is no statistically significant difference between the thrust-to-total power for floating and grounding the thruster. This is because when considering the uncertainty in these calculations, their possible value ranges overlap. Table 3.5 shows thrust results for running the H6 with the downstream, reverse-orientation cathode compared to the centrally mounted cathode. For the 300 V condition, the external cathode produces a slightly higher thrust-to-total power than the internal cathode, while in the 150 V condition, the large increase in discharge current causes a decrease in the thrust-to-total power with the external cathode even though an increase in thrust is seen. The next subsection shows how these differences impact total efficiency at these operating conditions.

3.2.2 Total Efficiency from Thrust Stand Data

Table 3.6 shows the calculations of total efficiency for grounding and floating the thruster body with internal cathode operation, and also for operating the thruster with the external cathode while floating the thruster body. Total thruster efficiency was calculated using the following formula from Section 1.5:

$$\eta_{tot} = \frac{T^2}{2P_{tot}\dot{m}_T}. \tag{3.1}$$

Thruster Configuration	V_D	I_D	P_{tot}	T	η_{tot}	η_{tot} $uncer.\pm$
Grounded, Int Cath	300.1 V	18.00 A	5.44 kW	393.3 mN	66.5 %	±0.7
Floating, Int Cath	300.1 V	17.70 A	5.35 kW	385.8 mN	65.0 %	±0.7
Floating, Ext Cath	300.7 V	18.44 A	5.59 kW	404.4 mN	68.4 %	±0.7
Grounded, Int Cath	150.5 V	18.66 A	2.85 kW	249.2 mN	50.9 %	±0.5
Floating, Int Cath	150.5 V	18.79 A	2.87 kW	252.0 mN	51.7 %	±0.5
Floating, Ext Cath	150.1 V	19.71 A	3.00 kW	253.9 mN	50.3 %	±0.5

Table 3.6: Thruster Efficiency

This table shows that at a constant flow rate of 20 mg/s and with internal cathode operation, while there are no significant differences in thrust-to-total power between floating and grounding the thruster as shown in the previous subsection, differences in performance become apparent when looking at the total efficiency. For the higher operating voltage of 300 V, there is a ∼1.5 % decrease in efficiency when floating the thruster and a ∼1 % increase in efficiency when floating the thruster at 150 V.

Between internal and external cathode conditions at 300 V, there is a 3 percentage point increase in efficiency. This is an actual difference, because the error propagated uncertainty of these parameters does not cause the possible range of values these numbers could have to overlap. It is a slightly higher increase than that seen by Jameson when comparing the thrust stand derived performance of operating the H6 with an internal cathode when comparing it to operation with the standard, upstream, external cathode configuration for this same nominal operating condition. She saw a 2 percentage point increase. [58] For the 150 V condition, the total efficiency decreased by about 1 percentage point. To further explore the breakdown of these changes in efficiency, additional diagnostics were used so that the utilization efficiencies shown in Eqn. 1.18a could be calculated and compared.

3.2.3 ExB Probe Results

Various methods have been used to analyze ExB probe traces to determine the fraction of each ion species' current. A list of commonly used methods with brief descriptions are listed below:

1. **Peak Heights** - uses the magnitude of the peak heights to describe the relative current of each ion species.

2. **Triangle Fitting** - uses a triangle fit to the peak and half-width at half-maximum (HWHM) to estimate the area around each peak to take into account the effect of peak broadening. The HWHM on one side of the curve is chosen for the fit estimate.

3. **Gaussian Fitting** - uses a Gaussian distribution to describe the curve around each visible peak by isolating each of these portions of the total trace and fitting them separately.

4. **Variable Exponential Fitting** - similar to Gaussian Fitting, however, in addition, this method allows the exponent for velocity in the exponential function to range anywhere between 2 (a Gaussian distribution in velocity) and 4 (a Druyvesteyn distribution in velocity).

As pointed out in the sources that describe and demonstrate these methods, the issue with all of these approaches is that they do not describe all the space between the distributions, and hence they do not explain the entire ExB probe trace [56, 58]. It is advantageous to more fully characterize these ExB probe traces, which are obtained directly through thruster measurements, for a number of reasons. A few are listed below:

1. The quest to fully understand thruster dynamics is still underway, and if there is additional information already present in the data we collect that could give

us further insight into this, then it would be helpful to extract it.

2. When trying to compare different operating conditions, or changes in how the thruster is being operated (such as cathode location), fully characterizing the data that is being used to do so, in a way that minimizes or eliminates the introduction of biases, makes identifying differences in the data an easier, more straightforward task, and increases confidence in the reported results.

3. Further along the lines of the previous reason, finding a method that is as simple, straightforward, and complete as possible, that does not introduce bias into the data and that can be applied to a broad set of data will bring us closer to a standard for analyzing this data that will allow more effective comparison between research papers from various authors and institutions, and between various thrusters or plasma sources. For example, not all plasma sources, operating conditions, or ExB probe placement locations will produce an ExB probe trace that has distinct peaks or that has the same relative broadening of each peak; so, if the analysis method assumes certain things about these elements of the trace, then it will be hard to carry out analysis of some traces and/or compare the results to other traces.

Figure 3.14 shows the results of a new method for analyzing ExB probe data applied to a trace obtained using the H6 with an internally mounted cathode and taken 2 m downstream from the thruster exit plane on thruster centerline. For all of the ExB probe measurements shown, a probe bias voltage resolution of 0.5 V or less was used, and at least 2 traces were averaged together. Since each trace had the same set of bias voltages, each corresponding data point across all the traces taken were averaged together to produce the resultant trace. The stated uncertainty in the measurement values of the instruments used to take the data was propagated through this averaging and the fitting performed on the trace. As seen in Fig. 3.14(a), the

entire ExB probe trace can be described with a composite Gaussian fit where each Gaussian distribution in the description is of the form:

$$I(V) = \frac{1}{\sigma\sqrt{2\pi}} e^{-\frac{(V-V_o)^2}{2\sigma^2}} \tag{3.2}$$

which is a Druyvesteyn distribution in velocity since voltage $\propto (velocity)^2$, Eqn. 2.3c. This means this distribution $\propto e^{(velocity)^4}$. This is physically accurate because the ExB probe is a velocity selector producing velocity distributions, and a Druyvesteyn function illustrates a steady state distribution of particles in a constant and unvarying electric field with mainly elastic collisions between particles and neutral atoms.

Even though there are some inelastic collisions in the plume in the vicinity in front of the probe, such as charge exchange (CEX) collisions, there are not enough inelastic collisions, and hence not enough of a transfer of energy from the distribution of particles in question, the ions, to its surroundings, the neutrals, in order for the ions to come into equilibrium with the surroundings. Instead, the ions are in steady state with their surroundings because the inelastic collisions that occur produce a steady, non-zero rate of energy transfer between the system and the surroundings. Another way to state this is that the ions and the neutrals are not the same temperature, therefore they are not in equilibrium, which would be described by a distribution with $e^{(velocity)^2}$ (meaning $\sqrt{voltage}$ would be in the exponential function of the distribution). Figure 3.14(b) shows the breakdown of the composite fit into the individual distributions that are summed to give the fit shown in Fig. 3.14(a). The R^2 value, the reduced chi-squared value, and the average standard deviation of each point from the fit function, which are statistical indicators of the goodness of fit, are also stated in this figure.

Figs. 3.15(a)-(f) show how the distributions were picked and summed together to take into account the space between each hump in the ExB probe trace. First, a distribution was fit to each area that looked like it formed a separate distribution,

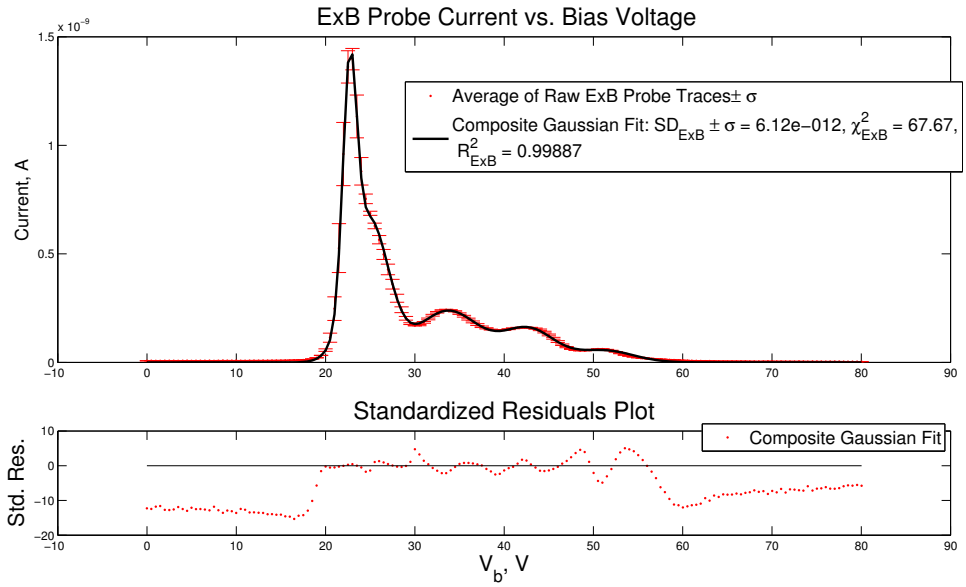

(a)

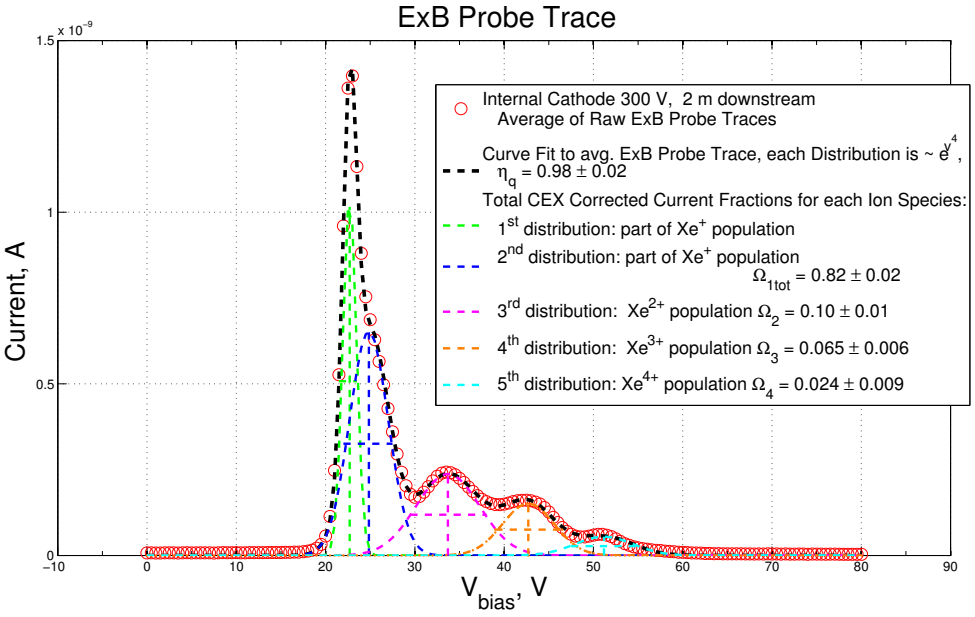

(b)

Figure 3.14: (a) An ExB probe trace 2 m from the thruster's exit plane with the thruster running at 300 V and 20 mg/s with the internal cathode. This graph also shows the total curve fit to the trace, made up of the addition of multiple Druyvesteyn distributions, along with its corresponding reduced chi-squared (χ^2) and R^2 values. The standard deviation (SD) of each point from the curve fit is shown with error bars, and the average of these SDs is stated in the legend. (b) The breakdown of the total fit showing each of the Druyvesteyn distributions that were summed to create the curve fit shown in (a).

taking into account the neighboring distributions and how their overlap would sum to describe the space between the distributions. This initial fitting, which was done "by-hand," had to sum to a fit that would be relatively close to the final fit (compare 3.15(f) to 3.14(a)). Next, this rough fit was fed into a MATLAB chi-squared fitting routine as the initial guess, and the routine came up with the final fit shown in Fig. 3.14. Figure 3.14(b) also states the CEX corrected current fraction of each ion species, and the resultant charge utilization efficiency. These parameters are found using the following equations from Section 1.5 [55]:

$$\Omega_i = \frac{I_i}{\sum_{i=1}^{N} I_i} \tag{3.2a}$$

$$\eta_q = \frac{\left(\sum_{i=1}^{N} \Omega_i/\sqrt{Z_i}\right)^2}{\sum_{i=1}^{N} \Omega_i/Z_i}. \tag{3.2b}$$

The current fractions, Ω_i, were found by using the height of the peak of each distribution and the uncertainty of this value, which was found using error propagation that took into account the standard deviation and hence the spread of the distribution functions. The CEX correction was applied using the method described by Shastry [56]. As also seen in Fig. 3.14(b), the peak representing the singly charged xenon ions is made up of two distinct distributions instead of one. To investigate the possible physical meaning of this, the acceleration voltage associated with the center of these distributions was needed. While this probe was not calibrated with an ion source, relative values could still be obtained by using the bias voltage at the center of each of these distributions, V_{probe}, and other probe parameters to calculate ZV_{accel} using Eqn. 2.4. The first peak of singly charged ions at $V_{probe} \simeq 23$ V corresponds to a $ZV_{accel} \simeq 151$ V. The second peak at $V_{probe} \simeq 53$ V, which represents a larger

portion of the singly ionized xenon population, has a corresponding charge number times acceleration potential of ∼178 V.

The remaining three distributions at $V_{probe} \simeq 35$ V, 43 V, and 51 V correspond to ZV_{accel} values of about 349 V, 527 V, and 741 V respectively. These values are about two, three and four times 178, while 151 is not a near multiple of 178. Given these values, the first two distributions seem to represent singly charged ion populations formed by two separate ionization zones, which Haas saw evidence of when he took axial, internal, Langmuir probe measurements along channel centerline using the P5 Hall thruster [126]. Perhaps with this more efficient thruster, the H6, the first ionization zone is also very close to the acceleration zone such that the first population of singly charged ions is not mainly lost to the walls as observed by Haas with the P5. Therefore, in this analysis, the height of the first two peaks was added together to represent the total current value for the singly charged ions, and the last three peaks were taken to represent the populations of doubly, triply, and quadruply charged ions. A similar check was performed on all of the ExB probe traces analyzed in this thesis to determine if a peak was a separate charge species or part of the charge species from the previous distribution.

The top of Fig. 3.16 shows a comparison between the ExB probe trace analyzed in Fig. 3.14(a) and the trace for the same operating condition and cathode location during the tests that compared running the thruster with the internal and external cathode. For these tests, the ExB probe was further downstream than in the test that produced the data in Fig. 3.14 due to test setup limitations. However, the same analysis method could be applied to this data, even though all of the peaks are not immediately apparent from glancing at the trace. This analysis is shown in Figs. 3.17(a) & 3.18(a) along with the current fractions and charge utilization efficiency obtained from them. For internal cathode operation at this discharge voltage, these values are comparable to those in Fig. 3.14(b).

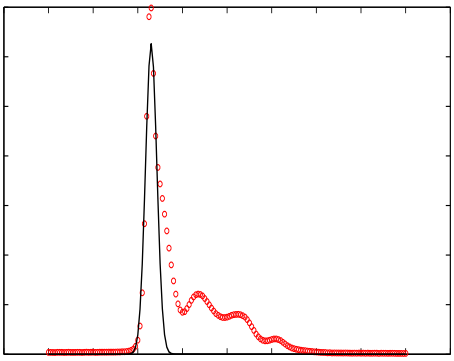

(a) manual fit estimate for the first distribution

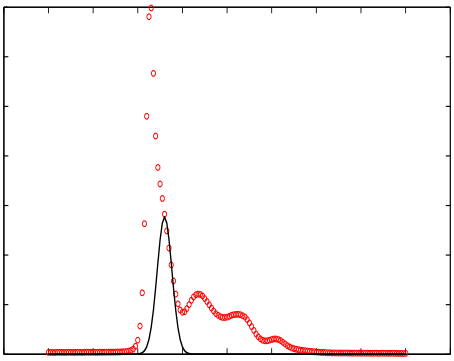

(b) for the second distribution

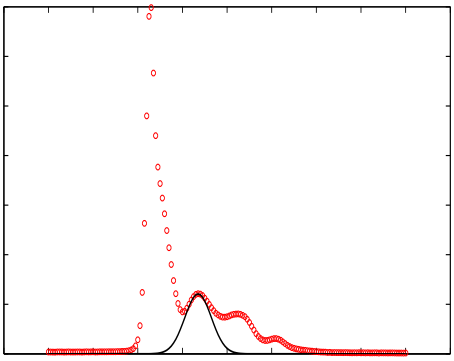

(c) for the third distribution

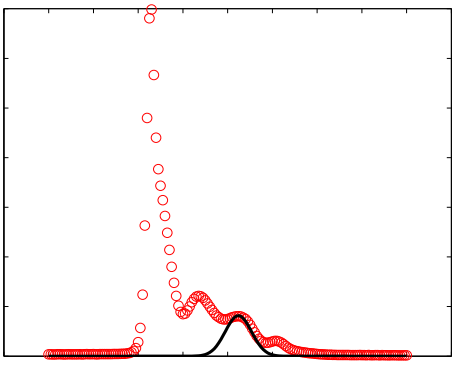

(d) for the fourth distribution

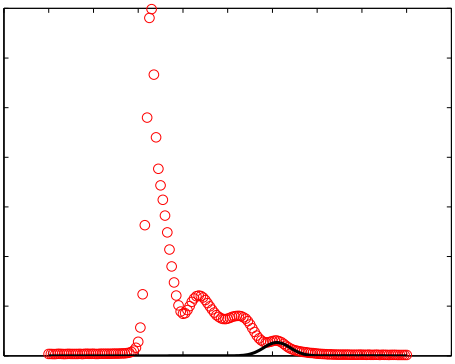

(e) for the fifth distribution

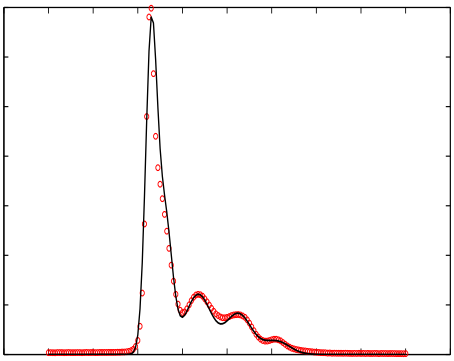

(f) summation of all five distributions

Figure 3.15: (a)-(e) A series of graphs depicting the steps taken to obtain a fit function estimate that was then used as the starting guess in the chi-squared fitting routine. The guess had to be close enough for this particular routine to obtain a solution. Each hump was fit to a Druyvesteyn distribution taking into account the fact that when the distributions are added together, the space in between the distributions is the sum of the two neighboring distributions that overlap in that area. (f) shows the total estimate and how the space in between the humps can be described by the neighboring distributions.

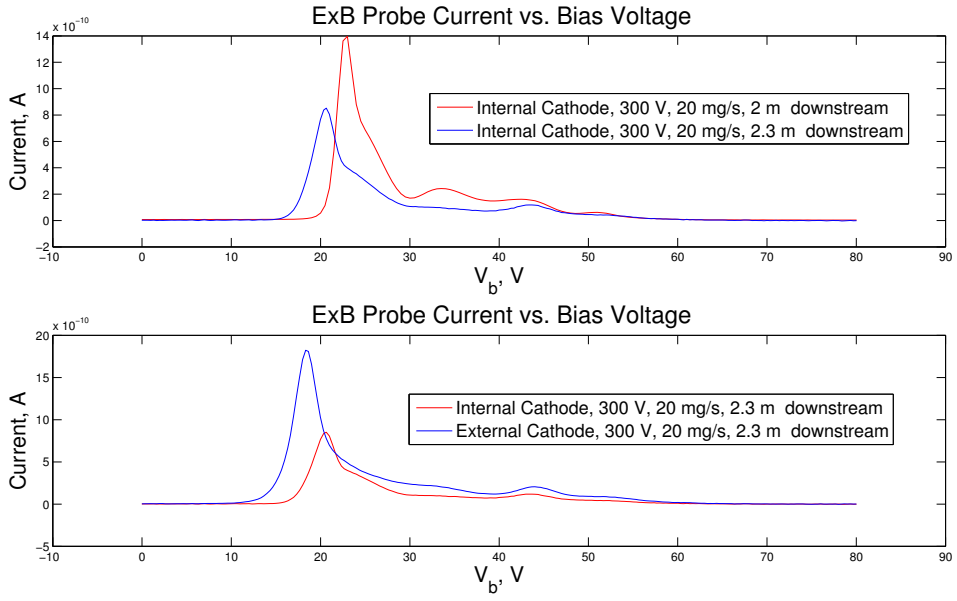

Figure 3.16: The top graph in this figure shows the ExB probe trace at 2 m downstream (shown separately in Fig. 3.14(a)) compared to the ExB probe trace 2.3 m downstream (shown by itself in Fig. 3.17(a)). Both of these traces were taken with the thruster running at 300 V and 20 mg/s with the internal cathode. The bottom figure shows a comparison between the probe trace for the thruster running with the internal cathode and the external cathode. In both cases, the probe took data 2.3 m downstream. These two traces are shown separately in Figs. 3.17(a) & 3.17(b) respectively.

Cathode Location	V_D $uncer.\pm$	I_D $uncer.\pm$	$\dot{m}_A$ $uncer.\pm$	P_{tot} $uncer.\pm$	Ω_i $uncer.\pm$	η_q $uncer.\pm$
External	300.2 V ± 0.1	18.41 A ± 0.03	20.0 mg/s ± 0.2	5.565 kW ± 0.008	$\Omega_1 = 0.81$ ± 0.01 $\Omega_2 = 0.10$ ± 0.01 $\Omega_3 = 0.042$ ± 0.007 $\Omega_4 = 0.043$ ± 0.004	0.97 ± 0.02
Internal	300.1 V ± 0.1	18.08 A ± 0.03	20.0 mg/s ± 0.2	5.465 kW ± 0.008	$\Omega_1 = 0.84$ ± 0.01 $\Omega_2 = 0.07$ ± 0.01 $\Omega_3 = 0.049$ ± 0.003 $\Omega_4 = 0.037$ ± 0.001	0.98 ± 0.01
External	150.28 V ± 0.07	19.73 A ± 0.03	20.0 mg/s ± 0.2	3.004 kW ± 0.004	$\Omega_1 = 0.87$ ± 0.01 $\Omega_2 = 0.13$ ± 0.01	0.99 ± 0.02
Internal	150.32 V ± 0.07	18.98 A ± 0.03	20.0 mg/s ± 0.2	2.894 kW ± 0.004	$\Omega_1 = 0.81$ ± 0.02 $\Omega_2 = 0.19$ ± 0.02	0.99 ± 0.02

Table 3.7: Charge Utilization Efficiency Results - Cathode Location, Internal vs. External

The bottom graph in Fig. 3.16 shows the comparison between the ExB probe traces for the 300 V operating condition for the internal and external cathodes, and Figs. 3.17(b) & 3.18(b) show the analysis for the external cathode case. Even though the total current fraction of singly charged xenon ions is smaller in the external cathode case, it is not enough to make a significant difference in the charge utilization efficiency. Hence, the utilization efficiency remains the same within the propagated uncertainty for the 300 V 20 mg/s operating condition for the external cathode versus the internal cathode. For the 150 V condition, seen in Figs. 3.19, 3.20 & 3.21, the fraction of singly charged ions for the external cathode is larger than that for the internal cathode, but the charge utilization efficiency remains at around 99 %. A summary of all the ExB probe results, for both the 300 V and 150 V operating conditions, is shown in Table 3.7 along with the discharge conditions while these measurements were being made.

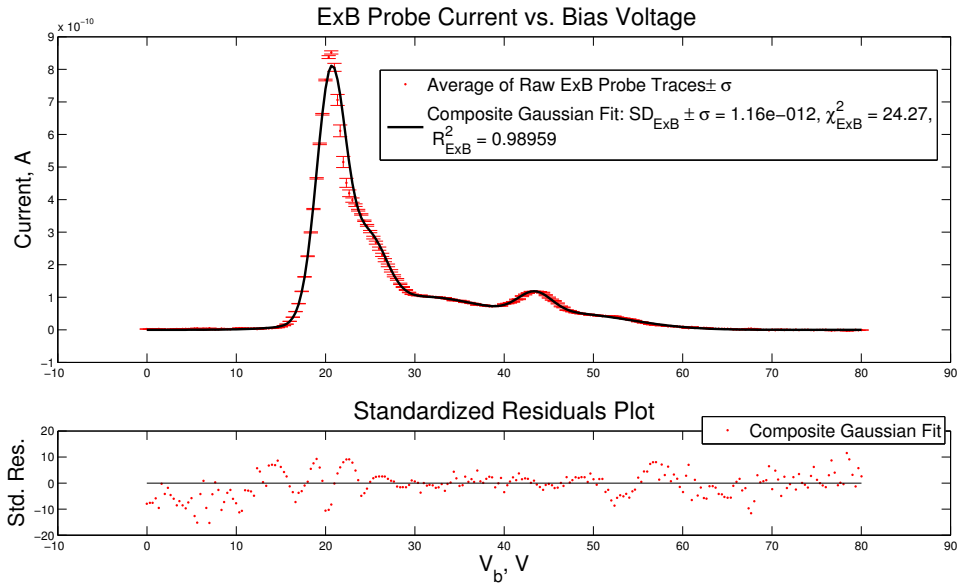

(a) Internal Cathode, 300 V and 20 mg/s

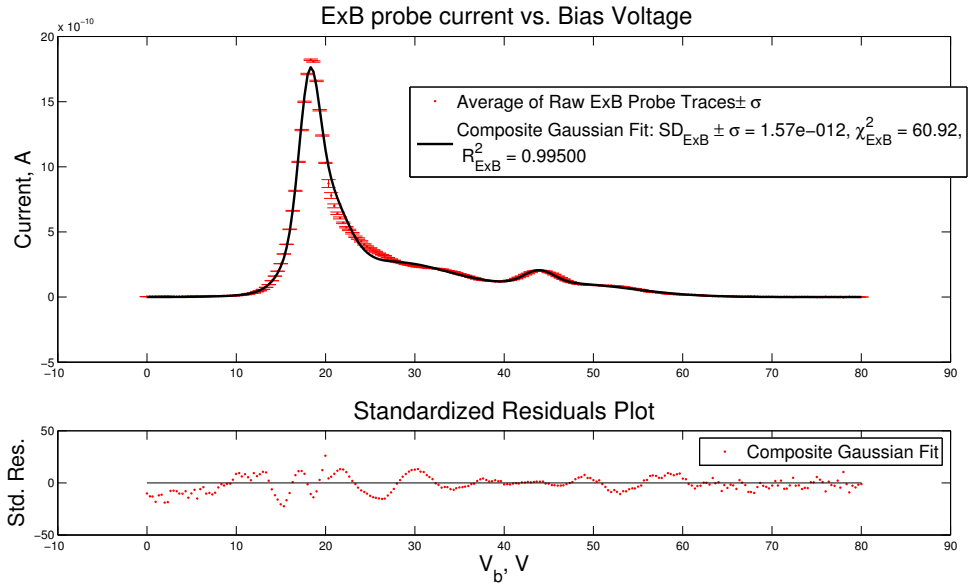

(b) External Cathode, 300 V and 20 mg/s

Figure 3.17: (a) An ExB probe trace 2.3 m from the thruster's exit plane with the thruster running at 300 V and 20 mg/s with the internal cathode. In addition, the total curve fit to the trace is shown, made up by the addition of multiple Druyvesteyn distributions. The legend shows the curve fit's corresponding reduced chi-squared (χ^2) and R^2 values. The standard deviation (SD) of each point from the curve fit is shown with error bars, and the average of these SDs is in the legend. (b) The same as (a) but for running the thruster at 300 V with the external cathode.

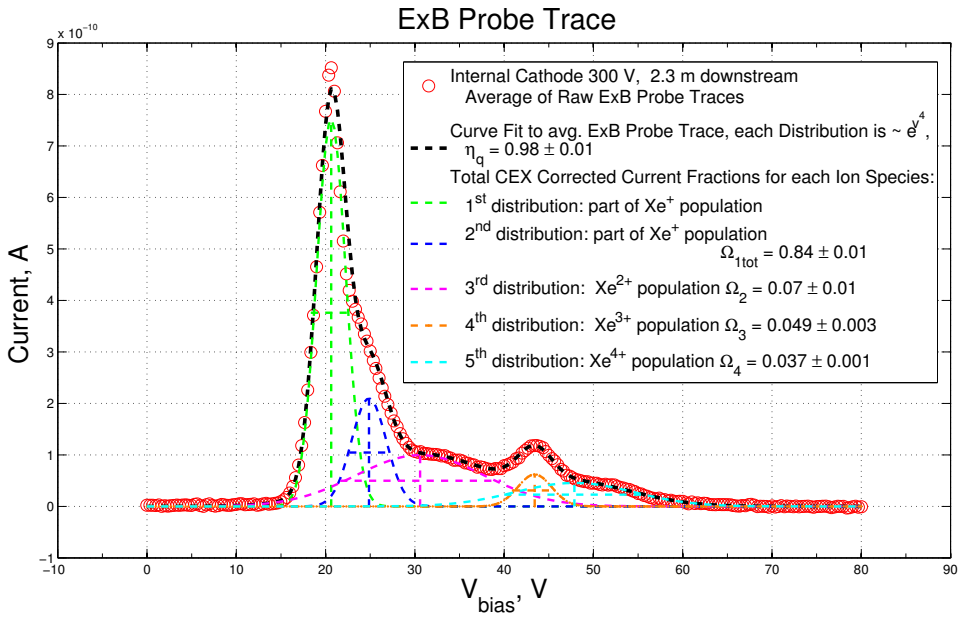

(a)

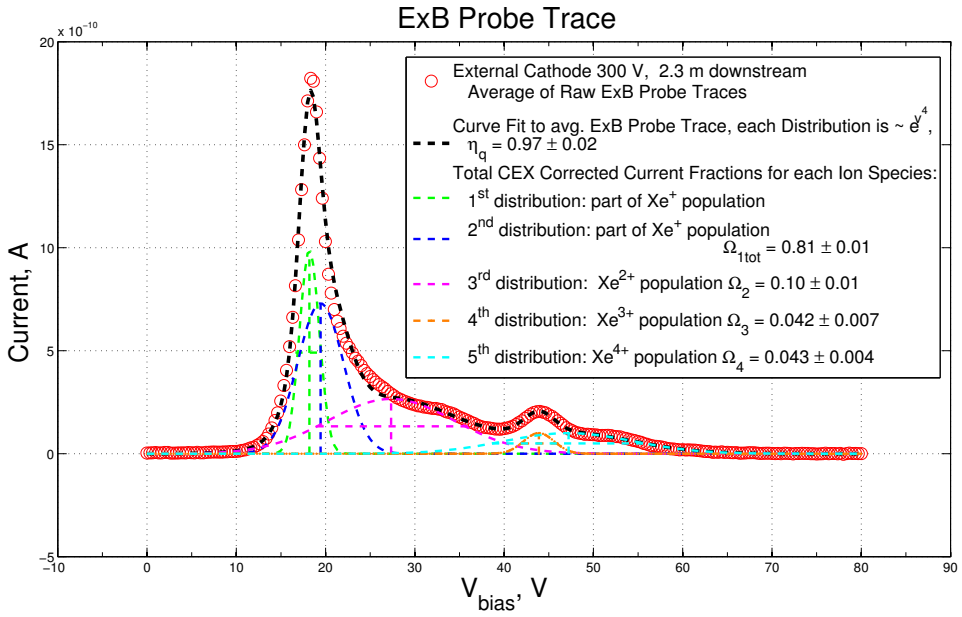

(b)

Figure 3.18: (a) The breakdown of the total fit showing each of the Druyvesteyn distributions that were summed to create the curve fit shown in Fig. 3.17(a). (b) The breakdown of the total fit showing each of the Druyvesteyn distributions that were summed to create the curve fit shown in Fig. 3.17(b).

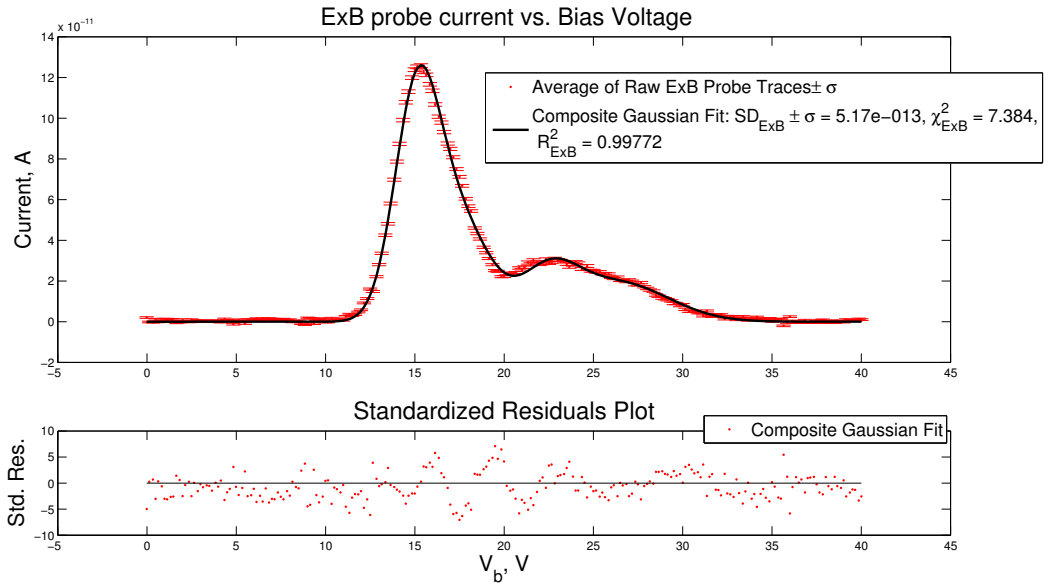

(a) Internal Cathode, 150 V and 20 mg/s

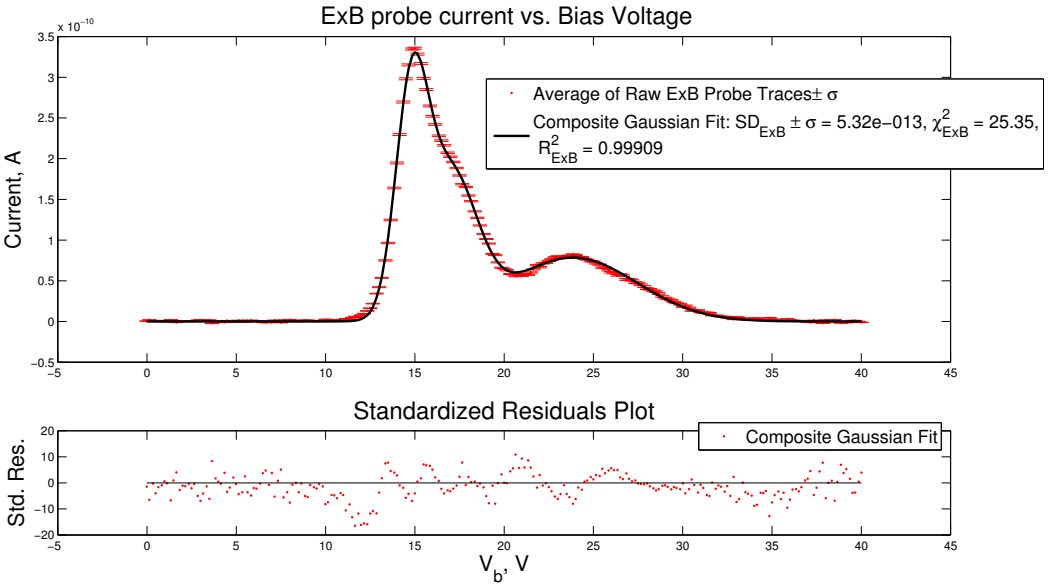

(b) External Cathode, 150 V and 20 mg/s

Figure 3.19: (a) An ExB probe trace 2.3 m from the thruster's exit plane with the thruster running at 150 V and 20 mg/s with the internal cathode. In addition, the total curve fit to the trace is shown, made up by the addition of multiple Druyvesteyn distributions. The legend shows the curve fit's corresponding reduced chi-squared (χ^2) and R^2 values. The standard deviation (SD) of each point from the curve fit is shown with error bars, and the average of these SDs is in the legend. (b) The same as (a) but for running the thruster at 150 V with the external cathode.

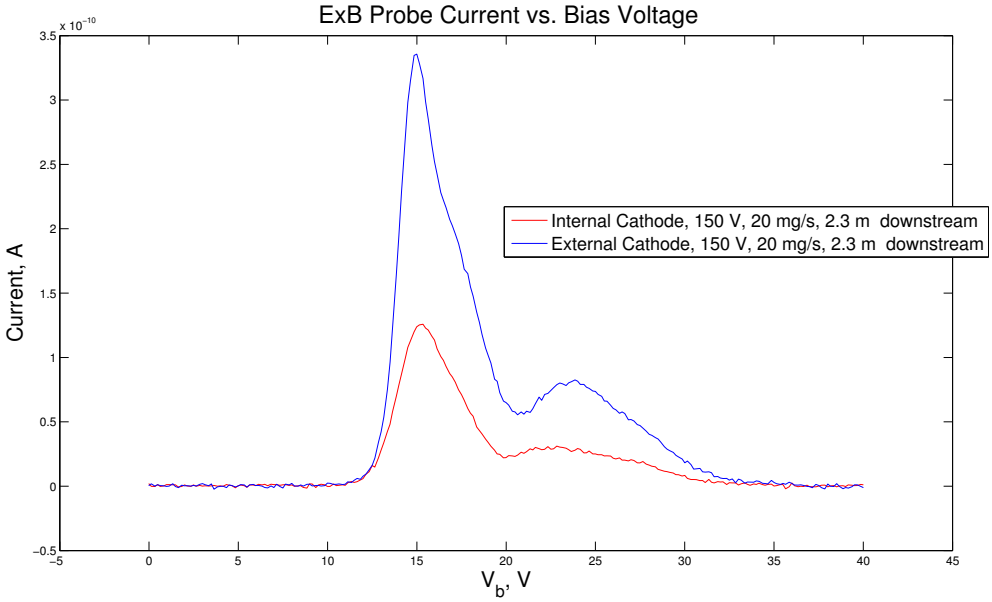

Figure 3.20: A comparison between the ExB probe traces taken 2.3 m downstream with the thruster running at 150 V for the internal cathode versus the external cathode. These two traces are shown separately in Figs. 3.19(a) & 3.19(b) respectively.

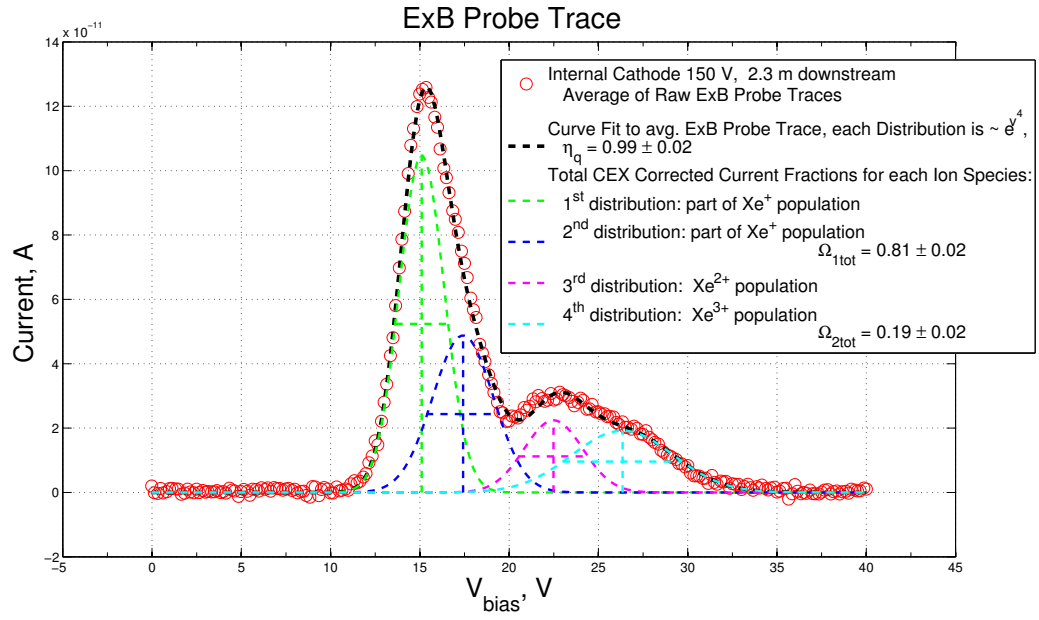

(a)

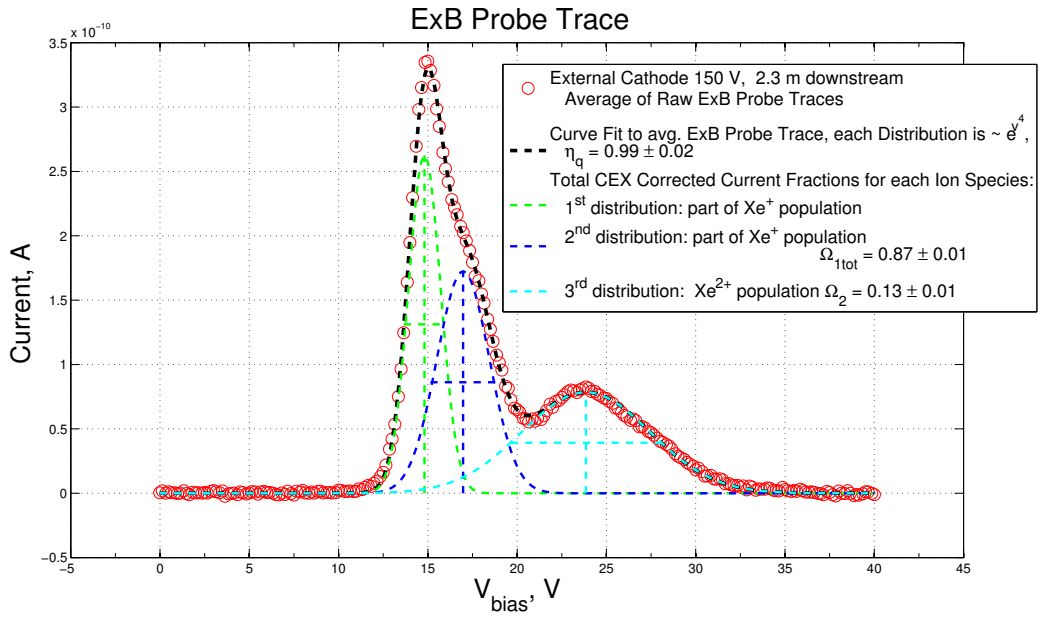

(b)

Figure 3.21: (a) The breakdown of the total fit showing each of the Druyvesteyn distributions that were summed to create the curve fit shown in Fig. 3.19(a) for internal cathode operation. (b) The breakdown of the total fit showing each of the Druyvesteyn distributions that were summed to create the curve fit shown in Fig. 3.19(b) for external cathode operation.

3.2.4 Retarding Potential Analyzer Results

Retarding potential analyzer (RPA) measurements were taken 11° from thruster centerline and at a radial distance of ∼3 D_T. A voltage bias resolution of ∼1 V was used and two traces were averaged together for each case. These measurements were taken on the opposite side to where the external cathode was located (see Figs. 3.6, 3.7, 3.9(b)). The RPA data was also analyzed using the chi-squared fitting routine used in subsections 3.2.1 & 3.2.3. Here it was used to fit a Gaussian function to the data, instead of taking the voltage value associated with the peak in the ion voltage distribution (IVD) (from -dI/dV) as the uncorrected, most probable voltage value, and instead of using the voltages corresponding to half the peak value to determine the full-width at half-maximum (FWHM). Using the chi-squared fitting routine resulted in finding that a single Gaussian distribution does not describe the data, but instead a superposition of two Gaussian distributions provides a very convincing fit (see Figs. 3.22 & 3.23).

The most probable voltage from the peak of the first Gaussian (V_{mp1}) was used for this analysis so that this analysis could be compared to the literature. The second distribution is most likely the result of a second ionization zone, which was mentioned in subsection 3.2.3. It is less likely that the second distribution, from this energy per unit charge measuring probe, represents multiply charged ions since multiply charged ions would be accelerated through the same or a slightly smaller potential drop and would therefore not produce a distribution with a higher acceleration voltage.

The full RPA analysis for the 300 V and 150 V conditions is shown in Figs. 3.24 & 3.25 respectively. These figures demonstrate that when a MATLAB smoothing filter is applied to the averaged RPA trace before taking the 1^{st} derivative to obtain a smoother dI/dV for the analysis, this filter does not affect the location of the uncorrected V_{mp}. In addition, these figures show that from the RPA traces themselves, the uncorrected most probable voltage (V_{mp}) is about the same for the external and

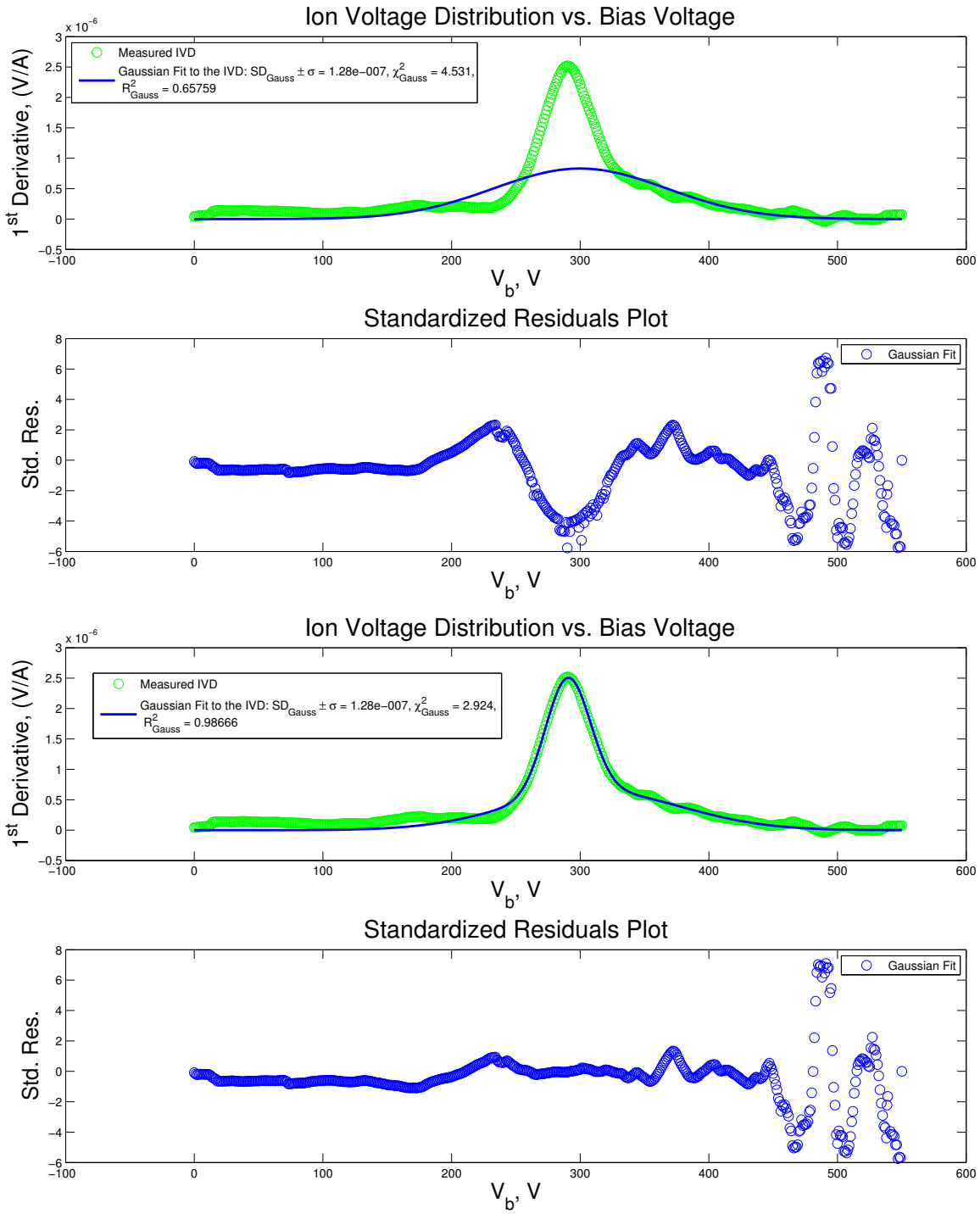

Figure 3.22: An example RPA trace at 300 V with the internal cathode showing what the best fit looks like when only one Gaussian distribution is used to describe the data (top two charts), and when two Gaussian distributions are used (bottom two charts).

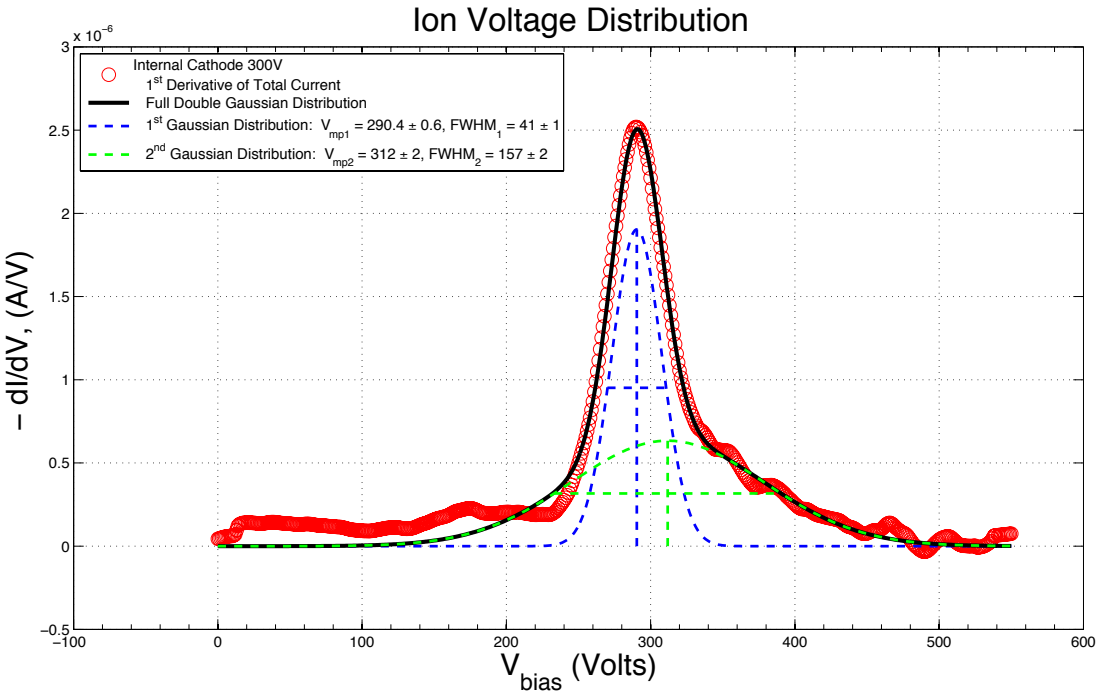

Figure 3.23: For the fit with two Gaussians (shown in the bottom two charts in Fig. 3.22), this graph shows the Gaussian functions that form the total fit. The fit function is a superposition of these two Gaussian distributions.

internal cathode cases. However, from Table 3.8, once the LP's measurement of local plasma potential, V_p, is used to adjust these values (by subtracting V_p from the uncorrected V_{mp}) a distinct difference between V_{mp} for the internal and the external cathode cases is seen. (See subsections 3.3.1 & 3.3.2 for details on how V_p was obtained.)

The voltage utilization efficiency was calculated from the corrected V_{mp} using the following equation from Section 1.5:

$$\eta_V = \frac{V_{mp}}{V_D}. \tag{3.3}$$

The internal cathode voltage utilization efficiencies are comparable to the literature.[16, 55, 58] For the 300 V condition there is a 3 percentage point increase in the voltage utilization efficiency, and for the 150 V condition there is a 4 percentage point increase in the voltage utilization efficiency for the external cathode over the internal cathode. Tables 3.8 & 3.9 also show the operating conditions while the RPA was

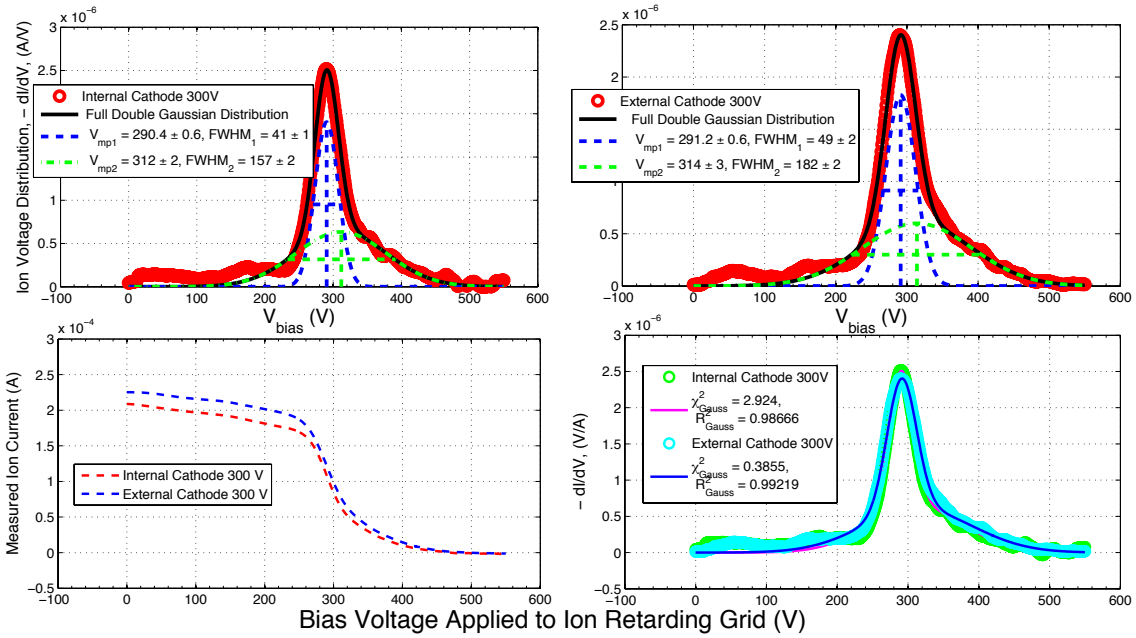

(a)

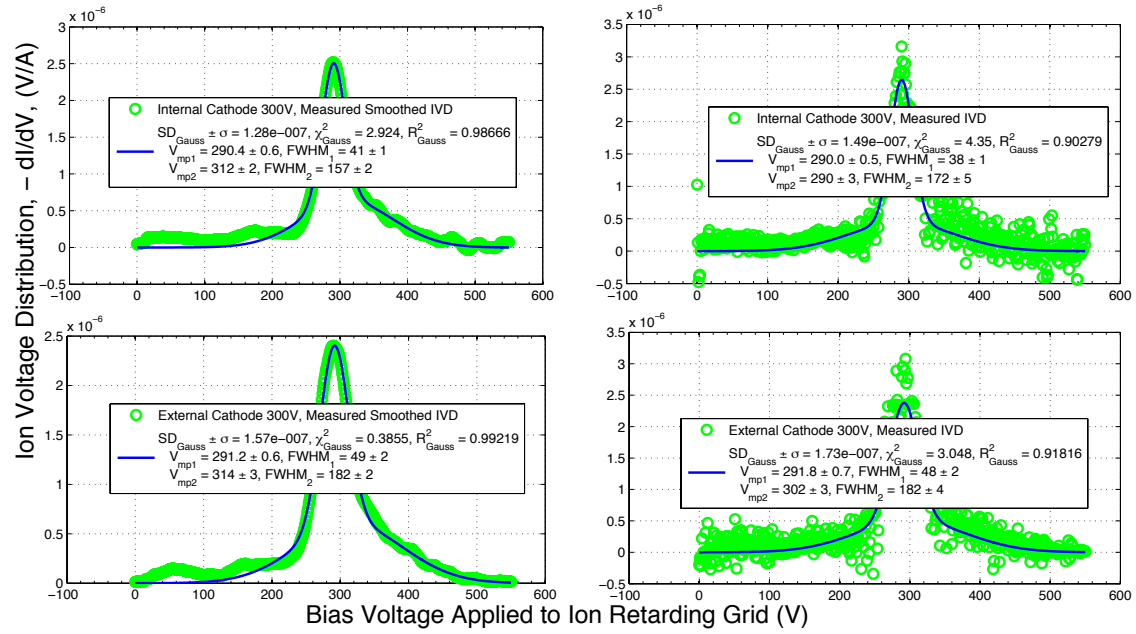

(b)

Figure 3.24: (a) The full RPA analysis for the 300 V condition comparing the case with the internal cathode to the external cathode. The bottom left graph compares the two averaged RPA traces. The top two graphs show the two Gaussian functions that form the total fit to the IVD, where the IVD comes from the first derivative of the RPA trace. The bottom right graph shows the IVDs for the two cases plotted on the same axes. (b) For the 2 cases, one with the internal cathode and the other with the external cathode, this graph shows the resulting V_{mp} and $FWHM$ when a smoothing function is applied to the averaged RPA trace before the derivative is taken to obtain the IVD (the graphs on the left) versus what these values would be if no smoothing is applied (graphs on the right).

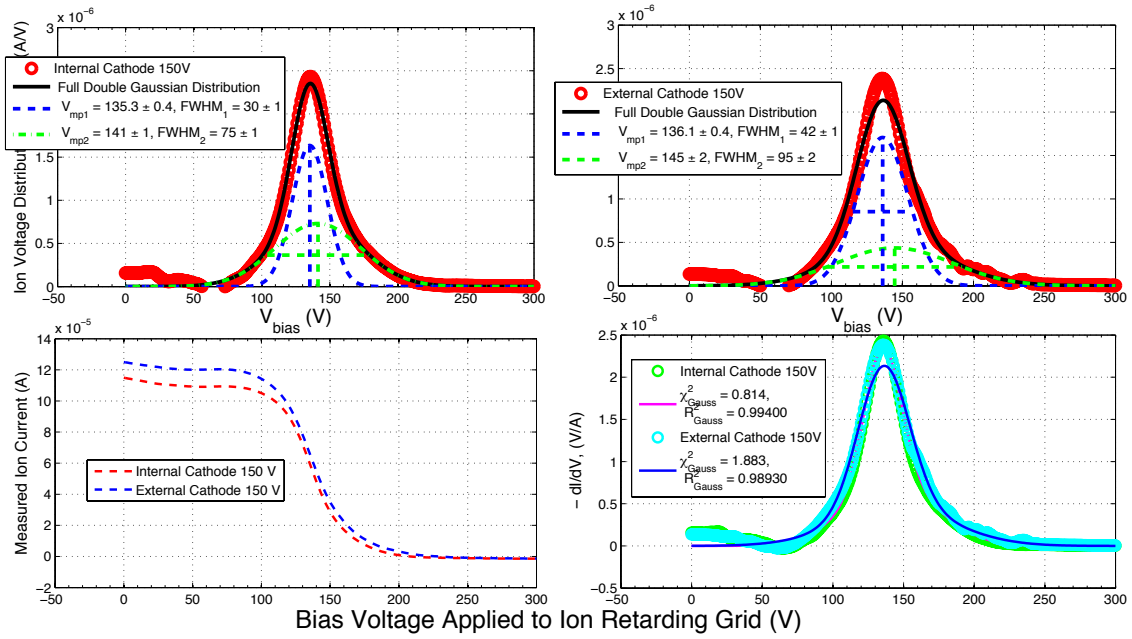

(a)

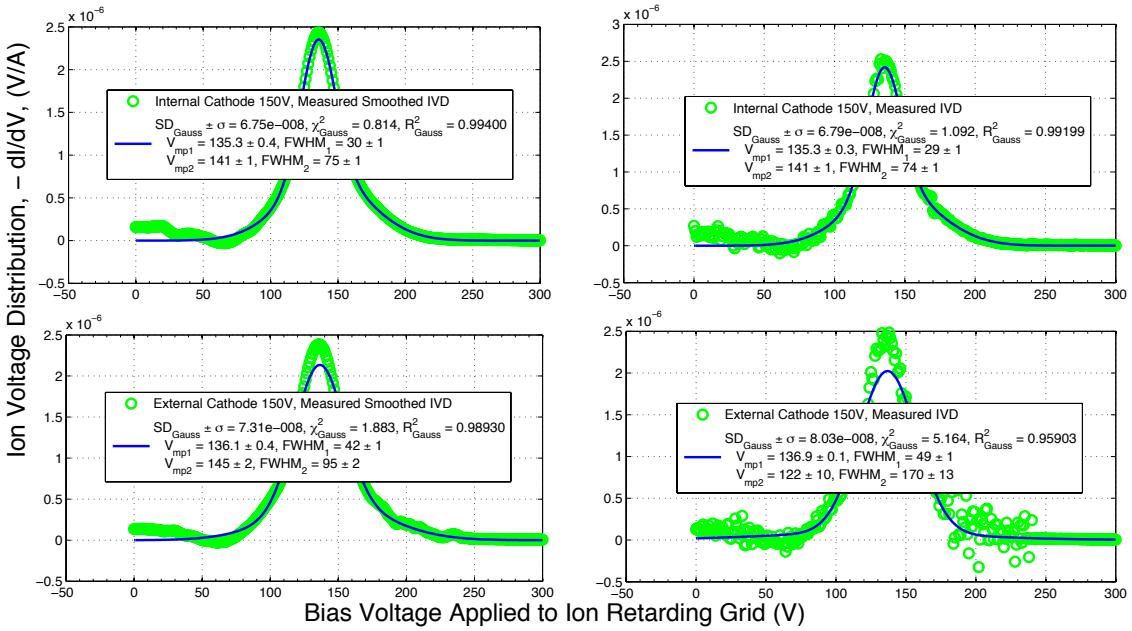

(b)

Figure 3.25: (a) The full RPA analysis for the 150 V condition comparing the case with the internal cathode to the external cathode. The bottom left graph compares the two averaged RPA traces. The top two graphs show the two Gaussian functions that form the total fit to the IVD. The bottom right graph shows the IVDs for the two cases plotted on the same axes. (b) For the 2 cases, one with the internal cathode and the other with the external cathode, this graph shows the resulting V_{mp} and $FWHM$ when a smoothing function is applied to the averaged RPA trace before the derivative is taken to obtain the IVD (the graphs on the left) versus what these values would be if no smoothing is applied (graphs on the right).

taking data including the cathode-to-ground voltage. The last column in Table 3.9 is $V_D + V_{c-g} - V_p$ calculated from the relationship between the cathode-to-ground voltage, discharge voltage, most probable (or acceleration) potential and plasma potential. This relationship is depicted in Fig. 1.6. Here this expression will be called V_{accel_0}.

V_{accel_0} appears to represent the potential drop available for accelerating ions from the DC component of the thruster's potential profile. This is seen by comparing it to the corrected V_{mp}. V_{accel_0} is comparable to the corrected V_{mp} for the nominal condition the thruster was designed for, while the corrected V_{mp} is lower than this value for the 150 V condition, which is an off-nominal condition. To determine if this line of reasoning holds, these parameters would need to be checked for other off-nominal operating conditions as well. Therefore, another line of reasoning that suggests V_{accel_0} represents only one component of the potential profile available for accelerating the ions is that the corrected V_{mp_2} (from the second Gaussian distributions in -dI/dV) would be even larger than V_{accel_0} for the 300 V cases and for the external cathode 150 V case. This suggests that the ions are also gaining energy from oscillations in the plasma potential field similar to what was observed for ion energies in hollow cathodes and reported in Refs. [127, 128].

3.2.5 Faraday Probe Results

The guard-less Faraday probe used in these experiments to take data 2.5 D_T from the thruster exit plane was described in Section 2.9. A guard ring was not added to the probe because a downstream distance of 2.5 D_T was still considered near-field,[55] where the Debye length is too small to meet the gap spacing requirement. From Table 3.16 in subsection 3.3.2, the Debye length in this area ranges from $\sim 1 \times 10^{-5}$ to $\sim 2 \times 10^{-4}$ m and the recommended ring-probe spacing is less than 10 Debye lengths[16], which would have required a gap of at most 0.1 mm.

Cathode Location	V_D	I_D	P_{tot}	RPA V_{mp}	LP V_p	Corrected V_{mp}	η_V
	uncer.±	*uncer.*±	*uncer.*±	*uncer.*±	*uncer.*±	*uncer.*±	*uncer.*±
External	300.24 V	18.44 A	5.576 kW	291.2 V	8 V	284 V	94.5 %
	±0.07	±0.02	±0.006	±0.6	±1	±1	±0.4
Internal	300.16 V	17.93 A	5.424 kW	290.4 V	16 V	275 V	91.6 %
	±0.07	±0.02	±0.006	±0.6	±1	±1	±0.4
External	150.29 V	19.64 A	2.989 kW	136.1 V	7 V	130 V	86.2 %
	±0.05	±0.02	±0.003	±0.4	±1	±1	±0.7
Internal	150.35 V	18.86 A	2.874 kW	135.3 V	12 V	124 V	82.3 %
	±0.05	±0.02	±0.003	±0.4	±1	±1	±0.7

Table 3.8: Voltage Utilization Efficiency - Cathode Location Internal vs. External

Cathode Location	V_D	V_{cg}	RPA V_{mp}	LP V_p	Corrected V_{mp}	$V_D + V_{cg} - V_p$
	uncer.±	*uncer.*±	*uncer.*±	*uncer.*±	*uncer.*±	*uncer.*±
External	300.24 V	−7.430 V	291.2 V	8 V	284 V	285 V
	±0.07	±0.004	±0.6	±1	±1	±1
Internal	300.16 V	−9.773 V	290.4 V	16 V	275 V	275 V
	±0.07	±0.006	±0.6	±1	±1	±1
External	150.29 V	−8.525 V	136.1 V	7 V	130 V	135 V
	±0.05	±0.005	±0.4	±1	±1	±1
Internal	150.35 V	−8.650 V	135.3 V	12 V	124 V	130 V
	±0.05	±0.005	±0.4	±1	±1	±1

Table 3.9: Coupling Voltage Comparison - Cathode Location Internal vs. External

A sweep rate of 1°/s and an effective sample rate of around 7 points per second was used to take the FP data. In addition, two sweeps per operating condition were taken, first a sweep in the direction of decreasing angular values, and then the reverse sweep, where the probe retraced its steps back to the position it started from. A sweep radius of 2.5 D_T was chosen so that the FP would pass behind the external cathode when taking data for this cathode orientation. This was done so that the entire rotational probe arm would not pass between the cathode and thruster, which would have most likely interfered with the steady state conditions given the amount of cables and probes that were on this arm. The current not collected by the probe, because it was blocked by the cathode also counts towards discharge current and

produces thrust. Therefore, in post-processing this additional current was accounted for by mirroring the plume on the side opposite of where the external cathode was placed, as shown in Fig. 3.27. While the plume is most likely not symmetric in this plane due to the external cathode's positioning, an axisymmetric plume was used here as a first-order estimate.

Data was taken in a circular arc from +110° to -110° relative to thruster centerline for sweeps with the external cathode. The range of interest was +90° to -90°, and data was taken over this more extended range so that any observed oscillations induced in the probe setup at the end of the rotational arm due to starting up and stopping the rotational motion stage would not impact the data over the range of interest; however, these types of transients did not seem to be present in the data.

The same downstream distance of 2.5 D_T was also chosen for the centrally mounted cathode case for a direct comparison of the results. However, data was only taken from +110° to -20° with the centrally mounted cathode. The sweep did not extend all the way to -110° to prevent it from knocking into the location where the external cathode was parked when it was not in use. At $\sim$1 D_T downstream from the thruster's exit plane and 2.5 D_T radially to the side of thruster centerline, the cathode was far enough away from the main part of the thruster's plume so as not to interfere with operation; however, the probe's cables and wiring that was looped behind the rotational arm, and the fact that the FP was moved through a circular arc with a radius of 2.5 D_T made it so that going any further than -20° would have caused it to collide with the external cathode. Since the plume is relatively symmetric with the centrally mounted cathode configuration, in post-processing the data this was addressed by reflecting the data from +110° to +20° over to the area from -20° to -110°.

Figure 3.26 shows an example of how all the Faraday probe data was prepared for analysis. The data points were binned in order to find an average trace that represented the data without using smoothing. This was done by first sorting the

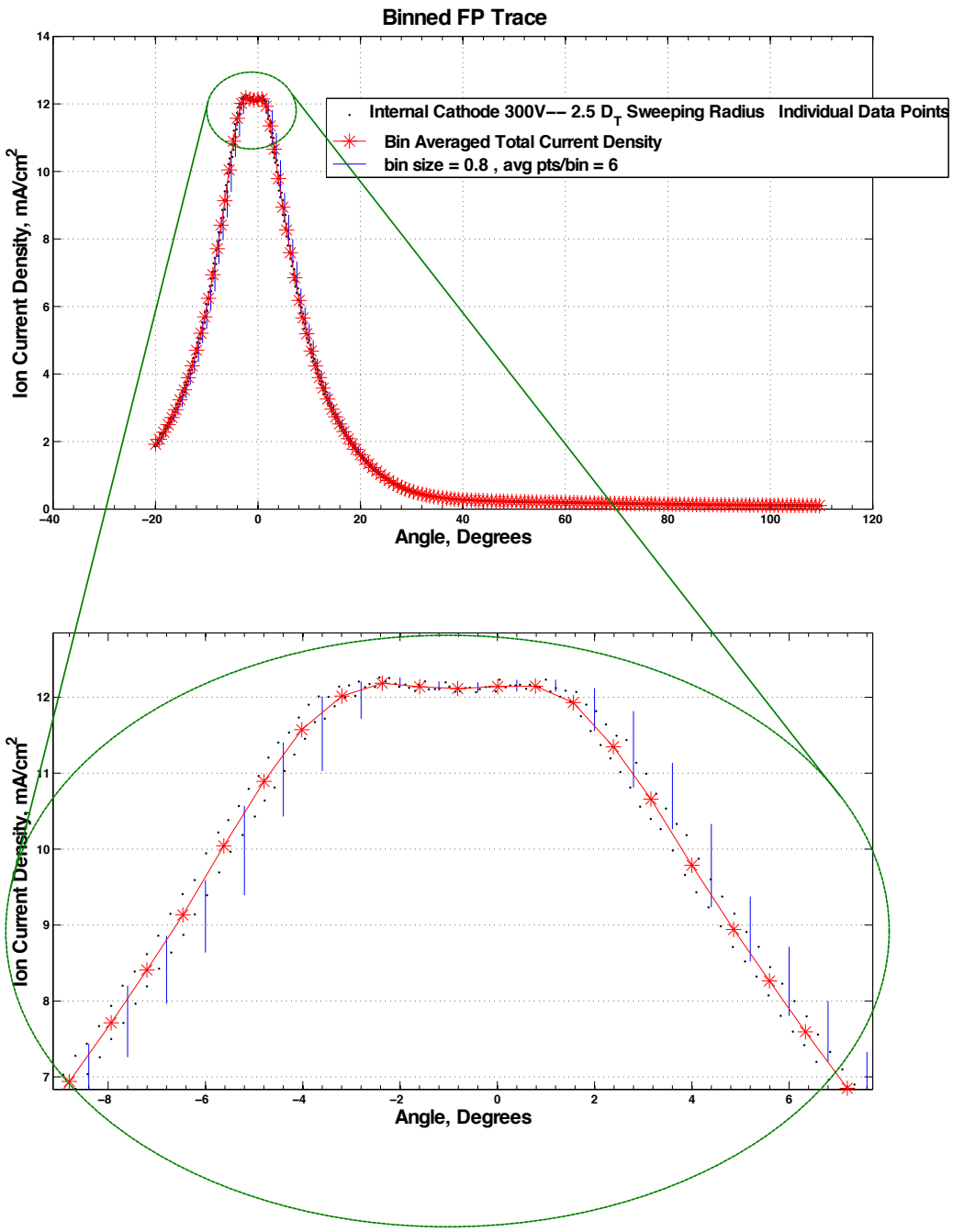

Figure 3.26: The graph at the top shows a Faraday probe trace taken 2.5 D_T downstream with the thruster running at 300 V and 20 mg/s. The raw data is shown from the initial sweep and the return sweep. These points were sorted into consecutive bins that were 0.8 degrees in width to obtain an average of 6 points per bin. To see the bins in more detail, a zoomed in portion of this graph is shown at the bottom. The blue lines mark the beginning of the bin to the left of the line, and the top and bottom of each blue line indicate the smallest and largest ion current density values of the points within that bin. Each red asterisk shows the average degree and current density of the points within the bin, and the red line that runs between these values shows the resultant trace from using the binning method to average the trace. The same method was used on all the other FP data sets analyzed here.

data in order of decreasing angle, and picking a bin size that was large enough to ensure a minimum of 5 points per bin to allow the distribution of points in each bin to tend towards a Gaussian distribution[129, 130], and small enough to allow key features in the data to still be resolved. On average there were 6 points per bin and a range of 5-8 points per bin for this data set.

The angle and ion current density and their uncertainties for each bin were found by averaging together the x and y values of the points in the bin and propagating the x and y uncertainties of each data point through this averaging. The uncertainty of the angle for each data point was mainly from the alignment error in the probe around thruster centerline and was estimated to be $\pm$ 0.625°. This relatively large error was due to the size of the armature that was needed for the thruster setup structure that was in place at the time (see Fig. 3.9(b)). The error propagation through averaging the x values in each bin was carried out neglecting any correlation in the uncertainty of the degree values. The error in the ion current density was calculated from the error in the measured voltage values, probe surface area, and shunt resistance. The shunt resistance and measured voltage uncertainty were taken from the printed uncertainty values on the specification sheets of the measurement instruments used. The probe surface area uncertainty was calculated from the error in the probe's diameter, which was mainly due to the variation in its diameter around the probe's circumference.

A single set of Faraday probe sweeps was taken at one background pressure and distance from the thruster. The beam current was found by integrating over a degree range from -42° to 42°. This span gave results that matched the literature for the internal cathode conditions [16, 55, 58], and the same degree range was used for the external cathode cases for direct comparison.

Brown incorporated various FP correction factors into the equations for the total and axial beam currents. These included the distance, area and beam divergence correction factors. The need for these correction factors stemmed from the fact that

the integral in the ion beam equation, Eqn. 1.12, assumes a point source for the ions but given the annular geometry of the thruster, it is essentially two point sources. [16]

The distance correction factor accounts for the difference in distance of the beam ions from various parts of the channel to the probe surface. The area correction factor addresses the fact that the angle of the beam ions to the probe surface is different from the central point source model and also changes throughout the probe's sweep. The third correction factor, which is for beam divergence, arises when calculating the axial component of the beam current and accounts for the difference in the divergence of a beam ion originating from channel centerline versus thruster centerline.[16] These correction factors were not applied to the FP measurements taken for this thesis given the distance of the probe from the thruster. For example, the first two correction factors would have amounted to less than a 1.5% correction to the total beam current.

The equations used to calculate the total and axial ion beam current, divergence half angle, and the efficiency parameters that can be determined from these values are discussed in Section 1.5. Error propagation through the integration used to find the total and axial beam currents yield high uncertainties given the number of expressions that are being added together. These errors far outweigh the small correction factors discussed previously, which is another reason why they were not applied.

In the literature, relatively low uncertainties of 3% for the total beam current and 5% for the axial component of the beam current were estimated by considering the spread in current density values from various FP designs and noting that the correction factors, and the effect of various facility background pressures and radial downstream distances were taken into account.[16] This estimate of relative random error between values calculated from raw measurements is different from propagated error, which is the result of translating the random errors of raw measurements through the equations used to obtain the calculated parameters.

The tabulated values for the results from the Faraday probe measurements are

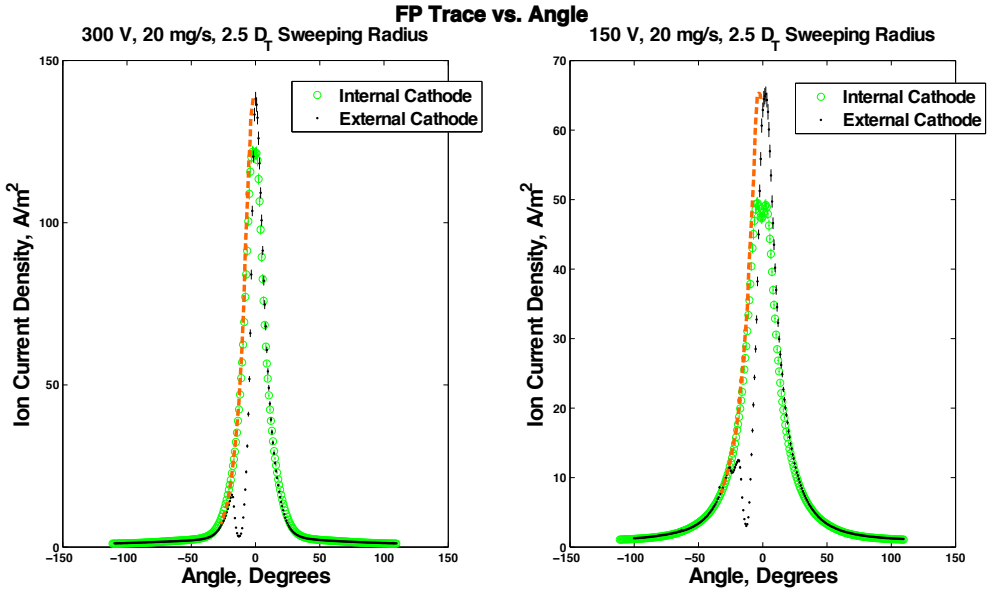

Figure 3.27: These graphs show the Faraday probe traces and error bars when running the thruster with the internal cathode compared to the external cathode for both operating conditions tested. Since these FP traces, taken at a downstream radius of 2.5 D_T, had the probe pass behind the external cathode when it was being used, part of the current that would have been collected by the probe was blocked by the cathode. Since this current counts towards discharge current and produces thrust, and assuming that to first order the plume is axisymmetric, this additional current was accounted for by mirroring the plume on the side opposite of where the external cathode was placed. The dashed orange line shows how this was done.

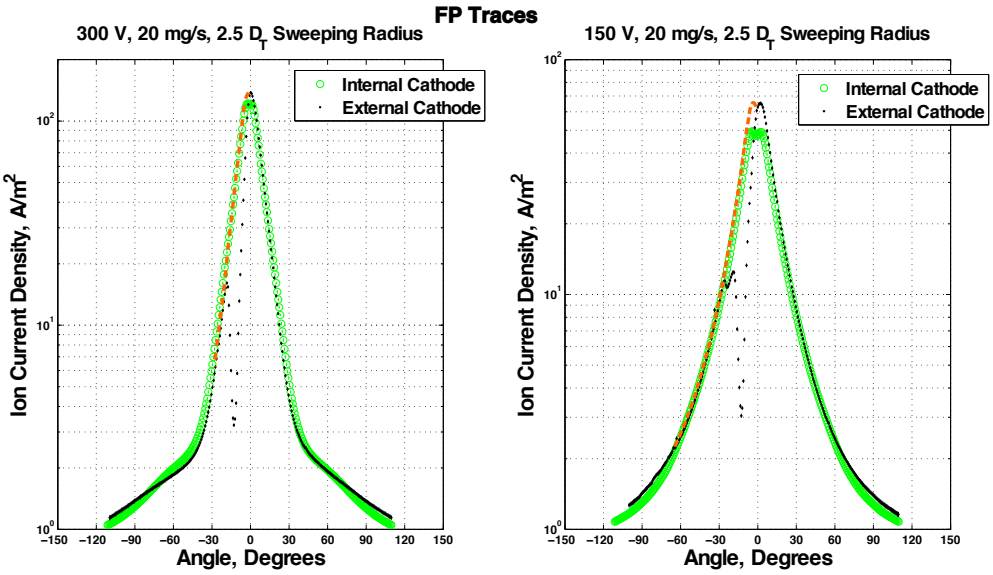

Figure 3.28: These graphs show the same Faraday probe traces as in Fig. 3.27 but with the y-axis on a logarithmic scale so that differences between the internal and external cathode cases in the large-angle-magnitude regions for both operating conditions can be seen more clearly.

Cathode Location	V_D	I_D	P_{tot}	I_{ion_T}	θ_B	η_B	η_{Div}
	uncer.±	*uncer.*±	*uncer.*±	*uncer.*±	*uncer.*±	*uncer.*±	*uncer.*±
External	300.3 V	18.39 A	5.563 kW	14 A	18 °	70%	90%
	±0.1	±0.03	±0.008	±6	±2	±30	±100
Internal	300.1 V	17.84 A	5.396 kW	14 A	19 °	80%	89%
	±0.1	±0.03	±0.008	±5	±2	±30	±95
External	150.34 V	19.59 A	2.982 kW	14 A	22.6 °	70%	85%
	±0.07	±0.03	±0.004	±4	±0.9	±20	±64
Internal	150.36 V	18.84 A	2.871 kW	12 A	23.3 °	70%	84%
	±0.07	±0.03	±0.004	±3	±0.8	±20	±57

Table 3.10: Current and Beam Utilization Efficiencies - Cathode Location Internal vs. External

Note:** η_{Div} **and its error are reported with one extra digit to make it easier to understand. The values with the proper number of significant figures are: 100 ± 100 (Ext 300 V), 100 ± 100 (Int 300 V), 90 ± 60 (Ext 150 V) & 80 ± 60 (Int 150 V).

shown in Table 3.10. The discharge voltage, current and total power values shown in this table are those averaged over the time the Faraday probe measurements were

being taken. Due to the high uncertainty that resulted from the error of the raw measurements being propagated through equations involving integration over and the square of certain values, differences in the total ion current, divergence half angle, current utilization, and divergence utilization between cathode configurations are not resolved.

3.2.6 Total Efficiency from Probe Data

Table 3.11 shows the results for the mass utilization efficiency, ion exhaust velocity, and specific impulse along with the probe derived values used to calculate these parameters in order to facilitate their comparison. The uncertainty of these numbers for both operating conditions makes it so that differences between running with the internal and external cathode can not be determined. These uncertainties are as large as they are because of the Faraday probe-measurement-calculated parameters used to obtain these values.

When calculated using the thrust measured by the thrust stand, the Isp is 2,000 ± 1,000 s for the external cathode at 300 V compared to 2,300 ± 800 s for the internal cathode. These correspond to exhaust velocities of 20 ± 10 km/s and 22 ± 8 km/s respectively. For the 150 V operating condition, the values are 1,400 ± 400 s and 14 ± 4 km/s for the external cathode and 1,700 ± 400 s and 16 ± 4 km/s for the internal cathode. Again, the uncertainty of the FP derived parameters that these variables are still functions of gives these values large error bars.

In Table 3.12, the thrust, thrust-to-power, and total efficiency were calculated using the probe's utilization parameters. The equations for these variables are explained in Section 1.5. In addition, the average of the thruster's discharge conditions, while the probes were taking data, is also listed. Table 3.13 shows these parameters calculated from the thrust stand results. These values were first presented in subsections 3.2.1 & 3.2.2, and they are repeated here for ease of comparison with their

Cathode Location	I_{ion_T} $uncer.\pm$	Ω_i $\pm uncer.$	$\dot{m}_{ion_T}$ $uncer.\pm$	η_m $uncer.\pm$	T $uncer.\pm$	v_e $uncer.\pm$	I_s $uncer.\pm$
External (300 V)	14 A ± 6	$\Omega_1 = 0.81$ ± 0.01 $\Omega_2 = 0.10$ ± 0.01 $\Omega_3 = 0.042$ ± 0.007 $\Omega_4 = 0.043$ ± 0.004	17 mg/s ± 7	80% ± 30	300 mN ± 200	20 km/s ± 10	2,000 s $\pm 1,000$
Internal (300 V)	14 A ± 5	$\Omega_1 = 0.84$ ± 0.01 $\Omega_2 = 0.07$ ± 0.01 $\Omega_3 = 0.049$ ± 0.003 $\Omega_4 = 0.037$ ± 0.001	17 mg/s ± 6	90% ± 30	300 mN ± 200	20 km/s ± 10	2,000 s $\pm 1,000$
External (150 V)	14 A ± 4	$\Omega_1 = 0.87$ ± 0.02 $\Omega_2 = 0.13$ ± 0.02	18 mg/s ± 5	90% ± 20	200 mN ± 100	13 km/s ± 5	1,300 s ± 500
Internal (150 V)	12 A ± 3	$\Omega_1 = 0.81$ ± 0.02 $\Omega_2 = 0.19$ ± 0.02	16 mg/s ± 4	80% ± 20	200 mN ± 80	13 km/s ± 4	1,300 s ± 400

Table 3.11: Mass Utilization Efficiency, Effective Exhaust Velocity and Specific Impulse

corresponding probe derived values. Here in Table 3.12 as well, the uncertainties of the probe-measurement-calculated parameters, and the Faraday probe parameters in particular, propagated through additional calculations to obtain these values makes resolving differences between these quantities for the internal and external cathode impractical.

This highlights the importance of including uncertainties with reported calculations when drawing conclusions from the data. Given the number of calculations and the nature of the calculations that are done to go from the parameters measured by the probes to a total thruster efficiency and thrust, the propagated error ends up being quite large. Therefore, when looking to compare the thrust and efficiency between the instances of thruster operation presented here, it is best to look at the thrust stand derived results from Table 3.13. This probe data is best for looking at the parameters directly measured to help interpret the results, and to get an idea of how various components of the thruster's efficiency and produced thrust are influenced by different properties of the discharge.

Still, probe data has to be interpreted with caution. As seen when comparing Tables 3.12 & 3.13, the probe derived thrust, thrust-to-power, and total efficiency are much lower than the thrust stand derived quantities by varying degrees when

Cathode Location	V_D	I_D	P_{tot}	T	T/P_{tot}	η_{tot}
	uncer.±	*uncer.*±	*uncer.*±	*uncer.*±	*uncer.*±	*uncer.*±
External	300.24 V	18.42 A	5.570 kW	300 mN	60 mN/kW	50%
	±0.05	±0.01	±0.004	±200	±40	±60
Internal	300.1 V	17.95 A	5.427 kW	300 mN	60 mN/kW	50%
	±0.05	±0.01	±0.004	±200	±40	±60
External	150.30 V	19.65 A	2.991 kW	200 mN	80 mN/kW	40%
	±0.04	±0.01	±0.002	±100	±40	±40
Internal	150.34 V	18.88 A	2.879 kW	200 mN	70 mN/kW	30%
	±0.04	±0.01	±0.002	±80	±30	±20

Table 3.12: Thruster Efficiency from Probe Data

Cathode Location	V_D	I_D	P_{tot}	T	T/P_{tot}	η_{tot}
	uncer.±	*uncer.*±	*uncer.*±	*uncer.*±	*uncer.*±	*uncer.*±
External	300.7 V	18.44 A	5.588 kW	404.4 mN	72.4 mN/kW	68.4%
	±0.1	±0.03	±0.008	±0.2	±0.1	±0.7
Internal	300.1 V	17.70 A	5.350 kW	385.8 mN	72.1 mN/kW	65.0%
	±0.1	±0.03	±0.008	±0.3	±0.1	±0.7
External	150.07 V	19.71 A	2.994 kW	253.9 mN	84.8 mN/kW	50.3%
	±0.07	±0.03	±0.004	±0.2	±0.2	±0.5
Internal	150.48 V	18.79 A	2.868 kW	252.0 mN	87.9 mN/kW	51.7%
	±0.07	±0.03	±0.004	±0.2	±0.2	±0.5

Table 3.13: Thruster Efficiency from Thrust Stand Measurements

comparing operating configurations. This is in large part due to plume physics that can alter ion velocity, such as charge exchange (CEX) collisions. CEX takes place when an atom and an ion of this same particle type exchange electron(s) but not momentum. In the Hall thruster plasma environment, the neutrals have a much lower energy than the ions. The neutral propellant has a temperature of 300-500 K, which corresponds to ∼0.03 to 0.04 eV, whereas the ions, when operating at 150 V to 300 V have temperatures of ∼130 eV to 280 eV. Therefore, these CEXs, which happen in the thruster's near field region, result in slow moving ions. These collisions occur between facility or anode and cathode neutrals and beam ions, and they can

impact the amount of current collected by the probes at various angles in different ways.

Using the acceleration zone plasma conditions from Table A.7, the average distance an ion accelerated in the thruster channel's accel zone can travel downstream before experiencing a charge exchange (CEX) collision can be calculated. This term is called the mean free path. From [7] it is defined as:

$$\lambda_{MFPXe^+} = \frac{1}{n_n Q_{Xe^+}^{Xe}}, \tag{3.4}$$

where n_n is the neutral number density in m^{-3}, and $Q_{Xe^+}^{Xe}$ is the CEX collision cross section. The xenon gas temperature of 500 K corresponds to a neutral number density of 3.9×10^{19} m^{-3} using the ideal gas law. From Ref. [131], $Q_{Xe^+}^{Xe}$ is $\sim$55 $\times10^{-20}$ m^2 for ion energies around 280 eV, and $\sim$52 $\times10^{-20}$ m^2 for ion energies around 130 eV. This means $\lambda_{MFPXe^+} \approx 5$ cm for all operating conditions considered here. Also of note is that the $Q_{Xe^{++}}^{Xe}$ for doubly ionized xenon with neutral xenon at these plasma conditions is $\sim$25 $\times10^{-20}$ m^2, which makes $\lambda_{MFPXe^{++}} \approx 10$ cm for all operating conditions considered here.

Within 5 cm from the acceleration zone, most of which is outside of the channel, the neutral number density still rounds to the same order of magnitude but has decreased to the point where the mean free path is about an order of magnitude larger. Still, the CEX collisions that do occur in the near-field plume have an impact that is noted enough for it to be accounted for in various correction factors to probe measurements and in simulation due to the fact that these slow moving ions behave differently in the plume. Examples of this can be found in the following references: [56, 104, 132].

Some of these CEX collisions occur far enough upstream or within the acceleration zone such that they do not change the ion's trajectory and therefore, when collected

by a downstream probe, give an accurate indication of the thrust and efficiency the thrust stand measures. While other CEXs occur just downstream of the acceleration zone after these ions have contributed to thrust and cause a decrease in these ions' speed making them more susceptible to changes in direction due to local fields within the plume and due to collisions.[16, 132] This changes the amount of current detected by the probes (given that $I \propto v$ and that flux is not conserved, since there are collisions), and the distribution of the current that is collected.

The amount by which the collected current changes will vary depending on the type of probe being used, the probe's location within the plume (i.e., angle and radial distance), charge species, operating condition, and even operating configuration. One example of the last item in that list is the different downward sloping angle of the "wings" of the FP traces (which is the current density collected at large angles with increasing angle) between the internal and external cathode configurations for both the 150 V and 300 V conditions. This is most easily seen in Fig. 3.28.

Unless these effects can be properly modeled in a way that can account for these differences, the significance of the probe results will be affected. The probe derived parameters that are the most impacted by these plume dynamics are the beam, divergence and mass utilization efficiency, because they depend on a total sum instead of peak values and so the errors in each component of the sum accumulate a larger overall error. The total ion current in the central beam region may in fact be higher than what could be measured from the plume downstream of the thruster exit plane.

In addition to the fact that the overall current magnitude may be higher in the central beam region, differences between the internal and external cases may have also been altered by a difference in the plasma's Debye length with each condition. This is because the Debye length is directly correlated to the size of the sheath surrounding the probe. For example, in a less dense, higher electron temperature plasma, which results in a larger Debye length and hence a larger effective collecting

area for the probe, the current density may appear higher when the collected FP current is divided by the probe area itself. For FP measurements, it is also important to note that the total current value obtained from summing the current density across the entire hemisphere in front of the thruster may be larger than the discharge current because at each data taking location, the probe can also collect current from nearby locations that have been redirected due to the probe bias.

3.2.7 Other Performance Parameters

Table 3.14 shows the results for the ionization power, ionization cost per beam ion, electron current, and ionization fraction. The same trends discussed in Section 1.5 were seen for these variables calculated here for the internal cathode configuration between the 150 V and 300 V operating conditions. However, in order to draw conclusions about differences in these parameters for the cathode operating configurations, more accurate ion current measurements would be needed. This ion current measurement not only impacts the determination of the beam, divergence and mass utilization efficiencies, as discussed in the previous subsection, but also heavily influences the calculation of the parameters in Table 3.14.

For example, since careful measurements with the non-invasive thrust stand concluded that thruster efficiency increased for the 300 V condition when using the external cathode, and given the measured voltage and charge utilization efficiencies, this would imply that before the influence of CEXs and electric fields in the plume, the current utilization efficiency should also be higher for the external cathode relative to the internal cathode. This would result in a decrease in the cost per beam ion for the 300 V condition with the external cathode versus the internal cathode. However, with the FP measurements that were made, the table shows that differences in these parameters between the cathode configurations can not be seen. These concerns with the FP measurements also affect the electron leakage current fractions shown in Table

Cathode Location	P_{min} *uncer.*±	P_D *uncer.*±	P_{jet} *uncer.*±	P_{loss} *uncer.*±	$\epsilon_{B_{min}}$ *uncer.*±	ϵ_B *uncer.*±
External (300 V)	0.3 kW ±0.1	5.530 kW ±0.004	4 kW ±2	1 kW ±2	20 eV ±10	100 eV ±100
Internal (300 V)	0.3 kW ±0.1	5.387 kW ±0.004	4 kW ±1	1 kW ±1	20 eV ±10	100 eV ±100
External (150 V)	0.21 kW ±0.05	2.953 kW ±0.002	1.8 kW ±0.5	0.9 kW ±0.5	16 eV ±6	80 eV ±40
Internal (150 V)	0.20 kW ±0.05	2.839 kW ±0.002	1.5 kW ±0.4	1.1 kW ±0.4	18 eV ±6	110 eV ±40

Table 3.14: Ionization Power and Ionization Cost per Beam Ion

3.15, because these calculated values are also dependent on these measurements.

The ionization fractions, which are also shown in Table 3.15, were calculated using the LP derived electron number density at 3 D_T downstream and 11° from centerline, 2 D_T downstream and 30° from centerline, and 2 D_T downstream and 58° from centerline, along with the neutral number density calculated from the internal ionization gauge pressure reading of 1.3×10^{-5} Torr (discussed in subsection 2.3.1) using the ideal gas law. For the most part, there is no discernible difference between the two cathode configurations for both operating conditions, and this is mostly due to the large error of 20% in the ionization gauge reading. However, at larger angles these fractions show an increase in ionization for the external cathode at 2 D_T / 30° during 150 V operation, and at 2 D_T / 58° during 300 V operation.

On a positive note, with careful LP measurements, the electron densities themselves can be more informative plume measurements given the fact that the electrons are even more mobile than the ions, and not directly influenced by CEXs. Various LP derived parameters will be discussed in detail in subsection 3.3.3 of the next section.

Cathode Location	I_D	I_{ion_T}	I_e	r	$\Theta_{ion_T 1}$	$\Theta_{ion_T 2}$	$\Theta_{ion_T 3}$
	uncer.±	*uncer.*±	*uncer.*±	*uncer.*±	*uncer.*±	*uncer.*±	*uncer.*±
External	18.39 A	14 A	5 A	0.3	0.8%	0.32%	0.20%
(300 V)	±0.03	±6	±6	±0.3	±0.2	±0.08	±0.05
Internal	17.84 A	14 A	4 A	0.2	0.8%	0.25%	0.11%
(300 V)	±0.03	±5	±5	±0.3	±0.2	±0.05	±0.03
External	19.59 A	14 A	5 A	0.3	0.8%	0.6%	0.27%
(150 V)	±0.03	±4	±4	±0.2	±0.2	±0.1	±0.07
Internal	18.84 A	12 A	6 A	0.3	0.8%	0.39%	0.18%
(150 V)	±0.03	±3	±3	±0.2	±0.2	±0.09	±0.04

Table 3.15: Electron Current and Ionization Fraction

Note: The ionization fractions are associated with the following data taking locations:** $\Theta_{ion_T 1}$ **: 3** D_T **/ 11°,** $\Theta_{ion_T 2}$ **: 2** D_T **/ 30°, and** $\Theta_{ion_T 3}$ **: 2** D_T **/ 58°.

3.3 EEDF

3.3.1 Langmuir Probe Druyvesteyn Method Analysis Procedure

Langmuir probe data was obtained using the high-speed dual Langmuir probe (HDLP) system discussed in Section 2.10. The cylindrical LP used with this system had a diameter of 0.5 mm (0.02 in.) and a length of 10 mm (see Fig. 2.5(b)). Figure 3.29 shows the locations where data was taken for each operating condition tested. Measurements were taken at 11° from thruster centerline and a radial distance of ∼3 D_T, and also at 30° and 58° with a radial distance of ∼2 D_T. These measurements were taken on the opposite side to where the external cathode was located.

The recommendations outlined in Ref. [116] were closely considered in choosing the probe tip size, in designing the Langmuir probe itself, and in constructing the probe setup in order to remove as many systematic biases as possible, and to ensure that the Druyvesteyn method, which was used to calculate the EEDFs and the parameters derived from it, was being applied properly. For example, the application of this method requires the current to the probe be much smaller than the maximum current that can be supplied by a reference counter-electrode placed close to the probe,

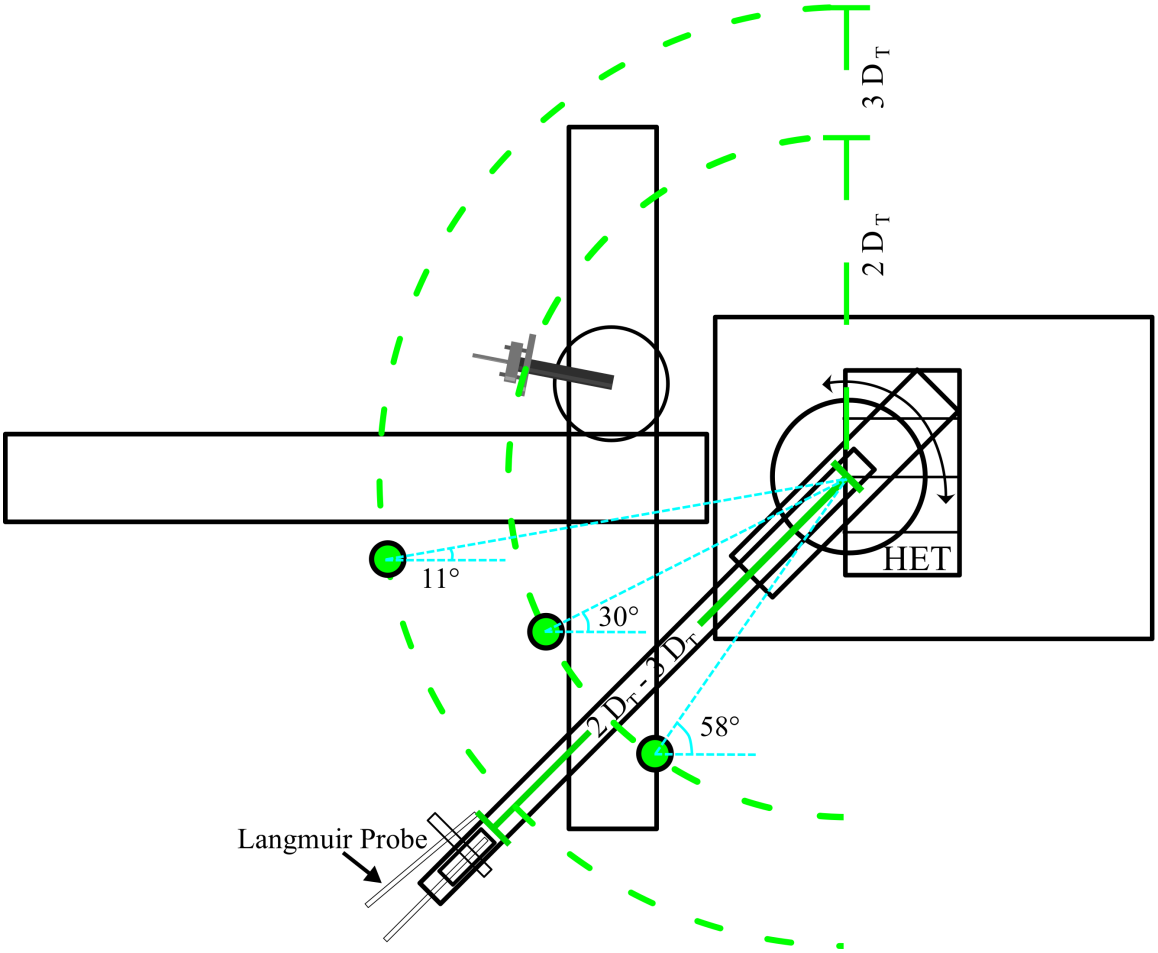

Figure 3.29: This diagram shows the locations where Langmuir probe data was taken relative to the rest of the experimental setup for all operating conditions.

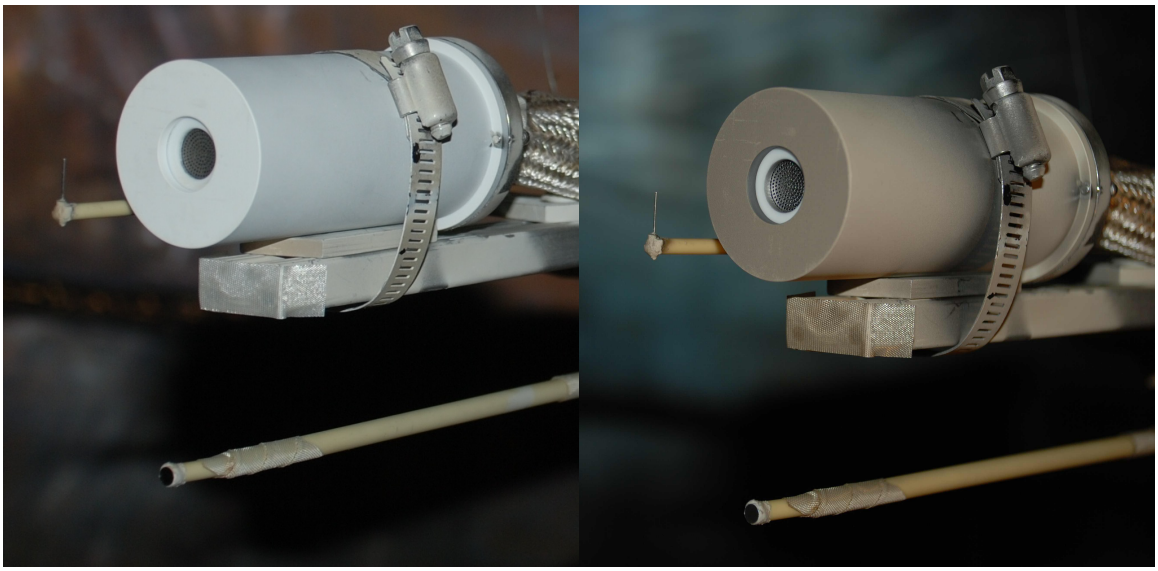

(a) Before Testing (b) After Testing

Figure 3.30: (a) A picture of the Langmuir probe along with the other probes on the rotating armature before testing. (b) A picture of the Langmuir probe and other probes after testing.

a low-perturbation, telescoping probe design, and that the following possible sources of systematic error are negligible or accounted for:

- low energy electron depletion due to probe circuit resistance
- chamber surface resistance from contaminated chamber walls
- probe surface contaminants
- electron current collection being influenced by probe orientation with respect to the B-field.

Given the probe orientation, shown in Fig. 3.9(a), the EEDFs were obtained for the component of the electron energy that is perpendicular to the probe surface. Since the probe is oriented pointing upward, and the plume leaving the Hall-effect thruster is a flowing plasma vectoring in a direction perpendicular to the probe, if the electrons have a drifting component to their motion, then the calculated EEDFs will capture this behavior. A picture of the Langmuir probe before and after testing are shown in Fig. 3.30.

The LP analysis that was used followed the steps outlined in subsection A.1.2 starting with step 3, but skipping over the ion number density calculation in step 4a.,

the T_e calculated with the assumption of a Maxwellian electron distribution of step 5, and step 14, since an OML regime analysis was not used. Following the advice of Ref. [116], step 4 in its entirety was also skipped since it was said to create more error than it could address for EEDF measurements. Lieberman & Lichtenberg indicate that when the electron current is very small, attempting to eliminate the ion current from the probe trace can cause errors in the electron current. [111]

The electron number density and electron temperature were calculated by integrating the EEDF as mentioned for the electron number density in step 11. Equations (6.6.19) & (6.6.20) along with $T_{eff} = \frac{2}{3}\langle\epsilon\rangle$ from the text under these equations in Ref. [111] were used. The electron number density is assumed to be equal to ion number density through quasi-neutrality. [133, 134] Instead of steps 11 through 13, the determined electron density and temperature were used as the initial guesses in the MATLAB chi-squared fitting routine (also used in subsections 3.2.1, 3.2.3 and 3.2.4), to determine the form of the EEDF that described the data.

The distributions that were tried are the Druyvesteyn (equation shown in Fig. A.7(b)), Maxwellian (Fig. A.7(b) & Eqn. 2.9), and drifting Maxwellian (Eqn. 2.13). In addition, a Maxwellian + energy shift distribution was tried, but it did not fit any of the EEDFs. The form of this equation can be found in the literature. [122] The parameters of the best fitting distribution were taken as the values of those parameters for that trace. Then the Debye length was calculated using these values and Eqn. 2.5.

The results, which include the calculated EEDFs for each operating condition along with each fit distribution that was tried (besides the Maxwellian + energy shift distribution), and the electron temperature and density parameters of the best fit along with their uncertainties are shown in figures in subsection 3.3.3 and Appendix D. The chi-squared fitting algorithm took into account the uncertainty of the data points and other parameters included in the distribution equation when calculating

the uncertainties of the parameters obtained from the fit. All of the Langmuir probe derived parameters for each operating condition are reported in Table 3.16.

Before the analysis was carried out, and after the null probe's current was subtracted from the active probe's current, steps to prepare the trace for analysis were taken that are described in the next subsection.

3.3.2 LP Analysis Without Smoothing Functions

Since Langmuir probe data was being taken here at frequencies slower than this Hall-effect thruster's breathing mode, and since these oscillations also show up in the plasma parameters, it means these parameters were changing over the course of each LP sweep. Therefore multiple traces had to be averaged together in some way to obtain a trace that represented the average plasma conditions. A number of different techniques have been used to do this. Unfortunately, many of those options can introduce bias into the data or make it difficult to propagate the error through the analysis procedure.

During the analysis of the experiments described in Appendix A.2.1.2, the process of combining multiple traces and smoothing the resulting trace produced an LP I-V characteristic that was more easily analyzable. Here an analysis preparation step that took this idea a step further was used. This was the process of binning the data from multiple traces. At each spatial location, data was taken at a sample rate of 100,000 points/second for 8 seconds. This resulted in around 800,000 points over the sweep range of -20 V to 50 V split over about 160 traces since data was taken at a sweep rate of 10 Hz and both the positive and negative sloping sides of the sine wave used to take the data constitute a full LP trace. The binning method involved first sorting all of the data points into order of ascending voltage, splitting the sweep range into equally sized portions, and then placing each of the data points into the appropriate bin.

Next, for each bin an average representative current and voltage value was obtained by averaging the current and then the voltage values of all the points in that bin together. Error was propagated through this averaging by starting with the uncertainty in the DAQ's voltage measurements from its specification sheet, which was 5 mV, the error from measuring the resistance values of the shunts, and the error in measuring the gain of the probe circuitry box, and propagating this error through the calculation of both the active and null current using the equation at the top of the procedure in Appendix B.3. From here the error was then propagated through the subtraction of the null current from the active current, and through the averaging in this binning procedure.

To determine the bin size to use, a value that was four times the uncertainty in the voltage was started with. However, given the fact that two derivatives had to be taken on the data, and as seen from Fig. 3.31, this bin size had to be increased until the first and second derivatives were resolved. A bin size of 1 V was decided on for a total of 70 bins with about 10,000 points per bin. This approach eliminated the need for using the MATLAB smoothing function that was used previously (Appendix A.2.1.2). Figures 3.32 & 3.33 show the bins, original points, and the resultant averaged trace at one spatial location for one of the operating conditions.

Error analysis was continued through the rest of the calculations to determine if there was a statistically significant difference in the EEDF between the control cathode testing configuration and the case where the proposed EEDF control method was applied. As seen from the results reported in Table 3.16, the error bars for the electron temperature, voltage shift, electron density and Debye length are relatively small due to the applied method. This is in large part because of the number of points per data taking location, which when averaged together create a very small error for each point of the resultant trace. This means that even after taking two derivatives, the resultant error still allows differences between the operating conditions to be seen.

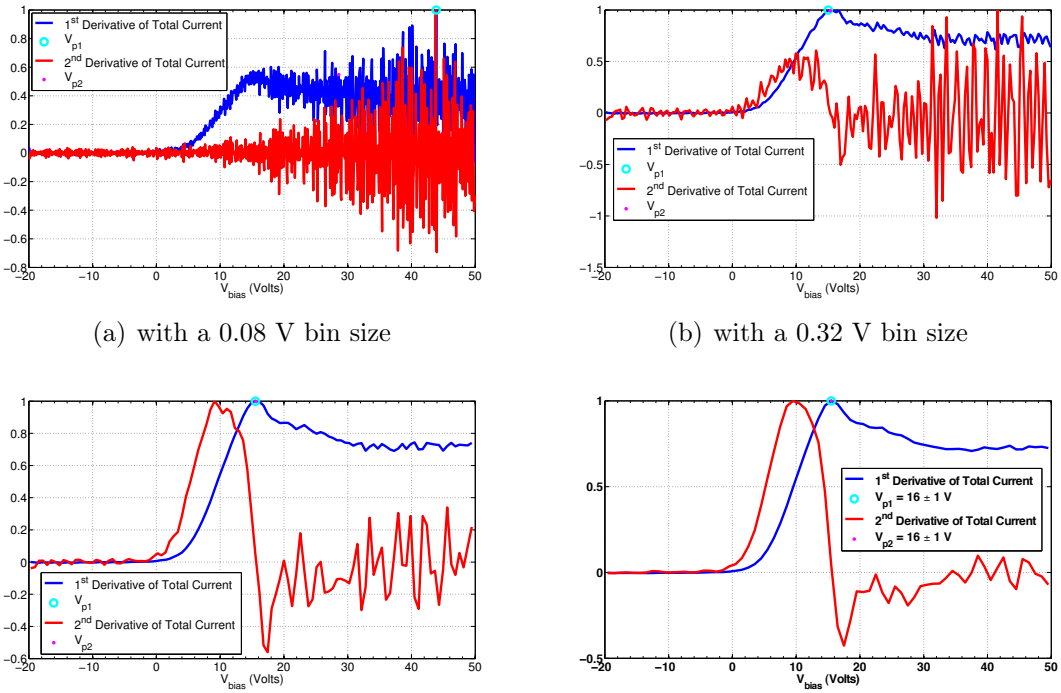

(a) with a 0.08 V bin size

(b) with a 0.32 V bin size

(c) with a 0.64 V bin size

(d) with a 1 V bin size

Figure 3.31: (a)-(d) A series of graphs showing how increasing the bin size used for the initial Langmuir probe trace affected the 1st and 2nd derivatives of the LP trace.

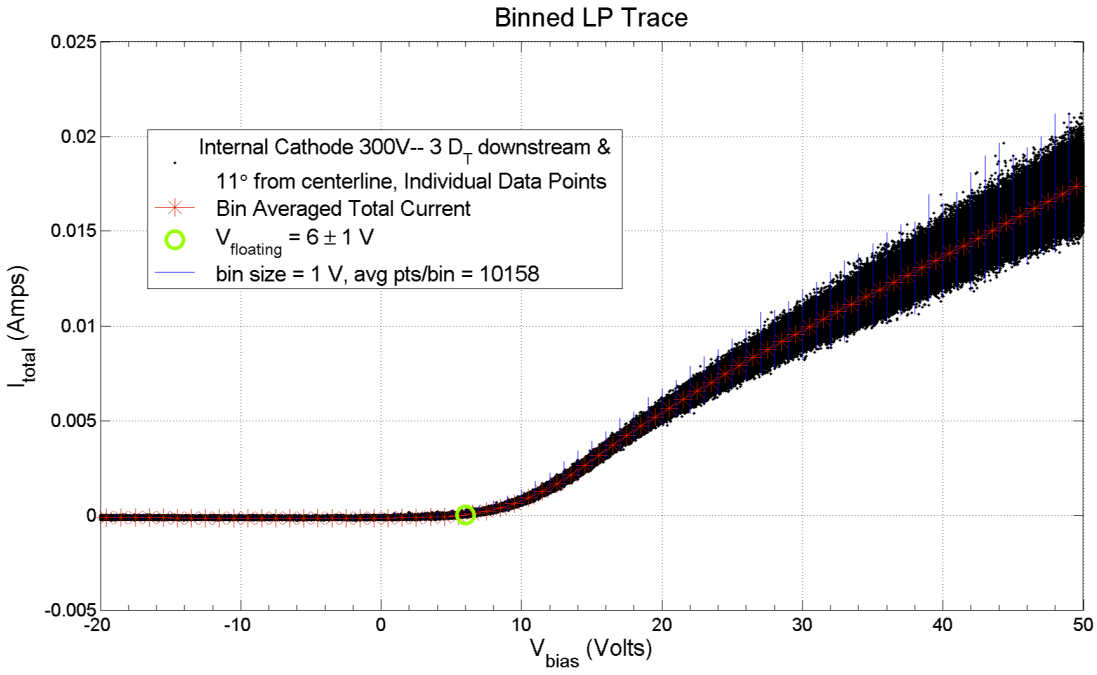

Figure 3.32: A graph showing how the raw Langmuir probe data points were binned to create an average trace. A bin size of 1 V was chosen for reasons depicted in Fig. 3.31. This trace is for the 300 V internal cathode condition, however the same method was used for all cases. The blue lines mark the beginning of the bin to the left of the line, and the top and bottom of each blue line indicate the smallest and largest current values of the points within that bin. Each red asterisk shows the average voltage and current of the points within the bin, and the red line that runs between these values shows the resultant trace from using the binning method to average the trace. See Fig. 3.33 for an enlarged view of a portion of this figure.

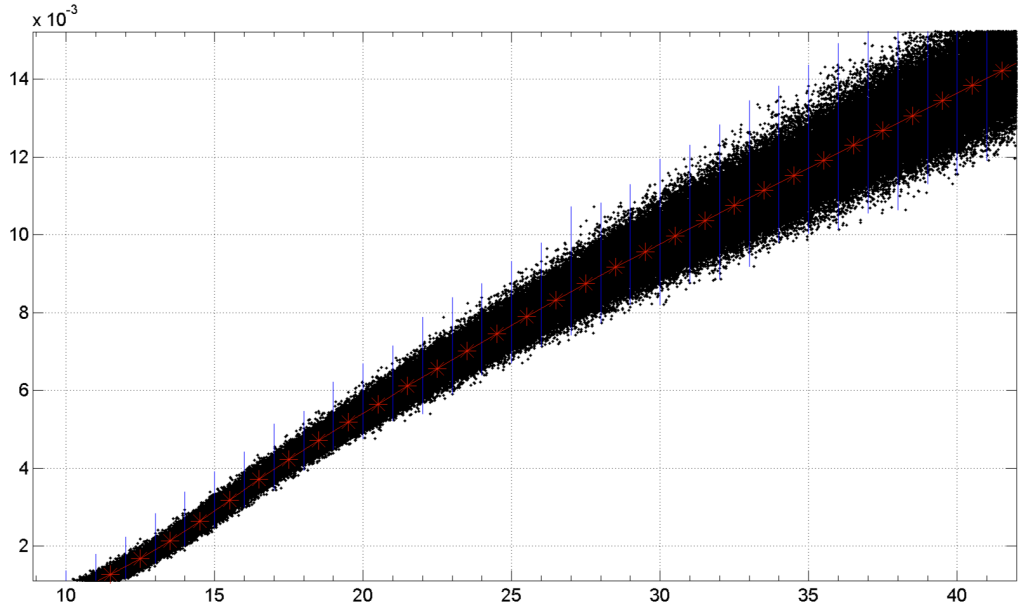

(a)

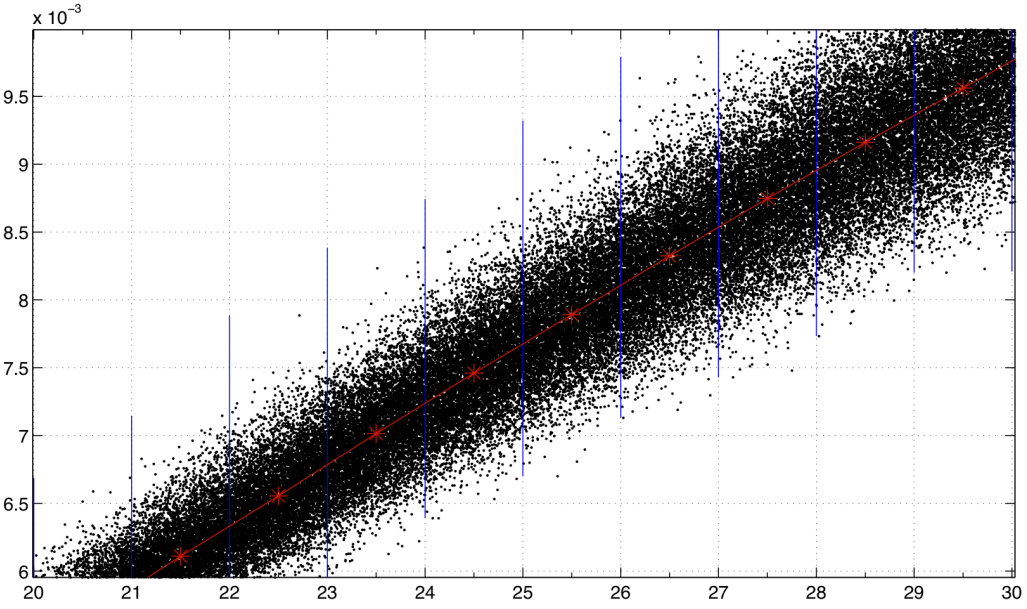

(b)

Figure 3.33: (a) & (b) These graphs show Fig. 3.32 zoomed in on one area to show the bins and data points more clearly. The blue lines mark the beginning of the bin to the left of the line, and the top and bottom of each blue line indicate the smallest and largest current values of the points within that bin. Each red asterisk shows the average voltage and current of the points within the bin, and the red line that runs between these values shows the resultant trace from using the binning method to average the trace.

The only parameter with a relatively large error is the plasma potential given the fact that it is found as the maximum point of the first derivative, so its error is ± the bin size, instead of the calculated uncertainty of the voltage value of that point. Even though the plasma potential error is relatively large compared to the error on the other parameters, differences can still be seen between the operating configurations.

The combination of the binning method and Druyvesteyn method to evaluate the Langmuir probe traces allowed for a robust calculation routine in the sense that 1. it did not rely on graphical methods of fitting straight lines to portions of the trace to estimate plasma parameters as is the case with other analysis procedures, and 2. it did not make any assumptions about the form of the electron energy distribution when calculating the plasma parameters. Therefore, this procedure can make it easier to analyze a large number of traces quickly, and traces that are over various standard LP regimes.

3.3.3 EEDF Results

Figures 3.34 through 3.36 for the 300 V conditions and Figs. D.1 through D.3 in Appendix D for the 150 V conditions show that the EEDFs in the plume of the Hall thruster for the operating conditions tested are clearly non-Maxwellian, and are not Druyvesteyn either, but instead are Maxwellian with a velocity drift component of varying degrees in the direction perpendicular to the probe. Even distributions that look Maxwellian at first glance, such as the distributions for the external cathode conditions in Fig. 3.37(a) are actually still better described by a drifting Maxwellian EEDF as seen from the chi-squared value for the closest Maxwellian fit compared to the closest drifting Maxwellian fit in Figs. 3.34(b) & D.1(b).

Figures 3.37, 3.38 & D.4 show the EEDFs in various combinations so that trends in the data can be seen more easily. The EEDFs are presented in their non-normalized form, which is the normalized form multiplied by the number density so that differ-

ences in the sizes of the distributions in addition to differences in the shapes of the distributions can be compared. From these plots and Table 3.16 it is clear that for the EEDFs in the various locations in the plume where data was taken, the external cathode conditions contain less of a velocity shift, for the most part, in addition to a lower overall electron temperature than in the corresponding internal cathode conditions, especially at the 3 D_T / 11° location, which is in the main part of the beam. Specifically, the electron temperatures were on average about half the magnitude of their internal cathode data counterparts. In line with this, the plasma potential was significantly lower for all the external cathode conditions.

Also of note is the fact that the electron number density was about 30-70% larger in the 300 V condition with the external cathode, outside of the central peak region (which covers points 2 D_T / 30° and 2 D_T / 58°) compared to the internal cathode configuration, and about 40-50% larger during 150 V operation in this region. Since the external cathode was pointing towards this area where this data was taken, the results are not necessarily symmetric, so data would have to be taken at 2 D_T / -30° & 2 D_T / -58° to see if these trends were the same there. On the contrary, for both 150 V and 300 V operation, the peak region electron number densities were comparable between the cases. Through quasi-neutrality, these results also apply to the ion number densities.

Still, these results suggest that since the cathode was pointing towards the thruster channel in the external cathode conditions, additional CEX collisions may have been taking place, which would have caused more high energy ions to take on a slower speed and be redirected towards larger angles in the plume, decreasing the amount of electron and ion current seen at small angles, such as at 3 D_T / 11°. This further supports the conclusions drawn about the Faraday probe data and CEX in subsections 3.2.6 & 3.2.7, and suggests that there may have actually been an overall increase in total ion current for the external cathode configuration relative to the internal cathode

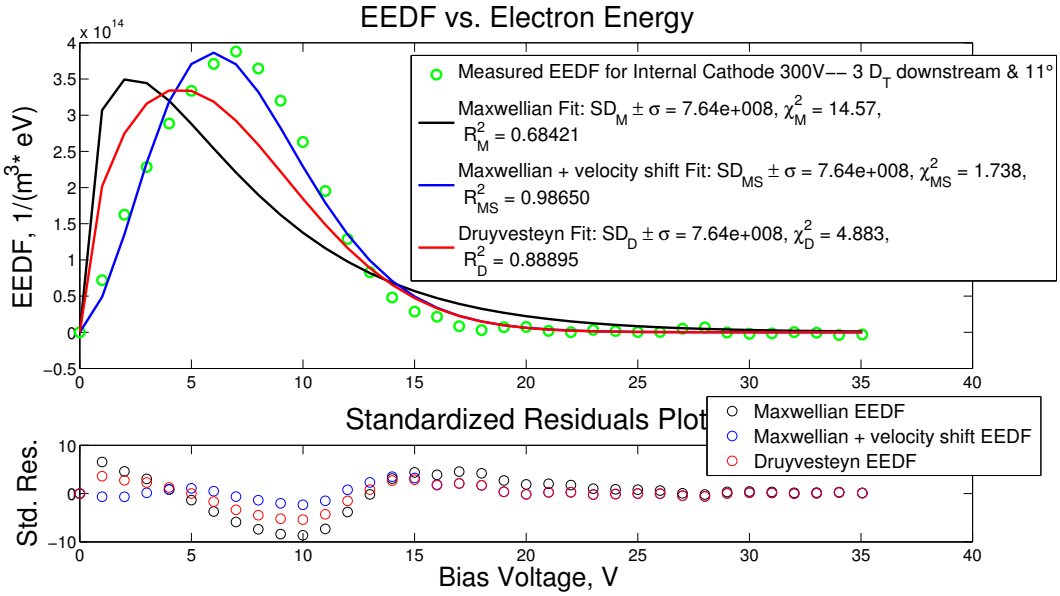

(a)

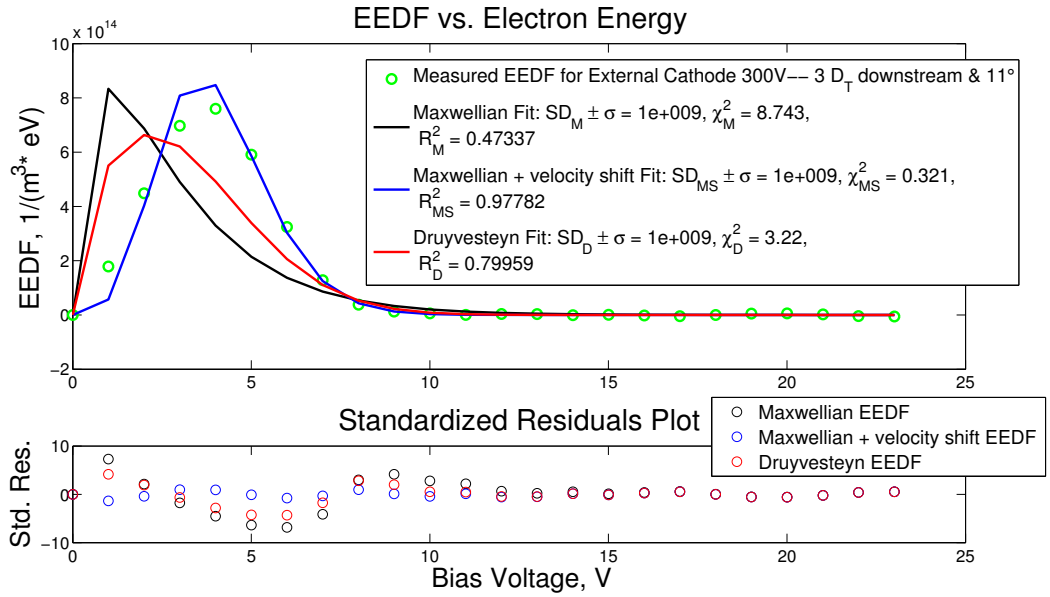

(b)

Figure 3.34: (a) A plot showing the Maxwellian and Druyvesteyn functions that were fit to the EEDF at the 3 D_T 11° location while running the thruster at 300 V with the internal cathode to determine the form of the distribution. The legend shows each curve fit's corresponding reduced chi-squared (χ^2) and R^2 values, and the average of each point's SD from the fit function. (b) The same as 3.34(a) but for running the thruster at 300 V with the external cathode.

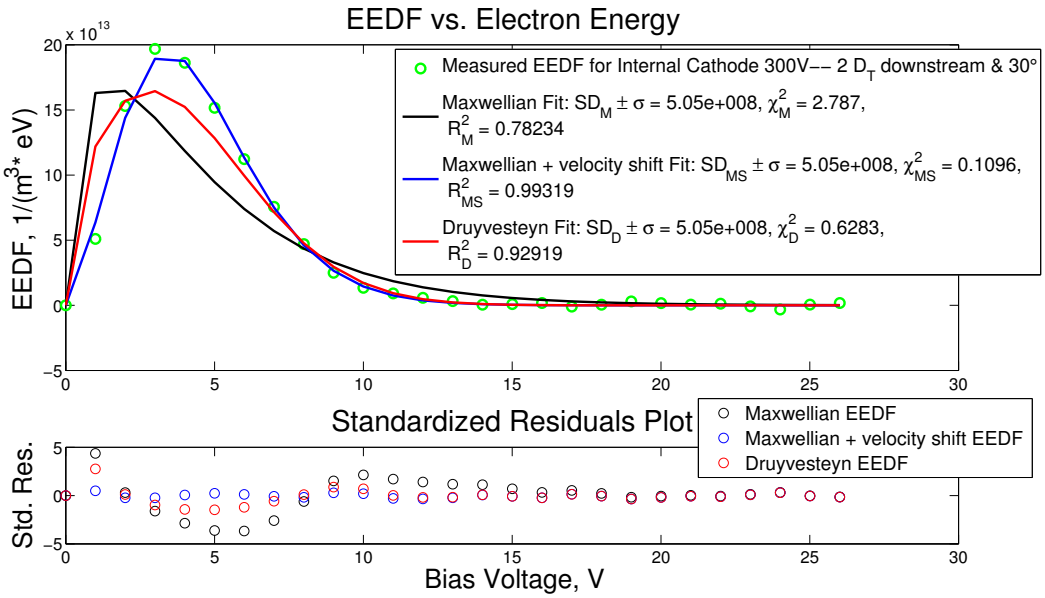

(a)

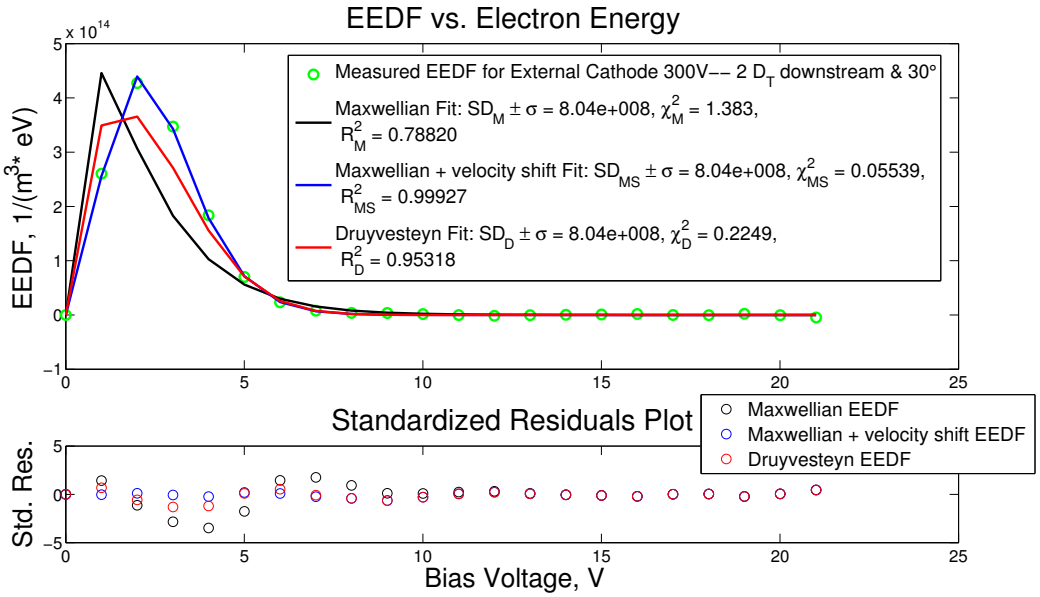

(b)

Figure 3.35: (a) A plot showing the Maxwellian and Druyvesteyn functions that were fit to the EEDF at the 2 D_T 30° location while running the thruster at 300 V with the internal cathode to determine the form of the distribution. The legend shows each curve fit's corresponding reduced chi-squared (χ^2) and R^2 values, and the average of each point's SD from the fit function. (b) The same as 3.35(a) but for running the thruster at 300 V with the external cathode.

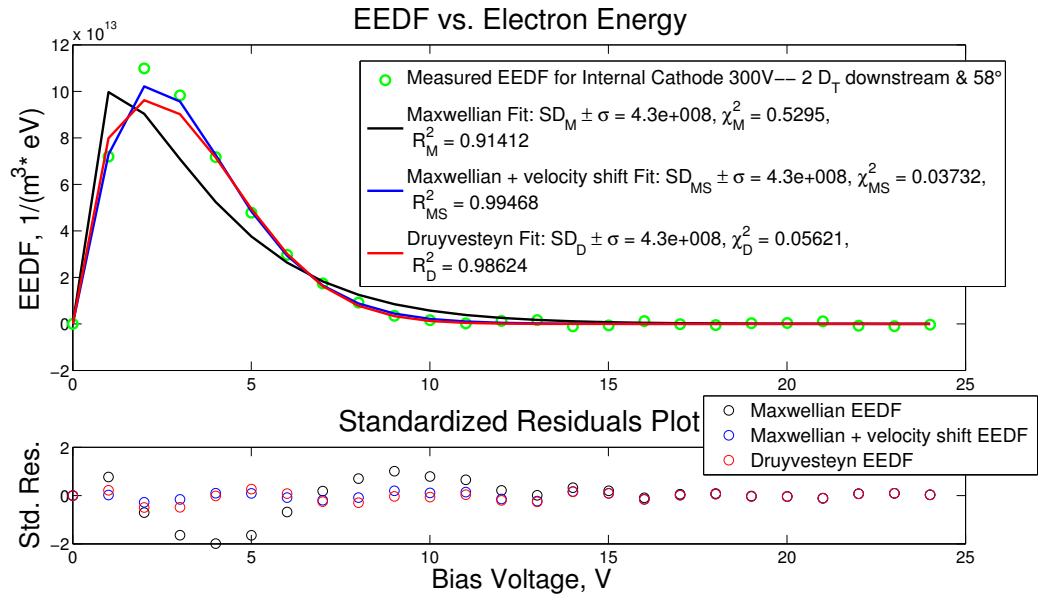

(a)

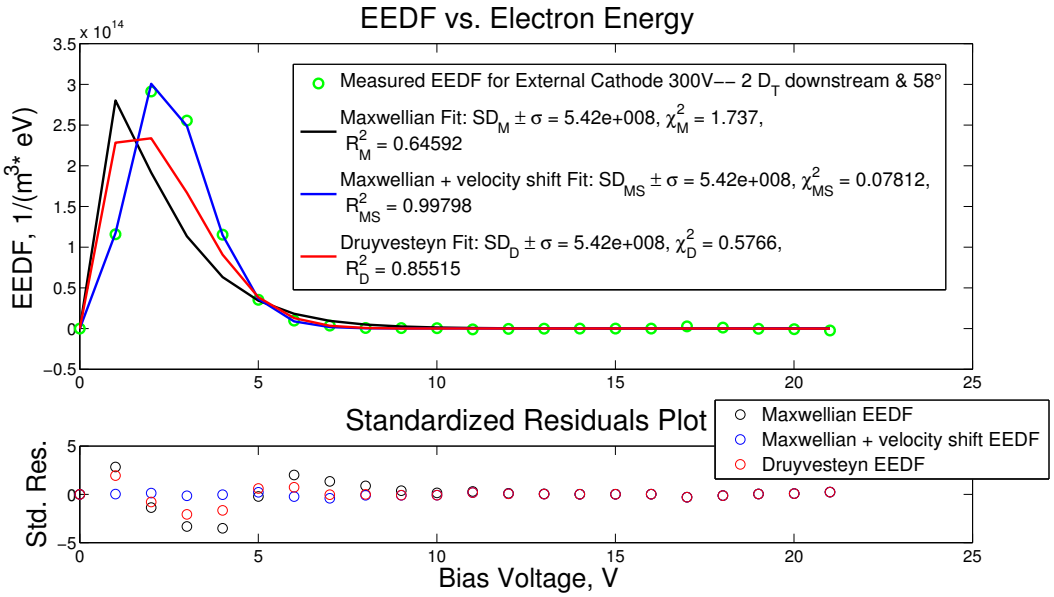

(b)

Figure 3.36: (a) A plot showing the Maxwellian and Druyvesteyn functions that were fit to the EEDF at the 2 D_T 58° location while running the thruster at 300 V with the internal cathode to determine the form of the distribution. The legend shows each curve fit's corresponding reduced chi-squared (χ^2) and R^2 values, and the average of each point's SD from the fit function. (b) The same as (a) but for running the thruster at 300 V with the external cathode.

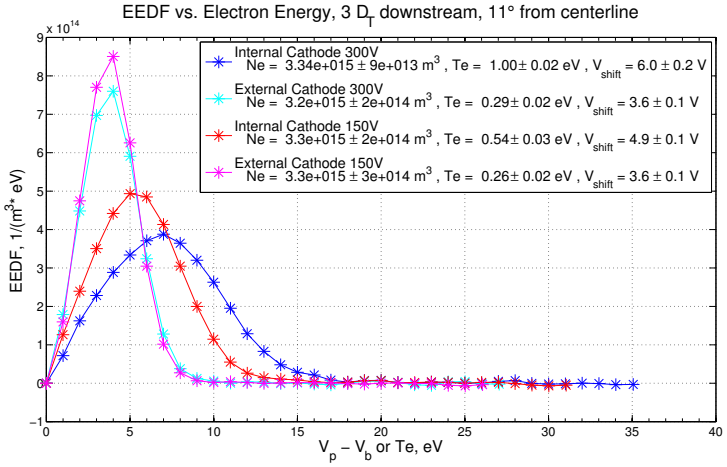

(a)

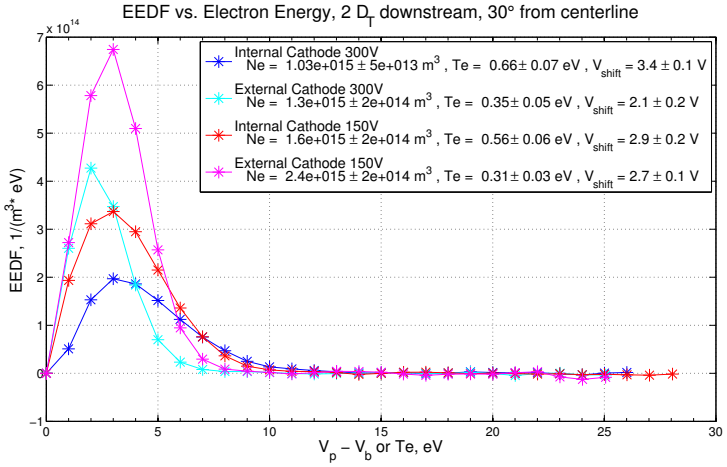

(b)

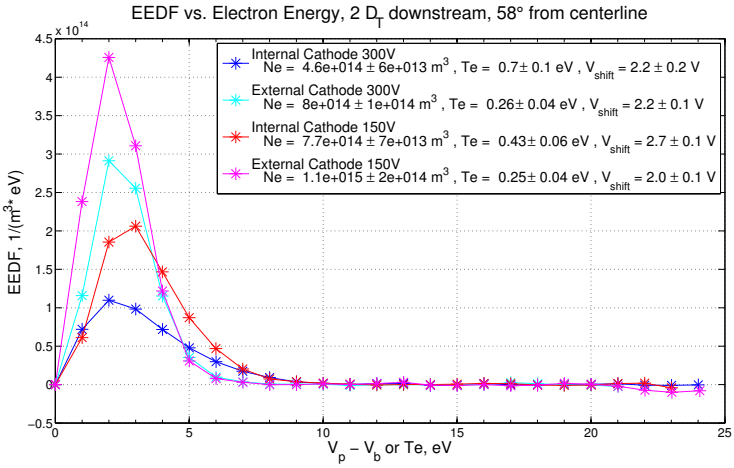

(c)

Figure 3.37: (a) - (c) Shows the EEDFs from all operating conditions and configurations on the same graph for each location where data was taken.

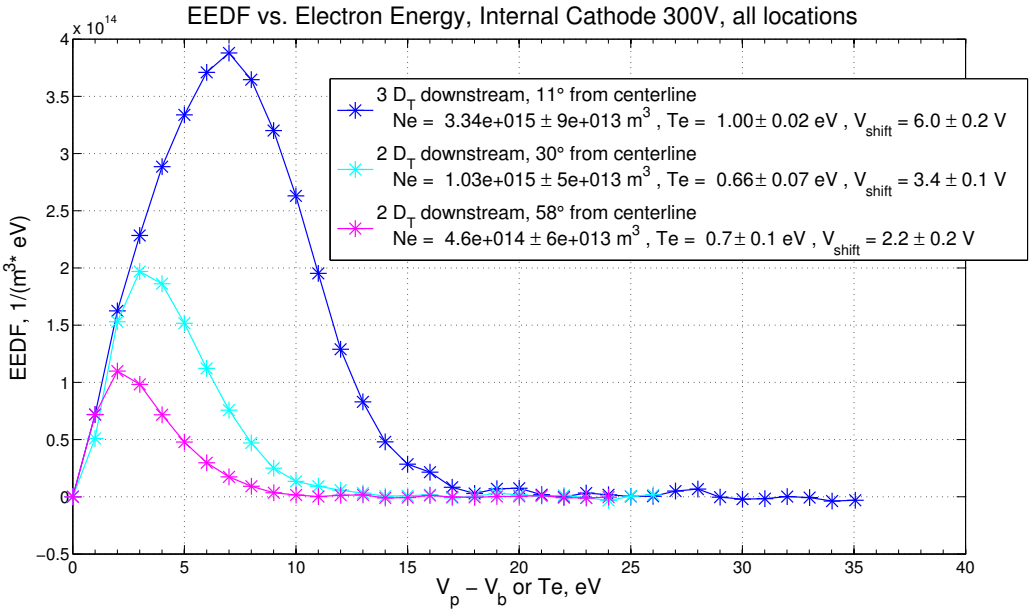

(a)

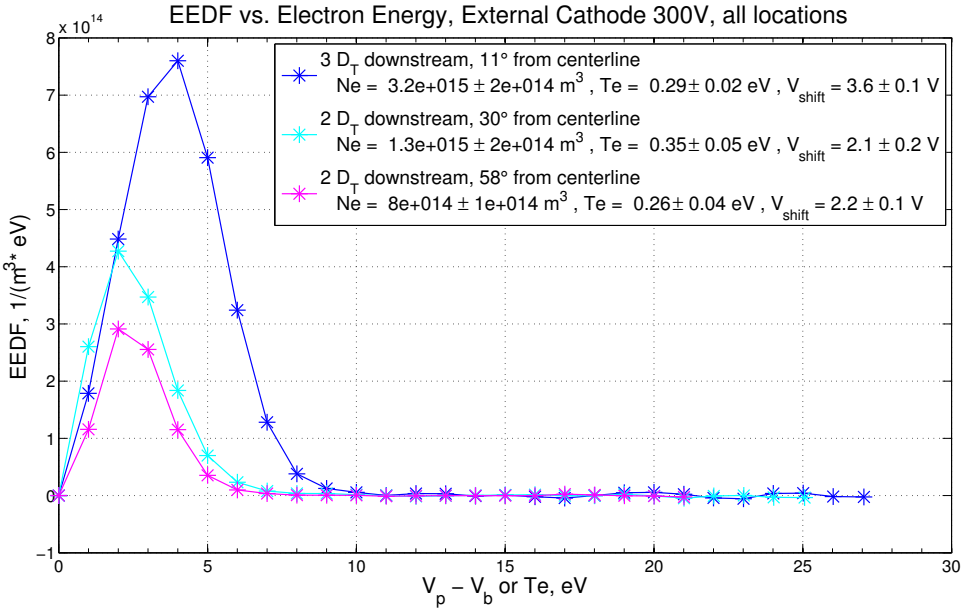

(b)

Figure 3.38: (a) & (b) Shows the EEDFs from all locations where data was taken on the same graph for each 300 V cathode operating configuration.

Cathode Location	V_D *uncer.*±	I_D *uncer.*±	R_{probe}	θ_{probe}	V_p *uncer.*±	T_e *uncer.*±	V_{shift} *uncer.*±	N_e *uncer.*±	λ_D *uncer.*±
External	300.24 V ±0.07	18.44 A ±0.02	3 D_T	11°	8 V ±1	0.29 eV ±0.02	3.6 V ±0.1	3.2x10^{15} m^{-3} ±0.2	7.1x10^{-5} m ±0.4
			2 D_T	30 °	6 V ±1	0.35 eV ±0.05	2.1 V ±0.2	1.3x10^{15} m^{-3} ±0.2	1.2x10^{-5} m ±0.1
			2 D_T	58 °	6 V ±1	0.26 eV ±0.04	2.2 V ±0.1	8x10^{14} m^{-3} ±1	1.3x10^{-4} m ±0.1
Internal	300.16 V ±0.07	17.93 A ±0.02	3 D_T	11°	16 V ±1	1.00 eV ±0.02	6.0 V ±0.2	3.34x10^{15} m^{-3} ±0.09	1.29x10^{-4} m ±0.02
			2 D_T	30 °	11 V ±1	0.66 eV ±0.07	3.4 V ±0.1	1.03x10^{15} m^{-3} ±0.05	1.9x10^{-4} m ±0.1
			2 D_T	58 °	9 V ±1	0.7 eV ±0.1	2.2 V ±0.2	4.6x10^{14} m^{-3} ±0.6	2.9x10^{-4} m ±0.3
External	150.29 V ±0.05	19.64 A ±0.02	3 D_T	11°	7 V ±1	0.26 eV ±0.02	3.6 V ±0.1	3.3x10^{15} m^{-3} ±0.3	6.5x10^{-5} m ±0.4
			2 D_T	30 °	6 V ±1	0.31 eV ±0.03	2.7 V ±0.1	2.4x10^{15} m^{-3} ±0.2	8.4x10^{-5} m ±0.6
			2 D_T	58 °	5 V ±1	0.25 eV ±0.04	2.0 V ±0.1	1.1x10^{15} m^{-3} ±0.2	1.1x10^{-4} m ±0.1
Internal	150.35 V ±0.05	18.86 A ±0.02	3 D_T	11°	12 V ±1	0.54 eV ±0.03	4.9 V ±0.1	3.3x10^{15} m^{-3} ±0.2	9.5x10^{-5} m ±0.4
			2 D_T	30 °	9 V ±1	0.56 eV ±0.06	2.9 V ±0.2	1.6x10^{15} m^{-3} ±0.2	1.4x10^{-4} m ±0.1
			2 D_T	58 °	8 V ±1	0.43 eV ±0.06	2.7 V ±0.1	7.7x10^{14} m^{-3} ±0.7	1.8x10^{-4} m ±0.1

Table 3.16: Langmuir Probe Calculated Parameters - Cathode Location Internal vs. External

configuration in both the 300 V and the 150 V operating conditions.

Table 3.16 also shows the Debye length is smaller for all external cathode operating conditions at all locations where data was taken compared to their corresponding locations and operating conditions when the internal cathode was used, which further supports the discussion at the end of subsection 3.2.6 on the Faraday probe data and the Debye length.

The fact that the EEDFs are drifting Maxwellian distributions means that in the direction perpendicular to the probe, electron-electron collisions (which would create a Maxwellian plasma if they dominated) were not occurring frequently enough to offset a shift in their motion that had been imposed. As explained in subsection 2.10.1.1, this velocity drift is a shift in the guiding center motion of the electron, as opposed to a potential well energy shift, and examples of the plasma and field conditions that can cause this type of shift in a device are listed there. For the Hall thruster, what can be said from these results is that this shift is most likely due in part to the cathode's influences on the plume, and not the ions dragging electrons downstream with them in order for quasi-neutrality to be maintained.

This can be seen by calculating the velocity shift that corresponds to the potential shift obtained from the drifting Maxwellian function by using the equation that relates the two discussed in the text under Eqn. 2.10. From Table 3.16, the potential shifts ranged from 3.6 V to 6.0 V at the 3 D_T / 11° location across all operating conditions. These correspond to velocity shifts on the order of 10^6 m/s, whereas the beam voltage values of 130 V and 280 V correspond to ion velocities of 10-20 km/s. For comparison, to match the ion speed, a voltage shift of only 1 mV would be required. Further investigation would be needed to understand why there is this disparity and what exact mechanisms impose this velocity shift on the emitted electrons. However, it is most likely from the kinetic energy gain or "kick" the electrons receive from the potential difference between the insert and keeper, and then also between the keeper

and the ambient plasma balanced by some other mechanism that causes the shift to show up as a velocity drift and not an energy shift. Therefore, what can be concluded from this evaluation and Fig. 3.37(a) is that in the external cathode case, a large portion of that velocity shift is being directed towards the thruster channel as opposed to out in the plume, and is therefore able to be more directly utilized there.

The fact that this redirection of energy still resulted in a decrease in efficiency for the 150 V condition can be understood in the following way. The component utilization efficiencies calculated from the RPA & ExB probe showed an increase in voltage utilization and the same charge utilization for the external cathode compared to the internal cathode, and from the discussions in subsections 3.2.6, 3.2.7, and this subsection it is suspected that there was also an increase in current utilization efficiency. This implies there was also an increase in the mass utilization. In addition, the changes to the EEDF were comparable to those in the 300 V condition, and in the 300 V condition these EEDF changes were correlated with an increase in thrust stand measured thruster efficiency. Therefore, the fact that the thrust stand measurements for the 150 V condition showed a decrease in total efficiency suggests that either the divergence efficiency was much lower for the external cathode case than the internal cathode case at the thruster exit plane, or that there are other factors at work affecting thruster efficiency that are not captured or accounted for with the measurements or calculations made.

CHAPTER IV

Conclusions

4.1 Summary of EEDF Control Performance Results & Suggested Future Work

The goal of this research investigation was to improve thruster efficiency in the high thrust-to-power regime through EEDF control by specifically targeting the ionization cost per beam ion. To that end, first, a neutral gas injection scheme was tried with an inductively coupled plasma as the test-bed. This experiment revealed that the addition of this flow did not change the shape of the EEDF or increase ion number density significantly enough to be a promising approach for improving efficiency in the Hall thruster. There was only a 10% increase in ion number density accompanied by a 10% decrease in electron temperature.

The results from this study led to the theory that introducing heavy particles with electrons in metastable states that had enough energy to ionize the thruster's propellant could improve thruster efficiency through EEDF control. This was studied through gas mixing using both experimental and computational means and a hollow cathode as the test-bed. The outcome showed that another atom is not a good energy delivery method for increasing the ionization rate, because although the cross section for atom-atom collisions is much higher than electron-atom collisions, the speed of the

particle, which also factors into the collision frequency takes away gains associated with the larger cross section. In addition, this particle speed deficit is not made up for by the small fraction of regularly present metastable atoms in the gas being mixed in for this plasma condition when calculating the propellant ion production rate for the metastable neon atom-xenon atom collision. Therefore, the ion production rate for this scheme was several orders of magnitude lower than that of electron-xenon atom ionization.

A metastable neon number density that is two orders of magnitude larger than that of the electrons would be needed to compensate for its lower collision frequency to allow metastable neon-propellant atom ionization to even be comparable to electron-propellant atom ionization in the insert plasma environment. This would require a neon to xenon gas density ratio of 2×10^5 to 1 (i.e., a neon gas mixing ratio of $2\times10^7\%$). In the Hall thruster channel's ionization/acceleration zone (see. Table A.7 for the plasma parameters in these areas) the trends would most likely be similar, and this would flood the channel with neon neutrals, which would completely change the plasma conditions there, creating a negative affect on thruster efficiency in other ways. For example, it would greatly reduce the Hall current which aids in setting up the spatial electric field responsible for accelerating the ions to produce thrust.

This motivated the realization that in order to control the EEDF to improve thruster efficiency, the energy of the electrons alone needed to be directly altered in a way that took advantage of features that occur naturally within the Hall thruster environment. This led to the reverse-orientation cathode (or reverse-flow cathode) EEDF control method. This strategy sought to bring the source of electrons inside the thruster's separatrix yet still outside the main ion beam to make it easier for the electrons to reach the thruster channel. The intention was to decrease the amount of energy the system used to get the electrons to the channel so that a larger portion of the available energy would be used for ionization and accelerating ions. This approach

translated into manipulating the EEDF by trajectory redirection in order to shift the entire distribution to higher energies in the location where ionization occurs.

Experiments were carried out to investigate the feasibility and benefit of running a Hall-effect thruster with a downstream, reverse-orientation cathode at two operating conditions using the H6 Hall thruster: the nominal 300 V 20 mg/s and 7% CFF condition, and the same operating condition but at 150 V. For the 300 V condition, the total thruster efficiency, derived from thrust stand data, increased by 3 percentage points with the external cathode compared to the standard case with a centrally mounted cathode; however, it decreased by 1 percentage point for the off-nominal 150 V condition.

In the various downstream locations in the plume where data was taken, the EEDFs calculated from the LP measurements showed that the external cathode conditions contain less of a velocity shift, for the most part, in addition to about half the electron temperature of the corresponding internal cathode conditions. The electron number density was about 30-70% larger in the 300 V condition with the external cathode, outside of the central peak region compared to the internal cathode configuration, and about 40-50% larger for 150 V operation in the same region. For both 150 V and 300 V operation, the peak region electron number densities were comparable between cathode configurations. Through quasi-neutrality, this also applied to the ion number densities. Still, these results suggest that since the cathode was pointing towards the thruster channel in the external cathode conditions, additional CEX collisions may have been taking place, which would have caused more high energy ions to take on a slower speed and be redirected towards larger angles in the plume, decreasing the amount of electron and ion current seen at small angles, such as at 3 D_T / 11°.

It was also realized that the velocity shift component of the electrons' drifting Maxwellian distributions, which were on the order of 10^6 m/s, and directed per-

pendicular to the probe (most likely in the axial direction) are a couple orders of magnitude higher than the ion velocities, which were 10-20 km/s. Therefore, this shift is most likely due in part to the cathode's influences on the plume, and not the ions dragging electrons downstream with them in order for quasi-neutrality to be maintained. This means that in the external cathode case, a large portion of that energy shift is being directed towards the thruster channel as opposed to out in the plume and is therefore able to be more directly utilized there.

In order to determine why the efficiency still decreased for the 150 V condition, the Faraday probe measurements were consulted. However, high accuracy measurements of ion current density that could speak to the value of this parameter in the acceleration zone where thrust is produced were not obtained. In spite of this, from the thrust stand and other probe measurements that were taken for the two cathode configurations, it could be surmised that with the reverse-flow cathode, more of the system energy was able to go towards increasing ionization in addition to accelerating the ions.

This can be understood by looking at the various component utilization efficiencies. For the 300 V condition, the voltage utilization efficiency increased by about 3 percentage points and the charge utilization efficiency remained about the same within the uncertainty of the measurements. For the 150 V condition, the voltage utilization efficiency increased by 4 percentage points for the external downstream cathode, and the charge utilization efficiency remained the same. The three remaining component efficiencies that can differ between the cathode configurations when calculating total efficiency are mass, current, and divergence utilization, which are all functions of the ion beam current. Therefore, since these efficiency components are all multiplied together to obtain the total efficiency, the total ion current must have also increased in the 300 V condition. For the 150 V condition, it was hypothesized, using clues from the FP and LP data, that the total ion current may have increased for the

external cathode configuration as well, which would mean the divergence utilization would have decreased quite substantially, and caused the overall 1 percentage point decrease in total efficiency.

Unfortunately, the large uncertainties in the Faraday probe measurements not only affected the ability to draw direct conclusions about three of the utilization efficiencies (mass, current, and divergence), but also the cost per beam ion, loss power, electron back-streaming current, and Isp parameters. In addition, there were concerns about CEX and differences in sheath size and hence effective collection area between the cathode configurations changing the overall and relative accuracy of the FP measurements. Moreover, even if more precise plume measurements were extracted from the FP data by taking a larger number of data points per data taking location along the sweep path to reduce the size of the error bars, the question of whether these measurements are indicative of the conditions at the thruster exit plane, where thrust is produced, would remain.

These issues are suspected to be the cause for the large gap in the magnitude of the total thruster efficiency calculated using the plume measurement probes as compared to using the thrust stand. In addition, since this measurement affects three of the utilization efficiencies used to calculate total thruster efficiency, it is all the more important that these measurements be accurate. Therefore, it is recommended that a non-invasive diagnostic be used to measure the ion current density profile, total ion current and beam divergence, and that these parameters be measured near the thruster exit plane upstream of the location where CEX would alter the current that produced thrust instead of using the Faraday probe.

In addition to providing more accurate thruster performance data and additional measurement details to determine if there are other factors at work affecting thruster efficiency that are not captured or accounted for with the measurements or calculations currently made, this would also help set the course that future EEDF control

research should take to further refine an approach to improving thruster efficiency. More accurate measurements would do this by allowing an investigation to target more of the elements of electron dynamics that go into bringing about increases in thruster efficiency. Therefore, if non-invasive diagnostics could also be used for measuring the other parameters that go into calculating thruster utilization efficiencies, so that these measurements could also be made close to where thrust is produced, this would be ideal.

In future research, it may also be advantageous to revisit the gas mixing scheme for HETs and look at low-power methods for creating and injecting beams of metastable neon or argon atoms directly into the channel in the ionization zone while using xenon or krypton as the main propellant. This would allow a more targeted way of increasing ionization using Penning ionization, and would avoid the issue of flooding the channel with neutral auxiliary gas in order to increase the number density of naturally occurring metastable atoms.

4.2 Summary of Application of New Analysis Techniques & Suggested Future Work

A new method for analyzing ExB probe data was developed that describes the entire trace, including the space between the peaks that represent the different charge species. In addition, the new approach is robust enough to be easily applied to various types of traces, including ones where distinct peaks are not immediately apparent for each charge state. This new method revealed that the part of the trace representing the singly charged xenon ion population is actually made up of two distinct distributions which were attributed to two separate ionization zones within the thruster. When the same method was applied to the RPA data, it also revealed a second peak, which could also be evidence of a second ionization zone upstream from

the main ionization region.

In addition, a binning technique was applied to the Faraday probe and Langmuir probe data as a preparatory step for analysis, which resulted in not having to use smoothing functions during the analysis. When derivatives of the LP trace needed to be taken during the analysis, it was found that increasing the bin size and making sure to have taken several hundreds of thousands of data points (which is not an issue when using state-of-the-art, high-speed diagnostic equipment) allowed for successful application of the binning method in these instances as well. It is recommended that analysis techniques that minimize the introduction of systematic bias and that make it more straightforward to propagate error through the analysis process continue to be instituted in analyzing data. This will streamline the techniques used so that detailed standard analysis procedures that are used across the field will develop naturally. This will allow easier comparison between experimental results from research investigations within the field.

Detailed reporting of experimental procedures and the analysis steps used as done here will also aid in this process. Being able to more easily compare thruster research results will facilitate in modeling efforts and in finding patterns between various thruster designs and their performance, which will only aid in the process of creating even more efficient thrusters.

4.3 Summary of EEDF Control Computational Results & Suggested Future Work

The MCHall simulations were carried out to investigate electron trajectories in the DC component of the thruster fields when using a reverse-orientation cathode compared to a centrally mounted one. The results from these simulations showed that even with a cathode pointing towards the channel, the bulk of the electrons

would still not arrive to the channel as the result of the static component of thruster conditions. The mechanism by which electrons from a centrally mounted cathode arrive at the channel is still not fully understood, and it is postulated that some sort of turbulent transport mechanism is allowing or causing it. Likewise, the reverse-flow cathode relies on the same or similar physics to get electrons to the channel. Given the fact that this new cathode position causes differences in thruster performance can perhaps provide more clues about what this mechanism is. This is another reason why determining the total ion current density more accurately in both cathode configurations is crucial, as it also reveals the electron backstreaming component which is tied to classical and anomalous electron cross-field transport (CFT). (See Section 1.9 for information and references on anomalous CFT.)

Given that fundamental aspects of thruster operation such as anomalous cross-field transport have not yet been understood, and the lack, therefore, of predictive thruster models, a significant aspect of implementing the proposed reverse-flow cathode EEDF control method needed to be guessed through exploration during the experiment itself— the exact downstream distance and angle for the cathode, which would at least demonstrate the potential of this method. The downstream location used was determined by taking thrust measurements at various positions. Due to the time consuming nature of this process and finite resources, this process was in no way carried out in an exhaustive manner. For one, there may have been a cathode angle and position that would have created a clear increase in thruster efficiency at the off-nominal 150 V condition as well.

Therefore, these experiments also further highlighted the need for a fully predictive HET performance model for bringing about significant increases in efficiency due to the time and cost involved in carrying out iterations through experiment. Until then, it is risky to try out drastic differences in thruster design. A fully predictive model would answer the question of why the downstream cathode position explored

did not increase thruster efficiency at 150 V when it did at 300 V. Perhaps there is a physical reason for this difference, having something to do with the nominal operating condition the thruster was designed for, or it may be another reason like facility conditions.

A predictive model would also take all aspects of the thruster's operation including turbulent transport into account at the same time making it easier to obtain holistic design solutions that would allow us to reach the next stage in Hall thruster improvement, and that would allow broad application of the results to multiple thruster designs, operating conditions, and sizes. Specifically, higher thruster efficiency and a deeper level of understanding of HET dynamics during operation could lead to being able to operate thrusters at higher current densities without increasing propellant throughput and without leading to increased channel erosion. This would mean the amount of available thrust for a given thruster size would increase, and the kg/kW for the thruster would decrease. The performance models that are used to evaluate thruster efficiency are from a DC evaluation standpoint. As there is evidence that there are AC components of the thruster's behavior that are contributing to steady state conditions, until those are accounted for and incorporated, the picture of the breakdown of thruster efficiency is incomplete.

In closing, it is not being suggested that a downstream cathode in the manner implemented here be used for flight thrusters. Even though the cathode was out of the main ion beam, placing the cathode downstream near the main beam causes visible erosion to the cathode even after short running times. The fact that thruster efficiency increased for the nominal operating condition by rearranging its configuration, without adding any new operating parts, increased discharge power, or complexity to the system shows that part of the inefficiency of the HET is due to the location of the cathode with respect to the channel. This means that perhaps something else can be done besides placing the cathode in front of the thruster to remedy this.

Computational research would allow the exploration of whether an EEDF control approach similar to the one used here but more practical for in-space application could be found. For example, with the introduction of the erosionless, magnetically shielded HET and the development of heaterless cathodes, perhaps it may be advantageous to work towards placing a ring of small cathodes around the inside edge of the thruster channel (or one cathode at some location around the inside edge of the thruster channel) at a location that would be downstream of where the Hall current forms, and angled upstream. This would most likely require a slight reshaping of the thruster channel and simulation iterations to determine adjustments to the magnetic fields shape to keep the walls erosionless with the new cathode location(s). Another possibility that these results may be alluding to is that perhaps there is a different channel geometry that would allow a centrally mounted cathode to be the most efficient cathode location.

APPENDICES

APPENDIX A

Initially Proposed Methods of EEDF Control

A.1 Proposed Neutral Gas Injection Method

A.1.1 Question and Hypothesis

As stated in the introduction of this thesis, the goal of this research is to find a way to increase Hall-effect thruster (HET) efficiency through electron energy distribution function (EEDF) control. As a first step in addressing this challenge, an experiment was conducted with a test cell plasma source to test a neutral gas injection EEDF control scheme. Neutral gas injection was chosen because the number density of neutral atom and the neutral-electron collision frequency have a direct relationship (i.e. $\nu_c \propto n_n$). In addition, the introduction of this gas can indirectly affect the two other variables that go into determining collision frequency, which are the speed of the electron relative to the neutral atoms, and the collision cross section, which is a function of electron energy. This experiment sought to determine whether a counterflow of neutral gas into the plume of a magnetically enhanced inductively coupled plasma (ICP) would alter the EEDF of the plasma source enough to significantly increase ion number density.

A.1.2 Experimental Setup and Diagnostics

An 11 cm long helical antenna, constructed with 3.175 mm (1/8 inch) diameter copper tubing, was wound around a 10 cm diameter Pyrex tube so that an inductively coupled plasma could be obtained when gas was run through the Pyrex tube. The helical antenna was water-cooled, and driven at 13.56 MHz and 500 W using an RF power supply. An L-type matching network was placed between the antenna and power supply and manually tuned so that there was zero reflected power during testing. At the input to the matching network, the load capacitor is in shunt to ground, and the inductor and tune capacitor are in series with the antenna at the output. Electromagnets were set up around the Pyrex tube and antenna to create an axial B-field with a peak intensity of 8 mT (80 G) at 49 A, in order to achieve a more dense, blue-core plasma. See Fig. A.1 for pictures of the experimental setup inside and outside of the chamber.

The exit plane of the jet tube, which had a 5.74 mm diameter and produced the backflow of neutral gas, was positioned 38 cm downstream of the ICP's exit plane. Argon gas was used for both the plasma source and the jet flow. The ICP had a flow rate of 500 sccm, and the flow rate for the neutral jet was 150 sccm. These experiments were conducted in the vacuum chamber called JLVTF that is described in Section 2.1. The base pressure during these experiments was on the order of 10^{-6} Torr. Pressure gauges were placed at the bottom of the chamber. The base pressure was obtained using an external ionization gauge, and the Pirani gauge portion of an MKS 979B multi-gauge was used to obtain pressure measurements when there was gas flow. See Fig. A.2 for schematics of the experimental setup inside and outside of the chamber and a list of some of the experimental parameters. The operating pressure with and without the neutral flow was around 3 mTorr. Through the ideal gas law, and using T = 300 K, this gives a background neutral density on the order of 10^{19} m^{-3}.

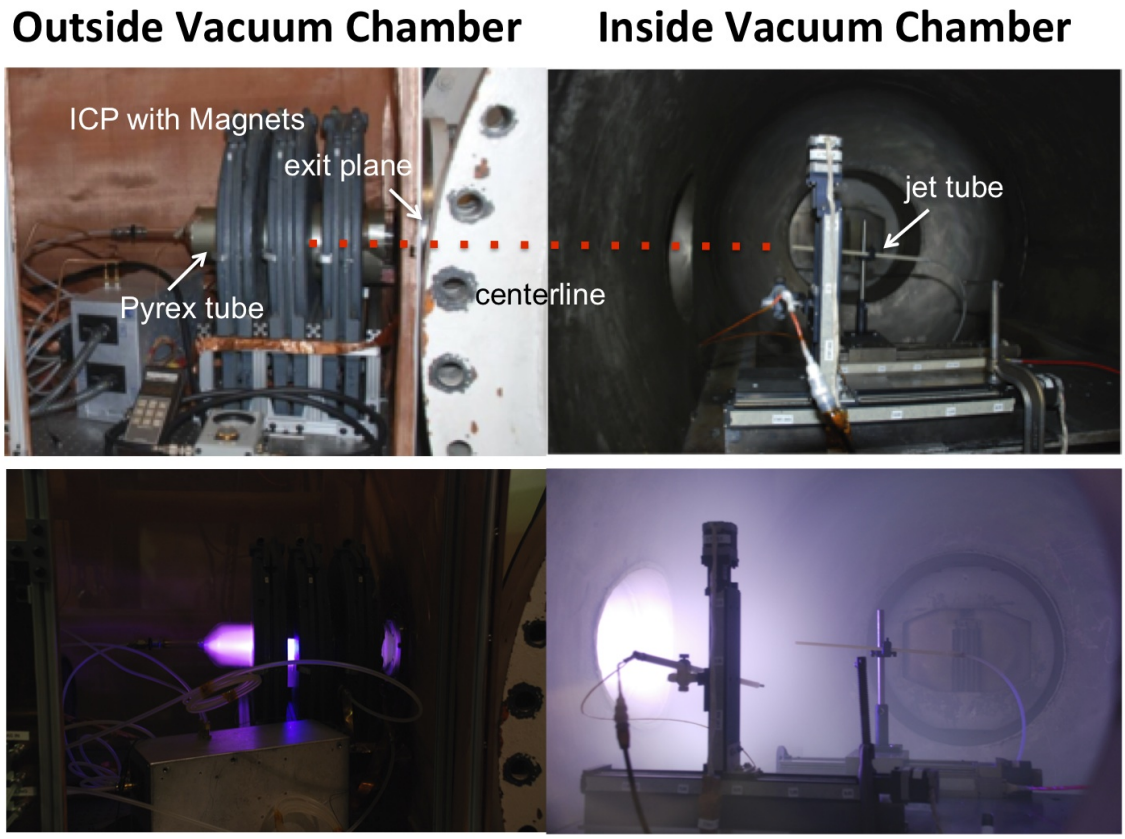

Figure A.1: Picture on the top left: A side view of the experimental setup outside the vacuum chamber showing the Pyrex tube, electromagnets, gas line, water cooling lines, and electrical equipment. Picture on the top right: The experimental setup inside the vacuum chamber showing the neutral gas jet tube, and the motion stages with the LP mounted on them. Pictures on the bottom: The experimental setup outside and inside the chamber during operation showing the Pyrex tube as plasma was generated on the left, and the plasma flowing from the tube into the vacuum chamber where the neutral flow was introduced and where measurements were taken on the right.

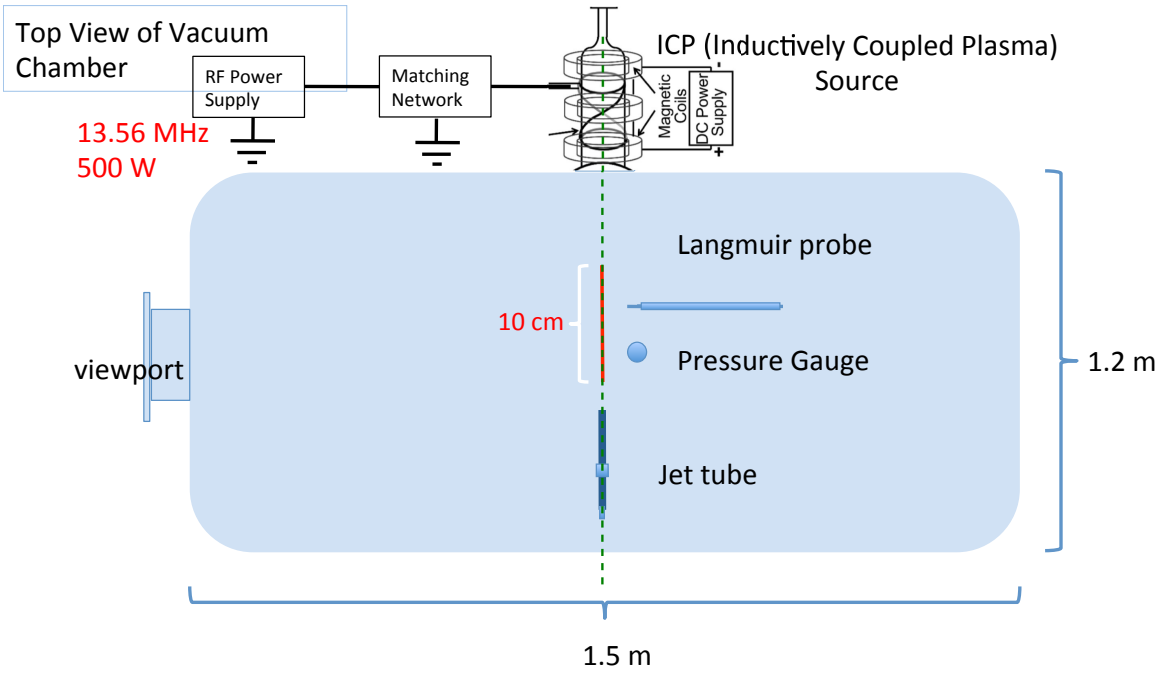

(a)

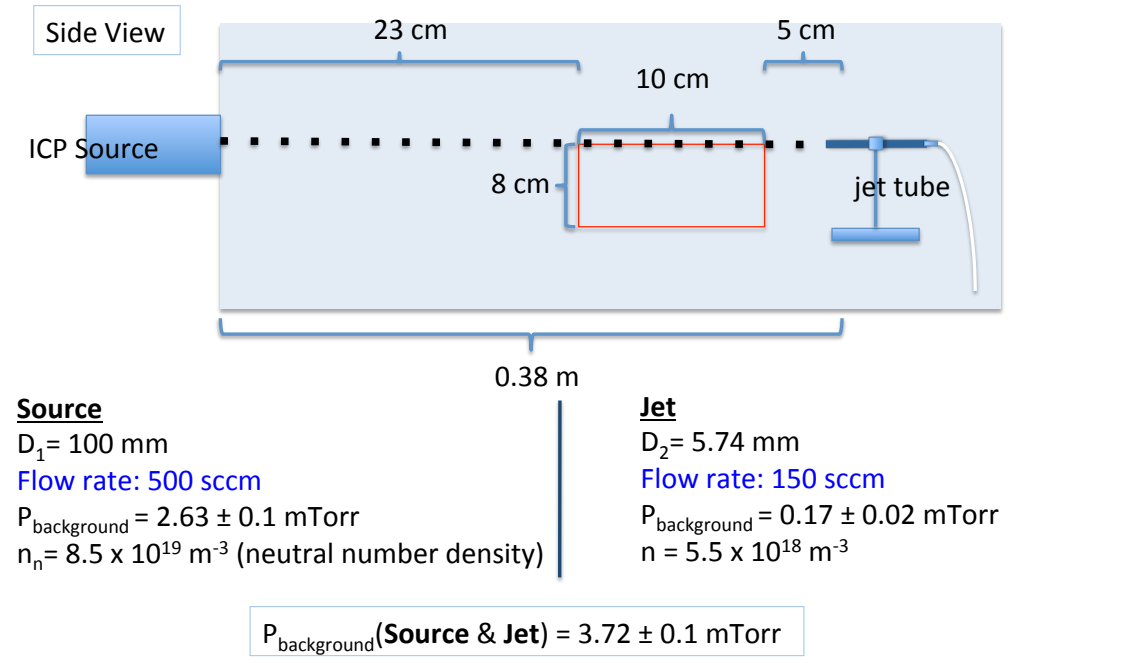

(b)

Figure A.2: Diagrams of the experimental setup pictured in Fig. A.1. (a) Top view of the experimental setup. Data was taken with the LP in an area within a plane parallel to the ICP's centerline that was 10 cm long and shown in red. (b) Side view of the experimental setup. The area where data was taken was 8 cm wide and 23 cm downstream from the ICP's exit plane.

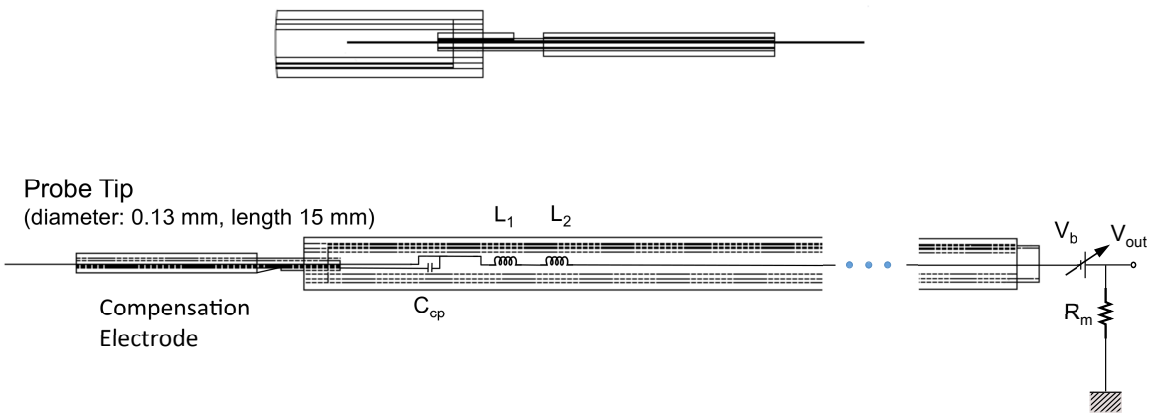

Figure A.3: A schematic showing the lab-built RF compensated LP pictured in Fig. A.4. The two inductors (called chokes) are labeled L_1 and L_2. The first harmonic of the plasma's AC fluctuations, which were collected by the probe tip and were further sampled by the compensation electrode were filtered out by these chokes, which have a resonant frequency of 13.56 MHz.

Measurements were obtained using a lab-built RF compensated Langmuir probe (LP) along with a Hiden LP controller. The tungsten probe tip was 0.13 mm in diameter and 15 mm in length to place the probe in the orbital motion limited (OML) regime for the plasma densities expected for this plasma source. Since some aspects of the Langmuir probe analysis presume the probe was operating within this regime, this assumption was verified at the end of the analysis using the plasma densities calculated, and this analysis procedure is detailed at the end of this subsection. The LP, shown in Fig. A.3, is a DC diagnostic meant to collect a steady current at each voltage that is applied to the tip. For this reason, the RF oscillations in the plasma would distort the resulting I-V trace. One way to deal with these fluctuations is to remove them from the signal, which was accomplished using a circuit incorporated into the probe. This circuit consisted of a compensation electrode, a capacitor and two inductors.

First, the probe was fit with an auxiliary electrode, which had a much larger total exposed surface area relative to the probe tip. This electrode was wound around the shaft of the probe as close to the tip as possible, and was capacitively coupled to the

probe's circuit. The capacitor was chosen so that it was large enough to be a short circuit to these fluctuations but small enough to be a broken wire to DC current so that the only DC signal being collected by the probe was through the probe tip. The purpose of the wound compensation electrode was to obtain a stronger sampling of the RF fluctuations than the probe tip itself could obtain in the region where the probe tip was collecting data. Then, the first harmonic of this AC component of the LP signal could be filtered out by two RF chokes with resonant frequencies of 13.56 MHz, which were placed after the capacitor and in series with the probe tip as seen in Fig. A.3. Two chokes were used instead of one to raise the impedance of the circuit even more, as recommended by Chen. [110, 112]

Similar to a Hiden designed RF compensated LP, only chokes for the fundamental frequency of 13.56 MHz were used, and not for the second harmonic of 27.12 MHz as well. [106] The chokes were followed by a coax cable which went to the electronics. Data taken with this lab-built probe connected to the Hiden LP controller show no distinguishable differences when compared to LP data taken with a Hiden RF compensated LP connected to the Hiden LP controller. See Fig. A.4 for pictures of the probe components and the completed probe. A representative set of LP trace obtained from this experiment is shown in Fig. A.5.

The EEDFs and other plasma parameters presented in the results subsection A.1.3 were obtained using the following steps to analyze the raw Langmuir probe data.

1. Twenty LP traces were obtained for each spatial location. The Hiden system produced traces that had the same voltage values across the voltage sweep range for all the traces taken, so for each location within the data taking area, an average trace was calculated by taking the average of the current values at each voltage data point. See Fig. A.5.
2. The resulting trace was smoothed using the MATLAB smooth function. See Fig. A.5.
3. The floating potential is where the electron and ion currents are equal. Therefore, it is the zero net current location on the I-V trace profile. [110]
4. Next, the ion current portion of the trace was subtracted from the rest of the I-V trace. This was done in the following way:

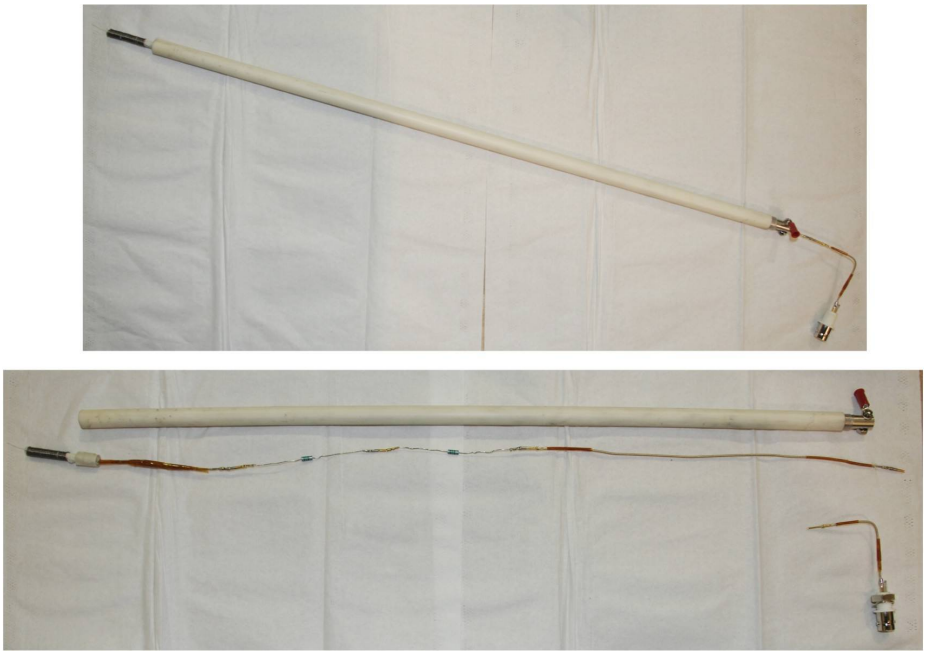

(a)

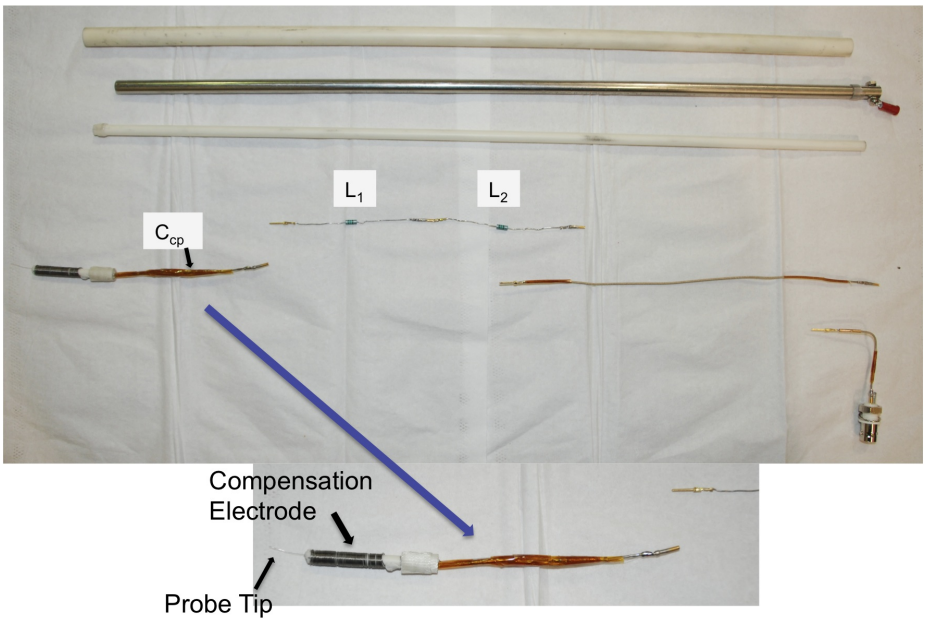

(b)

Figure A.**4:** Pictures showing the RF compensated Langmuir probe constructed using a metal support and shielding tube that was then mostly covered from the plasma using a second alumina tube. The schematic for this probe is in Fig. A.3. (a) Photograph of the completed LP (above) and the inner circuitry of the probe (below). (b) Picture showing all the components of the LP (above) and a close up of the compensation electrode near the tip of the probe (below).

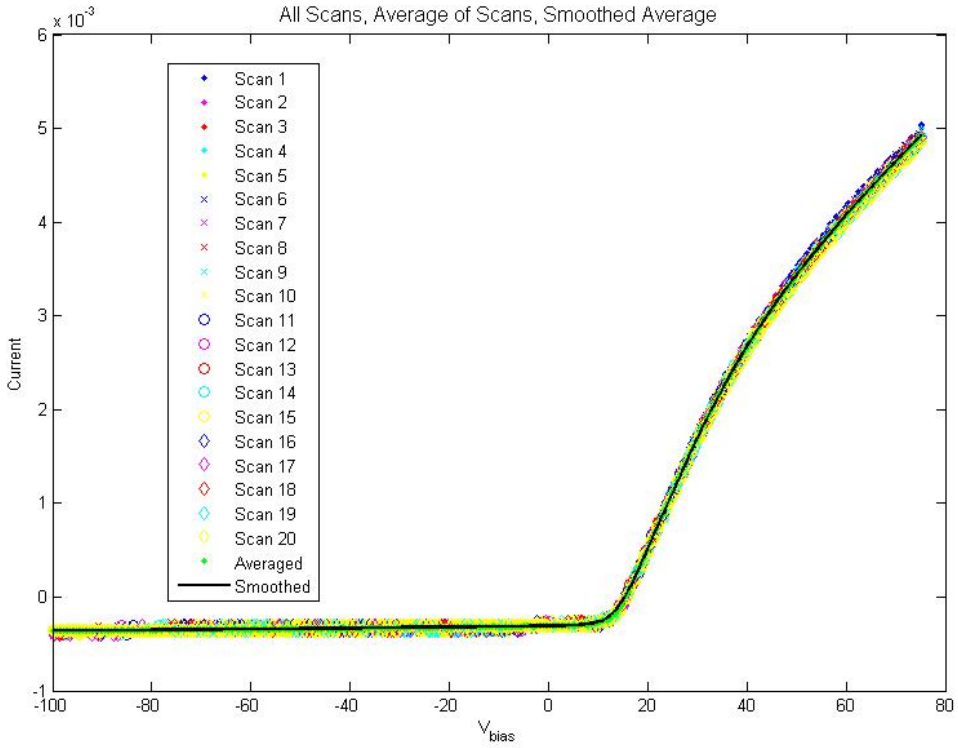

Figure A.5**:** A representative set of LP traces obtained at a single spatial location during this experiment. From the 20 traces, an average trace was calculated and then smoothed to be used for finding the plasma parameters presented in subsection A.1.3.

a. A straight line was fit to the square of the averaged and smoothed I-V trace in the ion saturation region well below the floating potential where the curve shows a linear trend. The ion number density was calculated using one of the parameters of this fit with the equation shown in Fig. A.6. [135]
b. Then, this line was extrapolated across the entire voltage range of the I-V trace.
c. Lastly, the square root of this fit was taken and subtracted from the averaged and smoothed I-V trace. The resulting trace represented the collected electron current. See Fig. A.6. [135]

5. To find the electron temperature, T_e, the logarithm of the electron current was found, and a straight line was fit to the portion of the electron retardation region that shows a linear trend, starting from the floating potential. See Fig. A.7(a). The electron temperature in eV is the inverse of the slope of the fit line. This process assumes the EEDF is Maxwellian. [110]
6. The first derivative of the electron current was taken using the average of the two derivatives around each point, and the resulting profile was smoothed using the MATLAB smooth function. See Fig. A.8.
7. The plasma potential was found as the peak (the first peak if there are two) in the smoothed first derivative trace. See Fig. A.8. [135] The first peak was used because the second peak is electron current associated with ion beams. [117]
8. The second derivative of the electron current was obtained by taking the derivative of the first derivative, using the average of the derivative on the two sides of each point. The resulting trace was smoothed using the MATLAB smooth function. See Fig. A.8.
9. The plasma potential can also be found as the first trough in the second derivative to make sure this matches up with the value found from the first derivative to verify that smoothing did not distort this aspect of the trace. See Fig. A.8.
10. The EEDF was calculated using the equation for $g_e(V_b)$ from the Druyvesteyn Method for interpreting LP data, which uses the second derivative of the I-V trace, and is shown in Fig. A.7(b).
11. The theoretical Maxwellian and Druyvesteyn EEDF shapes were determined using the electron temperature from the slope method discussed in step 5, the electron number density calculated by integrating the EEDF, and the plasma potential obtained from the first (and second) derivatives. Under the assumption of quasi-neutrality, which is applicable to this plasma source, electron and ion number densities are equal [133]; therefore, the ion number density calculated in step 4a. should be close in value to the electron number density obtained from the EEDF.
12. The EEDF curves were normalized by summing over the entire function and dividing by this value to make the area under the curve equal to one.
13. The EEPF was determined by multiplying the EEDF by $1/\sqrt{V_s - V_b}$ and then plotting this expression with the y-axis on a logarithm scale. In this form, a Maxwellian distribution is a straight line. [111] See Fig. A.9(a).

14. Lastly, the conditions for the probe having taken measurements in the OML regime are verified using the plasma parameters calculated using this analysis procedure to make sure that the portion of these calculations that came from OML theory (namely the equation for the ion number density in step 4a.) is valid for the combination of this plasma source and the probe size used. The three conditions that must be satisfied are the following:
    a. ($r_p < 3\ \lambda_D$) The probe radius was less than three times the Debye length, where the Debye length is calculated using the electron temperature from step 5 and the ion number density from step 4a. [136]
    b. ($\lambda_{MFP} > 100\ \delta$) The sheath was collisionless. Electrons that enter the sheath were collected by the probe without collisions, which means the mean free path was much larger than the sheath thickness [111, 136] (by say at least 2 orders of magnitude). The sheath thickness was estimated to be about 5 times the Debye length, which was a valid assumption for this plasma source, as seen when calculating sheath thickness in terms of the Debye length, argon ion mass, and electron mass using equation 3.2.25 from [137]. The mean free path was calculated using the neutral number densities shown in Fig. A.2(b) and the elastic neutral-electron collision cross section for Argon gas and 4 eV electrons from [7] p. 51 Figure 4-3 since this is the dominant collision process for this gas. This implies that the mean free path for all other particle collision combinations in this plasma source were larger than this value. Therefore, if this mean free path satisfies this condition, then all the others (including ion-atom, electron-ion, and inelastic electron-atom collisions) do as well.
    c. ($l_p > 100\ \lambda_D$) The probe tip length was much larger than the Debye length (by say at least 1 - 2 orders of magnitude) so that one can assume the probe tip was an infinite cylinder in OML calculations. [111]

LP data was collected in an 8 cm $\times$ 10 cm radial cross-section of the plasma source with a 1 cm resolution beginning 23 cm downstream of the ICP's exit plane. These details are shown in Fig. A.2.

A.1.3 Results, Analysis and Conclusion

As seen from Fig. A.8, in the first derivative of the LP I-V trace, the transition between the electron retardation region and electron saturation region usually contained two peaks. The second peak is evidence of ion reflection (ion beams). [117] Therefore, when the first peak was taken to be the plasma potential, and the electron number density obtained from the resulting EEDF was comparable to the ion number density

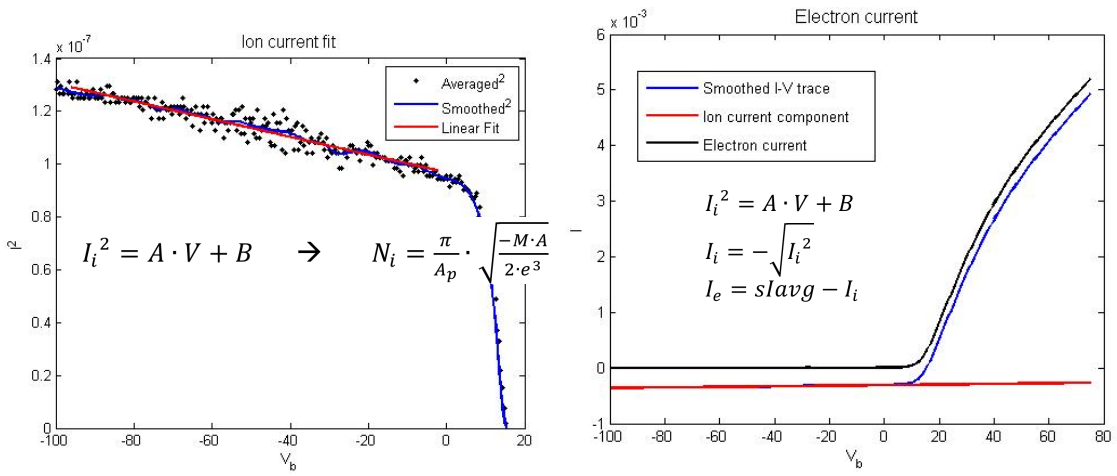

Figure A.**6:** To obtain the ion number density and to subtract the ion current portion from the Langmuir probe trace, first a straight line was fit to the square of the averaged and smoothed I-V profile in the ion saturation region well below the floating potential where the curve shows a linear trend. The ion number density was calculated from the slope of this fit using the equation shown on the left in this figure. In this equation, A_p is the probe area in m^2, M is the mass of an argon ion in kg, and A is the slope parameter in the current-squared fit. The figure on the right shows how the ion current portion of the trace was subtracted, leaving the electron current I-V trace. These portions of the analysis including the equations are from Ref. [135]

calculated in step 4a. (which is expected given the assumption of quasi-neutrality for this plasma source [133]), it showed that this interpretation of the two peaks did not contradict other assumptions made about the plasma source.

The shape of the EEDFs calculated from the LP traces compare well to the literature. For instance, Godyak et al. conducted experiments with an inductively coupled argon discharge using a 13.56 MHz driving frequency and various powers up to 200 W. The plasma densities that were obtained were on the order of 10^{16} m^{-3} for operating pressures of ∼1 mTorr. [140] In addition, Ramamurthi et al. carried out simulations for this scenario using a one-dimensional model containing an EEDF module. [139] As seen from Fig. A.9, both experimental and computational electron energy probability functions (EEPFs) depart from a Maxwellian distribution in similar ways. Most notably, there is dearth of low energy electrons. The primary reason for this lack of thermodynamic equilibrium is the lower electron–electron collision rate in these

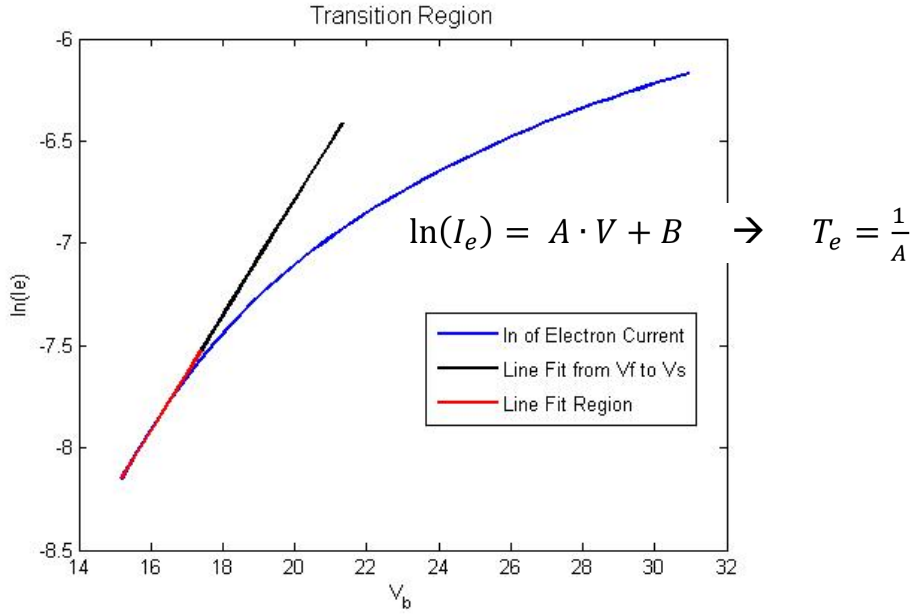

(a)

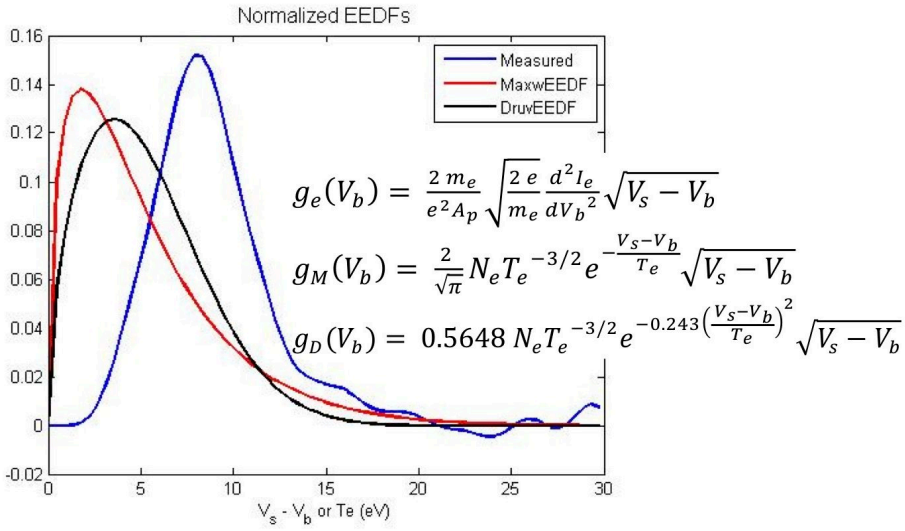

(b)

Figure A.7: (a) This graph shows how the electron temperature was determined from the slope of the logarithm of the electron current. See step 5. (b) This graph shows how the EEDFs were calculated. In the equations, $g_e(V_b)$, $g_M(V_b)$, and $g_D(V_b)$ are the calculated, Maxwellian and Druyvesteyn EEDFs respectively. A_p is the probe area in m^2, m_e is the electron mass in kg, V_s is the plasma potential in V, and V_b is the probe bias voltage in V. These equations are from Refs. [111] & [138]. See steps 10 & 11 for more details.

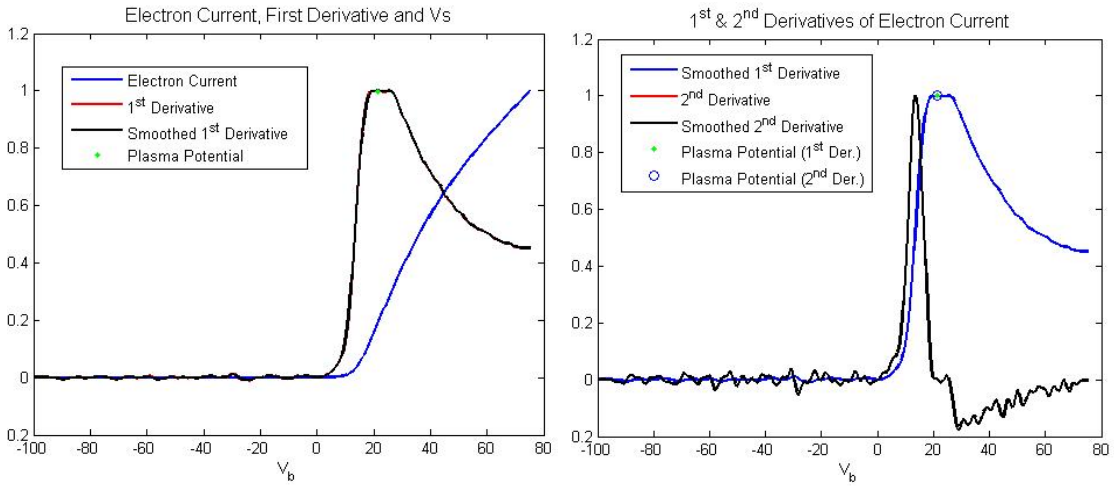

Figure A.8: These plots show representative, scaled, first and second derivatives from the data acquired, and the plasma potentials obtained from them. See steps 6 - 9 for the details of how these values are calculated.

Table A.1: A Comparison of the Range and Average Values for Various Plasma Properties between the Two Test Scenarios

Plasma Parameter	Type	ICP Source Characterization	ICP Source + Neutral Flow
Floating Potential (V)	Range	15.1940 – 18.2600*	15.1940 – 18.2600*
	Average	16.7558*	16.7912*
Plasma Potential (V)	Range	15.6320 – 23.0780*	17.3840 – 22.6400*
	Average	19.4236*	20.1536*
Ion Number Density (x$10^{16} m^{-3}$)	Range	2.0058 – 3.0684*	2.2950 – 3.2458*
	Average	2.4656*	2.7552*
Electron Temperature (eV)	Range	3.0287 – 7.9564*	3.2767 – 6.1904*
	Average	5.1047*	4.4847*

Note: These numbers are calculated from Langmuir probe measurements and represent raw values, not the number of significant digits.

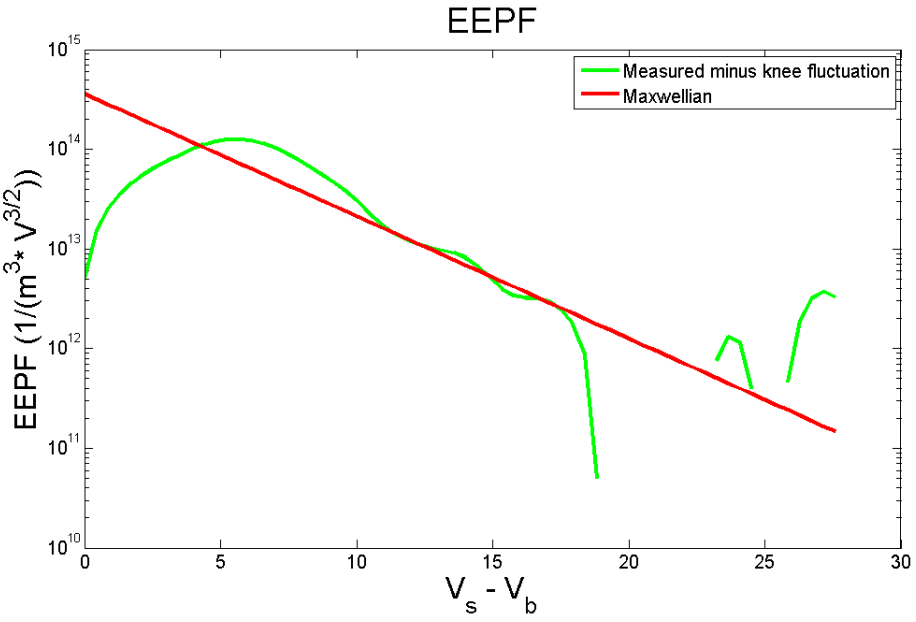

(a)

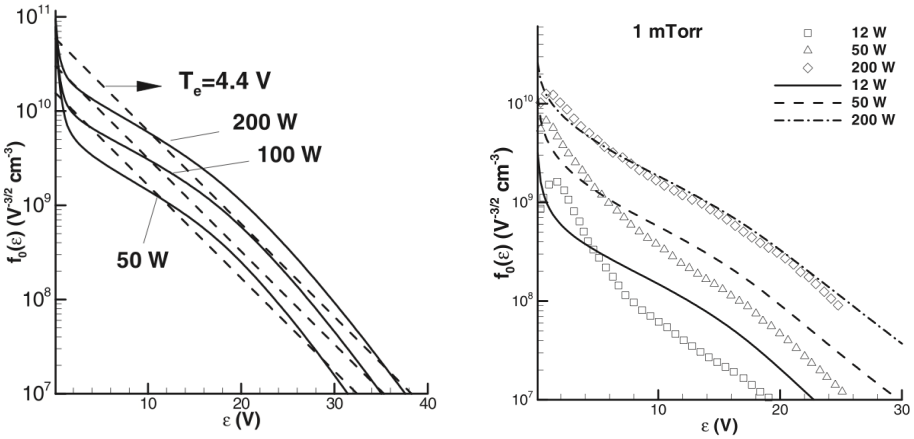

(b)

Figure A.**9:** (a) The EEPF 28 cm downstream from the exit plane of the ICP source in this study (without neutral jet flow, green line) compared to a Maxwellian distribution at the electron temperature and electron number density of the plasma source at that location (red line). This trace is representative of the overall shape of the EEPFs calculated for all the data obtained in this experiment. (b) Figure on the Left: Data from Ref. [139] showing a comparison between Ramamurthi's simulated EEPFs (solid lines) and Maxwellian EEPFs (dashed lines) as a function of total energy for 1 mTorr. Figure on the Right: Graph from Ref. [139] showing a comparison between Godyak's experimental EEPF data (symbols), from Ref. [140], and Ramamurthi's simulated data (lines, dashed and solid) of Godyak's experimental system in Ref. [140]. Ramamurthi's data is the same data shown here in part (b) on the left.

low-pressure plasmas. [141]

When comparing the data in A.9(a) & A.9(b), it can be seen that the EEPFs from this experiment deviate from their Maxwellian counterparts in the low energy range in a similar way to those in Godyak and Ramamurthi's experiment. This provides confidence in the EEDF data obtained and the conclusions that can be drawn about the introduction of a counterflow of neutral gas as a potential EEDF tailoring method when comparing the EEDFs of the control and test scenarios.

As seen in the electron energy probability function (EEPF) comparison, the shape of the EEDFs for this plasma source do not fit standard Maxwellian distributions, and they also do not have the shape of a Druyvesteyn distribution (Fig. A.10), which is $\propto e^{(voltage)^2}$. These EEDFs are more likely drifting Maxwellian distributions where the drifting energy is superimposed on the isotropic electron energy, requiring further analysis or measurements to verify the Maxwellian electron energy values and to distinguish the drifting energy component. [117]

The other plasma parameters obtained from the LP data are shown in tabular form in Table A.1. Over the data collection area, the range and average values of the floating and plasma potentials were very similar between the two cases. In addition, the average ion number density was slightly higher for the case with neutral flow and the average electron temperature was slightly lower. This result implies that the electron-neutral impact ionization collision frequency increased from the increase in neutral gas density and these additional inelastic collisions decreased the electron temperature.

While both of these parameters in the scenario when using the neutral jet had a $\sim$10% difference from the control case, the portion of this difference that is above the relative error between measurements for these values is not significant enough to create a substantial increase in HET efficiency if applied to a Hall thruster. This relative error, as opposed to the absolute error of LP measurements that comes from Langmuir

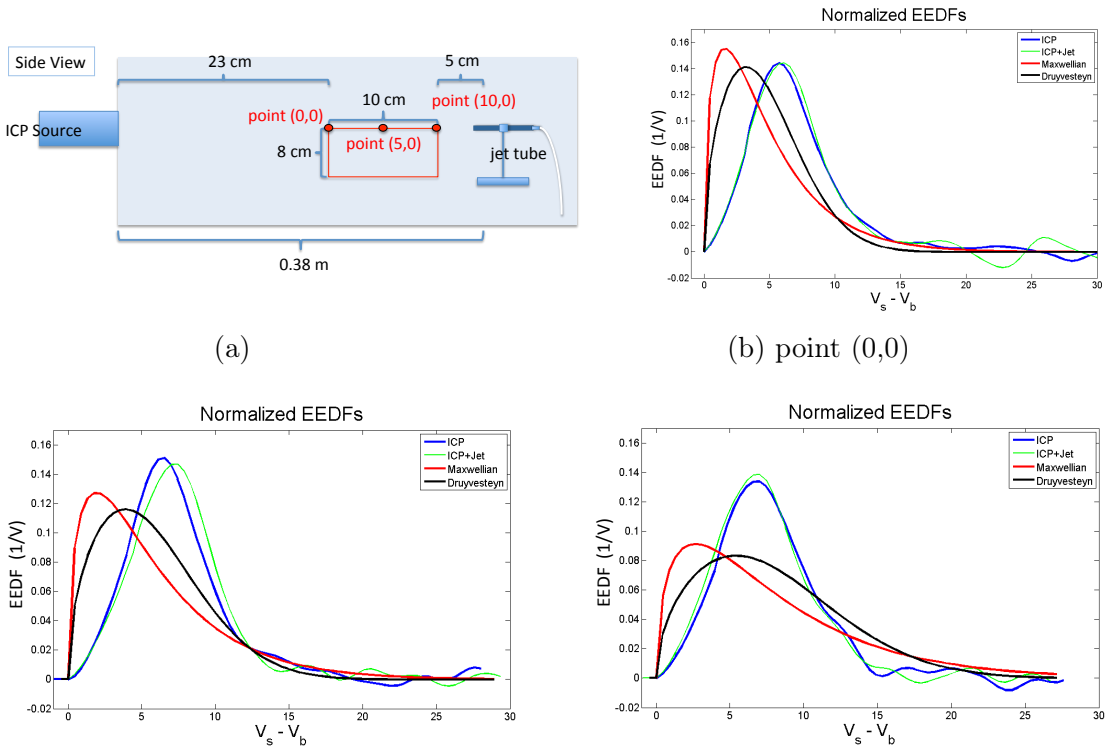

(a)

(b) point (0,0)

(c) point (5,0)

(d) point (10,0)

Figure A.10: (a) Diagram showing where the LP data for the EEDFs in (b) - (d) in this figure were taken. The charts shown in (b) - (d) all compare the EEDFs of i. the ICP source without neutral gas injection (labeled ICP and represented by a blue line), ii. the ICP source with neutral gas injection (labeled ICP+Jet and represented by a light green line), iii. a standard Maxwellian distribution at the average T_e and N_e between the two test cases at that location (labeled Maxwellian and represented by a red line), and iv. a standard Druyvesteyn distribution at the average T_e and N_e between the two test cases at that location (labeled Druyvesteyn and represented by a black line).

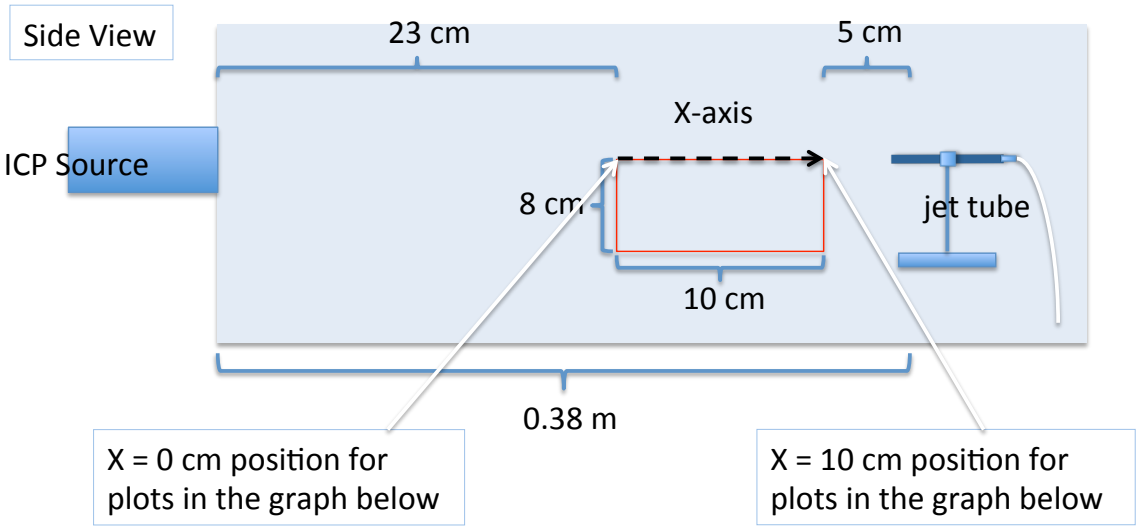

(a)

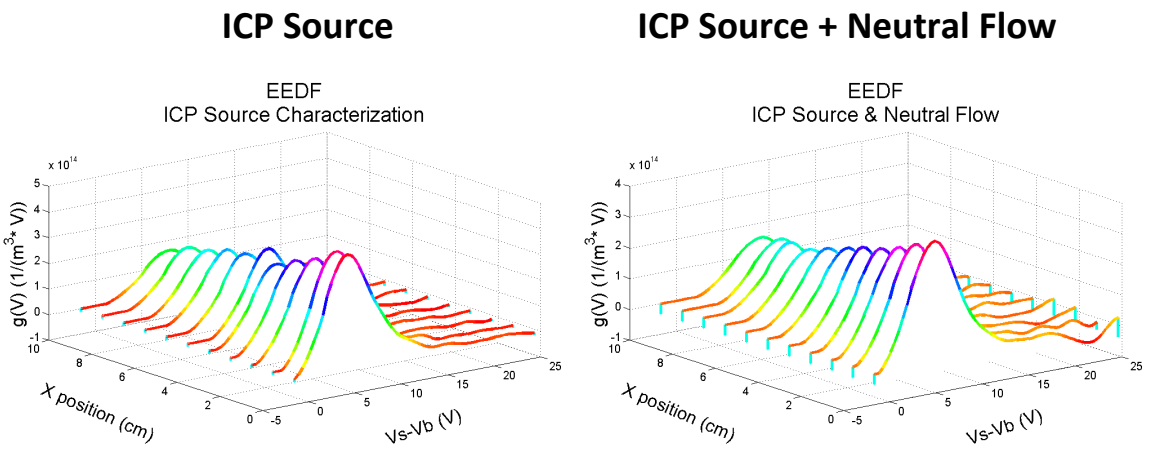

(b)

Figure A.11: (a) A diagram showing where the LP data for the EEDFs in (b) were taken. (b) The EEDFs in these plots were not normalized so that the relative number densities at each x-position in addition to changes in the shape of the distribution function along the centerline can be seen. This is because $g_e(V_b)$ has units of $1/(\mathrm{m}^3{*}\mathrm{V})$; therefore, the total area under these curves gives the number density.

probe theory, is due to a combination of uncertainties from values such as the various components of the Langmuir probe measurement system (i.e., the measured probe tip length, the measured shunt resistance, and the voltage measurement device error), and from error inherent in the various graphical extrapolation methods used to obtain the plasma parameters from the LP trace in this data analysis. [106, 142]

Similarly, the introduction of this flow did not change the shape of the EEDF for the various spatial points in the data collection area, as seen from Figs. A.10 & A.11. Any differences seen are within the resolution/error of the measurement and analysis techniques. Since control over the EEDF was sought in order to develop effective methods to increase HET efficiency, these results led to the idea that the ability to adjust the population of a narrow energy range of electrons was needed. Therefore, the next EEDF control method that was investigated sought to control the ionization process through EEDF tailoring by using atoms that contained electrons in excited states with enough energy to ionize xenon atoms.

A.2 Proposed Gas Mixing Method

The goal of this dissertation research was to develop an easily implementable method for improving Hall-effect thruster (HET) efficiency through electron energy distribution function (EEDF) control, specifically targeting beam ion production efficiency by minimizing effective ionization cost per beam ion. After exploring a neutral gas injection scheme, discussed in Section A.1, the results led to proposing an inert gas mixing method for tuning the number density of the bulk and tail electron energy populations towards the dissertation objective. In other low temperature plasmas (LTPs), inert gas mixing has been shown to be an effective method for altering the electron temperature and number density. [120] In addition, simulations have predicted that when one of these gases is a small percentage of the mixture, its naturally present, small fraction of metastable states have a greater effect on the plasma; and the

superelastic collisions that ensue create plateaus, holes and peaks in the EEDF. [143]

With inert gas mixing in an HET, both gases would be introduced through the anode gas flow line, and in the case of the initial experiment described in the succeeding subsection, both gases were fed through the cathode flow line. The purpose of the cathode experiment was to try out running a plasma source with a gas mixture, and to obtain EEDFs from LP measurements to determine what general techniques would be needed for the purpose of verifying EEDF control.

A.2.1 Cathode Experiment

A.2.1.1 Experimental Setup

This gas-mixing experiment was carried out in the Cathode Test Facility (CTF), which is described in Section 2.2. The chamber's base pressure was 1×10^{-7} Torr for these tests.

A lab-built lanthanum hexaboride (LaB_6) cathode, developed at PEPL for carrying out various preliminary experiments to study electron dynamics in Hall-effect thrusters, and which is discussed in detail in Section 2.5, was used as the plasma source in this test bed, gas-mixing experiment. The hollow cathode is the main source of electrons for the thruster, and can be operated with a smaller scale production and a shorter turn-around time. Therefore, a cathode serves as a good platform for examining the experimental methodology of various electron dynamics studies for HETs, and for obtaining preliminary results. The cathode was run in triode configuration with an external annular anode, mimicking a conventional Hall thruster, but without anode flow. This configuration draws the plasma outside of the cathode and creates a more stable plume. See Fig. A.12 for a picture of the cathode running in triode mode, and see Fig. A.13 for a schematic and picture of the experimental setup.

Table A.2 shows the cathode's operating conditions for the two cases investigated in the analysis. Argon gas was used as the main propellant, and nitrogen as the

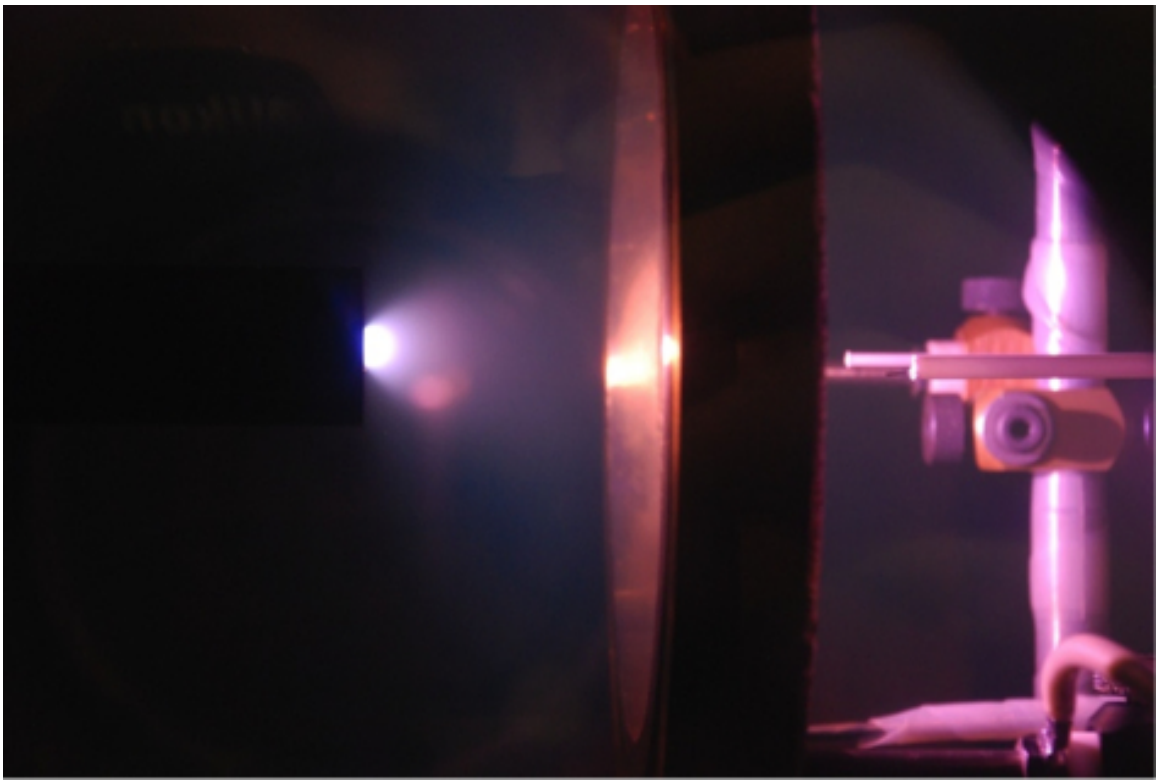

Figure A.12: This figure shows the cathode plume in triode mode. The plasma fans out towards the edges of the anode and is noticeably brighter in this mode. The Langmuir probes and the anode's support structure are seen on the far right in this photo.

Table A.2: Cathode Operating Conditions for the Gas Mixing Experiment

	100% Argon	99% Argon, 1% Nitrogen
Chamber base pressure (Torr)	1×10^{-7}	1×10^{-7}
Flow rate (sccm)	25.0 ± 0.3	24.7 ± 0.2, 0.30 ± 0.03
Anode voltage (V)	32	32
Anode current (A)	4.97	3
Keeper voltage (V)	32	36.3
Keeper current (A)	6	6
Heater voltage (V)	3.47	16.34
Heater current (A)	0.59	2.49

Comparable operating conditions were obtained for the case with and the case without nitrogen gas mixing. The anode voltage and keeper current were set values. The cathode was allowed to establish the anode current and keeper voltage difference needed to maintain the discharge due to the different gas flow compositions in the two cases.

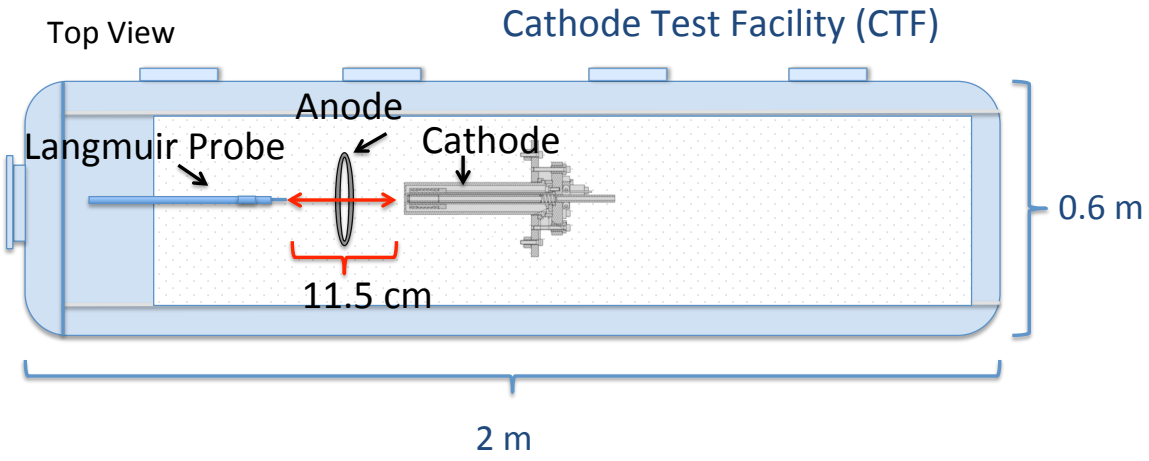

(a)

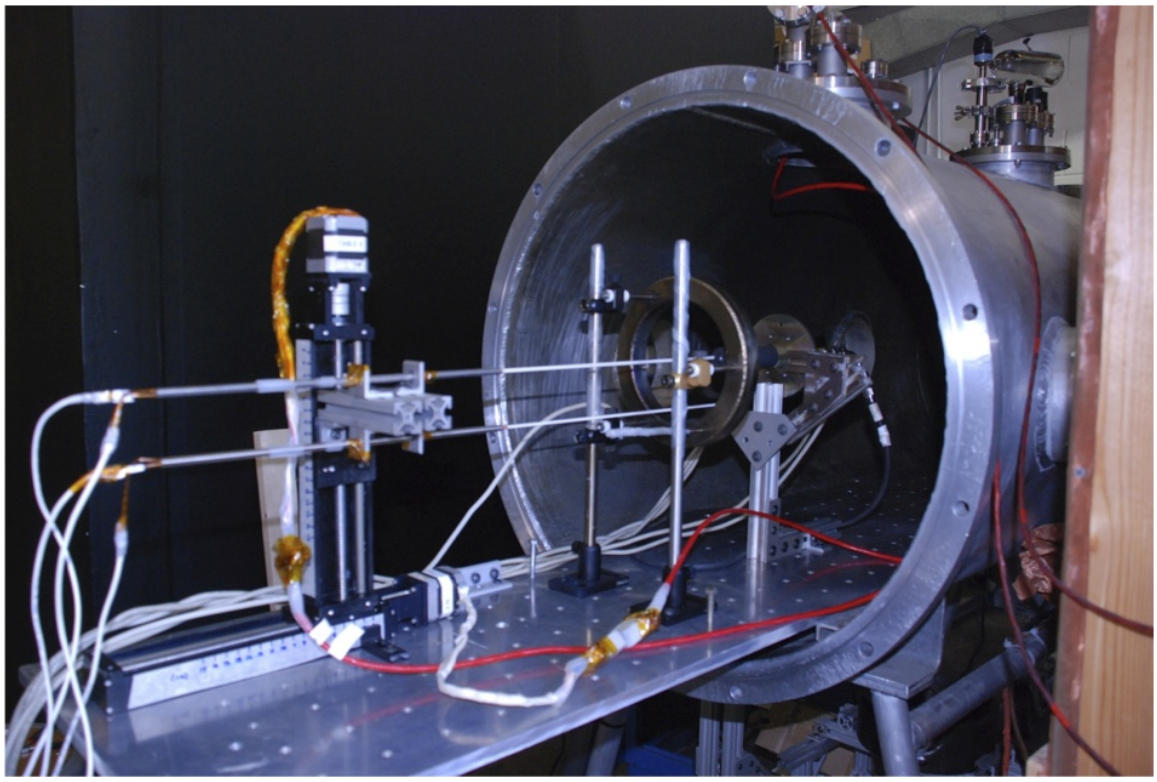

(b)

Figure A.13: (a) This schematic shows how the cathode, anode and LP were oriented in CTF for the gas-mixing tests. (b) A picture of the test cell experimental setup drawn in part (a)

auxiliary gas so the results could be compared to those of the experiment carried out in Ref. [120]. In order for the cathode to maintain steady operation, the current the anode drew and the potential difference that was established between the keeper and cathode were slightly different in the two cases. These differences can be attributed to the different gas compositions, which affected the plasma parameters as well. This will be seen in the Langmuir probe analysis. Unit Flow Controllers (UFCs) from the 7300 series were used to establish and maintain the argon and nitrogen gas flows. The error bars for the gas flow shown in the table were calculated using the specification sheets for these controllers. For both the control and the gas-mixing cases studied in this initial test, the total flow rate was 25 sccm, the keeper current was limited to 6 A and anode voltage was set to 32 V.

The cathode's heater was also used to help maintain the operating condition during the tests. A higher heater current was needed to maintain the plasma discharge in the case with nitrogen gas mixing. In order to understand why this is the case, it is first important to note that the ionization threshold energy of N_2 is around 15.6 eV, which is comparable to that of argon at 15.78 eV. In addition, the dissociation energy of molecular nitrogen is only a few eV in a low-pressure plasma in the presence of argon gas, and the ionization threshold energy of atomic nitrogen (N) is less than that of argon at around 13 eV. The reason why diatomic gases, such as nitrogen, require more power to produce a plasma is to make up for the many inelastic energy loss processes that occur for molecular gasses such as vibrational and rotational excitation. [121, 144, 145] Still, when adding up the total power the cathode received from the power to the anode, keeper, and heater for the two cases, the difference is about 1.5 W—$\sim$353 W for the control case and $\sim$354.5 W for the gas mixing case, which is only a 0.4% increase from the control case.

A lab-built, high-speed dual Langmuir probe (HDLP) system, which is described in Section 2.10, was used to obtain measurements of electron density, electron tem-

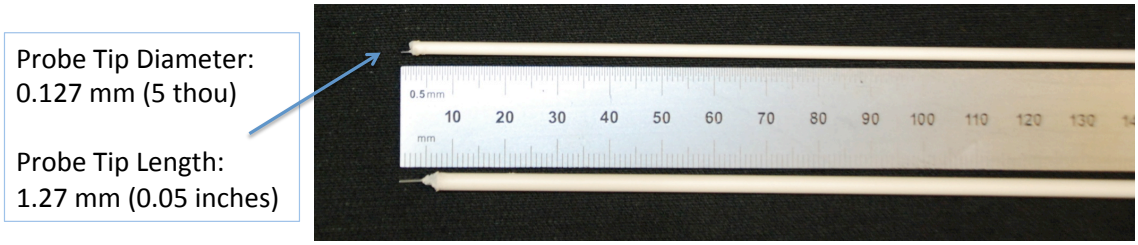

Figure A.14: The upper Langmuir probe in this photograph was used in this experiment.

perature, plasma potential, and the EEDF. For this experiment, a sweep rate of 15 kHz along with a data acquisition (DAQ) system with a 1 MHz maximum sampling rate were used. A picture of a close up of the probe is shown in Fig. A.14 and the probe as part of the experimental setup is shown in Fig. A.13. LP data was obtained on cathode centerline 11.5 cm downstream from its exit plane (Fig. A.13(a)). The LP used for these experiments had a 0.127 mm probe tip diameter and a probe tip length of 1.27 mm (Fig. A.14).

A.2.1.2 Analysis Method, Results and Comparison to the Literature

The bottom row of graphs in Fig. A.15 shows the 25 LP traces taken from the first 25 negative-sloping sides ($dV/dt < 0$) of the triangle waveform used to obtain the traces for the two test cases. These current-voltage (I-V) characteristics were then combined and the resultant trace for each case is shown as the black line in the top row of plots. The smoothed version of this trace, which was used for the analysis, is the red line in these same plots. The traces were combined by making use of the fact that the 1 MHz sampling rate is not evenly divisible by the 15 kHz triangle wave used to obtain the Langmuir probe characteristics, and the analog nature of the function generator used to create the voltage sweeps. This caused the set of voltage values from one sweep cycle to the next to be staggered. Combining 25 of these traces resulted in an effective voltage resolution of about 0.08 V for both cases.

This resolution allowed more precise EEDFs to be obtained in the analysis than

what would have resulted with just one of these traces. This is due to the fact that the dominant frequencies of a cathode discharge are much higher than those of an HET (from 40 kHz to 2 MHz for cathodes vs. around 10-30 kHz for HETs) [146–149], so at a 15 kHz sweep rate, the plasma oscillation frequencies caused these traces to not be time-resolved for this plasma source. Since the sweep rate was slower than the oscillations, the fluctuations affected the collected current of the I-V trace, making analysis more challenging before enough traces were combined to have a sufficient number of data points to be able to average or to smooth out these oscillations. Some of the data points in the combined trace had the same voltage value to the 4th digit after the decimal place. For these point pairs, the average of the current values (the dependent variable) was used in their place.

As also seen in Fig. A.15, the LP traces from the plasma with nitrogen contained a considerable amount of additional noise. This noise may in part be due to the additional inelastic processes that are present for diatomic gases, which begin at a low threshold energy of 0.02 eV and result in vibrational and rotational excitation of the nitrogen molecules. [143] However, the process of combining multiple traces and smoothing the resulting trace produced an LP I-V characteristic that was easily analyzable for this case as well. The LP analysis that was used followed the steps outlined in subsection A.1.2 starting with step 2, and skipping over the ion number density calculation in step 4a., and therefore also step 14, since an OML specific equation was not used in the analysis. The electron number density was calculated by integrating the EEDF as explained in step 11, and is assumed to be equal to ion number density through quasi-neutrality. [133, 134]

The results showed that when 1% of the total gas flow was substituted with nitrogen, there was a ∼10% increase in electron temperature from 3.2 eV to 3.6 eV along with an increase in plasma potential from 46 V to 48 V. In addition, the number density decreased by ∼60% from 5×10^{17} m^{-3}, with a pure argon plasma, to 2.2×10^{17}

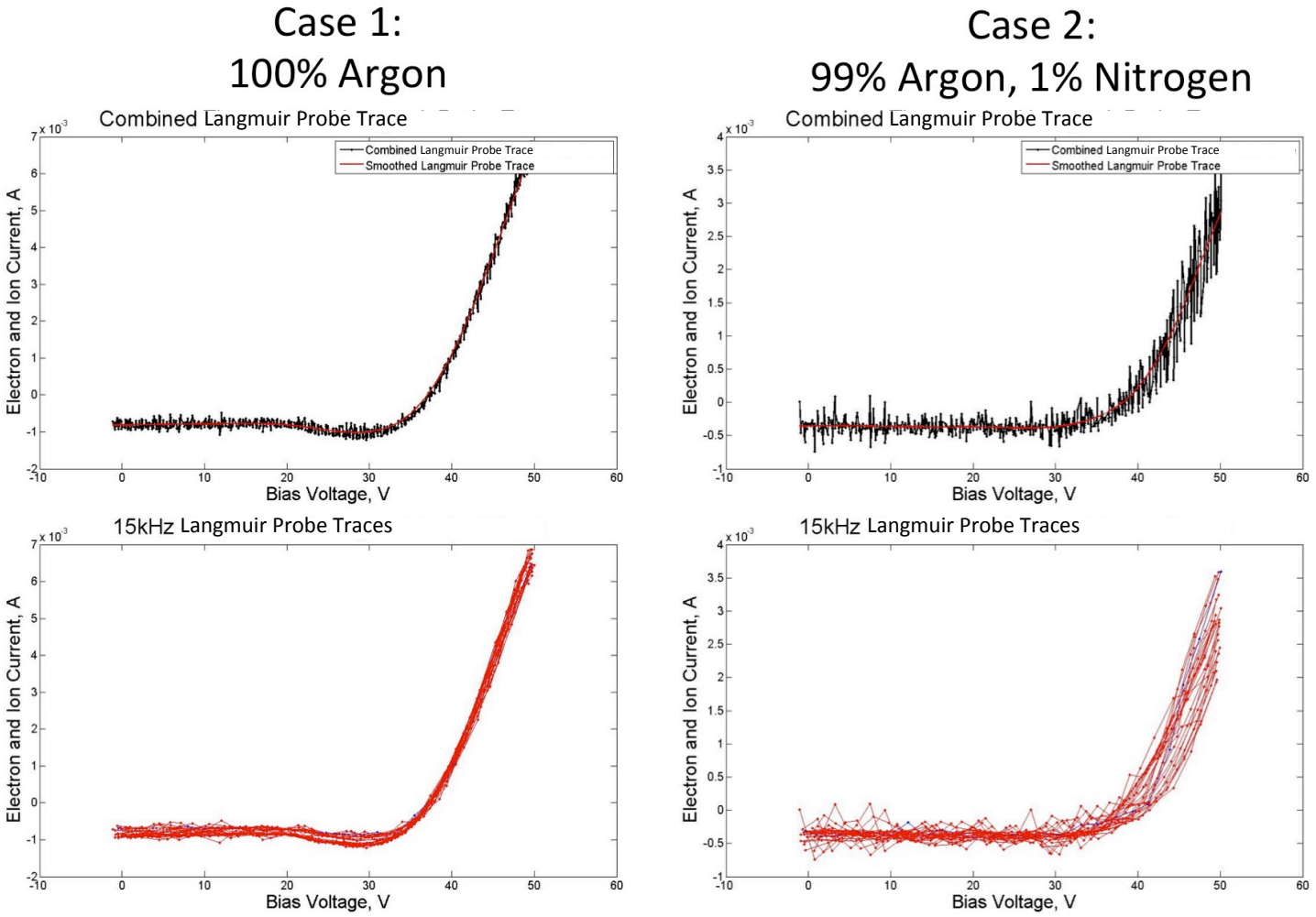

Figure A.15: The plots on the second row of this figure show the first 25 15-kHz Langmuir probe traces taken from the negative-sloping sides ($dV/dt < 0$) of the sweep for the control and the gas-mixing cases. In the top row, the black line in these plots shows the LP characteristic that results from combining these 25 traces. The red line is the smoothed version of this trace, which is what was used in the analysis.

Table A.3: Gas Mixing Plasma Parameter Results

	100% Argon	99% Argon, 1% Nitrogen
Floating Potential V_f (V)	37.0161*	38.0959*
Electron Temperature T_e (eV)	3.1928*	3.5526*
Plasma Potential V_s (V)	46.1882*	48.2535*
Number Density N_e (m^{-3})	4.9597x10^{17}*	2.1912x10^{17}*

Note: These numbers are the raw calculated values, not the number of significant digits. These values are still subject to the same error bars that are generally associated with plasma parameters calculated from Langmuir probe data. [151]
Various calculated plasma parameters for the cases with and without nitrogen gas are shown in this table. The electron temperatures were calculated by taking the inverse slope of the natural log of the electron current portion of the I-V trace. This standard way of calculating T_e assumes a Maxwellian electron energy distribution.

m^{-3} (Table A.3). This is consistent with experimental results in the literature. Bai et al. used an inductively coupled plasma (ICP) and took measurements 16 cm downstream with an RF-compensated LP. They found that when the gas composition was changed from pure argon to 83.3% Ar and 16.7% N_2, the electron number density, N_e, decreased from 4.0×10^{16} m^{-3} to 2.0×10^{16} m^{-3} and the electron temperature remained relatively unchanged at 2.8 eV. [150] (The different trend in T_e may be due to the difference in the way this parameter was calculated.) In tests carried out by Pu et al. where argon also made up 83.3% of an Ar-N_2 ICP plasma, they also saw a decrease in N_e from 2.7×10^{17} m^{-3}, with a pure argon plasma, to 1.7×10^{17} m^{-3}, and an increase in T_e from 3.4 eV to 3.8 eV. [120]

In this experiment, for the case with 1% nitrogen mixing, the EEDF contained more distinct plateaus and peaks. Fig. A.16 shows the EEDFs in normalized form. From this graph, it can be seen that there are relatively more low energy electrons and less intermediate energy electrons for the gas mixing case as compared to the pure argon case. This may be due to the additional inelastic processes that lead to vibrational and rotational excitation of nitrogen molecules, which decreases the

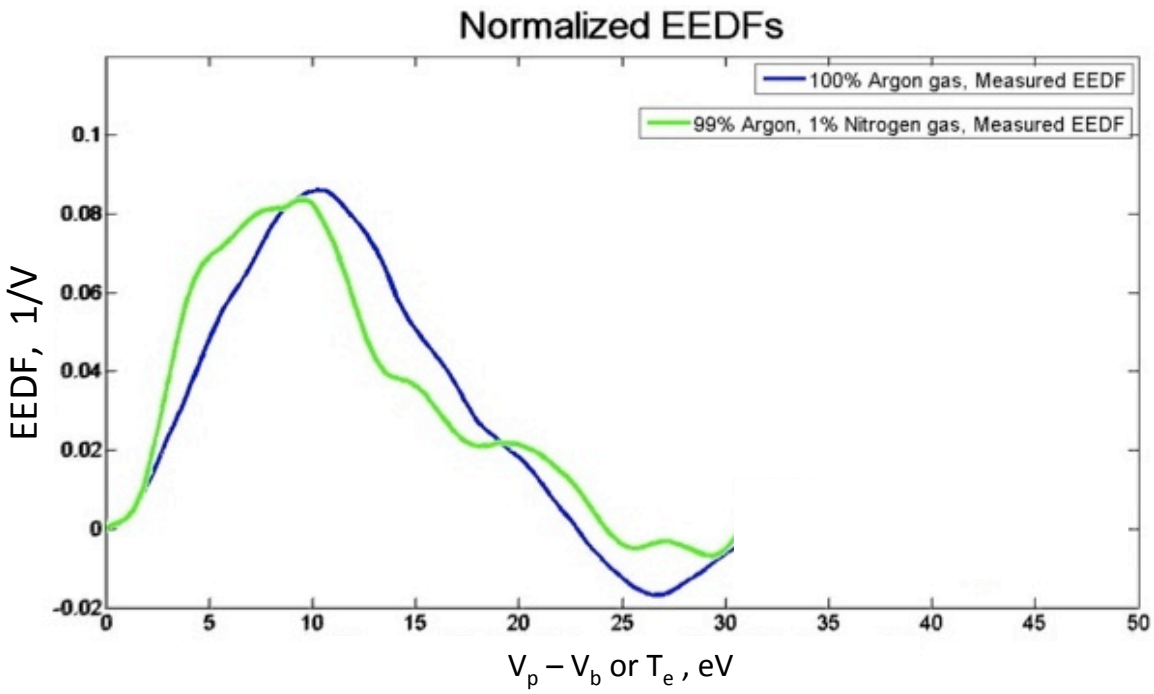

Figure A.16: This diagram compares the EEDF for the case with a pure argon plasma to that with 1% nitrogen. For the case with nitrogen gas, there are more distinct plateaus and peaks in the EEDF.

translational energy of various electron populations. In addition, in the high-energy region between 20 eV and 23 eV, there are relatively more electrons for the case with nitrogen mixing. The next subsection will delve into an explanation for all of these results.

A.2.1.3 Discussion

N_2 and Ar have comparable ionization threshold energies (as stated earlier), the ionization cross-section of nitrogen is larger than that of argon by almost an order of magnitude, nitrogen has a relatively low dissociation energy under the conditions in this plasma mixture, and the ionization threshold energy of N is less than that of argon even though it has a much smaller atomic mass than argon. [144, 145, 152, 153] If these properties alone were considered, this would lead to an increase in ion number density and therefore an increase in N_e as well with the gas mixing used in this

experiment, which is not what was observed. Therefore, other processes must have a more dominant influence on the plasma properties and steady state conditions, which led to the significant decrease in N_e that was seen in this experiment and in the literature. In order to understand what the commanding interactions were, it is first useful to understand the shape of the EEDF for a pure Ar and a pure N_2 plasma.

Jovanović et al. explain that in a pure argon plasma, which does not have a number of smaller energy inelastic processes that the electrons can lose energy to, the electrons can build up a higher energy before experiencing an inelastic collisional process. This leads to a relatively larger number of ionization events than in a pure nitrogen plasma, and therefore a drastic decrease in the steady state number of high energy electrons, and a relatively larger number of ions and electrons. [121]

Pu et al. point out that in a pure nitrogen plasma, a high energy tail can be generated by nitrogen in metastable states that are involved in superelastic collisions. The abundance of inelastic collisional processes (that produce vibrational and rotational modes of the nitrogen molecules) result in small decreases in the energy of various electron populations, including the high-energy tail population. This means there is less chance of a drastic decrease in these tail electrons' energy due to ionization compared to a pure argon plasma. Consequently, in a pure nitrogen plasma, the ion and electron populations are smaller, and a lower N_e decreases the electron-electron collision frequency, which allows more electrons to reach higher velocities, thus creating a steady state, high-energy electron population and an increase in the average electron temperature. [120]

Therefore, in looking at the EEDF of the case with N_2 mixing in this experiment as an amalgamation of the EEDFs for the two individual gases, the presence of more electrons in the high-energy tail of the EEDF is most likely due to the influence of nitrogen's metastable states, which Gorse et al. demonstrate can have an effect on the overall blend even when that gas is a very small percentage of the total flow. [121, 143]

Due to the increase in the relative number of high-energy tail electrons, the overall electron temperature increases, and due to the decrease in the percentage of argon and the additional inelastic processes that the electrons' energy is going towards with the addition of nitrogen, the ion and therefore also the electron number densities decrease.

This also explains why the heater current had to be higher in the gas-mixing case to maintain a stable discharge. While the total power being delivered to the discharge in the two cases was about the same, in the control case, more power was going to ionization (meaning there was more ion and electron current) which is why the anode current was higher at fixed voltage, and the keeper voltage was lower at fixed current. In the gas mixing case, more power was going to other inelastic processes (besides ionization), which meant less ions were available to heat the insert, (which happens when they accelerate through the insert's sheath and bombard it, see Ref. [13]). This process helps to sustain the discharge, so the heater current had to be higher in the gas-mixing case when the ion density was lower.

The results from this experiment showed that the desired and achieved increase in the high-energy tail of the steady state EEDF did not result in an increase in ionization. If the high-energy electrons are hindered from being used to ionize the main propellant, it defeats the purpose of introducing them. Therefore, to determine whether the effect of metastable states could be used directly in ionizing the main propellant, instead of depending on the intermediate step of superelastic collisions with electrons, and to allow this interaction to take place more readily by removing the energy sink of vibrational and rotational modes induced by inelastic collisional processes involving molecular gases, the influence that mixing in certain monatomic gases had on the ion number density (and the EEDF) was explored.

It was decided to investigate these propellant-auxiliary gas combinations through calculations before running further experiments. This would facilitate in gaining even

deeper insight into the types of collisions that dominated the steady state conditions, the number densities of the neutral, excited state, and ionized populations that were present in the plasma for each gas type, and how the metastable states of the auxiliary gas impact electron temperature and ion number density through changes to the EEDF. These calculations, which were carried out towards the goal of resolving whether an EEDF tailoring approach that made use of gas-mixing could translate into an overall increase in thruster efficiency, are explained in the next subsection.

A.2.2 Cathode Calculations

A.2.2.1 Theory (Neon or Argon + Xenon or Krypton)

The concept behind this method is to mix an auxiliary gas (with the main Hall thruster propellant) that has naturally occurring metastable electron states with energies larger than the ionization threshold of the main propellant. Metastable states are excited atomic levels that an electron can occupy without decaying back to its ground state. This is because there are either no transition paths or only forbidden transitions to the ground state from this higher level. The forbidden transitions are not allowed due to electric dipole selection rules, which mean they have a very low probability of occurring. Therefore these atoms have a longer lifetime than usual excited states, and in relatively dense gases, they tend to be de-excited through collisions. [154, 155] When these metastable atoms collide with atoms that have a lower ionization potential than the metastable state electron energy, there is a large cross section for the metastable atom ionizing the neutral atom. This type of inelastic collision is called Penning ionization. [156]

The propellants that were considered were xenon and krypton. It was desired to use an inert auxiliary gas as well so that corrosion, contamination, and the handling of harmful chemicals would not be a concern. The inert gases of interest to serve as auxiliary gases were those that had metastable state energies higher than the

ionization cost for creating XeII & KrII (i.e., Xe^{+1} & Kr^{+1}) but lower than the ionization cost for Xe^{+2} & Kr^{+2}. The reason for this is because doubly charged propellant decreases thruster efficiency. [16] The first and second ionization energies of xenon are around 12 eV and 21 eV, which means the ionization cost per beam ion for singly and doubly ionized xenon are $\epsilon_{Xe_1} \approx 12$ eV, and $\epsilon_{Xe_2} \approx 33$ eV. For krypton, the first and second ionization threshold energies are about 14 eV and 24 eV making $\epsilon_{Kr_1} \approx 14$ eV, and $\epsilon_{Kr_2} \approx 38$ eV. [16, 62, 157]

To search for metastable states of inert gases that fit this criteria the NIST Atomic Spectra Database's list of energy level transitions ([158]) was used with the following selections:

- On the text input line next to 'Spectrum,' the symbol of the element was entered followed by the charge state (i.e., I = neutral, II = singly-charged, etc.).
- Under 'Output Options'
  - ASCII (text) was chosen for the 'Format output,'
  - the box next to 'No JavaScript' was checked, and
  - under the drop down list for 'Energy Level Units' eV was selected.
- Under 'Additional Criteria'
  - under 'Wavelengths in' the radio button next to 'Vacuum (all wavelengths)' was toggled, and
  - the boxes next to 'Allowed (E1)' and 'Forbidden (M1,E2,...)' under 'Transition Type' were checked in order to find metastable states that do not even have a listed forbidden transition to the ground state.
- Then the 'Retrieve Data' button was pressed.

The data output from the NIST website was transferred to a .xlsx file where only the numerical data from the energy transitions (the columns labeled Ei and Ek) was kept. Then the energy level transitions data from this file was processed using a MATLAB program written to find the metastable states of the element in question. The MATLAB program achieved this using the following actions:

1. Accept the NIST and Excel generated .xlsx file as input using the xlsread function.
2. Sort the data rows according to the lowest to the highest values in the Ei column.
3. Search through the data starting at the last row (corresponding to the highest Ei) and determine if any of the rows before it contains an Ek with the same energy as the Ei.

Inert Gas	Metastable Energy (eV)	Paschen Notation	Racah Notation	L-S Coupling
Neon	16.6 eV	$1s_5$	$2p^5 3s$	$^3P_2$
	16.7 eV	$1s_3$	$2p^5 3s'$	$^3P_0$
Argon	11.5 eV	$1s_5$	$3p^5 4s$	$^3P_2$
	11.7 eV	$1s_3$	$3p^5 4s'$	$^3P_0$
	13.98 eV	$3d'_4$	$3p^5 3d$	$^3F_4$

Table A.4: Inert Gas Metastable States and Their Configuration

4. If that Ei value is not found in any of the rows above it, then it is a metastable energy level and should be saved in a running list of these values.
5. Then, sort the resulting list of metastable states from lowest to highest, remove zeros and remove duplicates.
6. Write the metastable array to a .xls file.

Following this procedure, the auxiliary gases chosen were Neon and Argon. Neon has metastable states of interest with energy levels of ∼16.6 eV & ∼16.7 eV, and Argon has a metastable state of ∼13.98 eV that fit the criteria. See Table A.4 for the atomic configuration of these energy levels in various notations. These notations were used to identify them in the literature for determining cross sections.

The calculations carried out in the next subsection were done to determine the fraction of naturally occurring metastable atoms of the auxiliary gas in a plasma mixture with the plasma conditions present in the cathode insert region. Then portions of that analysis were used to look at the collision frequency and production rate of the Penning ionization process, to compare it to those of the electron-propellant atom ionization process to see if it could contribute in a significant way to the fraction of ionized propellant. Finally, the results from the analysis were translated to the plasma conditions in the Hall thruster channel and to gas mixtures with larger fractions of auxiliary gas.

A.2.2.2 Calculations

First the reaction rate constant for the main ion production method in a hollow cathode plasma, electron-propellant atom ionization, represented by $k_e^{Xe^+}$ for xenon propellant and $k_e^{Kr^+}$ for krypton were calculated. These electron impact ionization processes have the following collision equations:

$$\begin{aligned} Xe + \tilde{e} &\rightarrow 2e + Xe^+ \\ Kr + \tilde{e} &\rightarrow 2e + Kr^+ \end{aligned} \tag{A.1}$$

The reaction rate constants were calculated from cross section data and the EEDF, and were related to collision frequency through the following equation:

$$\nu_e^{Xe^+} = n_{Xe} Q_e^{Xe^+} \bar{v}_e^{Xe} \tag{A.2}$$

(and similarly for krypton. This equation is from Ref. [7] where $\nu_e^{Xe^+}$ is the collision frequency for producing Xe^+ by neutral atom electron bombardment, with units s^{-1}, n_{Xe} is the number density of neutral xenon atoms, with units m^{-3}, $Q_e^{Xe^+}$ is the cross section for producing Xe^+ by electron bombardment, with units m^2, and $\bar{v}_e^{Xe}$ is the relative velocity between the xenon atom and the electron, with units of m/s. In this equation, $k_e^{Xe^+} = Q_e^{Xe^+} \bar{v}_e^{Xe}$, and since both of these variables are functions of energy, k can be calculated in the following way:

$$k_e^{Xe^+} = \int_{\epsilon_e^{Xe^+}}^{\infty} g(T_e, \epsilon) \left(\frac{2\epsilon}{m_e} \right)^{1/2} Q_e^{Xe^+}(\epsilon) d\epsilon. \tag{A.3}$$

This equation is from [159], where m_e is the electron mass, with units of kg, ϵ is energy, with units eV, $\epsilon_e^{Xe^+}$ is the threshold ionization energy, and $g(T_e, \epsilon)$ is the electron energy distribution function, with units 1/eV. The ionization reaction rate

constant was calculated using a Maxwellian distribution [111]:

$$g_M(V_b) = \frac{2}{\sqrt{\pi}} T_e^{-\frac{3}{2}} e^{-\frac{(V_s - V_b)}{T_e}} \sqrt{V_s - V_b} \tag{A.4}$$

whose units are 1/eV. The equation is written in this way to relate it to how it is calculated from Langmuir probe measurements from an experiment. In this equation, T_e is the electron temperature in eV, and $V_s - V_b$ is the electron energy, which when measured in experiment is found from the difference between the bias voltage of the probe, V_b, and the ambient plasma potential, V_s, which is calculated from probe data.

For these calculations of the atom-electron ionization reaction rate constant, the cathode plasma parameters in Table A.5 were used for both xenon and krypton, $Q_e^{Xe^+}(\epsilon)$, which was on the order of 10^{-16} cm^2, was taken from Ref. [160] (p. 1470, Table V), and the following summation was used with the tabulated cross section values to estimate the reaction rate coefficient:

$$k_e^{Xe^+} \approx \sum_{\epsilon_e^{Xe^+}}^{200eV} g_{M(+v)}(V_b) \left(\frac{2e(V_s - V_b)}{m_e} \right)^{1/2} Q_e^{Xe^+}(\epsilon_1 = V_s - V_b)(\epsilon_1 - \epsilon_0). \tag{A.5}$$

Here, ϵ_1 is the current energy, and ϵ_0 is the previous energy. See Fig. A.17 for the graph of the reaction rate constant at each energy with error bars before the total coefficient is determined through summation. The error bars were found using error propagation and the uncertainty in $Q_e^{Xe^+}(\epsilon)$ stated in the reference and the error in the electron beam energy. The beam energy uncertainty was deduced using the spread in the beam energy at full width at half height (FWHM) from the reference. [160] Assuming the beam energies form a Gaussian distribution, the equation that relates FWHM to the standard deviation: $FWHM = 2\sqrt{2\,ln\,2}\,\sigma$, was used to estimate the electron beam error.[129] The graph for krypton is similar in shape. After summation, the ionization reaction rate constant of xenon, $k_e^{Xe^+}$, is $\sim 1 \times 10^{-17}$ m^3/s, and for krypton it is $\sim 2 \times 10^{-18}$ m^3/s.

T_e	1.5 eV
V_S	22 V
V_b	V_S - $\epsilon_e^{Xe^+}$ to V_S - 200 V
ΔV	10 V
ϵ	$\epsilon_e^{Xe^+}$ to 200 eV

Table A.5: Hollow cathode plasma parameters used in the calculations of the ionization reaction rate constant for Xe and Kr.

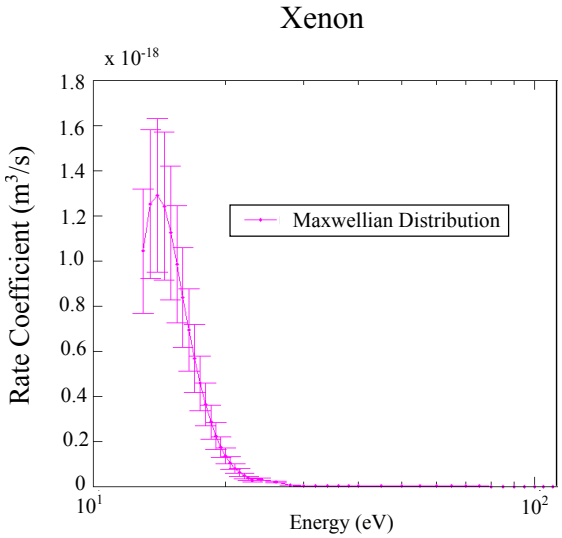

Figure A.17: This diagram shows the reaction rate coefficient versus energy for xenon, $k_e^{Xe^+}$, for a Maxwellian EEDF.

Next, taking neon as the auxiliary gas (see Table A.4), assuming a mixture percentage of 10%, and exploring its use in augmenting the ionization rates in both xenon and krypton plasmas, the collisional processes affecting the number density of metastable neon needed to be considered. With an extensive computation such as this one, visualization of the components and their significance in the overall calculation is useful in conveying the path taken and the thought process used to determine the results. Therefore, the creation and destruction processes are depicted in Fig. A.18, where the Ne metastable states are $1s_3$ & $1s_5$ with energies of 16.7 eV & 16.6 eV respectively. The atomic equations corresponding to each of these interactions along with the terminology used to search for their cross sections in the literature are stated in Eqns. A.6 - A.13 for neon mixed with xenon. The same equations can apply to a neon-krypton mixture with Kr substituted for Xe.

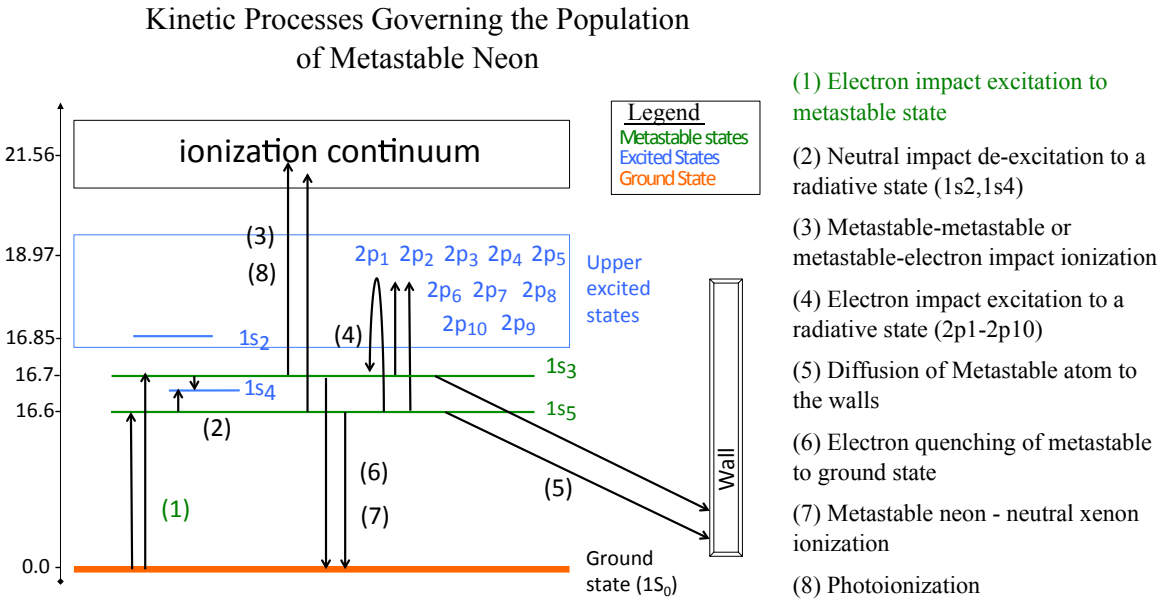

Figure A.18: This diagram shows a simplified electronic energy level diagram for the neon atom in order to represent the interactions that play a significant role in the creation and destruction of metastable neon atoms. This is done by showing the energy level transition from the metastable state that the electron undergoes for each of these events. The number for each collision corresponds to the numbers in the text.

(1) Electron impact excitation to a metastable state (an inelastic collision)

$$Ne + \tilde{e} \rightarrow Ne^m + e \tag{A.6}$$

(2) Neutral impact de-excitation to a radiative state ($1s_2$,$1s_4$) (with the appearance of new radiation or super-elastic quenching of radiation)

$$\begin{aligned} Ne^m + Ne &\rightarrow Ne^* + Ne + h\nu \\ Ne^m + Ne &\rightarrow Ne^* + \widetilde{Ne} \end{aligned} \tag{A.7}$$

where h is Planck's constant, ν is the frequency of the photon released when the electron in the metastable state within the neon atom decays to a lower energy level, and $h\nu$ is the photon's energy.

(3) Metastable-metastable or metastable-electron impact ionization

(a) metastable-metastable de-excitation through dissociative recombination (a special case, this molecular ion is a short occurrence)

(b) metastable-metastable ionization (pooling ionization, Penning ionization)

(c) electron impact ionization (stepwise ionization)

$$Ne^m + Ne^m \rightarrow e + Ne_2^+ \rightarrow \widetilde{Ne} + \widetilde{Ne} \tag{A.8a}$$

$$Ne^m + Ne^m \rightarrow \tilde{e} + Ne^+ + Ne \tag{A.8b}$$

$$Ne^m + \tilde{e} \rightarrow 2e + Ne^+ \tag{A.8c}$$

(4) Electron impact excitation to a radiative state ($2p_1$-$2p_{10}$) (electron quenching)

$$Ne^m + \tilde{e} \rightarrow e + Ne^*(\rightarrow e + Ne + h\nu) \tag{A.9}$$

(5) Diffusion of metastable atom to the walls

$$Ne^m \rightarrow Ne \tag{A.10}$$

(6) Electron quenching of metastable atom to its ground state

$$Ne^m + e \rightarrow \tilde{e} + Ne \tag{A.11}$$

(7) Metastable neon - neutral xenon ionization (associative ionization(AI) and Penning ionization(PI))

$$Ne^m + Xe \rightarrow NeXe^+ + e$$

$$Ne^m + Xe \rightarrow NeXe^* \rightarrow Ne + Xe^+ + e \tag{A.12}$$

(8) Photoionization (radiative ionization)

$$Ne^m + h\nu \rightarrow Ne^+ + e \tag{A.13}$$

The above atomic collisions can be combined into a kinetic model (Eqn. A.15) that can be used to determine the steady-state metastable number density from a balance of the sum of the rate of change, in the populations of the particle species, of all the creation and destruction reactions.[111, 161] Table A.7 shows the cathode insert region plasma parameters used in carrying out the calculations for each rate constant in order to solve this equation. Some of the terms in Eqn. A.15 were cancelled. These terms were other collisional processes by which metastable neon can be created or diminished including various combinations of 3-body reactions (involving heavy particles and electrons), and collisions with the array of charged species for the two gasses being mixed.

The reason why these terms were neglected is because this was a "first level" estimate where the contribution of two-atom collisions were included, but that of their charged states and of 3-body collisions with neon metastables were not. More specifically, these terms were disregarded here for a combination of a few reasons: 1. The number densities of the charge species within the mixture are at least one order of magnitude less than that of their neutral counterparts 2. In plasmas where the ionization fraction is over a few percent, electron-atom collisions tend to dominate over ion-atom and atom-atom collisions.[162] 3. While the probabilities of three-body collision involving neon metastable atoms at the temperatures and pressures present in the cathode insert region and Hall thruster channel plasmas is not heavily documented in the literature, they may or may not be a major contributor according to [163]. Using [164] and [165] these reaction rates can be estimated to be on the order of 10^{-32} cm^6/s, which with the highest densities of neutral atoms present in

the plasmas considered would give a collision rate on the order of 1 s^{-1}. From the results of this calculation, it will be shown that this destruction rate does not have the largest order of magnitude. Given this rough estimate (which may or may not be applicable to the temperatures and pressures of these plasmas) and the fact that this is a first level estimate, three-body collisions were not included.

For collisions involving electrons, the appropriate version of Eqn. A.3 was used, and for collisions involving only heavy particles, Eqn. A.14 from [7, 111] was used:

$$k(T_{gas}) = v^{th}_{heavy} Q(T_{gas}) = \left(\frac{8 k_B T_{gas}}{\pi M_a}\right)^{1/2} Q(T_{gas}) \tag{A.14}$$

where v^{th}_{heavy} is the relative thermal velocity between two heavy particles, $Q(T_{gas})$ is the gas temperature dependent cross section for the collision of the two heavy particles, k_B is the Boltzmann constant, and M_a is the mass of the atom if both of the heavy particles involved in the collision are the same element, or the reduced mass if they are different elements.

$$\begin{aligned} \overset{(1)}{N_e k_e^{Ne^m} N_{Ne}} = N_{Ne^m} \Bigg\{ & \overset{(2)}{k_{Ne}^{1s_{2,4}} N_{Ne}} + \overset{(3a\&b)}{k^i_{Ne^m} N_{Ne^m}} + \overset{(3c)}{k^i_e N_e} + \overset{(4)}{\left[\sum_{x=1}^{10} k_e^{2p_x}(1-b_x)\right]} N_{Ne} \\ & \overset{(5)}{+ k^{wall}_{diff}} + \overset{(6)}{k^Q_e N_e} + \overset{(7)}{k^{Q,Xe^+}_{Xe} N_{Xe}} + \cancel{k^Q_{Xe^+} N_{Xe^+}} \\ & + \cancel{k^Q_{Ne^+} N_{Ne^+}} + \cancel{k^Q_{2Xe} N^2_{Xe}} + \cancel{k^Q_{2Ne} N^2_{Ne}} + \overset{(8)}{\cancel{k^i_\nu}} \Bigg\} \end{aligned} \tag{A.15}$$

Using Table A.6, which shows the results from calculating each term in Eqn. A.15, other assumptions can made to cancel more terms. (3a&b) $k^i_{Ne^m}$, can be neglected

Table A.6: Plasma Environments of Interest for Inert Gas Mixing

Collision Description	Notation for k	Cross Section Q(T)	Effective Velocity	Rate Constant (k)	k*N_x
(1) Electron impact excitation to a metastable state	$k_e^{Ne^m}$	10^{-18} cm^2	10^8 cm/s	10^{-12} cm^3/s	10^3 s^{-1}
(2) Neutral impact de-excitation to a radiative state ($1s_2$,$1s_4$)	$k_{Ne}^{1s_{2,4}}$	10^{-19} cm^2	5×10^3 cm/s	10^{-15} cm^3/s	10^0 s^{-1}
(3a&b) Metastable-metastable impact ionization	$k_{Ne^m}^i$	10^{-15} cm^2	–	–	–
(3c) Metastable-electron impact ionization	k_e^i	10^{-16} cm^2	–	–	–
(4) Electron impact excitation to a radiative state ($2p_1$-$2p_{10}$)	$k_e^{2p_x}$	10^{-15} cm^2	10^8 cm/s	10^{-7} cm^3/s	10^8 s^{-1}
(5) Diffusion of metastable atom to the walls	k_{diff}^{wall}	–	–	–	10^4 s^{-1}
(6) Electron quenching of metastable atom to its ground state	k_e^Q	–	–	10^{-10} cm^3/s	–
(7) Metastable neon - neutral Xe or Kr ionization	k_{Xe}^{Q,Xe^+},k_{Kr}^{Q,Kr^+}	10^{-15} cm^2	5×10^3 cm/s	10^{-12} cm^3/s	10^5 s^{-1}

The values filled in with a dash are associated with terms that it was realized could be neglected while progressing through the calculation, except for the diffusion constant where the other values are not relevant because it is calculated differently. Values are presented in cm^2, cm/s, and cm^3/s, because these are the units most commonly used in the literature. These calculated values are for the case of mixing with xenon or krypton propellant and most are rounded to the nearest order of magnitude. The description of the columns is as follows: The 'Collision Description' and 'Notation for k' follow from Eqns. A.6-A.13 above. For collisions involving electrons, the 'Cross Section' shows the order of magnitude of this parameter across the range of electron temperatures considered for the EEDF used. For collisions involving heavy particles, what is shown is the cross section at the gas temperature. The 'Effective Velocity' for the electrons is calculated using the electron temperature for that plasma environment and $v_e = \sqrt{(2eT_e)/M_e}$, the velocity component of Eqn. A.5. For the heavy particles the velocity is calculated using v_{heavy}^{th} in Eqn. A.14. The 'Rate Constants' were calculated using Eqn. A.5 or Eqn. A.14, and 'k*N_x' was calculated by multiplying the rate constant by the number density of the species colliding with the metastable neon atom. However, for the first table entry it is the rate constant times the neutral neon number density. The references for the Q or k values listed for the collisions are as follows: (1) [166] p.1369 Table 3, (2) [163] Table IV, for Q value, (3a&b) [167] Table I, (3c) [168] Table 2 & [169] Figure 1, (4) [170] p.6 Table IV, p.3 (calculated taking branching ratios into account, and checked against Table II & Figure 3), (5) [171], [172] equation 6, [173] equation 20, and [174] equations 19-21, using Lennard-Jones potentials: [175] p. 539 equation (8.2-44), p. 1110 Table I-A, p. 567 equations (8.4-8) & (8.4-9), and p. 1127 Table I-M, and then compared with [176] Table I, (6) [167] Table V, (7) [177] p. 4273, 4275, and Fig. 2, [178], [179] equation 12 and Tables 2 & 3, and [179, 180] (for krypton).

because while its rate constant is $\sim 10^{-12}$ cm^3/s, when multiplied by Ne^m the result will not be larger than term (4) in this equation. (3c) will also not be larger than (4) because it has cross sections that are an order of magnitude lower than (4) and both involve collisions with electrons. (6) has a rate constant that is smaller than that of (4) so it can also be disregarded.

(8) Photoionization, k_ν^i, from Eqn. A.13 was also not included in this estimate. While its cross sections, $\sim 10^{-17}$ cm^2, can be obtained from Ref. [182] Figures 17 & 18, since these cross sections are dependent on the photoelectron energy, and hence on the wavelength of the incident photon, estimating the reaction rate for the plasmas considered would also require other pieces of information. These pieces of information, which were not readily available include the light spectral distribution in the cathode insert region and the HET ionization zone during operation with the gas mixture (or at least the main propellant) along with absolute intensity values for wavelengths of 260 nm and less. 260 nm is the wavelength corresponding to the energy difference between the highest metastable state and the ionization threshold, which is $\sim$4.8 eV. In addition, the total power going into each spectral line in this wavelength range would need to be estimated using a collisional radiative model so that photon number densities at each wavelength could be estimated. Therefore, photoionization was not included in this first level calculation.

A.2.2.3 Results and Conclusion

With these assumptions and the values shown in Table A.6, Eqn. A.15 reduces to Eqn. A.16. Both krypton and xenon as the main propellant round to the values shown in this equation assuming a Maxwellian distribution function for terms involving collisions with electrons. The neon metastable fraction, compared to neutral propellant atoms is therefore around 5×10^{-6}, and compared to neutral neon atoms, it is $\sim5\times10^{-5}$. Error propagation was not carried through the entire calculation to

Table A.7: Plasma Environments of Interest for Inert Gas Mixing

	Insert	HET Channel	HET Ioniz./Accel. Zone
Pressure	3 Torr	3-6 mTorr	2 mTorr
Gas Temp	1000 K	∼500 K	∼500 K
Neutral Xe (or Kr) Density	$1x10^{22}$ m^{-3}	$9x10^{19}$ m^{-3}	$4x10^{19}$ m^{-3}
Neon Density (10%)	$1x10^{21}$ m^{-3}	$9x10^{18}$ m^{-3}	$4x10^{18}$ m^{-3}
Electron Density	$1x10^{21}$ m^{-3}	$5x10^{17}$ m^{-3}	$1\text{-}4x10^{18}$ m^{-3}
Electron Temperature	3 eV	5 eV	15-40 eV
Plasma Potential	13 V	300 V	100-300 V

This table lists the cathode insert plasma parameters used for the gas mixing calculations and the anode channel and acceleration zone parameters used to estimate the impact gas mixing would have on the Hall thruster. The insert gas pressure was calculated using the method outlined in [13] Appendix B. Insert gas temperature close to the insert was estimated from orifice thermocouple measurements done by Trent and McDonald while running the lab-built cathode in CTF as ∼1,300 K, which compares well to [181]. Gas temperature in certain areas of the insert region could be as high as 2000 K - 4000 K [13, 181], but the value used was rounded to 1000 K because the charts for the diffusion calculations only went up to 1000 K. The neutral gas density in all three cases was calculated from the ideal gas law using the stated pressure values. Neon density is a stated value of 10% of the main propellant neutral density. The electron density for the cathode insert was estimated to be 10% of the neutral propellant density, and this fraction compares well to [181]. Insert electron temperature and plasma potential are from the measured values from [181]. The HET channel and accel. zone parameters are for the H6 at 300 V and 20 mg/s and assume quasi-neutrality. 'HET Channel' refers to the area near the anode and 'HET Ioniz./Accel. Zone' refers to the region where the ionization and acceleration zones overlap at the end of the channel. The source for the plasma parameters for these regions is [55].

the final figures, because error bars were not indicated for all the values used from the literature, and since some of the values, such as the diffusion calculations were calculated from theory where no error bars were given. However, these results compare well to the literature. For example, Boffard et. al. used a hollow cathode with a pure neon discharge, which they stated had a neon metastable atom fraction of 3×10^{-6}. [183] Given the fact that 1. the calculations presented here are a rough first order approximation, 2. there may be differences in their hollow cathode source compared to the one used in this analysis, and that 3. in this analysis the plasma was a combination of neon and another inert gas, the values obtained here appear to be a reasonable upper limit on the metastable fractions that could be expected from this type of application. Therefore, further conclusions can be based on these results.

$$N_{Ne^m} = \frac{N_e k_e^{Ne^m} N_{Ne}}{k_{Ne}^{1s_{2,4}} N_{Ne} + \left[\sum_{x=1}^{10} k_e^{2p_x}(1-b_x)\right] N_e + k_{diff}^{wall} + k_{Xe}^{Q,Xe^+} N_{Xe}}$$

$$5\times10^{16} m^{-3} = \frac{5\times10^{24} m^{-3} s^{-1}}{2s^{-1} + 1\times10^{8} s^{-1} + 1\times10^{4} s^{-1} + 1\times10^{5} s^{-1}} \tag{A.16}$$

The collision frequency for metastable neon-propellant atom ionization in the insert environment using Eqn. A.2 and the values from Eqn. A.16 is 1×10^5 s^{-1}, where 20% of the these collisions result in associative ionization products (represented by the first equation in Eqn. A.12) and the other 80% result in the Penning ionization products shown as the second reaction. Given the population of metastable neon that was calculated, this collision frequency results in an increase in the production rate of xenon or krypton ions of $\sim5\times10^{15}$ $cm^{-3}s^{-1}$.

Even though the energy dependent cross sections for electron-atom collisions involving Xe or Kr are $\propto10^{-16}$ cm^2, which is lower than the metastable neon-propellant atom ionization cross sections by an order of magnitude, the corresponding reaction rate constants ($k_e^{Xe^+}$ & $k_e^{Kr^+}$) in the insert region, assuming a Maxwellian electron

energy distribution are $\sim 1\times10^{-9}$ cm^3/s & $\sim 4\times10^{-10}$ cm^3/s respectively. These values are 2-3 orders of magnitude larger than that of metastable neon-propellant atom ionization (see (7) in Table A.6) since the electron velocities are so much higher than the heavy particle velocity. (To obtain these values, the same equation from earlier in this section (Eqn. A.5) was used, but with the cathode insert conditions from Table A.7.) When these numbers are multiplied by the neutral number densities, they lead to collision frequencies of $\sim 1\times10^{7}$ s^{-1} & $\sim 4\times10^{6}$ s^{-1}, which result in ion production rates of $\sim 1\times10^{22}$ cm^{-3}s^{-1} & $\sim 4\times10^{21}$ cm^{-3}s^{-1}.

This shows that the production rate of Xe or Kr ions for associative and Penning ionization using the fraction of naturally present neon metastable atoms, when adding in neon gas at 10% of the neutral propellant number density, is several orders of magnitude lower than that of electron-atom ionization. The major contributing factors to this in spite of starting with a higher ionization cross section are 1. the lower velocity of the heavy particles as compared to electrons, and 2. the lower fraction of metastable neon atoms as compared to electrons.

A metastable neon number density that is two orders of magnitude larger than that of the electrons would be needed to compensate for its lower collision frequency to allow metastable neon-propellant atom ionization to even be comparable to electron-propellant atom ionization in the insert plasma environment. This would require a neon to xenon gas density ratio of 2×10^{5} to 1 (i.e., a neon gas mixing ratio of 2×10^{7}%). In the Hall thruster channel and ionization/acceleration zone (see. Table A.7 for the plasma parameters in these areas) the trends would most likely be similar, and this would flood the channel with neon neutrals, which would completely change the plasma conditions there, creating a negative affect on thruster efficiency in other ways. For example, it would greatly reduce the Hall current which aids in setting up the spatial electric field responsible for accelerating the ions to produce thrust.

These calculations, along with the experiment in subsection A.2.1, explored the

proposed tailoring method of dispatching electrons with the energy needed for ionization using a neutral atom delivery method via the introduction of associative and Penning ionization through inert gas mixing, and without adding any additional energy to the system. The purpose of these calculations was to determine if this could make a significant increase in thruster efficiency by raising the ionization fraction in the Hall thruster plasma environment. This was done by carrying out the calculations for the cathode insert region and extrapolating to the case of the Hall thruster. Specifically, these calculations shed light on the types of collisions that played a significant role in the steady state conditions of the plasma, and explored how the metastable states of the auxiliary gas influence ion number density.

From these results, it was realized that in order to increase HET efficiency through EEDF control, the electrons' energies have to be adjusted directly— not through or involving neutral collisions, because particle velocity plays a large role in the reaction rates for the collisions that would be needed to transfer this energy. This led to the EEDF tailoring method discussed in the body of this thesis where the position of the cathode was adjusted to allow more of a direct acceleration path for the electrons to the channel, in the hopes of decreasing the amount of energy the system used to get them to there, so instead a larger portion of the system's energy could be applied to increasing ionizing collisions and the acceleration of ions. This approach translates into manipulating the EEDF by electron trajectory redirection in order to shift the entire distribution to higher energies in the location where ionization occurs. See Chapter III for the results from that study.

APPENDIX B

Experimental Procedures

This Appendix is a collection of the procedures developed and used for maintaining, running and in some cases building the main equipment and experimental diagnostics employed for the testing carried out in this thesis. Citations and credits are given where needed. Plans to add this section to the thesis were implemented after it was decided by the Lab Director that it would be prudent to have the procedures used to conduct the experiments described in the thesis associated with that thesis. This furthers the repeatability of a scientific experiment— which is key to the reporting of any research investigation, assists those coming afterwards using the same or similar facilities and experimental instruments in carrying out other research campaigns, and can aid in the electric propulsion community's effort towards procedural standardization to facilitate more straightforward comparison between investigations done in different laboratories.

It is important to note that these procedures are a culmination of years of learned and passed-on knowledge and trial and error experience of the generations of graduate students who have conducted research at PEPL under the guidance of the Lab Director and within the electric propulsion and plasma science communities. This official recording of some of this knowledge is also the result of an effort started by

these graduate students to not only pass the details of this information on to the next generation by a combination of word of mouth and internal documents, but to also encourage the next generations to write down all of the details involved in these procedures so that none of this information would get lost over time.

B.1 MCHall Code Description

B.1.1 Standalone Code Methodology

Outline of Simulation Methodology for StandaloneSeedSingleElectron_simple.m from MCHall

This code and MCHall were developed by Dr. Michael McDonald, see reference [85]
Other References: Written communication with Dr. McDonald in 2014
The code description here was written by Kimberly Trent and Dr. Michael McDonald
March 2014

This algorithm is a bare bones variant of the full MCHall computational model. It sources an electron with zero velocity from position r0 at time t0 and tracks its course until it leaves the domain of the simulation. The code is set up to also take account of any additional electrons the seeded electron creates through ionizing collisions during its trek.

Note: Line references refer to lines in the code being described

1. Initial conditions: z0 (in meters), r0 = [x0 y0 z0] (in meters), t0 (in seconds), v0 = [v_x v_y v_z] (line 91, in m/s), and eV = electron energy (line 95, in eV). To seed an electron from a centrally mounted cathode, set z0 = 0.001, r0 = [0 0 z0], eV = 2 and v0 = [0 0 0]. For other cathode seeding locations, where all of the electron's energy is directed parallel to thruster centerline, as a first order approximation, set eV = 0 and v = [0 0 3.25E6] to represent the electron's energy gain from falling through a ∼30 V potential drop from the cathode to the ambient plasma.
2. To see what happens to a secondary electron that is born in front of the outer pole in the near field try: z0 = 1.25 r_c, r0 = [r_c 0 z0], eV = 0 and v0 = [0 0 0] where r_c is the distance from thruster centerline to channel centerline. Also try other values to get a sense of how electrons seeded at various positions, energies and velocities behave in the simulation.
3. Note that in this code the eV value is used in calculating the collision frequency (line 144) to determine if a collision takes place in a given time step, and when there is a collision, the electron's new energy (eV) is determined based on the collision type, which is randomly selected (lines 174-199). From that new eV, the new velocity magnitude is then calculated for that time step along with a randomly determined new velocity vector that is scaled to the new velocity magnitude (lines 212-218). If a collision does not take place then the E and B fields' effects on electron velocity and position are what are calculated in that time step to determine the new velocity and position. When a collision takes place in a given time step, E and B field influenced motion is not taken into account.
4. For E and B field influenced motion, the velocity vector is what is used (along with the interpolated E and B fields at the electron's position) to calculate the electron's new velocity and position, not eV. Then the new eV is calculated from the new velocity vector by first calculating the magnitude of the velocity vector (lines 158-160). Therefore, when setting an initial eV and an initial velocity vector for this code, the initial velocity vector will only be used if a collision does not occur in the first time

step and the initial eV value will only be used if a collision does occur in the first time step. The code comes set up with no collisions enforced (lines 149-150). However, this can be changed with lines 151-152, which will allow Monte Carlo collisions.

5. After the initial conditions are set (steps 1-2), LoadFields is used to import the B-field, E-field and neutral number density map. This nested function calls loadB_simple, loadE_simple, and loadN_simple to accomplish this. The code for the LoadFields function is at the very end of the StandaloneSeedSingleElectron script, and the load simple functions are separate .m files that can be run on their own to display plots that provide a visual of what they are doing to develop the fields and meshes needed for the simulation.

   Of note for loadE_simple.m: additional areas of the Vp field, closer to the thruster, are added in with probe data that has a lower spatial resolution than the rest of the Vp data used. This is done in lines 153 to 250. The MATLAB function pchip (Piecewise Cubic Hermite Interpolating Polynomial (PCHIP)) was used to fill in the mesh in this region using these data points. The final Vp field is visualized using the figure coded in lines 277 to 298. This additional area of the Vp field is highlighted in this figure. The E-field is calculated as the gradient of the Vp map in line 364 of the loadE_simple function.
6. Next the getFields2 nested function is called and passed electron position and energy (r & eV), and the E and B-fields (fields and locs) so it can interpolate these fields for the electron's starting location.
7. Then the main program loop begins which steps through each timestep and either collisions are considered, using the Monte Carlo method, or the equations of motion are integrated for each timestep. First, the local collision frequency is calculated. This collision frequency is compared to a random number, which determines if a collision occurs in that timestep. If it does, then the collision routine is carried out (lines 163-222) where the collision type is determined and a new, random energy and velocity are assigned to the electron. If a collision does not occur, then the function stepforward is called which applies the Boris algorithm. This is a "vxB integrator that separates E and B effects into separate intermediate steps" (quoted from the code comments). The code lists two references for this algorithm (lines 315-323). A new velocity and position for the electron are calculated from this algorithm, and a new energy is then calculated from this.
8. Next, within the timestep loop, getFields2 is called again to interpolate the E and B fields for the new electron position. Then the simulated time is increased by one timestep and step 7 is repeated until MaxNumTimesteps or MaxRunTime is reached.
9. The simulation outputs include: exit location (the key for these values is contained in the code), exit position (r = [x y z]), final energy (eV), electron lifetime (sim time), amount of time simulation took to complete (elapsed time), number of collisions, and a figure showing the electron trajectory relative to thruster location. For some initial conditions, to have the simulation continue until the electron exits the domain, MaxNumTimesteps needs to be increased from its current value of 1e5. It had to be increased to 1e9 for some of the simulations that were run.

B.1.2 Full MCHall Code Methodology

A Brief Outline of the Simulation Methodology for the Full MCHall Code

MCHall was developed by Michael McDonald, see reference [85]
Other References: Written communication with Dr. McDonald in 2014
The code description here was written by Kimberly Trent and Dr. Michael McDonald
July 2014

There are four program files (scripts) in the MCHall code. They are

1. MCHall_Batch.m
2. LoadDefaultRuntimeParams.m
3. MCHall_EnergyLoop.m
4. MCHall_AngularLoop.m

Each one is a function with input arguments and output. These scripts also contain nested functions, and local functions (aka. subroutines, or subfunctions). Calling MCHall_Batch from the command line runs the entire code. All the other scripts are carried out in the execution of the entire program. The purpose of each of the program files is as follows:

MCHall_Batch.m
Loads the runtime parameters from the LoadDefaultRuntimeParams.m file. Then it calls MCHall_EnergyLoop and passes these parameters to this portion of the code.

LoadDefaultRuntimeParams.m
This script contains all of the higher-level, user-defined parameters that one may want to change to run different types of simulations with the code. The types of parameters that can be adjusted in this program file are the total number of electrons seeded with RuntimeParams.EnergyN0 and RuntimeParams.SpatialN0, electron temperature with RuntimeParams.Te, and seeding from the cathode, the channel or a reseed case with
- RuntimeParams.seeding.cathode,
- RuntimeParams.seeding.channel and
- RuntimeParams.seeding.reseed. From this file options for collision parameters, the type of random number generator the program uses, timestepping parameters, and others can be chosen. This program file contains a number of comments that explain what all the settings are and what they do. Modify the parameters in this file, and save it with an identifying file name so that only one line of code in MCHall_Batch has to changed to have it grab the desired parameters for a particular run.

MCHall_EnergyLoop.m
Takes the runtime parameters as its input arguments and returns the location of the saved file that contains the outputted results from the simulation.

MCHall_AngularLoop.m
The StandaloneSeedSingleElectron_simple.m code (see subsection B.1.1 for details) is from this program file. This script is where the electron trajectory simulations happen for each energy for the array of ejection angles determined in this code. The program also creates a

local record that can be used to recreate each individual trajectory, which it compiles into a job record matrix, which it then passes back to MCHall_EnergyLoop.m for the saved output.

In more detail:

In MCHall_EnergyLoop, first the nested function ElecEnergDist is called. This function creates the electron energy distribution (EED). Within this nested function first the resolution for the distribution is determined from the parameter RuntimeParams.EnergyN0. This also determines the MinEnergy. The distribution is normally calculated from a Maxwellian distribution using RuntimeParams.Te; however, this can be changed to a different form on line 230 in this nested function. The maximum energy for an electron used in the run can also be adjusted by changing MaxEnergy within this nested function. The array energybins contains the range of energies from MinEnergy to MaxEnergy at the resolution determined from EnergyN0. Then the distribution function is calculated for each energy value in this range (energybins). Subsequently, an array, Energies, is created where each energy in energybins is repeated a number of times that is proportional to its representation in the distribution function and scaled by EnergyN0 (so that the total number of energies is around the number given by EnergyN0). Then a histogram for these Energies is plotted along with the normalized EED that is then scaled by the maximum number of electrons that is seeded for an energy within the entire range of electron energies.

Then, because of the rounding that takes place when determining the number of electrons to seed per energy level in the making of the Energies matrix, the total number of electrons seeded may be slightly different from EnergyN0, so after this nested function is called, this parameter is updated with the total number of elements in Energies in the variable EnergyN. This is also the number of random streams that will be used. One for each energy loop iteration.

Next, ElecSpatialDist is called which creates the electron spatial distribution, which is the ejection angle distribution of the electrons from the cathode. First the ejection angle resolution is determined from SpatialN0. This is determined differently depending on whether the ejection angle was chosen to be produced from a Gaussian distribution or a half Maxwellian distribution through RuntimeParams.SeedAngleType in LoadDefaultRuntimeParams. The MinEjectionAngle is determined from the resolution. The MaxEjectionAngle is 90 degrees. Then the distribution is calculated for the range of ejection angles (EjectionAngles) using either a Gaussian distribution or it can be calculated using a sine function if the half-Maxwellian option was chosen. If the latter option was chosen, make sure that the code to carry this out, as seen in the nested ElecSpatialDist function found in MCHall_EnergyLoop, is also added to the nested ElecSpatialDist function in MCHall_AngularLoop. Then an array, angles, is created where each angle in EjectionAngles is repeated a number of times that is proportional to its representation in the distribution function and scaled by SpatialN0. Then a histogram for these angles is plotted along with the normalized spatial distribution function that is then scaled by the maximum number of electrons that is seeded for an angle within the entire range of electron angles. Make sure the code chooses between the Gaussian or the sine function for this portion of the plot depending on what option was chosen for SeedAngleType. The code is currently set up to plot a sine distribution no matter what option has been chosen (line 329).

Then, because of the rounding that takes place when determining the number of electrons to seed per angle in the making of the angles matrix, the total number of electrons seeded across all the angles (for each energy) may be slightly different from SpatialN0, so after the ElecSpatialDist function is called, this parameter is updated with the total number of elements in angles in the variable SpatialN.

After this the electric, magnetic and neutral density fields and cross-sections are loaded using the nested function LoadFields. Next the number of cores the simulation will run on in parallel is determined if the RuntimeParams.multicore option was set to 1. Otherwise the simulation will not run in parallel. Then the main loop of the program is called using a parfor loop structure. This may throw an error messages if not running in parallel (i.e. if RuntimeParams.multicore = 0). In this case go into the code and change parfor to for on line 64). The parfor loop is called for the total number of energies, EnergyN, and the variable p is used by the parfor loop to step through total number of elements in Energies, which is EnergyN. An independent random number stream is created with each loop iteration using RandStream.create. A group of streams is created for each of these independent random number streams using NumStreams and stored in RuntimeParams.RandGen. This is accomplished with the following line of programming code (line 66):

```
rndstrm = RandStream.create(
      RuntimeParams.RandGen,'NumStreams',RuntimeParams.EnergyN,'StreamIndices',p);
```

Then this group of streams is sent to MCHall_AngularLoop, along with the fields, locs, and the energy in the array Energies that pertains to the particular index of the parfor loop iteration that is being carried out. This function then returns the results (from SpatialN electrons being seeded in an angular distribution from the seeding location with the initial energy determined by Energies(p)) in the array OutputFiles. Each OutputFiles(p) contains the job_record for that angular distribution of electrons at energy Energies(p). The job_record for each angulary-ejected electron (local_job_record in MCHall_AngularLoop.m) contains jobrecordelements number of entries. These 25 values are noted in the code with the following list and descriptions:

1. Unique identifier for each electron [uniqID]
2. Electron source energy [eV]
3. Electron source angle [theta] (radians)
4. Electron type (1 = primary, 2 = secondary, etc.) [etype]
5. Exit point. See function ApplyBoundaryConditions for label key [exits]

6–8. Electron final position before exiting [x,y,z]

9. Electron source time [t0] (0 for primaries, later for others)
10. Electron exit time (t_exit - t0 = lifetime)
11. # of trajectory bounces / mirrors [bounces]
12. # of Momentum Transfer Collisions [momxfer]
13. # of Excitation Collisions [excite]
14. # of Ionization Collisions [ionize]
15. Energy Loop Index (random number stream; max is total # of streams) [EnergyLoopInd]

16. Spatial Loop Index (random number substream) [SpatialLoopInd]
17. Timesteps recorded [RecTimesteps]
18. Timesteps simulated [SimTimesteps]
19. Initial Plasma potential at electron source point (V) [Vpenter]
20. Final plasma potential at electron exit point (V) [Vpexit]
21. Final electron energy at electron exit point (eV) [eVexit]

22–24. Electron Initial Position [x0,y0,z0]

25. Full Electron Trajectory (NumElectrons x 10 cell structure)

    1. t (seconds)

    2–4. r(t) = [x y z] (meters)

    5–7. v(t) = [vx vy vz] (meters/sec)

    8. Collision Type (1 = mom xfer, 2-4 = excit., 5 = ion.)
    9. Timestep index
    10. Plasma Potential Vp(t) (volts)

Then these values are saved to a master output file, which is the output for this code, and the individual record OutputFiles are deleted.

In MCHall_AngularLoop:

First, RuntimeParams.seeding.reseed is set equal to zero. If it is planned to run reseed cases from the simulation output then data from the entire trajectory of each electron seeded in the simulation needs to be saved, and this parameter should be set to 1. Next, a job_record cell matrix that is SpatialN x jobrecordelements in size is created (line 134). A matrix for storing secondary electrons from ionization events is also created called SecondaryElectrons. Then the program loops over the Ejection Angle Distribution Function with p as the loop index, which goes from 1 to SpatialN (a different dummy variable p from the one used in EnergyLoop). Next, the initial electron seed conditions are defined. z0=0.001 on line 163 (not 0 b/c the fields aren't defined there). If seeding from the cathode and it is not a reseed case and the cathode is not off center, then r0= [0.000 0 z0]; in line 180. If seeding from the channel then the position is defined on lines 203-207:

r = r_c; % channel centerline
phi_dum = 2*pi*rand(rndstrm); → this variable determines how the parameter r will break down into x & y components, i.e., where around the channel the electron will be seeded
z0 = L_c; → one thruster discharge channel length downstream, measured from the thruster's exit plane
r0 = [r*cos(phi_dum) r*sin(phi_dum) z0];
theta = 0; % doesn't matter since it's not used to compute v-hat (v-hat is chosen randomly on a unit sphere)

Then the uniqID identifier label for each electron is defined as uniqID = (angularID-1)*RuntimeParams.SpatialN + p; (angularID is the p value from the EnergyLoop program file). Next, the function SeedSingleElectron is called and passed r0, theta, eV, t0, fields, locs, uniqID, rndstrm, angularID, p, and RuntimeParams. This function returns record, secondaries, exittype, ionizerecord, and exciterecord.

Then any secondaries generated by the current e- are added to the list to seed later with

the line SecondaryElectrons = [SecondaryElectrons; secondaries]; on line 233. (record is defined in SeedSingleElectron, line 1460 as record(PointsRecordedSoFar,:) = [t r v CollisionType i Vp];). Then this output data is organized. First, a local_job_record cell matrix that is 1 x jobrecordelements in size is created (line 236), and the 25 pieces of information about this electron, listed earlier, are saved to the appropriate cell. entrypoint = 1 for these electrons (item 4 of 25). The full electron trajectory information is only saved if RuntimeParams.seeding.reseed is non-zero, lines 290-294. Otherwise only start and end values for the electron's trajectory are saved in the output.

Then local_job_record is saved to the aggregate output file for this spatial loop using job_record(p,:) = local_job_record; Next, the trajectories for the secondary electrons that were generated by the primary electrons and that were stored in SecondaryElectrons are determined by sending their information to SeedSingleElectron. The secondary electron cell matrix has the following elements: [uniqID, t, r] where r = [x y z]. A new random number substream is created for each electron to aid reproducibility:

rndstrm.Substream = RuntimeParams.SpatialN + i;

For these electrons:

theta = 0; % since v0 = 0 for secondaries, angle doesn't matter
r0 = SecondaryElectrons(i,3:5);
eV = 0; % this is assumed for energy conservation during ionization
t0 = SecondaryElectrons(i,2);
ParentUniqID = SecondaryElectrons(i,1);

lines 324-327. One thing to note about the while loop that handles the secondary electrons is that it will continue to loop as long as the loop counting integer is less than size(SecondaryElectrons,1). Also for the secondary electrons, ParentUniqID is passed for the uniqID, and RuntimeParams.SpatialN+i is passed as the p value for the SeedSingleElectron function. Then with the output returned by this function, any newly created secondaries (tertiaries, quaternaries) are added to the SecondaryElectrons matrix:

SecondaryElectrons = [SecondaryElectrons; secondaries]; (line 332).

Next, similar to how it was done for the primary electrons, a local_job_record cell matrix is created and all of the jobrecordelements for this seeded electron are recorded. Then this local file is saved to the aggregate record using:

job_record(RuntimeParams.SpatialN+i,:) = local_job_record; (line 401).

The number of Tertiaries is calculated on line 408. If it is a reseed case, or if toggle.showvis is set to 1, then the function particle_vis(record); is called, line 415. Then all of the data is saved to the output file given by RecordFilename, which starts with 'output-test-' and contains a date and timestamp. This is also the output for MCHall_AngularLoop.m, outputfn, which stores the full name and save directory information for this data file.

The nested functions make up the rest of the MCHall_AngularLoop.m program file. These are as follows:

1. stepforward
2. stepforwardv (just like stepforward except it only calculates a new velocity, and it uses a different sMatrix to calculate the velocity)
3. stepforwardr (just like stepforward except it only calculates a new position, and it uses the average of two times in its calculation of a new position)
4. getFields2
5. ApplyBoundaryConditions (similar to the Standalone code version except it is also passed uniqID,angularID and p). The description in the script says:

   "This subroutine is only entered if the electron has entered a region where the fields are undefined. Since the fields are defined up to the boundaries, entering this subroutine means an electron has already left the simulation and the only thing left to do is to ask where." (lines 672-675)

   The way that the exit points are determined are slightly different from in the Standalone code and any electrons that enter the region of the thruster at a radius less than the inner radius of the outer pole are considered to have entered the channel. For further detail, see lines 724–798.
6. MYINTERP_GETSPOTS_1D
7. ElecSpatialDist

   This creates an electron spatial distribution where the electron's release angle is governed by a Gaussian distribution with a mean value of theta = 0 deg which is on axis. An angle of pi/2 is in the same plane as the thruster radius. First the ejection angle resolution is determined from EjecAngleRes = .5 * pi/180; (line 826). This is also the MinEjectionAngle. The MaxEjectionAngle is pi/2. The EjectionAngles go between the Min and Max at an increment equal to the Res. Then the Gaussian Spatial Distribution is defined and then calculated for the EjectionAngles. (As currently written, this version of the nested function is only written for the Gaussian option. To add in the half-Maxwellian option, see description **above** in the third paragraph under "In more detail:" starting with the sentence "Then the distribution is calculated...".) Then the matrix angles is generated by repeating each ejection angle a number of times that corresponds to its proportion in the Gaussian distribution function and scaled by the total number of electrons wanted at various angles for each energy, which is SpatialN0 (really SpatialN). This is accomplished with the following line of code on line 841 within the for loop:

   ```
   angles = [angles;
     repmat(EjectionAngles(i),round(RuntimeParams.SpatialN0/etot*e_per_dist(i)),1)];
   ```

8. LoadFields
9. SeedSingleElectron

   This function sources an electron with zero velocity from position r0 at time t0 and tracks its course until it leaves the domain of the simulation. The code is set up to also take account of any additional electrons the seeded electron creates through ionizing collisions during its trek.

One of the differences between this function and the StandaloneSeedSingleElectron_simple.m version of MCHall (see subsection B.1.1 for details) is that in this version of the code, "no collisions, R1 = 1" is not enforced unless RuntimeParams.DisableCollisions = 1. If collisions are not disabled, then R1 = rand(rndstrm); which is line 1220. For collisions, more information is stored with the cases. For instance, the identifying information for any secondary electrons created is stored in the secondaries matrix. Also location information is recorded in the ionizerecord and the exciterecord for any of these cases that occur.

B.2 Dual Langmuir Probe Building Procedure

Steps for Making and Mounting Dual Langmuir Probes

HDLP system designed and developed by Dr. Robert Lobbia, see reference [14]
This probe building procedure was written by Kimberly Trent
with additions by Bakari Hassan and Christopher Bellant
Other References: Verbal communication with Dr. Lobbia in 2011
Version 2.0 December 2012

This procedure covers how to make a dual Langmuir probe where the tungsten conductor with an exposed probe tip serves as the active, Langmuir probe, and a second tungsten wire that is fully insulated from the plasma functions as the Null probe. Since both lines of this dual probe have identical circuitry (see Section B.4), are swept simultaneously through the same voltage range, have approximately the same length of wire, and the wires are very near to each other, the Null probe signal can be subtracted from the Langmuir probe signal to remove parasitic capacitance that occurs between the active probe and surrounding conductors that are at different potentials relative to the probes such as the grounded chamber surfaces. In addition, any electromagnetic interference (EMI) that the Langmuir probe may experience is also recorded by the Null probe, and hence subtracting its I-V characteristic from that of the active probe also accomplishes EMI rejection.

Note: It is best to always make a couple of extra probes when building a set of Langmuir probes for an experiment in case one does not come out as well, or in case one breaks while it is being incorporated into the experimental setup. This will minimize the chances of delays due to Langmuir probe issues while working towards pumpdown.

Phase 1: Probe Length & Pin Connections

1. Put on a pair of Nitrile or latex gloves while building the Langmuir probe so that oils from one's hands do not contaminate the probe.
2. Cut the lengths of wire needed.
   Note: use a wire cutter that does not split the wire as it cuts. After cutting the wire, check the tip under a microscope to make sure it is smooth and flat with no splitting down the length of the wire. If the cutter left a pointed tip, use a diamond file to level it off so that the tip is as close to a cylinder as possible.
   a. For the Null probe, the length of wire needed is equal to the sum of the following:
      i. length of probe (the alumina tube), plus
      ii. length for electrical connection at the back of the probe (0.5 to 1 in.), plus
      iii. length to bend over the top of the alumina tube (2 mm).
   b. For the active probe, the length of wire needed is equal to the sum of the following:
      i. length of the probe tip, plus
      ii. length of probe (the alumina tube), plus
      iii. length for electrical connection at the back of the probe (0.5 to 1 in.), plus

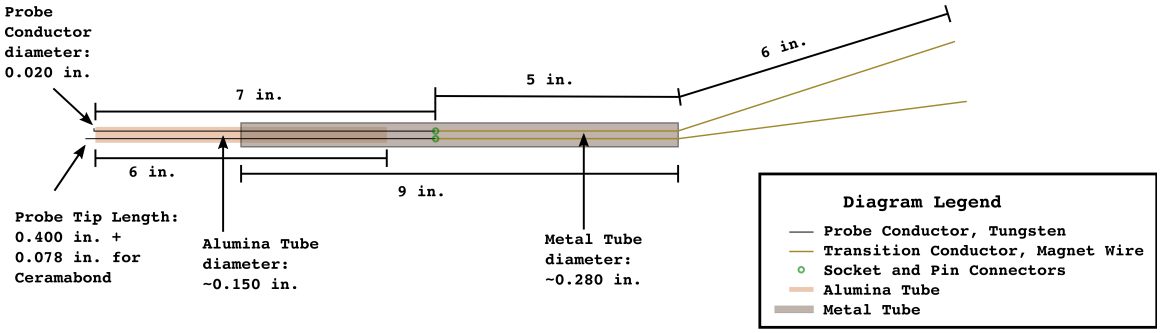

Figure B.**1:** A schematic of the dual Langmuir probe, pictured in Figure B.5, which was used to obtain data in the plume of a 6-kW Hall Thruster. Zoom in to see details.

iv. length to allow room for Ceramabond (2 mm). See Fig. B.1

Note: Consider intentionally cutting the wires to a longer length than needed, in case an error requires a portion of the wire to be cut. Also make sure all the cabling used are matched in length between the Null and LP lines (aside from the extra length of the LP's exposed tip) so that the Null probe can duplicate the capacitive coupling the LP probe lines experience as accurately as possible.

3. Insert the wires into the alumina tube to make sure the wire portions that extend out the top are the right length (probe length + 2 mm for the active probe and 2 mm for the null probe). Mark the location on the other end of the wires where they exit the end of the probe tube with a small piece of Kapton tape. It is preferable to use an alumina tube with two or more holes. This way both probe wires can be inserted into the same tube so that they are in close proximity to each other.
   Note: When using very thin tungsten probe wire (around 5 thou in diameter), a three inch piece of copper wire can be inserted up about an inch into each hole from the end of the tube to provide extra support for the fragile wire. See Fig. B.*2.*
4. Remove the wires from the alumina tube, attach socket connectors (either female barrel terminal or female D-Sub contact connectors) to the end of each tungsten wire. Crimp and solder the connectors to secure them to the wires. Since tungsten is a high temperature refractory metal, it will not melt at the temperatures used to apply the solder. Crimping the socket connector to the wire is what will mainly hold it in place. The solder is only being used to fill in any remaining gaps to keep the connector from rocking back and forth on the wire. Therefore, make the crimp connection as solid as possible.
   Note: When using a connector with a U-shaped as opposed to an O-shaped cup termination style, needle-nose pliers can be used to bend the metal flaps around the wires first so that crimping forms a more secure hold on the wires. Also, take care when choosing the crimp pliers that will be used for a given connector-wire diameter combination so that the wire(s) is/are secure but does/do not break off.
   Note: If copper wire has be used to reinforce the tungsten lines, as discussed in the note of the previous step, first cut the copper wire so that it ends at the same spot as the tungsten wire. Then, make sure the end of the copper wire is also secured inside of the connector along with the tungsten.

Phase 2: Probe Wire Insulation & Preparation for Ceramabond

1. Clean the portion of each wire that will extend out the front of the tube with very fine steel wool (#0, #00, or #000 range), and then with a KimWipe and 70-99% IPA. Only use a KimWipe and IPA if the probe wire is very thin to prevent the tips from bending or breaking.
2. Look at the tips to make sure no steel wool or KimWipe fibers were left on them.
3. Re-insert the wires into the alumina tube.
4. To prevent plasma from entering the back of the probe's alumina tube and interacting with the wires, there are two options: Either use Ceramabond to seal the wire-tube gap or wrap the wires with Kapton tape.
    a. If using Ceramabond: Loosely wrap the end of the exposed wires, that extend out the back of the alumina tube, with a little bit of Kapton tape to form diameters that are larger than the diameter of the tube's holes. Make sure the edge of the tape comes to where the wires were marked with a little bit of Kapton tape in step 3. This way the tape will act as a stopper to prevent the wires from moving up any more while ceramabonding the active probe tip and the Null probe in place at the top of the probe. If the wire can still rotate around inside the tube, lightly tape the connector side of the tungsten wires to the tube so they will not move around while ceramabonding the top of the probe. After this Ceramabond dries, remove the tape before ceramabonding the back end of the probe.
    b. If using Kapton tape: Wrap a layer of Kapton tape from the end of each wire and up far enough so it will cover about 1-2" of the wire in the tube. The taped wires should still be thin enough to be pushed up inside of the alumina LP tube, and should provide resistance to moving further once the wires are slid up to where the amount that extends out the front is the desired length. This way the wires will stay in place while applying Ceramabond to the top of the LP. The tape should also insulate the Null probe from the active probe. See Fig. B.2.
    Note: Use tweezers when wrapping Kapton tape around wires and connections in cramped spaces. Place the probe in a small electronics bench, multi-angle vise with nylon jaws for a gentle but secure hold.
5. Use small curved tip pliers to bend the tip of the Null probe (2 mm) across the top of the probe body so it can be secured to the top of the alumina tube with Ceramabond more easily in Phase 3. The wire only needs to be bent ∼45 degrees from the axis of the wire for this purpose.
6. Re-measure the length of the probe tip to make sure nothing shifted while taping the end of the wires in place.

Phase 3: Ceramabond Mixing & Application

1. Using a scale, measure the liquid and powder Ceramabond proportions in the way described on the Ceramabond containers for the amount needed. Mix the constituents together in a paper or plastic cup using a plastic knife. See Fig. B.3.
2. Apply the Ceramabond mixture to the tip of the alumina tube to secure the wires in place. It is best to use a small, disposable paintbrush with short, flexible, shed-resistant bristles to have the most control over the application of the Ceramabond and to create the smoothest seal. Ensure that the Null and active probes are not touching. The Ceramabond should be applied so that the Null probe tip is completely covered,

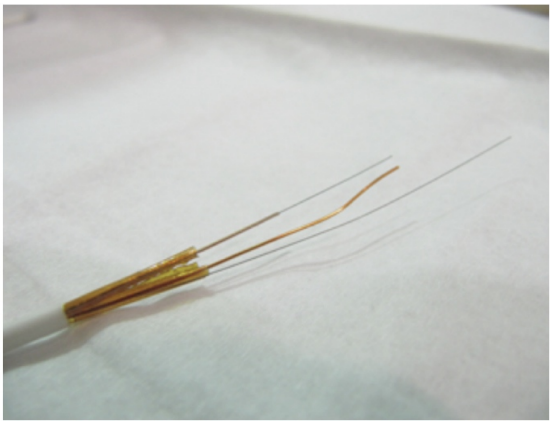

Figure B.**2:** Picture on the left: The top of the Langmuir probe showing the lengths allotted for the LP and Null probes. Picture on the right: The back of the Langmuir probe showing the Null and LP wires insulated from each other and held in place in the alumina tube using Kapton tape.

Figure B.**3:** Picture on the left: The components of the Ceramabond mixture, 571-L and 571-P. Picture on the right: 571-P in the small paper cup, and 571-L in the red cup before mixing.

and so that 2 mm of the base of the active tip is covered, leaving the desired tip length exposed. Make sure none of the Ceramabond gets on the rest of the active probe tip. Ceramabond should not only be applied to the top surface of the alumina tube, but also to the sides to ensure proper insulation. Care should be taken while applying the Ceramabond while also applying it expeditiously since Ceramabond dries rapidly. Once the sides and top of the mixture begin to form a thicker/drier layer it should no longer be used. Mixing more Ceramabond than needed helps with keeping it moist for longer. Practice on a dummy probe first to avoid mistakes. Then, make a fresh blend of Ceramabond to use on the actual probe.
Note: Make sure to measure the length of the active probe tip, by lining it up to a ruler while ceramabonding, to get the proper tip length. Note: If ceramabonding the back of the probe as well, do this later after the tip has air dried and will hold the wire in place. Revisit step 4a. for ceramabonding the back of the probe.

3. As directed, let the Ceramabond air dry for 1-4 hours.

Phase 4: Ceramabond Curing & Assembly of the LP

1. Once the Ceramabond on the probe has air dried, cure at 200 °F for 2 hours as directed. There is no temperature selector on the in-lab oven, so before putting the probe in the oven, guess the setting and check the temperature with the hanging in-oven thermometer until the right temperature is reached. This can be done towards the end of the time that the probe is air-drying.
2. While the Ceramabond on the probe is in the oven, cut two 11" pieces of magnet wire. This magnet wire will act as the joining wire between the probe's fragile tungsten wires and the BNC cables leading to the chamber feedthroughs. Then strip this magnet wire of the insulation it comes with as this insulation has been known to emit a sticky substance when it heats up at vacuum.
3. On one end of each piece of magnet wire, crimp and solder a male pin connector so that it can be connected to the probe's female pin connectors.
4. Thoroughly wrap each magnet wire in Kapton tape or cover with Weico heat treated fiberglass sleeving for insulation (depending on the temperatures of the application), leaving ∼0.5" portion of the end that does not have a connector attached exposed.
5. Once the Ceramabond on the probe has finished baking, check to make sure there are no holes in the Ceramabond that would cause the probe tips to not be properly insulated from each other and from the plasma. Any gaps on the order of a Debye length will allow plasma to get through.
6. Insert the magnet wire contact pins into the contact sockets on the ends of the active and Null probe wires, and solder these connections to keep them from slipping apart.
7. There are two options for insulating the probe wires and protecting them from damage where they exit the alumina tube. Either wrap them in high-temperature tape or use a metal tube, which can have the added benefit of reducing avoidable errors in the data. See further details below:

    a. If using high-temperature tape: Use Kapton tape to cover the exposed portion of the tungsten wires and the connectors to help insulate these wires and connectors from the plasma and from each other. Then wrap a 2-inch length of the probe (from 1 inch before to 1 inch beyond the end of the back of the alumina tube) in fusion or fiberglass tape (depending on the temperatures the back of the probe will experience in the plasma application it will be used for). This tape

provides support to the fragile tungsten probe wires to prevent them from getting damaged by rubbing against the back edge of the alumina tube. See Fig. B.4.

b. If using a metal tube:
   i. Make sure the wires will be insulated from the metal tube by wrapping Kapton tape around the exposed tungsten wires and connectors while making sure the tape does not cause these wires to be too thick to fit through the metal tube.
   ii. Then place the metal tube around the alumina tube, leaving the first few inches of the alumina exposed. See Fig. B.1.
   iii. Use fiberglass, Kapton or fusion tape to cover the area where the metal tube ends on the alumina tube to prevent plasma from going inside the probe. Also, tape over the area at the back of the probe where the magnet wires exit the metal tube. See Fig. B.5(b).
   Note: Surrounding the brittle alumina tube with a metal tube provides a more secure area for mounting the probes. See Fig. B.*6(a). When mounting the probes, if the metal tube is not grounded through the mounting system used, it can be grounded by taking a wire that is connected to ground on one end and that has a ring terminal crimped to the other end, placing a small p-clamp around the diameter of the tube and then connecting the wire to the tube by threading a screw through the ring terminal and p-clamp holes and securing it with a nut on the other end. See Fig.* B.*6(b). This will aid in further noise reduction and also in taking accurate LP measurements by bringing a grounded surface closer to the location where measurements are being made so that the plasma does not become starved of electrons as the active probe tip draws them from the plasma during a voltage sweep. If there is no source for replenishing these electrons in close proximity to where they are being removed, it can cause artifacts in the data.*

8. On the other end of each piece of magnet wire, secure a female solder-cup BNC connector. Then, wrap the connectors in Kapton or fiberglass tape up to where they will connect to their counterpart connector to help insulate them from the plasma.

Phase 5: LP Electrical Checks, Documentation & LP Vacuum Chamber Wire Preparation

1. Now that the LP is finished being constructed, perform electrical checks on it before incorporating it into the experimental setup to make sure the construction was successful.
   a. Using the BK Precision handheld multimeter, check for continuity between the probe tip and the BNC connector jack associated with the probe tip. Gently place one of the multimeter test leads against the LP tip.
   b. Use the BK Precision handheld multimeter to make sure the LP tip is not connected to the LP BNC shield, or to the Null BNC jack or shield.
   c. Use the Megger to check for isolation between the following pairs for 30 sec at 100 V:
      i. LP (jack) & Null (jack)
      ii. LP & LP shield
      iii. LP & Null shield
      iv. Null & LP shield

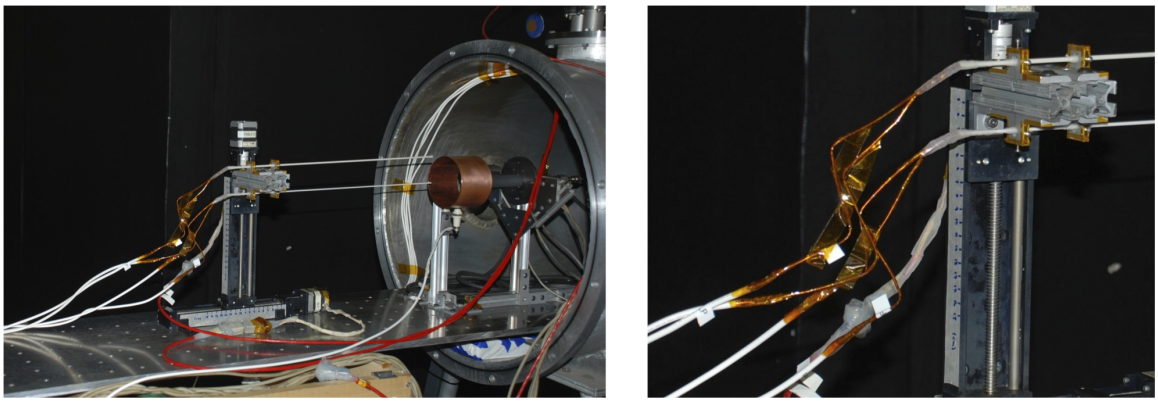

Figure B.4**:** Picture on the left: A picture of a Langmuir probe set up in the Cathode Test Facility (CTF) at PEPL for an experimental setup involving a cathode operating in triode mode with an external anode. Picture on the right: A close up of the back of the probes showing how the magnet wires are supported as they exit the alumina tube with fusion tape.

v. Null & Null shield

Note: The Megger resistance should be in the hundreds of MΩ to the hundreds of GΩ range for each pair listed above.

2. Label the magnet wire line connected to the LP tip as LP using a label maker and cover the label with Kapton tape.
3. Use an SLR camera to zoom in on the probe tip and take pictures of it before and after testing next to a ruler or some other item of fixed length to determine whether the probe tip changed in any way during testing. Ideally, the probe tip's length, shape and surface roughness should not change during the test. If it did, this means the probe's exposed surface area and shape were not constant while taking data which means that assumptions inherent in the LP analysis theory for a cylindrical probe of a cylindrical probe shape and a constant surface area would not hold. In a graphics software, determine how many pixels per inch the ruler or other item of fixed length is and use that to measure both dimensions of the probe. Or, measure both dimensions before and after with a micrometer, and only use the pictures to document surface roughness.
4. Cut lengths of co-axial cable that will extend from the end of the magnet wires to the chamber feedthroughs for the probes.
   Note: Make sure the total length of wires used is the shortest possible, but balance this with making sure parts of the cables can run behind structures in the chamber to keep as much of the cable out of the line of sight of the thruster as possible.
   Note: If the LP will be moved relatively close to the thruster during the experiment, use co-axial cables with high temperature insulation for the length of cabling that will be close to the probes, and cover it with high-temperature, expandable sleeving suitable for the temperatures that will be present in the application, such as Nextel or Nomex sleeving. This sleeving is made from a combination of fiberglass, silica, and/or ceramic. The remaining length of co-ax line can use standard co-ax cabling; however, cover the cabling that will be in the line of site of the thruster with Nextel sleeving to prevent shorting within these cables, which occurred previously when they did not have this additional sleeving over them even though these cables remained relatively far from the

(a)

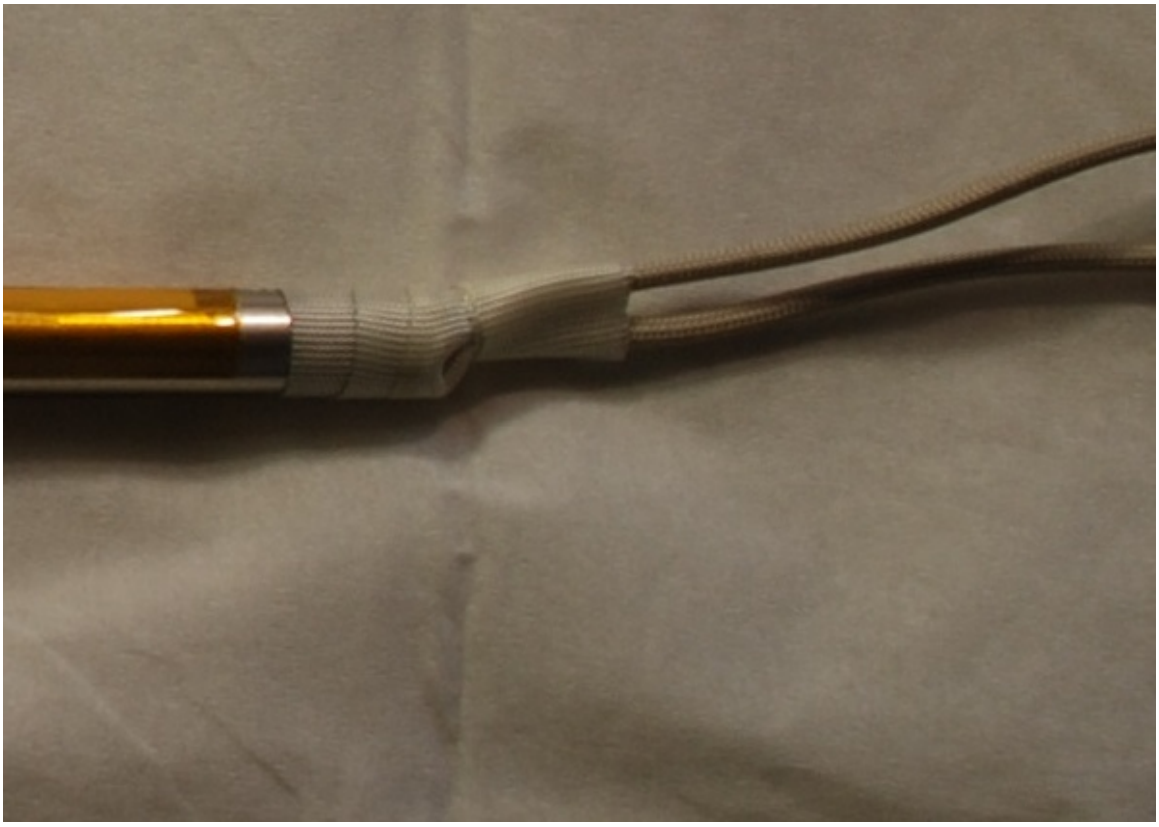

(b)

Figure B.**5:** Pictures showing a completed Langmuir probe constructed using a metal support and mounting tube. (a) A photograph showing the full completed Langmuir probe before being mounted in the chamber. (b) A picture showing how the back of the Langmuir probe where the fiberglass sleeving insulated magnet wires exit the metal tube are taped over with fiberglass tape.

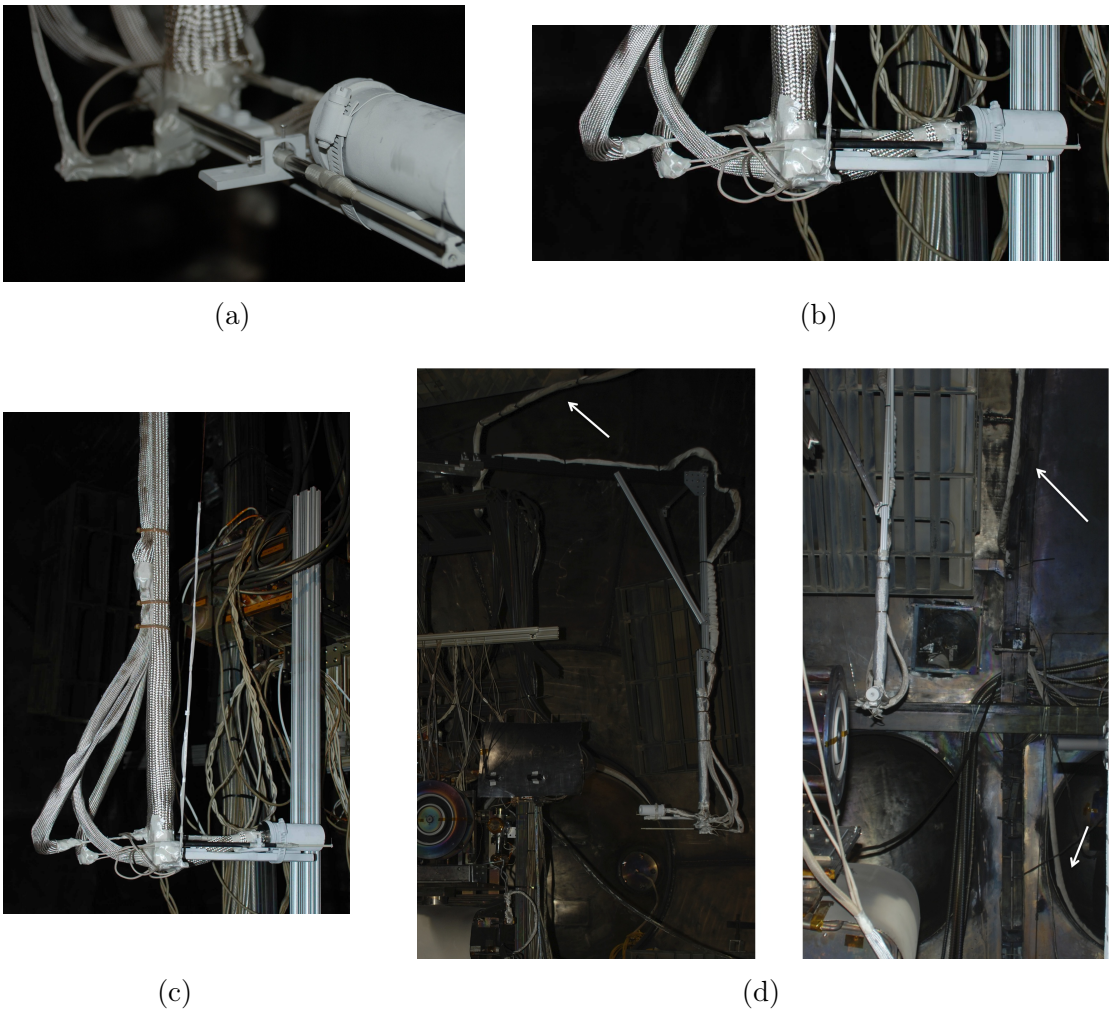

Figure B.**6:** Pictures showing a completed Langmuir probe constructed using a metal support and mounting tube mounted in the Large Vacuum Test Facility (LVTF) at PEPL. (a) A picture showing the Langmuir probe's metal tube used to secure the probe in position. (b) A photograph showing how the Langmuir probe's metal tube is grounded inside the chamber to the bottom of the arm extending from the movable tables used to position the probes. See step 7(b.)iii for more details. (c) A snapshot of how the Langmuir probe electrical lines are protected from the plasma plume using high-temperature sleeving. (d) An image with white arrows pointing to how the Langmuir probe electrical lines further back but still in the line of sight of the plasma plume are protected from the plasma plume using high-temperature sleeving.

thruster. See Fig. B.*6(d).*

5. Crimp and solder a male cable-clamp BNC connector to one end of these wires, making sure that the co-ax cable's braided shield is connected to the BNC connector's shield. Then, wrap the connector with Kapton, fiberglass or fusion tape up to where it will be connected to its matching connector.
6. Attach the appropriate connector to the other end of these wires for connecting to the chamber feedthroughs.
7. Connect the LP's two magnet wire lines to the two co-ax cables using the BNC connectors.
8. If parts of the connectors are still exposed after the connections are made, wrap this area in a high-temperature tape of choice.
9. Pull the expandable fiberglass, silica, and/or ceramic sleeving, mentioned in the note in step4, up over the connections and tape or zip tie the sleeving in place to keep the entire wire and the connections covered during testing. See Fig. B.6(c).

B.3 High-speed Dual LP (HDLP) Box Calibration Procedure

High-speed Dual LP v.1.0 (HDLPv1) Twin LP Current Sensors box Calibration Procedure

HDLP system designed and developed by Dr. Robert Lobbia, see reference [14]
This calibration procedure was transcribed by Kimberly Trent
Other References: Verbal and written communication with Dr. Lobbia in 2011, and the manuals for the equipment used
August 2011

The purpose of this procedure is to calculate the gain used in the calculation of the current of the LP I-V trace as mentioned in step 12 of the High-speed Dual LP v.1.0 (HDLPv1) System Run Procedure in Section B.4. The full equation for the current accounting for if the gain is different on both sides of the circuit is:

$$I_1 = \left(\frac{V_{1hi}}{G_{1hi}} - \frac{V_{1lo}}{G_{1lo}}\right)\frac{1}{R_1}$$

Equipment:

- Twin LP Current Sensors box (Dual-Symmetric Current Sensing Circuit) from Lobbia's thesis [14]
- Keithley DMM 2000
- GW Instek GPS-3033 Multi-Channel Laboratory DC Power Supply
- GW Instek GPS-3030DD Laboratory DC Power Supply
- Fluke Multimeter

Precautions when using the Twin LP Current Sensors box:

- Never apply voltage to the inputs of the amplifiers (banana jacks on the Twin LP Current Sensors box, which are the input connections for V_{IN}, V_B (or V_{LP}), and V_{NULL}) when amplifier is unpowered.
- Never apply a voltage to the outputs of the amplifiers (BNC connections on the Twin LP Current Sensors box, which are the output connections that go to the data recording equipment).
- The resistance with broken op amps continues to increase starting in the MOhms.
- If replacing the op amps in the Current Sensors box, make sure to wear an anti-static grounding wrist strap and to use an anti-static mat to protect the new op amps from static discharge damage.

1. Place the multi-channel DC power supply on an anti-static mat or surface, stack the Keithley DMM 2000 on top, and then a low ripple & noise DC power supply that can supply 10 V (such as the GW Instek GPS-3030DD) on top of that, see Fig. B.7. A Keithley 2410 can also be used instead as the voltage source.

Figure B.**7:** Pictures of the equipment setup for calibrating the Dual-Symmetric Current Sensing Circuit

2. Plug them into an outlet and turn them on. Set the precision on the Keithley to 6 1/2 for voltage measurements. The Keithley needs one hour to warm up to its rated accuracy. This particular DMM was chosen for the calibration because it has a greater resolution than the DAQ that will be used to record the measurements during testing.
3. After replacing the op amps (and without powering on the op amps), use the multimeter to check that the resistance between the inputs (V:low and V:hi) and the ground connection (the green banana input on the front of the box) is 110 kOhm if the shunts between V:hi and V:low are removed, or 55 kOhm if the shunts have not been removed. If it is not close to this value then check the internal connections.
4. Make sure all the equipment has warmed up for at least 30 minutes to 1 hour. Set the voltage on the power supply to 10 V using the Keithley to measure this value (without the Current Sensors box in between). Then set the current limit to a low value like 100 mA using the Fluke Multimeter. The current sensor box can measure a max of 200 mA.
5. Turn on the multi-channel power supply that will be used to power the Current Sensors box, the GW Instek GPS-3033, and make sure the output is off. Set the Voltage on both channels to 15 V and set the current limit to 0.5 A. Make sure the channel plus and minus connector ports are wired together as shown in Fig. B.9 & B.7.
6. Plug in the ±15 V & ground connections from the power supply into the Current Sensors box. Use a green cord for the ground connection to avoid confusion.
7. Turn the output of the power supply on. Make sure the light next to the output on/off button is green, and make sure the current goes from the allotted amount, of 0.5 A to ∼0.05 A. (If necessary, check with the Fluke to make sure it is applying a voltage).
8. Check to make sure the ground pin on the front panel of the power supply providing the 10 V is in fact grounded. If not connect it to ground using a green banana cable as shown in the Figure.
9. Use a banana wire to connect the 10 V output to an input on the Current Sensors box. There are two black and two red banana sockets, which are the input connections for V_{LP} (or V_B), V_{Null}, and two for V_{IN} respectively).
10. Connect the BNC cable to the output on the Current Sensor box that corresponds to

the input the 10 V is connected to. Connect the other end of the BNC cable to the Keithley, so it can measure the voltage once the 10 V signal goes through the voltage division network (see Fig. B.9).

11. Write down the voltage shown on the Keithley display.
12. Unplug the 10 V input from the input that was just measured.
13. Move the BNC cable to the next connection to be measured.
14. Then plug the 10 V into the next input that corresponds to this BNC and write down the voltage measured on the Keithley.
15. Repeat steps 9 through 14 once more so that all 4 voltage divider networks are measured.

To shut down the Dual-Symmetric Current Sensing Circuit without damaging the op amps follow these steps:

16. Unplug the 10 V input.
17. Disconnect the BNC cable.
18. Disconnect the ground connection to the 10 V supply, and turn off this 10V supply.
19. Make sure no voltage is being applied to the inputs of the current sensing box.
20. Turn off the power to the Current Sensor box.
21. Disconnect these power supply leads from the current sensing box.

B.4 HDLP Run Procedure

High-speed Dual LP v.1.0 (HDLPv1) System Run Procedure

HDLP system designed and developed by Dr. Robert Lobbia, see reference [14]
This operating procedure was transcribed by Kimberly Trent
Other References: Verbal and written communication with Dr. Lobbia in 2011, and the manuals for the equipment used
August 2011

Equipment:

- Twin LP Current Sensors box (Dual-Symmetric Current Sensing Circuit) from Lobbia's thesis [14]
- DAQ (General Standards PMC66-16AISS8AO4 8-channel 2 MHz DAQ Card)
- Dual Langmuir Probe, see **Dual Langmuir Probe Building Procedure**, Section B.2
- Keithley DMM 2000
- 20x Inverting Broadband Power-Amplifier from Lobbia's thesis [14]
- GW Instek GPS-3033 Multi-Channel Laboratory DC Power Supply
- Tektronix AFG 3101 Single Channel Arbitrary/Function Generator
- 2 GW Instek GPR-30H10D Single Output Linear DC Power Supplies (Amplifier Rails)
- Agilent InfiniiVision DSO-X 3024A Oscilloscope

General Notes:

- Refer to Fig. B.9 as you read through this procedure.
- If stacking equipment when running this setup in order to fit everything onto a given amount of counter space, make sure to place a piece of insulation, such as a rigid piece of clear Plexiglas (acrylic) between the stacked equipment to prevent arcing between pieces of equipment, also using a table with shelves or a light duty rack helps to keep the setup compact, see Fig. B.8.
- Do not place the front of some pieces of equipment behind others. Instead, keep the power connection, or back panel sides of all equipment on one side of the setup, and the front panel, interface sides of all equipment of the setup on the other side.
- Keep cables as neat and organized as possible to make it easier to check that cables are connected properly.
- Avoid Ground loops. Make sure each piece of equipment is only grounded through one path, see Fig. B.9.

Precautions when using the Twin LP Current Sensors box:

- Never apply voltage to the inputs of the amplifiers (banana jacks on the Twin LP Current Sensors box, which are the input connections for V_{IN}, V_B (or V_{LP}), and V_{NULL}) when amplifier is unpowered.
- Never apply a voltage to the outputs of the amplifiers (BNC connections on the Twin LP Current Sensors box, which are the output connections for the data recording equipment, i.e. a DAQ).

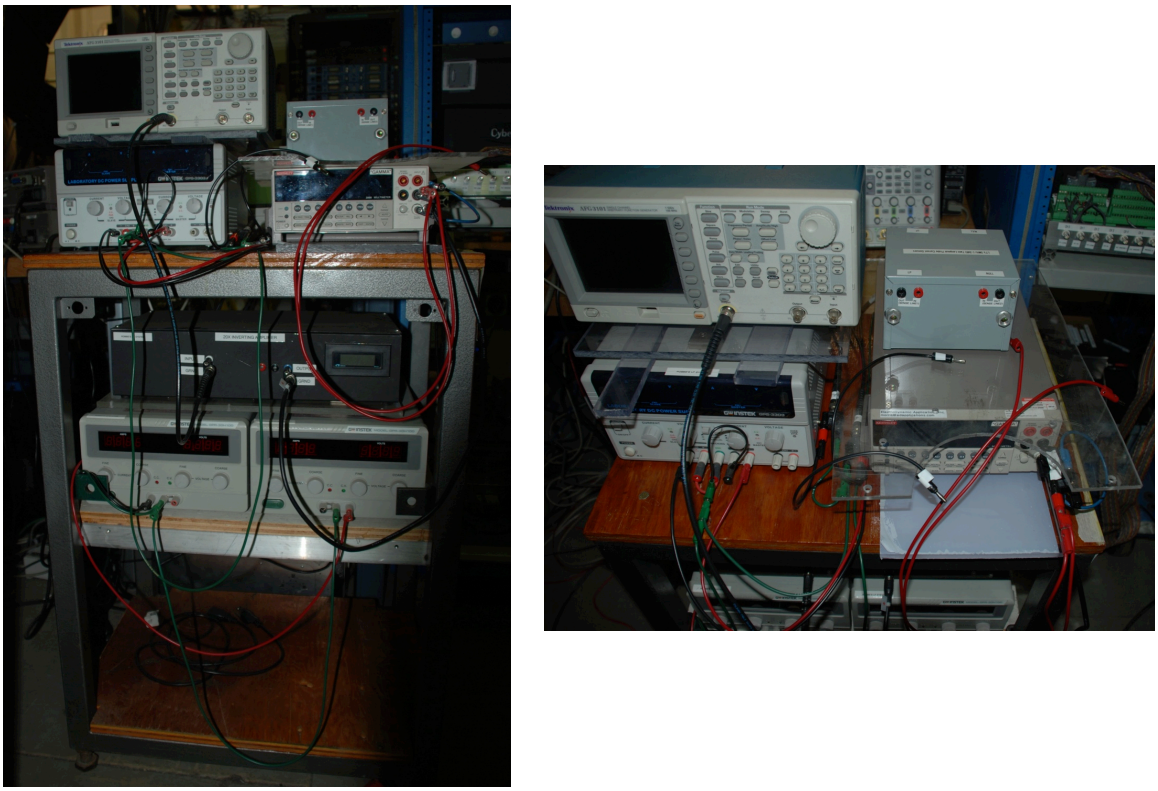

Figure B.**8:** A picture of the HDLP system set up for testing.

- Never power an amplifier with unconnected (floating) inputs. This isn't an issue with the Twin LP Current Sensors box since the inputs are connected to ground through the voltage divider network (110 kOhm). If this were not the case, then connect a voltage source (set initially to 0 V) to the inputs, then power on the amplifier.

Running the LP setup

1. Make sure the LP and NULL black banana connections and the function generator red banana connections are disconnected from the box so a voltage is not applied to the op amps before they are turned on.
2. Make sure the Keithley DMM 2000 is set up in line between the Amplifier and the Twin LP Current Sensors box to continuously measure current.
3. Turn on the multi-channel power supply that will be used to power the Twin LP Current Sensors box, the GW Instek GPS-3033, and make sure the output is off. Set the Voltage on both channels to 15 V and set the current limit to 0.5 A. Make sure the channel plus and minus connector ports are wired together as shown in Fig. B.9.
4. Plug in the ±15 V & ground connections from the power supply into the Current Sensors box. Use a green cord for the ground connection to avoid confusion.
5. Turn the output of the power supply on. Make sure the light next to the output on/off button is green, and make sure the current goes from the allotted amount, of 0.5 A to ∼0.05 A. (If necessary, check with a fluke to make sure it is applying a voltage).
6. Turn on the Tektronix AFG 3101 function generator. Make sure the output is off, and make sure it is connected to the Amplifier. Set the load impedance to High Z, and select sine wave output. To sweep from -20 V to 50 V once the signal is passed

through the -20x Amplifier, set the V_{pp} to 3.5 V, and Offset to -750 mV. Also set the frequency to the desired value (say 100 Hz for time-averaged sweeps).

7. Turn on the Amplifier.
8. Turn on the two GW Instek GPR-30H10D power supplies (rails) for the Amplifier and adjust their voltages. To sweep from -20 V to 50 V, set the rails to -30 V and 60 V– 10 V higher on each end.
9. Turn the function generator output on and check the Amplifier output on an oscilloscope, such as the Agilent DSO-X 3024A, and then turn the function generator output back off.
10. Plug the Amplifier output into the red banana ports on the back of the current sensing box, which are the input connections for V_{IN}.
11. Plug the two BNC outputs for the LP (V_{high} and V_{low}) into an oscilloscope.
12. With the plasma source on, plug the LP's pin connection and the Null's pin connection into the black banana ports on the back of the current sensing box, which are the input connections for V_{LP} (or V_B) and V_{Null}. Turn on the function generator, and check the output on the Keithley DMM to make sure the max current is less than 150 mA. The following relations along with the output on the scope can also be used to calculate the current:
    $I \sim (V_{high}\text{-}V_{low}/Gain)/R_{shunt} \sim \Delta V^*(10/1000\ \Omega) \sim \Delta V/100$ Since Gain $\sim 1/11$ and $R_{shunt} \sim 1000\ \Omega$.
    *Note: The max current of the measurement range of the Twin LP Current Sensors box is 200 mA given the shunt and dividing network resistor values, [14], and (200 x 100) mA*Ohm = 20 V gives the max voltage difference (between V_{high} and V_{low}) that should be seen on the scope in order for the measurements taken to fit within the measurement range for this particular Current Sensors box configuration.*
    Note: The voltage of the two sine waves will be reduced by a factor of ∼1/11 due to the voltage division network (i.e. ΔV = 70 V then V_{pp} = 6 V on scope).
13. Use the math function on the scope so you can see how the LP traces will look, and to make sure the sweep range chosen is covering the entire plasma LP I-V characteristics.
    a. Press the Function softkey and select g(t): Internal.
    b. Use the Operator, Source 1, and Source 2 softkeys to set up an arithmetic operation.
    c. Press the Function softkey and select f(t): Displayed.
    d. Use the Operator softkey to select a transform function or filter.
    e. Press the Source 1 softkey and select g(t) as the source. Note that g(t) is only available when you select a transform function in the previous step.
    f. If differentiation is too sensitive to the noise, set acquisition mode to Averaging
14. Plug the BNCs into the DAQ and make sure the 'Getting Started – Auto Time and Write.vi' is ready for taking and saving data to the computer. Record the channel that is being used for each record. Make sure to have a channel for each of the following values:
    a. V_1 (V_{LP}) low
    b. V_1 high
    c. V_2 (V_{NULL}) low
    d. V_2 high
15. Precautions and tips for using the General Standards PMC66-16AISS8AO4 8-channel

2 MHz DAQ Card with a LabVIEW interface are as follows:

a. Don't apply any more than ±15 (when the DAQ card is not powered) or ±25 V (when the card is powered) to any channel of this DAQ board.
b. On the VI set input mode to Single Ended which means that every channel measures a high relative to a common ground
c. The DMA is where it writes the data. It is green if it actually took all the data. You have to use a minimum sampling time in order for it to work.
d. When the buffer overflow button is red, it means data was lost. Redo that acquisition, or decrease the sampling rate and try again. If this doesn't work, open and run the Getting Started vi once to "reconfigure" the board. As a last resort, if the problem persists, reboot the computer.
e. Unplug the DAQ from the chamber before configuring the card and before turning on/off or changing the operating condition of the plasma source, as these events can introduce transients up to 10x the max steady state voltage, which could damage the DAQ.

16. Make sure everything plugged in as shown in Fig. B.9. Turn on the function generator's output, and then take and save data using Getting Started – Auto Time and Write.vi.
17. Turn off the function generator and unplug the LPs from the Current Sensors box until data will be taken again. Make sure to have a system for recording data file names and the corresponding probe position for each data point.
    Note: Cap the exposed banana connectors before setting them on any non-insulating surfaces.
    Note: Make sure the cathode is stable at each data point, and that the taking of data does not change the plasma source's steady state parameter values.

Shutdown Procedure

1. At this point, the LPs should be unplugged from the Current Sensors box.
2. Unplug the LP Current Sensors box leads from the DAQ.
3. Turn off the function generator.
4. Unplug the red banana inputs to the Current Sensors box.
5. Turn off the rails to the Amplifier.
6. Turn off the Amplifier.
7. Turn off plasma source.

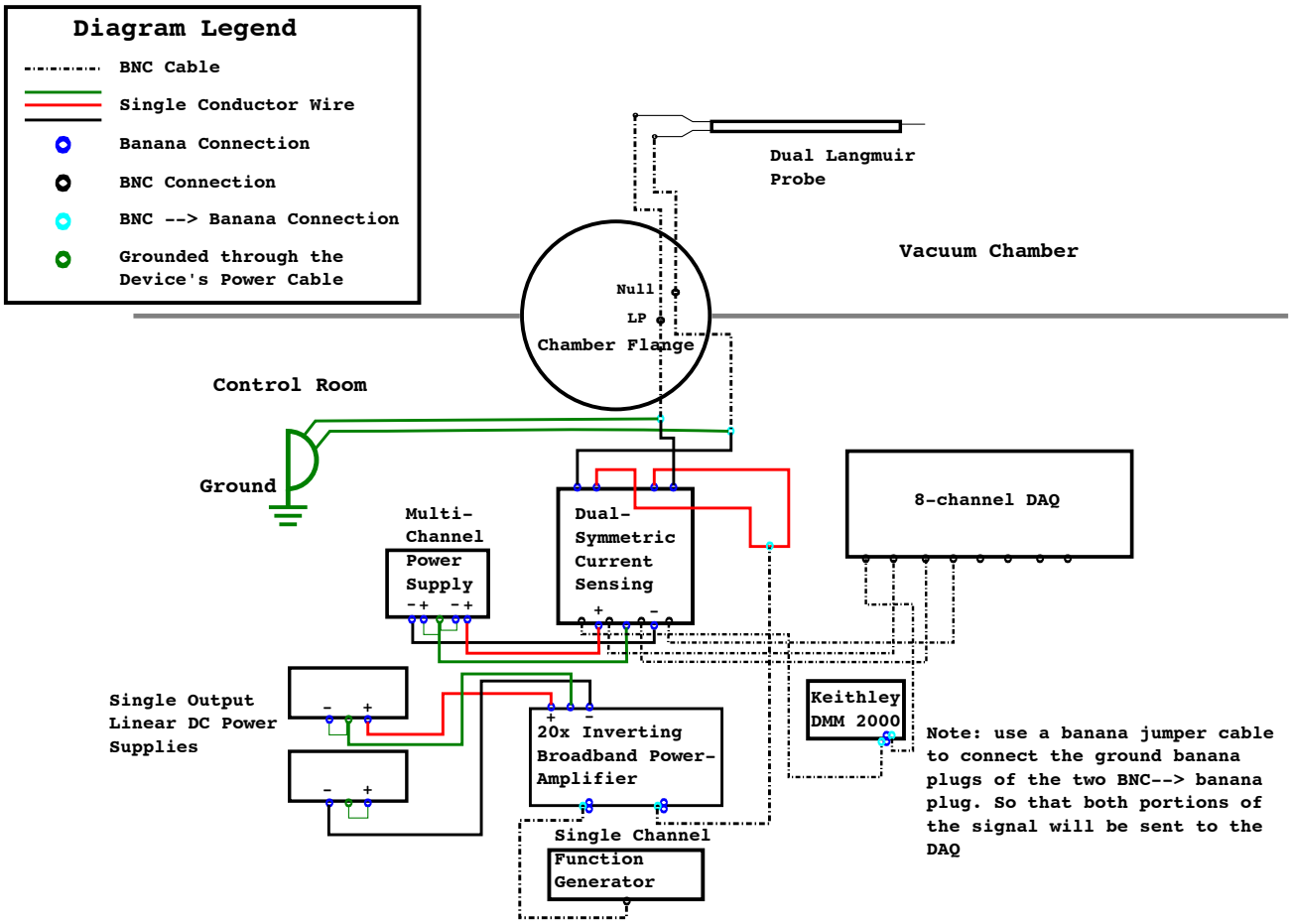

Figure B.9: Block diagram of the HDLP system connections. Based on a diagram drawn by Ray Liang and modified to include the dual Langmuir probe. Zoom in to see details.

B.5 RPA Run Procedure

Recommendations for Mounting the RPA in the Chamber, Taking Data, and Troubleshooting its Operation

written down by Kimberly Trent

References: PEPL's Procedures for Running Hall Thrusters v.1.1 (Guide to the West Side) (internal document), Operation of the PEPL Retarding Potential Analyzer by Jesse A. Linnell and Alec D. Gallimore (internal document), past and present PEPL members, and the manuals for the equipment used

- For the most accurate results and to reduce noise in the data, it is best to have at least four grids in the retarding potential analyzer (RPA). The first three grids are the floating grid, the electron repelling grid (which repels electrons from the plasma) and the ion retarding grid respectively. The fourth grid is an electron suppressor grid placed right before the collector to repel secondary electron emission (SEE) from the collector in order to send this current back to the collector to cancel out its effect on the measured current. In addition, this grid deflects SEE from the electron repelling grid and the ion retarding grid that is produced from ion collisions with these grids.
- When determining whether the RPA chosen or being designed will be suitable for a particular application, consider the spacing between the grids. Specifically, the grids need to be close enough so that the voltage gradient between the grids due to space charge is not larger than the voltage gradient applied to the various grids. Space-charge limitations are a concern because of the action of the grids in filtering out specific charge species by repelling or attracting particles of either negative or positive charge leaving a non-neutral plasma in its vicinity. If the potential between the grids is modified too much by the presence of this plasma, then it will affect the amount of current the collector acquires. To estimate grid separation, the expected plasma current density at the RPA inlet's downstream position, and the corresponding amount of current density between the grids (which is the inlet density reduced by the attenuation factor of each grid it passed through) will be needed. See Ref. [137] Section 3.4.2 & Ref. [106] for the equations to use to determine the grid spacing.
- Consider drilling holes in the back plate of the RPA and in the collector to allow the neutrals from the plume to flow through and not cause a build up of pressure inside the probe, which could negatively affect accurate data collection. See Ref. [184] which discusses this for ExB probes.
- The positioning of the RPA relative to the thruster will be dependent on the thruster, operating conditions chosen, and the experiment to be carried out. If four or more grids are being used, consider RPA locations that will allow for obtaining a signal that will be strong enough.
- The RPA is not very sensitive to alignment error since it has a large acceptance angle. A laser can be placed on top of the RPA with its front face flush with that of the RPA to make sure it is pointing to the chosen location on the thruster.

- Make sure there is a method in place for protecting the RPA from the thruster plume while it is not taking data using either a rotating shield as described in the **ExB Probe Run Procedure**, Section B.6, or by placing the probe on movable stages that can move the probe out of the thruster's plume, see Fig. 3.7 & Fig. 3.9(b).
- In order to reduce the flux of heat to the probe, cover as much of it as possible with graphoil or boron nitride spray depending on the application and the probe's distance from the thruster. See Fig. 3.9(a) for an example. Also protect the probe mount with graphoil, fiberglass sleeving or boron nitride spray, depending on the mount's design and the probe's distance from the thruster, to prevent sputtering of the mount material. See Fig. B.6(c) & Fig. B.6(d) for an example.
- Employ practices for protecting the cables of this probe and for checking out the probe prior to testing similar to those described in the procedure for Langmuir probes, called **Steps for Making and Mounting Dual Langmuir Probes**, Section B.2. Make sure to ground the RPA's metal enclosure.
- The RPA grid jack (or pin) and shield combinations were meggered at 600 V for 30 s since the highest voltage operating condition that would be tested (300 V) would require the ion retarding grid to be swept between 0-600 V. When meggering the RPA grids before incorporating the probe into the setup, if the grid isolation is not high enough (100s of MΩ to 10s of GΩ) and the probe was used for a previous test, try increasing the meggering voltage to 1000 V to zap any debris that may have been caught between the grids to see if this makes a difference. Repeat this a few times if it seems to be improving the isolation at 600 V. If this does not fully solve the problem, then the RPA will have to be taken apart so that each of the grids and the ceramic spacers can be cleaned. This had to be done regularly for the probe used since 'conductive soot' ends up getting deposited along the inner surface of the ceramic spacer rings, which decreases the electrical isolation between the grids. Therefore, make sure the RPA is designed in such a way that it can be easily disassembled for this cleaning process and then reassembled for testing. It was found that the inner RPA components had to be cleaned after each test with the 6-kW Hall Thruster after being positioned 2-3 thruster diameters downstream for taking data. The spacers were cleaned with sandpaper and then IPA and Kimwipes. The grids were cleaned with IPA and Kimwipes.
- See Fig. B.10 for a diagram of how to hook up the equipment used to take RPA data, and the electrical diagram for this probe.
- Follow the procedural tips listed in the **HET, Probe and LVTF Pre-Pump Down Checklist**, Section B.11.
- An ExB/RPA LabVIEW VI program was written to take and save the data. When taking data, make sure that 'Autorange' is selected on the Picoammeter.
- While taking data, if there are abnormal peaks in the lower and upper voltage regions of the trace, and all the procedural tips listed above were followed, try decreasing the voltage on the electron repelling and electron suppressor grid to a more negative value. See [106] Section 5.3.4.3 for detail on why.
- Check for repeatability of the measurements to determine if variations in the probe conditions (such as temperature and pressure) throughout testing had negligible effects on the data.
    - Take multiple sweeps one right after the other over a period of several minutes and make sure there is no drift between the different traces.

    - Run the voltage sweep from high to low voltage, and from low to high voltage. Compare the sweeps, and check for hysteresis.

- For additional words of advice and guidelines for taking RPA data that may be relevant to one's particular application, including probe calibration, see Ref. [137] Section 3.4.2 & Ref. [106].

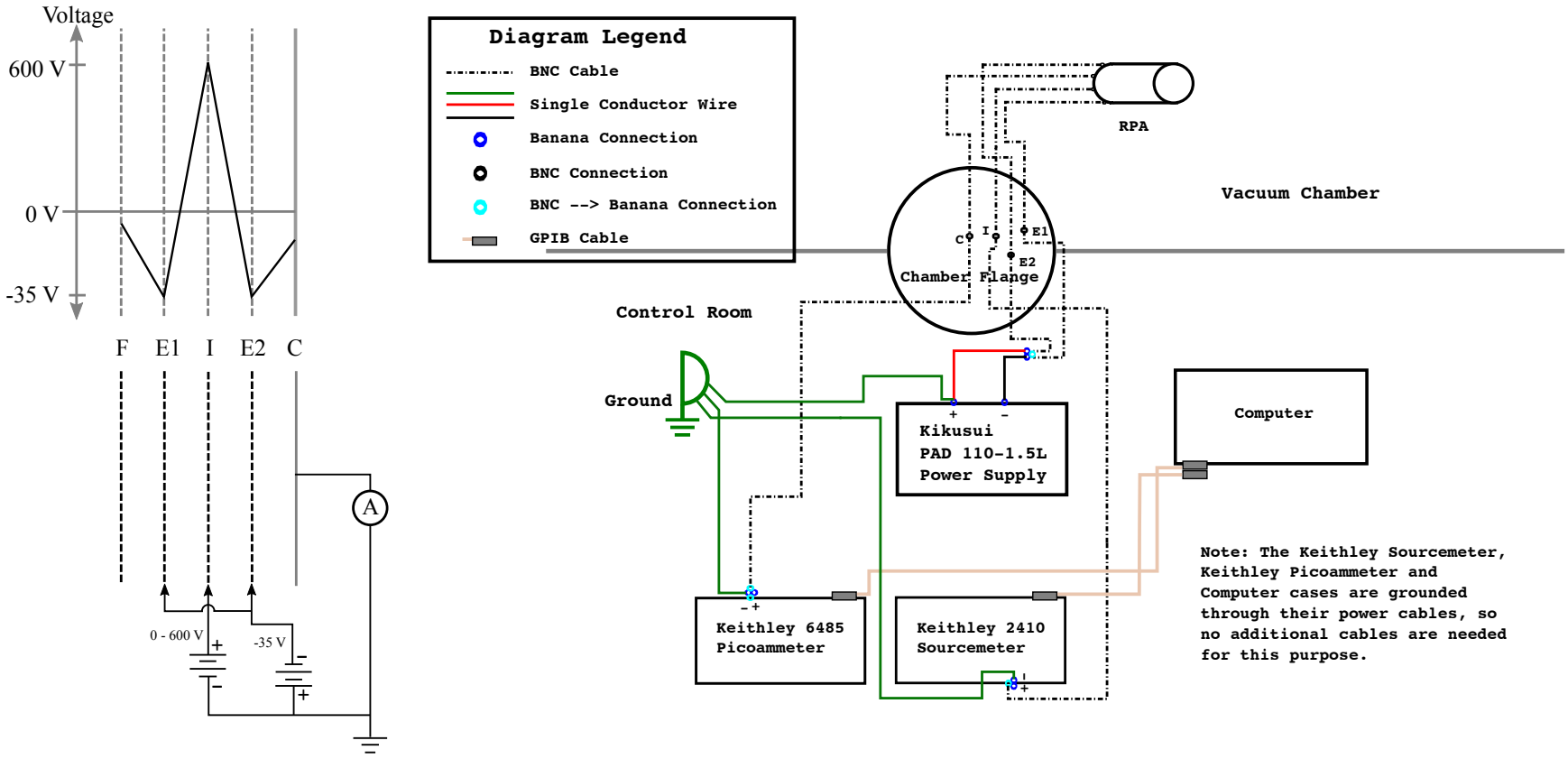

Figure B.**10:** Picture on the Right: Block diagram of the RPA system connections. Based on a diagram from Guide to the West Side and modified to show how the equipment was grounded for the tests conducted in this thesis. Zoom in to see details. Picture on the Left: RPA electric circuit, taken from Ref. [106] and modified to show how the grids were wired electrically for the tests conducted in this thesis.

B.6 ExB Probe Run Procedure

Recommendations for Mounting the ExB Probe in the Chamber, Taking Data, and Troubleshooting its Operation

written down by Kimberly Trent

References: PEPL's Procedures for Running Hall Thrusters v.1.1 (Guide to the West Side) (internal document), past and present PEPL members, Reference [184], and the manuals for the equipment used

- When determining how far downstream from the thruster's exit plane to place the probe, consider a balance between keeping the probe from overheating, by making sure it is not too close, and getting a large enough signal, by making sure it is not too far away. Typically, the probe is placed about 1-3 m downstream.
- Decide whether to align the probe with channel centerline or thruster centerline depending on the thruster, operating conditions chosen, the experiment to be carried out, and the probe's distance from the thruster.
- Incorporate a 3 or 4 screw leveling platform into the mount for the probe, as seen in Fig. 3.8(b). Then use a bubble level to determine if the platform is not slanted, and use the screws to easily adjust as needed. Also place the probe onto rails so that its horizontal position (parallel to the exit plane of the thruster) can be adjusted easily. Fig. 3.8(b) shows one way to do this by using two pieces of 80/20 that the probe and theta stage are secured to with screws whose heads are inserted into the top slot of the 80/20 and thread through the base of the theta stage, which the probe is secured to the top of, and that are then held into place with nuts. Thirdly, make sure there is a way to adjust the overall vertical height of the entire mount, such as the method used in Fig. B.11.
- Since the ExB probe has a very narrow acceptance angle due to its small inlet orifices at the two ends of the relatively long entrance collimator, the probe should be aligned using a laser and mirror.
    1. Use an optical tube attachment that can be screwed into the ExB probe, where the exit collimator would go during normal operation, and that can hold a laser centered in the holder so that its beam will be projected down the center of the probe and out through the orifice screwed onto the front of the entrance collimator.
    2. With the help of another person, adjust the vertical position of the probe using the height adjustment feature incorporated into the mounting structure.
    3. Place the mirror in front of the thruster at the location the ExB probe is to be lined up with and flush with that surface.
    4. Make sure the mirror reflects the laser light back to the probe's orifice or as close to that location as possible, at least to within 1 cm, however with the mount shown in these pictures and the alignment procedure described here, the laser light was easily able to be reflected back to the probe's orifice as observed visually. It helps to have two people for this process. One to hold the mirror and

one to adjust the probe to its final position using the rails the probe is mounted on.

5. If available, the probe can also be placed on a theta stage so that if any minor adjustments need to be made after pump down, this can be done without venting the chamber. Still, the best course of action is to make sure the probe is properly aligned before pumping down.

- Set up a graphoil shield that can be rotated in front of the probe to protect it from the thruster plume while it is not taking data using a motor that can be controlled from outside of the chamber. Make sure that when the shield is rotated away from in front of the probe that it is not in the line of sight of the probe or interacting with the plume.
- In order to reduce the flux of heat to the probe, cover as much of it as possible with graphoil. Also cover the probe mount with graphoil to prevent sputtering of the mount material. See Fig. 3.8(b).
- Employ practices for protecting the cables of this probe similar to those described in the procedure for Langmuir probes, called **Steps for Making and Mounting Dual Langmuir Probes**, Section B.2.
- An ExB/RPA LabVIEW VI program was written to take and save the data.
- Once taking data, if the data is only showing noise and all the connections have been checked, and the procedural tips listed above and in the **HET, Probe and LVTF Pre-Pump Down Checklist**, Section B.11, were followed, try switching the BNC connections outside of the chamber that are connected to the left and right electrode plates of the probe.
- See Fig. B.12 for a diagram of how to hook up the equipment used to take ExB probe data, a diagram of the circuitry inside of the ExB probe's Voltage Splitter Box, and the electrical diagram for this Box and the probe.
- The voltage splitter box contains circuitry to divide the voltage, being applied to the two parallel plates inside the probe, around facility ground. This is done so that while sweeping the bias voltage, probe induced perturbations to the plasma plume in the vicinity of the probe are minimized since the center of the test section stays at a constant value— around facility ground.
- Select an inlet orifice size to keep peak collected current at around 10^{-9} A to retain an acceptable signal to noise ratio. [184] To estimate inlet orifice size, consider the expected plasma current density at the inlet's downstream position.
- Check for repeatability of the measurements to determine if variations in the probe conditions throughout testing had negligible effects on the data.
    - Take multiple sweeps one right after the other over a period of several minutes and make sure there is no drift between the different traces.
    - Run the voltage sweep from high to low voltage, and from low to high voltage. Compare the sweeps, and check for hysteresis.
- For additional words of advice and guidelines for taking ExB probe data that may be relevant to one's particular application, see Ref. [184].

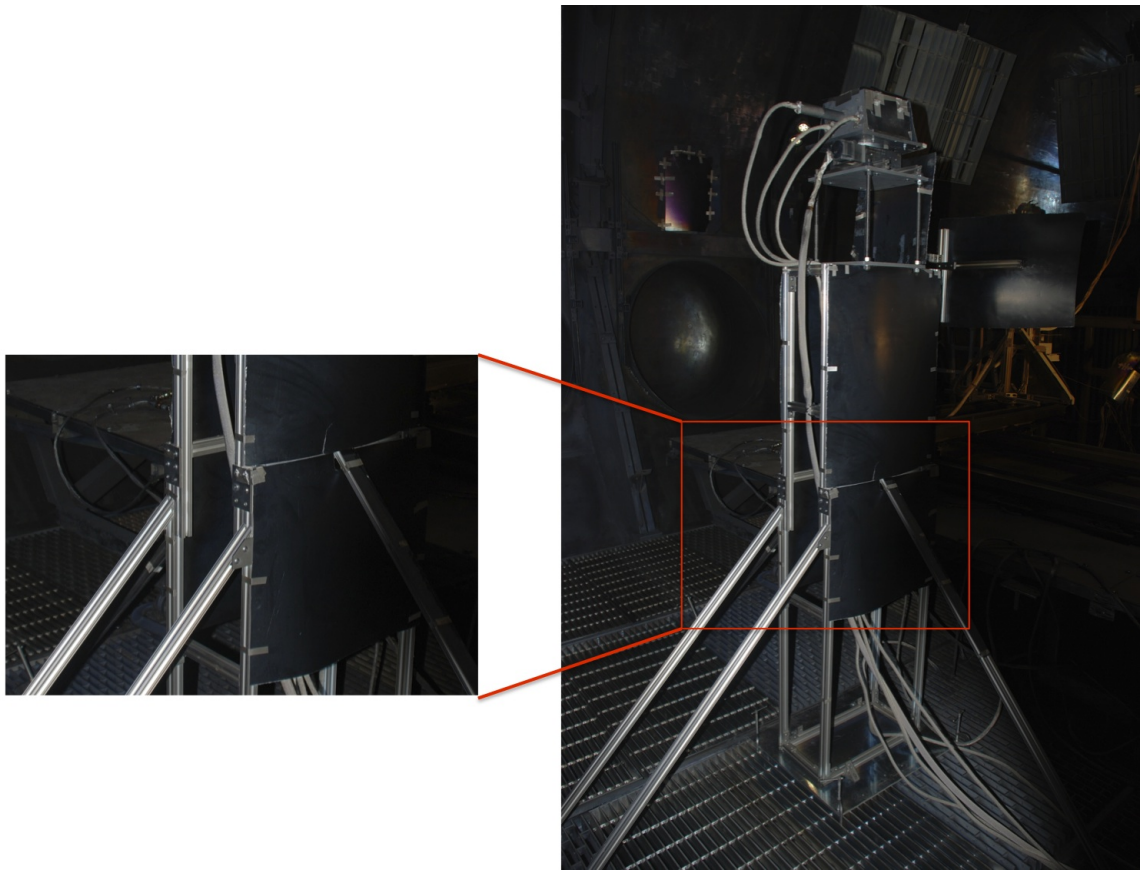

Figure B.**11:** Picture showing how the height of the ExB probe mount can be adjusted. By loosening the four rectangular braces at the front and back of the mount that are holding overlapping pieces of 80/20 rod together, the vertical rods forming top of the structure can be shifted up so that they overlap the bottom rods less making the structure higher, or shifted down so they overlap more and bring the probe to a lower height. The zoomed in portion of this picture shows the two rectangular braces at the back of the mounting structure. The other two are in the front.

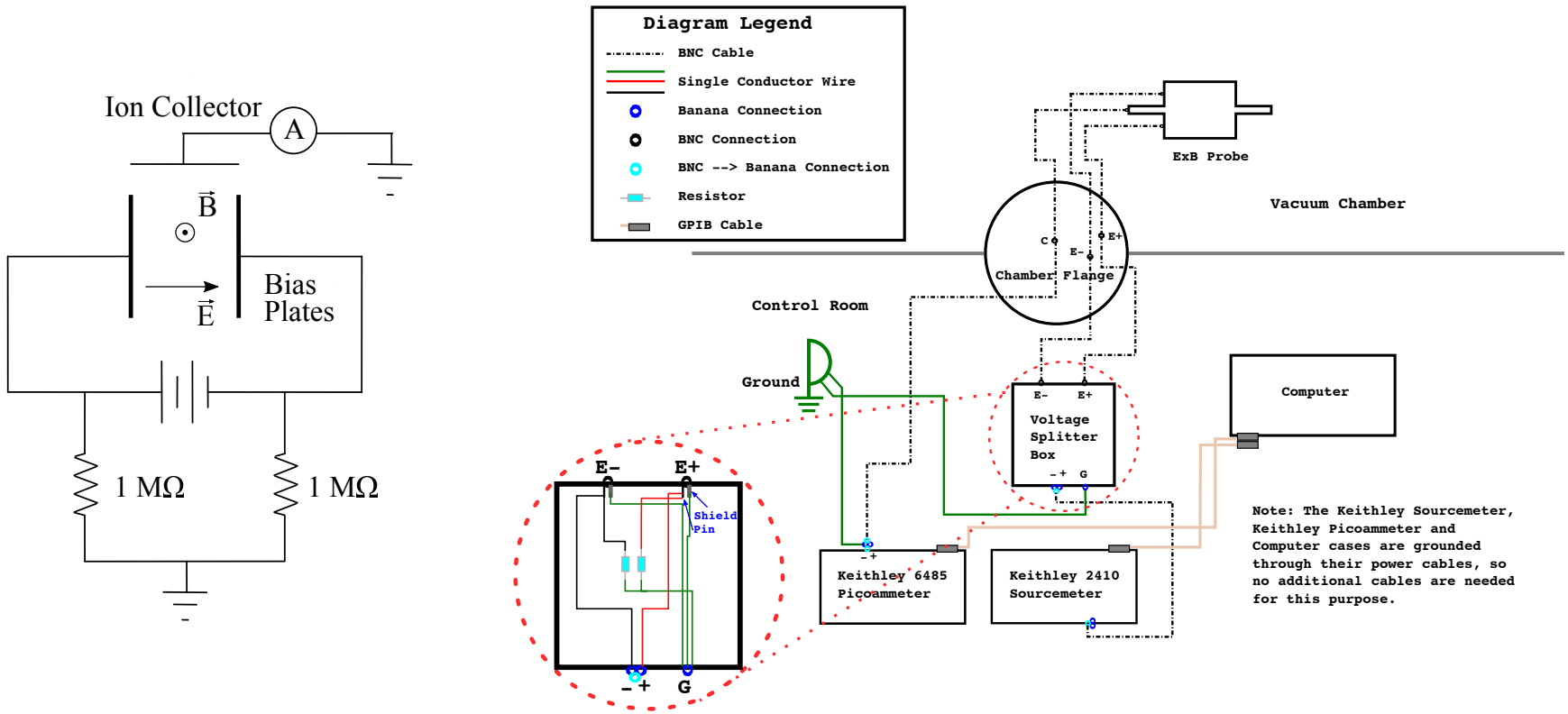

Figure B.**12:** Picture on the Right: Block diagram of the ExB probe system connections. Based on a diagram from Guide to the West Side and modified to include the Voltage Splitter Box circuitry. Zoom in to see details. Picture on the Left: ExB probe electric circuit, taken from Ref. [55] and modified to include the electric and magnetic field directions.

B.7 FP Run Procedure

Recommendations for Mounting the FP in the Chamber, Taking Data, and Troubleshooting its Operation

written down by Kimberly Trent

References: PEPL's Procedures for Running Hall Thrusters v.1.1 (Guide to the West Side) (internal document), past and present PEPL members, and the manuals for the equipment used

- Determine the type of Faraday probe (FP) needed for the application. There are magnetically-filtered, gridded, reduced acceptance angle, collimated, and nude Faraday probes. See Ref. [55] subsection 4.8.4 for more details.
- Decide if a guard ring is needed on the FP. This will depend on the Debye length in the region where the probe is placed. The purpose of this ring is to flatten the sheath at the edges of the probe collection area to create a uniform sheath across the entire collection surface. In order for this to happen, the gap between the probe and the guard ring has to be less than a Debye length to ensure that the sheaths of the two surfaces overlap. See Refs. [55] & [16] for the equations to use to determine spacing between the ring and the probe.
- The positioning of the FP relative to the thruster will be dependent on the thruster, operating conditions chosen, and the experiment to be carried out. Consider FP locations that will allow for obtaining a signal that will be strong enough.
- To have control over the radial distance of the probe from the thruster, in addition to the angular position, mount a linear stage on top of the theta stage. This way the theta stage can stay centered over the thruster exit plane while the length of the arm holding the probe changes its radial extent.
- A laser can be placed on top of the FP with its front face flush with that of the FP to make sure it is pointing to the chosen location on the thruster. To ensure that the probe is properly centered on the thruster, measure the radial distance between the front face of the probe and the center of the thruster when it is at +90° from centerline, 0°, and -90° from centerline, (while not moving the linear stage if using one), and make sure all the numbers match.
- Make sure there is a method in place for protecting the FP from the thruster plume while it is not taking data using either a rotating shield as described in the **ExB Probe Run Procedure**, Section B.6, or by placing the probe on movable stages that can move the probe out of the thruster's plume, see Fig. 3.7 & Fig. 3.9(b). For the tests conducted in this thesis, the cover position for the probes on the rotational arm was +150° and ∼3 thruster diameters from thruster centerline.
- In order to reduce the flux of heat to the probe, cover as much of it as possible with graphoil or boron nitride spray depending on the application and the probe's distance from the thruster. See Fig. 3.9(a) for an example. Also protect the probe mount with graphoil, fiberglass sleeving or boron nitride spray, depending on the mount's design and the probe's distance from the thruster, to prevent sputtering of the mount material. See Fig. B.6(c) & Fig. B.6(d) for an example.

- Employ practices for protecting the cables of this probe and for checking out the probe prior to testing similar to those described in the procedure for Langmuir probes, called **Steps for Making and Mounting Dual Langmuir Probes**, Section B.2.
- See Fig. B.14 for a diagram of how to hook up the equipment used to take FP data, and the electrical diagram for this probe.
  Note: A metal foil resistor was used for the FP measurements due to its low thermal drift. The 56 Ohm Texas Components S105K metal foil resistor used has a temperature coefficient of resistance (TCR) of $\sim \pm$ *1 ppm/°C.*
  Note: The shunt box can be set up with multiple shunt circuits so that multiple FPs can be run off of one shunt box, or so that an FP can easily be switched between different resistance values.
  Note: As shown in Fig. B.*14 & Fig.* B.*13, make sure to twist the wires going from the FP Shunt box to the datalogger to reduce noise. Also make sure to keep these wires as short as possible.*
- Make sure the datalogger lines that will be used for taking data have been calibrated.
- A Faraday probe LabVIEW VI program was written to take and save the data.
- Before pumping down, do a dry run of the Faraday probe angular sweeps to make sure none of the cables get caught and to make sure the VI is working with the tables as expected.
- Follow the procedural tips listed in the **HET, Probe and LVTF Pre-Pump Down Checklist**, Section B.11.
- Check for repeatability of the measurements to determine if variations in the probe conditions (such as temperature and pressure) throughout testing had negligible effects on the data. One way to do this if taking semi-circular spatial sweeps (which should go through at least +100° from centerline to -100° from centerline) in front of the thruster is to then retrace the probe's trajectory by sweeping it back in the opposite angular direction and comparing the traces to check for hysteresis.
- For additional words of advice and guidelines for taking FP data that may be relevant to one's particular application, see Ref. [16] Section 3.3.5 and Chapter 4.

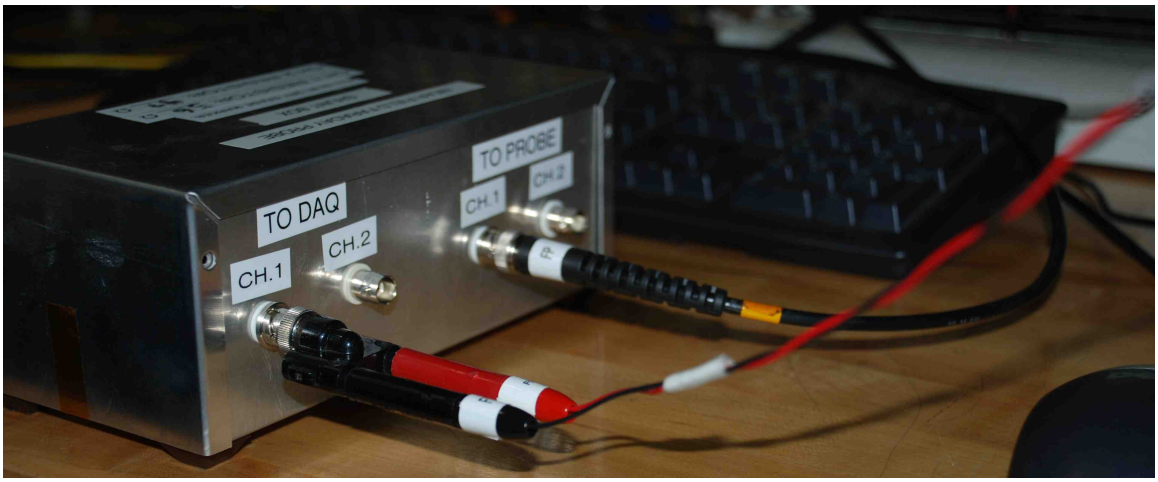

Figure B.**13:** Picture of the connections coming out of the FP shunt box and going to the probe and the datalogger. See Fig. B.14 for how the shunt box fits into the entire FP measurement circuit.

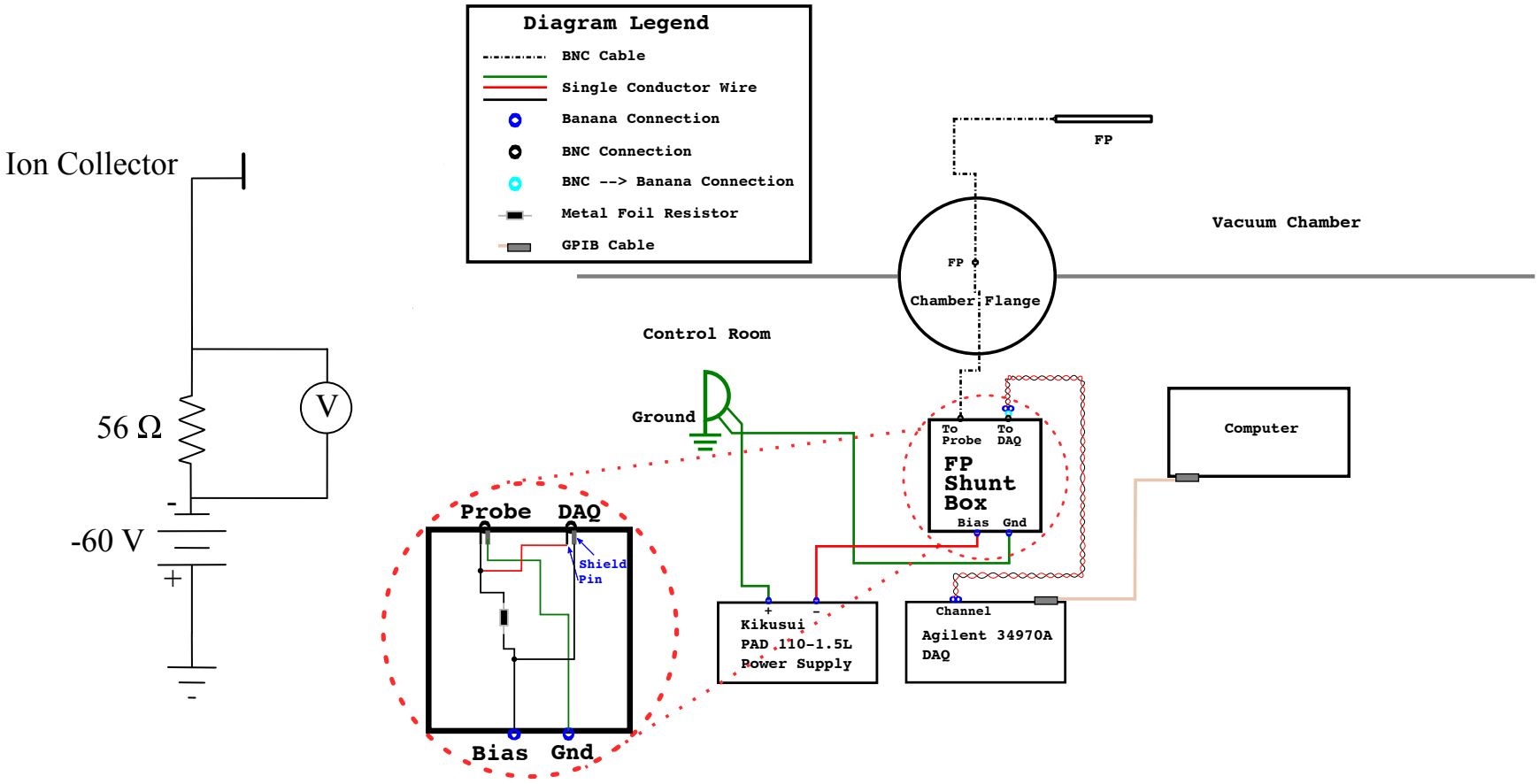

Figure B.**14:** Picture on the Right: Block diagram of the FP system connections. Based on a diagram from Guide to the West Side and modified to show the wiring inside of the shunt box. Zoom in to see details. Picture on the Left: FP electric circuit.

B.8 Thrust Stand Procedures

B.8.1 Thrust Stand Preparation

Thrust Stand Prep Instructions

by Kimberly Trent and Dr. Ray Liang

References: PEPL's Procedures for Running Hall Thrusters v.1.1 (Guide to the West Side) (internal document), and the Manuals for the equipment used

Version 2.0 February 2015

Equipment

- Thrust Stand
  - Inclinometer and inclination gear motor
  - Calibration (Cal) weight stepper motor and calibration wheel
  - Weights and pulley wheel
  - Mettler AE200 Balance Scale
  - Damper or Null Coil
  - Linear Voltage Differential Transducer (LVDT) transformer, mounting block, core and core connecting rod (Schaevitz model HR-100)
- Cole-Parmer Economical 200-mm Flatbed Recorder 2-Channels K-80550-30 or a data logger with isolated channels
- Thrust Stand Electrical Box
  - PID (Proportional–Integral–Derivative) Controller/Transducer (analog Stanford Research Systems (SRS) SIM960 PID controller, for the null or damper coil)
  - Trust Automation Inc. Linear DC Brush-Motor Servo TA105 amplifier used to drive the null coil
  - LVDT Controller (ATA-2001 LVDT amplifier)
  - Inclinometer and Cal weight readouts
- Thrust Stand's Refrigerated Recirculating Chiller and cooling shroud

Overall Procedure from Preparing the Thrust Stand through Mounting the Thruster on the Stand and Up to the Various Tuning, Checkout and Calibration Procedures to get the Thrust Stand Ready for Pump Down

1. Remove the thruster mounting stand and then the shroud from the thrust stand. Make sure all screws in the thrust stand are secure. They can become loose with the thermal cycling the thrust stand goes through, and from handling, such as the banging of the moving plate against the copper shroud. Make sure the LVDT core and bracket are securely attached to the moving plate. The LVTD core and coil need to be securely mounted for good measurements.
2. Make sure the thrust stand is free from debris and excessive amounts of collected dirt. Use a Kimwipe and IPA if needed.
3. Make sure null and damper plungers are not scraping the inside of their respective coil. Adjust the positioning if needed.

4. Make sure the LVDT core is not scraping along the LVDT coil. Adjust positioning if needed.
5. Make sure the LVDT coil is completely centered in the axial direction inside its mount. Since the coil will thermally expand around this position, and this is the location where the LVDT core will be placed (as detailed in a later step), it will be best if the thermal expansion is happening symmetrically around this point.
6. Make sure all the thermocouples are hooked up and are in the locations where temperature monitoring is desired.
7. Make sure all levels of the thrust stand are level using a bubble leveler in various places on each level of the thrust stand. If it is not level in the direction perpendicular to thrust, use the screw leveling system in the stand to adjust this. This is not an easy task as there is barely any room for the wrench to get in. Use vice grips to assist if needed. Level the stand in the direction parallel to thrust using the inclination motor. It is easier to make sure the mount where the thruster is placed is level if you make sure all levels of the thrust stand are level first. This includes the cylindrical podium that the thruster mounting platform is placed on top of. Use washers where the four screws are placed to obtain a level surface, then tighten everything down.
8. Place the shroud and thruster stand back on the thrust stand. Leave the two side panels off, as you will need to reach in to adjust the LVDT once the thruster is on the thrust stand. Make sure that the thrust stand's cooling lines are hooked up to the chiller lines and that there are no leaks at any of the connection points.
9. Mount the thruster in the chamber on the thrust stand. Hook up all electrical and gas connections. Make sure all electromagnet cables are twisted pairs. Make sure all electrical cables go through the waterfall clamp, and make sure the waterfall is set up as described in literature, see Ref. [185].
10. Make sure all Viton tubing has a torturous path (at least a half turn, 1 full turn to be extra safe, to prevent electrical arcs along the length of the tube). Align cathode(s) and probes.
11. Weigh the weights using EDA's Mettler AE200 scale if you do not have these values or if they have not been weighed in a while. You must cut all weights off their fishing line because this line will interfere with the measurements. Before you cut the weights off the line, make sure you record the length of fishing line between each weight. It's not crucial to replicate the previous lengths and spacing, but it could save time in case you get it way off (See Fig. B.15). More spacing between weights will be better than not enough, but you should be consistent. Make sure the stand inside of the scale where the weights are placed is level by using a bubble leveler. Clean off the surface of the weight stand to make sure it is free of contaminants. Make sure you give the scale the proper amount of time to warm up. See the manual for details and for setting choices given the environment you are making the measurements in. This step is important because the thrust stand measurements rely on accurately knowing the weight of these calibration weights.
12. Reattach the weights using bowline knots. Don't use half hitches after the bowline knot because if these are pulled too tight, the line will snap.
13. Make sure the location where the eyebolt screws into the back of the thruster is aligned with the thrust vector and the cal weight pulley system so that the calibration system will transmit all force from the cal weights to the thrust stand. [103]
14. Make sure that when a fishing line is strung across the pulley wheel and hooked onto

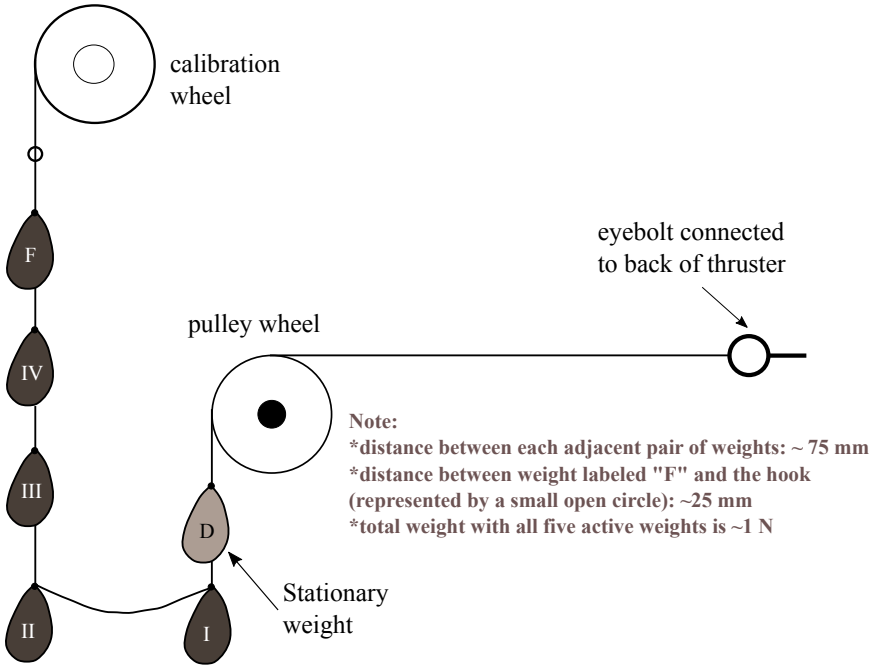

Figure B**.15:** Drawing of the thrust stand's weight calibration system. Based on a diagram from Guide to the West Side and modified to include the length of the fishing line between adjacent weights for the weight system that puts a total of ∼1 N on the thrust stand, and points out the Cal wheel, pulley wheel and eyebolt referred to in this procedure

the eyebolt on the back of the thruster, that it will be horizontally level (See Fig. B.15). You can check this by lightly resting a level on top of a test piece of wire strung tautly between these two points, or use a level that has hooks attached to its two ends so that it can be hung from the line.

15. Measure the length of line you will need between the pulley wheel and the eyebolt that screws into the back of the thruster. This is easiest to do once all the other weights and the hook are tied onto the fishing line. Use the hook to attach the weights into the motor line (which has a metal loop tied to the end of it) and then string the end of the fishing line across the pulley wheel. When you perform the calibration, the weights should basically form two sets of vertical lines.
16. With the eyebolt screwed into the back of the thruster, measure how much fishing line you will need to reach the eyebolt. Then create a loop bowline knot at that point in the line. Cut the fishing line, and hook the loop into the eyebolt. Verify that the fishing line from the back of the thruster to the pulley wheel is in fact horizontal (See Fig. B.15).
17. Turn on the thrust stand electrical box and plug in the LVDT controller, which is powered separately from the rest of the box. Make sure all pieces of equipment get the proper amount of warm up time. (The LVDT controller needs a 20 minute warm up, and the PID needs a 1 hour warm up). It was found that the Inclinometer and Cal Weight readouts need about a half hour to give proper readings.
18. Adjust the spring so that the moving plate of the thrust stand is free to move, and make sure the segments of the spring do not strike each other.
19. The weight of the thruster itself may have shifted the LVDT's rest position and the

compression of the thrust stand's spring, so now that the thruster is on the stand, make sure neither permanent magnet of the null and damper plunger is scraping the interior of the electromagnets (the coil). Adjust the permanent magnets as needed for centering. Do the same with the LVDT core and coil. If the thruster is not that heavy, this step should not be needed since they were already adjusted in one of the first step.

20. Make sure there are no other interferences to the moving plate moving freely, including within the waterfall, or any of the cables. Make sure none of the moving parts in the entire setup are rubbing against fixed components, as this will affect thrust measurements.
21. Pick an inclination and set it roughly. Check the thruster mounting platform with a bubble leveler. This may change as the thrust stand setup proceeds, but the inclination should be close before you continue to adjust the thrust stand.
22. Check the LVDT range by displacing the thrust stand platform some known distance and seeing what that corresponds to in terms of the change in LVDT voltage output. Use the BK precision multimeter and a long BNC cable to reach from the thrust stand electrical box to inside the chamber so the LVDT signal can be directly monitored. It is a good idea to determine the range to get an idea of the resolution of the LVDT. This will give an indication of what a voltage drift value corresponds to in terms of the shifted distance of the LVDT (and hence the stand platform's moved distance), and what this translates into in terms of thrust, so that this can be compared with the claimed error and resolution of the thrust stand measurements. Adjust this range if necessary using the procedure in the manual. If this was set previously to a range that will work for the planned tests, then it does not need to be done again.
23. Next, as detailed in the manual, first zero the LVDT controller with the LVDT unplugged from the controller. Then plug the LVDT back into the controller, use the BK precision multimeter and a long BNC cable to reach from the thrust stand electrical box to inside the chamber, and then shift the position of the core inside of the coil until the LVDT output reads zero again, by first loosening the core's mount and then tightening it back down once this position is found. This is the location where the core is completely centered within the coil, which is the location of best performance for the LVDT.
24. Once this is complete come back outside the chamber and use the BK precision multimeter to set this position to about 2 V manually using the LVDT controller. 2 V is a good setting but not mandatory. 0 V is not recommended, as PID stability can be an issue.
25. Adjust the inclination of the thrust stand again this time only using the motorized screw leveling system to its final value and check it using the bubble level in various places around the thrust stand's thruster mounting platform.
26. Calibrate the analog flatbed recorder if this will be used to obtain thrust measurements. *Note that the flatbed recorder may filter out high frequency noise.* If not, just make sure to be aware of how it works and that the pens are in the location you want them in, and that the ranges you need are set for each of them. See the procedure called **Thrust Stand Flatbed Recorder Calibration Instructions**, subsection B.8.2. If comparing to previous flatbed recorder charts, the lower pen had black ink and recorded the LVDT signal (range is $\pm$ 5 V), while the upper pen was red and recorded the PID signal. If using the Datalogger, both the PID and LVDT signals

should also be recorded. Make sure the data logger channels being used are calibrated.

27. Turn on the chiller for the thrust stand.
28. Follow the procedure called **Thrust Stand PID Tuning Instructions**, subsection B.8.3, to tune the PID controller using the Ziegler-Nichols tuning method. This procedure follows the one detailed in the SRS PID controller manual.
29. Determine the value indicated on the Weight Calibration potentiometer readout when each weight is fully loaded onto the thrust stand. Make sure the PID controller is in PID Control mode.
30. Then, unload all calibration weights (except for the first weight, which is called the stationary weight or dummy weight) from the thrust stand, and with the chiller still on, wait for all the thermocouple temperatures, PID and LVDT values to come to steady state. *Note: It is best to never unload the stationary weight from the thrust stand, as then there is no way to ensure that the fishing line will stay in the groove of the pulley wheel.* See Figure B.15.

A brief overview of the next steps, which are further detailed in the subsequent procedures (see **Taking Thrust Measurements**, subsection B.8.5)

1. Perform the thrust stand calibration while making sure the inclination is held constant because the application of the weights causes small shifts in the inclination as shown in figure 7 of Ref. [103].
2. Pump down the chamber.
3. Carry out the thrust stand calibration again at vacuum.
4. Take thrust measurements.
5. Perform post-test thrust stand calibration.

B.8.2 Thrust Stand Flatbed Recorder Calibration

Thrust Stand Flatbed Recorder Calibration Instructions

For the Cole-Parmer Economical 200-mm Flatbed Recorder (2-Channels K-80550-30)
Based on manual with additional details from conversations with the company's engineers
Recorded by Kimberly Trent in December 2014

* It's easier to follow this procedure for one channel at a time. So do one channel, then go back and do the same for the second channel
* In REC/CAL, CAL gives a full scale signal to the recorder. So for normal operation this button should be in the REC position. CAL permits periodic calibration of any full scale range and/or allows customizing to any full scale range.
* In STBY/REC, STBY shorts the input. Meaning the internal input circuit is grounded to allow accurate setting of ZERO. The input signal is not grounded and can be left connected. But just to be sure, it can be disconnected as done in the calibration procedure below.
* ZERO adjusts true ZERO (ground reference) to anywhere on the chart. Center ZERO for AC signals, full scale ZERO for negative going signals.
* To determine what your ZERO is, go to STBY to temporarily disconnect your input signal while grounding the recorders internal input.
* Input Range Switch or FULL SCALE SENSITIVITY sets the full scale chart reading with the ATTEN fully CCW.
* ATTEN has no effect in fully switched CCW position. Otherwise, it smoothly reduces sensitivity of fixed full scale range to overlap the next less sensitive position.
* Adjust CHART DRIVE RANGE to the desired chart speed. Choose 1 cm/min.
* Do not apply a high input voltage with the range switch in a millivolt position even though the recorder is overrange protected.
* See Manual for other tips and troubleshooting tips.

1. Load paper and pens into recorder as detailed in manual.
2. Switch ATTEN off by turning it fully CCW.
3. Turn STBY/REC to STBY and turn REC/CAL to REC (not to CAL as stated in the manual). Make sure the chart switch is OFF, and range is set to 10 mV. Then turn the power for the recorder ON.
4. Allow the recorder to warm up for 10 minutes
5. Turn ZERO full CCW (off the scale to the left side) and turn the LOW LIMIT fully CW. Then turn ZERO fully CW (off the scale to the right side) and turn HI LIMIT fully CCW. This causes Auto overage to be disabled so other adjustments can be made.
6. GAIN: Set ZERO knob to approximately mid scale and adjust the GAIN CW until the pen buzzes. Then turn CCW until buzzing stops then a few degrees more. Run ZERO over full range. If there is any buzzing at any point, back the GAIN CCW until it stops.
7. OFFSET: Turn ZERO to zero the pen on the chart paper. Adjust OFFSET for minimum shift of the pen while switching the Input Range switch between 50 mV and 100 mV (.1 V), which is where the ranges switch over inside the recorder. This ensures that this shift is a smooth transition. At optimum setting it is normal to have

a small shift (0.5%) at lowest mV ranges. Also check this when the ZERO is turned to about mid range (∼50 on chart paper). Don't forget to turn ZERO knob until pen on chart paper is back at 0 before the next step.

8. Calibrate Recorder Ranges: Use an accurate (0.5% or better) Voltage Source. Use the function generator feature on the Agilent InfiniiVision DSO-X 3024A oscilloscope (the Gen Out port) and adjust the output until it reads 10 mV on one of the calibrated BK precision 5491A DMMs. Set Input Range Switch to match voltage source input (10 mV). Connect it to the input for that particular channel by unplugging the BNC cable for that channel from the back of the thrust stand electrical box. Then change from STBY to REC.
9. Adjust SPAN until pen is at full scale. Change back to STBY and readjust zero with ZERO knob if necessary. Recheck full scale by switching back to REC and readjust SPAN if necessary. All ranges are now calibrated through this one range being calibrated. Check this by removing 10 mV input voltage, going to STBY in STBY/REC, switching to CAL in REC/CAL, and switching between all ranges using the Input Range Switch. Make sure the pen stays at full range.
10. Stay in STBY mode. Turn ZERO all the way CCW. Adjust LOW LIMIT until pen is half way between the sprocket holes and the paper 0.
11. Turn ZERO all the way CW. Adjust HI LIMIT until pen is approximately half way between the sprocket holes and the paper full scale value.
12. Then go to REC mode to start recording data.

B.8.3 Thrust Stand PID Tuning Instructions

Thrust Stand PID Tuning Instructions

For the analog Stanford Research Systems (SRS) SIM960 PID controller
Based on the procedure given in the controller's manual and PEPL's Thrust Stand Tuning Instructions by Dr. Bryan Reid (internal document)
with additions by Kimberly Trent
Version 2.0 February 2015

1. Make sure the inclination readout reads the value where the thrust stand's thruster mounting platform is level, as determined in the previous procedure called **Thrust Stand Prep Instructions**, subsection B.8.1. Also make sure the chiller is on. *Note: The LVDT position and PID controller output will change as the inclination of the thrust stand as well as the Setpoint on the PID controller are adjusted.*
2. While keeping the inclination constant, and while the PID Output is in "PID Control" mode, set the internal PID setpoint to a value that is as close to the LVDT voltage value as possible. The LVDT voltage is where the thruster naturally sits, which should be around +2 V, as set in the procedure mentioned in the previous step. This is the target LVDT position (in volts) that the PID controller will try to maintain. It is relatively arbitrary, but a position near where the thruster naturally sits works well, such as 0.002 V higher. If a completely different offset value away from the natural position of the thruster is chosen, which can also be done, make sure to stay well within the range of the LVDT. The difference between the Setpoint and the Measure values is the error signal we want the PID to minimize.
3. The LVDT output signal should be hooked up to a calibrated channel of the flatbed recorder or the data logger. The device used should have isolated channels. This is because the LVDT signal reference is not chassis ground, so the signal can be chopped or distorted if measured with a device that does not have isolated channels. Verify that the DC voltage value is correct as a check. Using the LVDT output, the natural oscillation frequency of the thruster on the thrust stand when it is displaced from it's natural resting position will be determined in a subsequent step.
4. Follow the Closed-loop Ziegler-Nichols procedure as outlined in the SIM960 Manual, which is also detailed here: First, disable **I** and **D** mode
5. Set **P** to some small value like 0.1. **P** is the proportional gain. It is multiplied by the error, and then the controller uses this amplified error to generate its three control signals, **P**, **PI**, & **PID**.
6. Then slowly increase **P** by a factor of 2 each time until the process starts to oscillate. Then back off in small amounts until stability is recovered. Finding the right value where stability is recovered is slightly tricky. You may want to repeat this step to make sure you get the same value.
7. Record this value of **P** as K_u, the "ultimate" gain. Also, observe the period of the oscillations, T_u on the data logger (or flatbed recorder).
8. From K_u and T_u, use the following chart to determine the values for **I** and **D** for whichever control scheme you want to use, **PID**, **PI** or **PID**:

Control	P	I	D
P	$K_u/2$		
PI	$2\ K_u/5$	$5/(4\ T_u)$	
PID	$3\ K_u/5$	$2/T_u$	$T_u/8$

9. If using **PID** Control, set P first. Then slowly turn up the integral gain (**I**) to some non-zero value. The gain that is needed depends on the mass of the thruster and the details of the setup. If the stand begins to oscillate reduce the integral gain.
10. Turn off Setpoint then turn it back on. Then to damp out the oscillations, set **D** (the derivative gain) by increasing its value if the null output current is oscillating wildly (i.e. hitting the stops). Also, try setting **D** before **I** if setting **I** first does not work.
11. To test the response, set Manual to 0 V, and turn on Manual mode. The thruster will oscillate in position. In Manual mode, the SIM960 output is set to the value indicated by the manual parameter.
12. Watch the LVDT position oscillate, then turn PID control ON under Output on the front panel to see the response. Adjust gains as necessary to obtain critically damped responses, which means that the time to get within 2% of steady state is about 1 period. The LVDT and PID Output signals should converge quickly on steady values. If the thrust stand amplifies the oscillations, immediately turn off PID control. The gains that were picked are not working, and need to be adjusted. See Chapter 2 of the manual for a description of the integral and derivative gains, and other options for setting them. As a rule of thumb, increasing derivative control will improve thrust stand accuracy and response time at the expense of stability. Increasing integral control should improve stability at the expense of response time.

Note: Ideally, the LVDT should not move when you apply weights. In practice, the LVDT may move slightly as the weight is applied but it should return to its original value quickly as the null coil returns the stand to its original position.

Note: Null coil heating can be an issue if too much current is driven; therefore, care needs to be taken when choosing gains for the PID controller (and the proper load spring).

B.8.4 Thrust Stand Weight Calibration Instructions

Thrust Stand Weight Calibration Instructions

From PEPL's Procedures for Running Hall Thrusters v.1.1 (Guide to the West Side)
with additions by Kimberly Trent
Version 2.0 February 2015

Perhaps the most important step for thrust stand operation is the thrust stand calibration. This calibration determines the conversion from the PID voltage output to actual thrust. Typically this is done when the chamber is under vacuum before the thruster is turned on, but a practice calibration before pumpdown is a good idea to ensure the process works properly. The following gives a description of how such a calibration is done.

1. When this calibration is done before pumpdown, make sure all large ports are closed on the chamber to minimize disturbances that could affect the thrust stand, and that the chiller is on. Wait for all temperature values to come to equilibrium
2. Make sure the inclination is held constant during the subsequent steps. Record the chiller and thermocouple temperatures.
3. Ensure the thrust stand is ready for calibration. The calibration gauge should indicate that only the stationary (dummy) weight is added to the thrust stand. Inclination should be held constant during entire calibration and subsequent data collection. PID controller should be set to ON (PID control, not manual). The strip chart should be on and zeroed, or if using the data logger, it should be on.
4. Record the PID controller output. This should be done (on the strip chart itself if using this, as well as) in a notebook or on a computer. Go back to just the stationary weight between each measurement (see figures 7 & 13 in Ref. [103]).
5. Move the calibration weights to the next configuration. The exact position for the next weight to be fully added to the thrust stand corresponds to a value on the inclination readout that was found using the weight calibration performed earlier in the **Thrust Stand Prep Instructions**, subsection B.8.1. Check the inclination, since the weights cause small shifts in the inclination (see figure 7 in Ref. [103]).
6. Repeat steps 4 and 5 until all weights have been added.
7. Repeat process in reverse until zero weights are added to the thrust stand. This allows for hysteresis in the calibration to be checked.
8. Repeat steps 4 through 7 anywhere from 2-5 times to obtain a calibration curve with a small enough Chi squared value. (see Ref. [103] p. 18, Section 2.6, Section 3.2.1, and Fig. 3.12 in this thesis).
9. Record end thermocouple temperatures.
10. Plot force vs. PID output. Check to make sure this is linear, by looking at the R squared value, Chi squared value, and residual plots. See Ref. [103], and Section 2.6, Section 3.2.1, and Fig. 3.12 in this thesis for additional details on the statistical indicators and the types of residual plots that are useful to look at for determining linearity.

B.8.5 Taking Thrust Measurements

Taking Thrust Measurements

From PEPL's Procedures for Running Hall Thrusters v.1.1 (Guide to the West Side)
(internal document)
with additions by Kimberly Trent
Version 2.0 February 2015

Once the thrust stand has been checked out before pumpdown, taking thrust measurements is relatively straightforward. However, there are a few things to be aware of while taking data. The following gives a description of the measurement procedure, as well as possible sources of error to keep in mind and correct for.

1. Ensure that the chiller is on and stable at 20°C.
2. Perform thrust stand calibration again at vacuum. The procedure for this is outlined in the previous section called **Thrust Stand Weight Calibration Instructions**, subsection B.8.4. Take as many sets of data as needed to "generate a calibration curve with small random errors, as described in those previous instructions. Examine the curve for signs of systematic bias and short-term drift, and compare to previous calibrations for signs of long-term drift. If the calibration indicates that the thrust stand is performing as expected, start the thruster and allow the operating parameters and thrust stand deflection to stabilize." (Ref. [103] p. 18).
3. Record PID control output when thruster is steady. Make sure the inclination is identical to its value during the calibration. Allow thrust stand to reach thermal equilibrium prior to taking a thrust stand measurement. After turning on the thruster each time after turning it off to record the zero (no thrust) PID null current signal, reaching thermal equilibrium will take about 10 minutes (when the thruster is turned on the first time, wait the standard 3 hours before taking any data) and is indicated by no drift in the null coil current and by the leveling of the thermocouple temperature data logged readouts. Thermal equilibrium is reached more quickly during testing because changes in power and thermal conditions between testing points are not as large as between thruster on/off. "Obtain a sufficient number of measurements of the thrust stand transducer signal [PID null current] to calculate a mean value with sufficiently small standard error" (around 5-25 measurements). Then "turn off the thruster power and flow rate and obtain measurements to characterize the zero (no load) transducer output." Thrust is equal to the PID null current at the test point minus the PID null current at zero thrust (which is measured directly after). This gives an automatic zero drift correction, which also accounts for the weight of the stationary weight. "The difference between the transducer output with the thruster on and under no load conditions will be considered the response for that operating point." (Quotations taken from Ref. [103] p. 18)
4. "Repeat this measurement cycle if possible to characterize the repeatability of thrust measurements." (Quotations taken from Ref. [103] p. 18)
5. Perform a thrust stand calibration at the end of the test. Repeat the calibration process detailed in step 2 after thruster operation in order to detect shifts in the thrust stand's responsiveness. This is a check to ensure that the thruster calibration

was consistent throughout the test. "If the calibrations taken before and after the thrust measurements indicate that the thrust stand response is stable (i.e. differences in the calibrations result in contributions to the total error estimate that are tolerable), compute the thrust from the measured response." Remember, frequent calibration minimizes errors. (From Ref. [103] p. 18 & 21)

- Since the chiller is not perfect, there will likely be some thermal drift associated with the thrust stand. This is due to the heat flux from the thruster causing elements to expand and shift, which is noticeable due to the sensitivity of the measurement. Typically this can be tracked by a shifting zero, which can be recorded periodically (as detailed in this procedure) and taken into account in data processing.
- Despite efforts to ensure the thrust stand is non-magnetic, the presence of magnets (such as on a Hall thruster) can cause shifting to occur that will also cause error in thrust measurements (magnetic taring). While this is more difficult to account for, tracking how the null current at zero thrust (the zero) changes with each magnetic field setting that will be used in your tests, with all other thruster circuits off, will give an idea of how to account for it in post-processing of the data.
- See Ref. [103] for additional possible sources of error to check for.

B.9 CTF Pumpdown Procedure

Detailed CTF Standard Operating Procedure (SOP)

by Kimberly Trent

References: Verbal and written communication with Dr. Michael McDonald in 2011, and previous CTF SOPs written by Dr. Matthew Domonkos and Dr. Kristina Lemmer (internal documents)

Last Revised: March 2014

Chamber Equipment:

- PHPK TM450 Cryopump, Compressor, Refrigerator & Lakeshore 818 Cryopump Temperature Monitor
- MKS HPS 925 MicroPirani Gauge & MKS PDR 900 Controller
- Varian 564 External Ion Gauge & Agilent Technologies XGS-600 Gauge Controller
- Edwards XDS35i Dry Scroll Pump & Stokes "High Vacuum" 3ST-3 Gate Valve

Pre-start Procedure

Go through the Pre-start Checklist in CTF's Logbook using the following steps:

1. Make sure all flanges are tightly bolted to the chamber.
2. Remove all tools and debris from the chamber.
3. Visually inspect the chamber and check that it is ready to be pumped down.
4. Open CTF's Logbook and record the date and your name.
5. Check the cryopump compressor's helium static pressure. It should be between 190 and 225 psi. The ideal is 210 $\pm$ 5 psi. (Check the compressor's manual if you need to add or remove helium.) Record the high static pressure in CTF's Logbook and any actions taken in the Notes section.
6. Clean the O-ring groove and flange surface on CTF's end cap with a Kimwipe and isopropyl alcohol. Also clean the area on the end cap that seals with the O-ring.
7. Clean & grease the O-ring and install it on the end cap.
8. Close the chamber by lining up the end cap with the flange surface using the cart and forklift assembly the end cap is attached to.
9. Use at least 5 bolts in an even and diametric pattern to keep the end cap in place and to insure good O-ring compression. Tighten the bolts in a "star" pattern. Make sure it is really tight so the O-ring does not get sucked into the chamber when the dry scroll mechanical pump is started. One way to ensure this is to make sure you don't see any spaces between the end cap and the mating flange.
10. Make sure the vent valve is closed and that any gas feed valves are closed. As an added precaution the opening of the vent valve can be capped off with a KF flange.
11. Turn on the cryopump temperature monitor. (The DT-470 silicone diode temperature sensor is installed in the TM 450 Cryopump, corresponding to curve # 6 of the stored standard curves in the Lakeshore 818 Cryopump Monitor.) The monitor needs 1 hour to warm up to achieve its rated specifications. It should read around 295 K.

Dry Scroll Pump Start-Up Procedure

1. Connect the muffler tube to the XDS35i dry scroll pump if this has not already been done. Also connect the flexible metal hose that goes between the gate valve and the mechanical pump if this was removed to move the chamber.
2. Turn on the MicroPirani gauge controller. If the pressure does not read 760 Torr, this can be set through the following menu selections: [Set] > 4 Setup > 2 Calibration > 2 Full Scale.
3. Open the gate valve using the switch on the blue box. If it isn't open, the pump will get quiet very quickly when it is turned on because it will only be pulling out the air in the hose up to the chamber. Open the gate valve so it can pump air out of the chamber itself.
4. Turn on the mechanical scroll pump using the power button at its base. Make note of the start time for turning on the pump.
   Note: The pressure should drop quickly. If it is not, look through a side viewport to make sure part of the O-ring did not get sucked in.
   Note: Do not tighten bolts while the chamber is under vacuum, because when the chamber is vented, the head of a weak or weakened bolt that is unable to withstand the additional pressure could snap off and become a projectile.

Cryopump Start-Up Procedure

1. After the scroll pump is turned on, wait until the chamber pressure reaches 50 mTorr. (This should take 60-90 min.) Record the amount of time that was needed to pump down to 50mTorr in CTF's Logbook.
2. At this point the Lakeshore Monitor has had enough time to warm up to give an accurate indication of the cryopump's starting temperature. Record this reference temperature in CTF's Logbook.
3. Close the gate valve, keep the pump on to keep the hose between the pump and gate valve evacuated. The pressure in this tube can rise relatively quickly.
4. Perform a leak check – the pressure of the chamber should not increase more than 10 mTorr in 5 min from 50mTorr. If the leak test fails, open the gate valve, let the pressure drop back to 50 mTorr, and perform the test again. Several iterations of this process may be needed. With each iteration, more outgassed material is removed. If the test still fails after 5 iterations, just as long as the rise is no more than 20 mTorr in 5 min the chamber will have a base pressure in the mid 10^{-6} Torr range. Record the final end pressure after 5 minutes (from 50 mTorr) in CTF's Logbook.
5. If the leak test is passed, open the gate valve to bring the pressure back down to 50 mTorr one more time, and turn on the water line to the cryopump.
6. Turn on the 220 VAC for the cryopump compressor using the disconnect switch box (PPB 10 (17) CIR 8,10,12), and turn on the compressor.
7. Close the gate valve.
8. Turn off the mechanical scroll pump.
9. Within 4-5 hours, the chamber pressure should be between $5x10^{-6}$ and $1x10^{-7}$ Torr, and the cryo temperature should be 15-17 K. Record the cryo's operating temperature in CTF's Logbook.
10. Turn on the Ion gauge controller. Wait an hour for it to warm up, and then record this base pressure in CTF's Logbook.
    Note: When using the HPS 919 Hot Cathode Controller, only degas when the pressure is below $5x10^{-5}$ Torr and don't degas for more than 2 hours. See manual for more details on when degassing may be necessary.

Shutdown and Standby Procedure
Go through the Shutdown Checklist in CTF's Logbook using the following steps:

1. Close all gas valves to the chamber and on the gas cylinders. Work your way from the cylinders to the chamber as you close the valves.
2. Turn off the Ion gauge and Pirani gauge controllers. If the ion gauge is left on while the pump is not on, the pressure may increase above the 10^{-4} Torr limit of the gauge and it and/or the controller may get damaged.
3. Turn off the cryopump compressor.
   Note: Do not vent the chamber until the temperature of the cryo has reached room temperature.
4. Turn off the water to the cryopump compressor and the 220 VAC disconnect for the cryopump.

Venting Procedure

1. Make sure the temperature of the cryo has reached room temperature.
2. Vent the chamber slowly so as not to affect any of the equipment in the chamber.

If Vacuum is Lost:
Turn off the ion gauge controller if it did not go off automatically. Keep the water to the compressor on until it cools down.

B.10 LVTF Cleaning Procedure

LVTF Cleaning Procedure

by Kimberly Trent with input from Scott Hall, Christopher Durot, Marcel Georgin, and others at PEPL (past and present members), and the Data Clean Corporation

Reason for Cleaning: The vacuum chamber walls get covered in layers of compacted carbon dust deposited from sputtering of the graphoil and carbon panel shielding used to cover sensitive diagnostic equipment and electrical lines in the chamber. Although carbon has a relatively low sputter yield, over time, sputtering of this material by the high energy ions from the plasma sources employed (mainly cathodes, Hall thrusters and Ion thrusters) still causes layers of carbon to build up on all the surfaces of the chamber. Therefore, the chamber requires regular cleaning, especially after major testing campaigns.

Equipment:

- Use full personal protective equipment (PPE) which includes appropriate respiratory masks, and exposed skin and face covering to guard against general dust, and specifically, carbon dust.
    - Respirators (half-facepiece respirator with a standard P100 particulate filter)
    - HEPA vacuums, with hoses and tools
    - HEPA air scrubbers (3)
    - Tyvek bunny suits (disposable cleanroom suits)
    - Nitrile or latex gloves
    - Safety goggles
- Flashlights
- Work lights
- Extension cords
- Ladders, 6’ 8’ 12’, Extension
- Mop sticks and reach poles
- Mops
- Microfiber towels
- Disposable lint free cloth such as Kimwipes
- Garbage bags
- Buckets & wringers
- Small handheld electric grinder/polisher outfitted with green Scotch-Brite scour pad attachments
- Scrub pads
- Fine grit sandpaper

Walls

1. To prepare for the cleaning, cover chamber structures that will not be cleaned with large pieces of Painter's plastic sheeting and tape them in place to protect these areas from carbon dust.
2. Mechanically clean chamber surfaces using scrubbers, electric polisher with green Scotch-Brite pad attachments and sandpaper. These cleaning fabrics were chosen because they did not scratch the stainless steel surface of the chamber during a spot test. For any new cleaning fabrics being considered, test a small area first to make sure it will not scratch the metal. Spray water on the surface before scrubbing to help contain removed particulate and limit airborne contamination.
3. HEPA vacuum and/or dry wipe the surface.
4. Once the entire chamber surface has been cleaned using the previous steps, then use 70/30 isopropyl alcohol (IPA)/DI water and a lint free cloth such as Kimwipes for a final wipe of cleaned surfaces.
   Note: Other cleaning chemicals were not used to avoid possible problems or issues during future pump down cycles. IPA was not used during the first two cleaning steps to limit extended exposure to this chemical since the chamber is a relatively enclosed area.

Under-grate Cleaning

1. Once the above parts of the chamber have been cleaned, remove accessible floor grates.
2. Remove all larger pieces of debris, hardware and tools that have dropped through the access grating over time to the bottom of the chamber.
3. Vacuum the floor of the chamber.
4. Mechanically clean chamber surfaces using scrubbers, electric polisher with green Scotch-Brite pad attachments and sandpaper with water only.
5. Once the entire chamber has been cleaned using the previous steps, then use 70/30 isopropyl alcohol (IPA)/DI water and a lint free cloth such as Kimwipes for a final wipe of cleaned surfaces.

Shroud Cleaning

1. Using ladders when necessary, reach through the shroud openings using vacuum extension nozzles to carefully vacuum accessible surfaces to remove loose particulates.
2. Wipe down as much of the inside and outside of the shroud as possible with a lint free cloth and IPA. Do not clean the cryohead that is inside of the shroud, just the shroud itself. Do not get the charcoal array on the head of the cryopump that is inside of the shroud wet.

Note: This job takes three full work days to complete using 4 professionally trained technical equipment cleaners. See Fig. B.16 for pictures of the chamber before and after cleaning.

Figure B**.16:** On the left: Pictures of areas of the chamber before cleaning. On the right: Pictures of the same areas of the chamber after the cleaning procedure was followed.

B.11 Thruster, LVTF & Testing Pre-Pumpdown Checklist

HET, Probe and LVTF Pre-Pump Down Checklist

Relayed by Dr. Mike Sekerak with additions by Kimberly Trent

Thruster

- ☐ Align and bolt thruster and remove the carry handles
- ☐ Connect gas feed lines
- ☐ Check that Viton gas feed tubes have a torturous path (so that no electrical arcs/breakdown can occur along the length of the tube)
- ☐ Connect all electric cables and make sure each electrical line is labeled on both sides of each connection point
- ☐ Make sure that only non-magnetic stainless steel hardware is used in chamber (and don't use zinc hardware in the chamber as it outgasses at vacuum)
- ☐ Check that cables are routed appropriately
- ☐ Make sure none of the cables are touching the thruster since it gets hot & check thruster body connections
- ☐ Make sure all connectors are taped over with either fiberglass or fusion tape
- ☐ Remove Kapton tape from channel wall retaining rings (H6 only)
- ☐ Perform electrical (continuity and isolation) checks with the BK Precision handheld 2880B multidisplay multimeter and the BM25 Megger
- ☐ Apply a small voltage (∼5 V) between the keeper & anode using the anode power supply and measure with a multimeter at the thruster itself to verify these lines are connected to the thruster
- ☐ Turn on the magnet power supplies to a nominal setting and verify the magnetic field strength in front of the thruster in a few key locations with the LakeShore 460 3-Channel Gaussmeter to make sure these lines are connected properly

Chamber

- ☐ Make sure beam dump is connected and operational
- ☐ Make sure thrust stand water lines are connected to thrust stand or that they form a closed loop (when thrust stand is not in chamber). Run the cooling system and check for leaks at the tube connection points since the cooling system will be run while the chamber is being used even if the thrust stand is not going to be used.
- ☐ Check that all ports and flanges are sealed
- ☐ Check that gas feed system computer controls are operational
- ☐ Add any new lines needed to the Data logging system & check that all Data logger lines are calibrated
- ☐ Check that Data logger is operational and recording
- ☐ Make sure all tools, ladders & garbage are removed from the chamber, and retrieve any items that fell below the grates
- ☐ Connect T-type thermocouples and check that thermocouples are datalogging
- ☐ Make sure all doors are closed
- ☐ Make sure chamber lights are off

- ☐ While going through the chamber pumpdown procedure, make sure to keep a log of important statistics such as the time for the blowers to start, chamber leak rate test results, mechanical and blower pump oil levels, base pressure, cryo temperatures at base pressure, notes on the maintenance carried out on the chamber before that pumpdown, thruster tested, and number of hours the thruster was on for.

Diagnostics

- ☐ Align probes and motion tables, and do a thrust stand check out if using the thrust stand
- ☐ Do a short representative practice run through the spatial test matrix to make sure cables won't snag on motion tables during the experiment
- ☐ Make sure all chamber cameras are hooked up and stream video
- ☐ Tape over any exposed open sockets, gas lines, and electrical connections to protect it from carbon dust and because plasma can cause noise in exposed probe lines
- ☐ Make sure graphoil flaps are taped over backs of large flanges that have electrical connections through them
- ☐ Make sure all diagnostics and exposed probe mounting surfaces are covered in graphoil
- ☐ Make sure cables are running behind supports so plasma doesn't see it
- ☐ Avoid creating virtual leaks from gas volumes of trapped air
- ☐ Move probes to their far position away from thruster and make note of their position
- ☐ Cover probes with shield (check that shield works)
- ☐ Megger the diagnostics for a length of time and to a voltage appropriate for each probe
- ☐ Apply a small voltage ($\sim$5 V) to the probes using a power supply outside of the chamber, and measure with a multimeter at the end of the electrical wire that connects to the probe to verify the connections
- ☐ Take the 'before' pictures for the probes and thruster and for the cathode's orifice with a lens that can zoom in on small features

B.12 LVTF Thruster Testing Procedure

LVTF Thruster Testing Procedure

Written down by Kimberly Trent

1. Turn on readouts for pressure gauges, wait a half hour for the machine to warm up before recording the pressure values.
2. Make sure that nitrogen discharge lines for pumps are venting properly and check the tank's liquid nitrogen levels.
3. Do vacuum electrical checks on thruster and diagnostics. First make sure to unplug all cables from the electrical box so as not to Megger across the datalogger or a power supply.
4. Once electrical checks are complete, make sure to plug all connections back into the box including the ground connection at the bottom, the connections for floating/grounding the thruster, and the connections for monitoring/data logging the thruster body ground current and floating voltage.
5. Record base pressures and cryo temperatures (once a half hour from when readout was turned on has passed).
6. Generate a new cathode heating record file.
7. Turn on computer with data logger and flow meter controllers if it isn't already on.
8. Open Agilent Benchlink Data Logger, choose the most recent setup. Make sure that on the main strip chart you have the base pressure, cathode-to-ground voltage, discharge current, and discharge voltage. Start the logging by pressing the play button.
9. Open Flow Vision Software and click on the ports for the cathode and anode flow meter readouts/controllers. Make sure polling is set to on. Record the pressure on the high side of the flow controllers as a rough indication of the remaining gas propellant (usually xenon) in the cylinder.
10. Evacuate flow lines starting as close to chamber as possible and working back towards the xenon bottle. Trace lines to each valve that needs to be opened. Don't go through the calibration lines. Make note of any changes to the pressure on the high side of the flow controllers.
11. Unplug motion stage controllers and diagnostic electrical cables from their chamber ports.
12. Turn on videos and turn on fans for electrical box and the thruster floating/grounding box.
13. Make sure probes are shielded.
14. Light the cathode and fire the thruster (see the separate procedures for this in subsections B.13 & B.14 respectively).
15. Make note of the time the thruster was turned on, and how long the thruster runs at each flow rate (which can be used to calculate the amount of xenon used to determine how many liters are left). It is also good to keep track of total thruster run time.
16. Plug motion stage and diagnostic cable connections back into their corresponding chamber ports.
17. Float the thruster body if desired for the experiment being conducted.
18. Monitor chamber pressure and cryo temps during thruster bake out or while waiting for thruster to reach steady state.
19. Record thruster operating conditions after bake out or settle in time.

B.13 Lighting the Cathode Procedure

LaB_6 Cathode Startup Procedure

Based on NASA JPL's Cathode Lighting Procedure
With additions by Dr. Mike McDonald, Kimberly Trent, and Dr. Mike Sekerak
Revision 2.3, 05/10/15

1. **Turn on gas flow to cathode.** Set gas flow to 10 sccm. The design range for the cathode used in these experiments is 5-15 sccm of Xenon.
    a. Wait for observed pressure rise in chamber before proceeding
2. **Configure voltage and current limits on the power supplies.**
    a. *Heater power supply:* Set the voltage limit to the maximum value so the filament can establish the voltage drop needed to draw the current it is being given. Set the current limit to 0 A.
    b. *Keeper power supply:* Set the voltage limit to 0 V. Set the current limit to 0.5 A. With a 10-turn potentiometer control knob for a 1.7 A (3.5 A) power supply, 0.5 A is about 3 turns (1.5 turns).
    c. *Magnet power supplies:* Set the voltage limit to the maximum value. Set the current limit to 0 A.
3. **Follow the heating schedule below to slowly ramp up the current so as not to break the heater wire.**
    a. Increase current levels over 15 seconds.
    b. Record times and voltages at start and stop of each heating current level.
    c. Cathode requires a heater power of ∼210 W for ignition. The 7.3 A @ 28 V is ∼210 W in the example below. Choose final current values so ∼210 W is supplied to the heater. With a thin (15 thou diameter or less) rhenium wire heater, do not increase current above 8 A. If 210 W is reached below 7.3 A, adjust heating schedule accordingly. During the 8 minutes monitor the current and voltage. If the voltage decreases, increase the current to maintain 210 W. Deposit 210 W for at least 8 min before trying to light so that the insert has time to become sufficiently hot to produce the required current. This will prevent sparking, rapid evaporation of the insert and rapid erosion of the orifice.

Heater Current	Time Start	Time Stop	Duration (min)	V_{Start} (V)	V_{Stop} (V)
1.0 A	*12:00:00*	*12:01:00*	**1**	*1 V*	
3.0 A	*12:01:15*	*12:03:15*	**2**	*9 V*	
5.0 A	*12:03:30*	*12:06:00*	**2.5**	*18 V*	
6.5 A	*12:06:15*	*12:09:15*	**3**	*25 V*	
7.3 A	*12:09:30*	*12:17:15*	**8**	*28 V*	

Note: the voltages recorded here are after the cathode had been operated for several tens of hours and close to a hundred heating cycles, and the drop in voltage at a given current is a recent development. This may indicate a degraded filament, or

may simply indicate improved frictional contact between the heater wire leads causing a reduced resistance. In any case, the voltages are intended as a guide but not an absolute requirement.

4. **Light the cathode to keeper.**
    a. Once ∼210 W has been deposited for 8 minutes, slowly increase the keeper voltage (up to 100 V max) and wait for current to start up and reach 0.5 A. When supply hits current control mode (little red light above the current knob will turn on), voltage should settle in at 15-30 V. Increase the voltage past where the keeper settles in so that if the cathode needs more heating, the cathode will not become unlit.
        i. If the cathode does not light at 100 V, the cathode is not hot enough. If you are depositing 210 W already, turn off the keeper supply, turn its voltage down to zero, wait 2 minutes and try again. If you are not, or if you just replaced the insert, turn up heater current in 0.1 A increments and wait two minutes at each increment before trying to light again. New inserts may require more than 210 W to light (in the past it was ∼240 W).
5. **Increase cathode current and flow.**
    a. With the cathode keeper drawing 0.5 A, slowly increase keeper current up to 1.6 A at a rate of approximately 0.1 A every few seconds. Stagger increasing the keeper current and decreasing the heater current
        i. Slowly turn heater current down and slowly ramp keeper current up while monitoring the cathode to ground voltage ($V_{C\text{-}G}$) on the strip chart. Until you get a feel for how the cathode behaves, try only decreasing heater current as $V_{C\text{-}G}$ is decreasing. While $V_{C\text{-}G}$ is increasing or remains steady, switch to increasing keeper current. This can ensure the cathode stays steady while the thruster is being lit. Once you get the feel for how cathode behaves during this step, alternate increasing the cathode current and decreasing the heater current at your own discretion. Stop when keeper current is 3.5 A and heater current is 3.5 A.
6. **Set Magnets**
    a. On magnet power supplies, set voltage limit to maximum (CW to stop), and current limit to 0 A (CCW to stop). This will ensure the power supply is in current-control mode with no current. Then turn on these power supplies.
    b. Set inner magnet coil and outer magnet coil to midway current values.
7. **Decrease cathode heater current.**
    a. Slowly decrease heater current to 0-2 A over ∼30 seconds (and turn off heater power supply if turning the heater down to 0 A).
    b. When cathode keeper current is at 3.5 A the voltage should be approximately 25 V. If this rises precipitously, it is a sign the cathode is not hot enough. *Note: In any event, the cathode is not stable for long-term operation (>10-15 min) with the keeper only. The main discharge should be started within this timeframe, see procedure in subsection B.14*
    c. Monitor the floating potential ($V_{C\text{-}G}$), because it forecasts cathode stability. If the potential steadily rises or falls, this could be succeeded by cathode instability.

B.14 Firing the Thruster Procedure

Procedure for Firing the Thruster

Based on "H6 Startup Procedure" by Dr. Mike Sekerak (original by Dr. Mike McDonald) (internal documents)
additional details written down by Kimberly Trent
Revision 3.2, 03/10/15

The basic outline of this "soft" startup is to light the thruster in a current-limited glow discharge to allow the cathode time to gently heat up without spitting or sparking, prolonging cathode life. Ignition will start with a stable operating voltage for the H6 of 150 V.

1. **Start-up Pre-Checks**
    a. Ensure two qualified lab personnel are present for thruster startup
    b. Ensure pre-operation electrical checks have been completed
    c. Ensure chamber pressure has stabilized
    d. Disconnect high-speed DAQ and other sensitive electronics from chamber before starting the thruster. Electrical noise from transients during startup has been known to damage DAQs and amplifiers.
    e. Enable video monitoring of thruster (or have a spotter watching the thruster through a viewport).
2. **Start LaB_6 Cathode per Cathode Starting Procedure (see Section B.13)**
    a. Keeper current: ∼3.5 A, flow Rate: 10 sccm
3. **Discharge Supply (AmRel)**
    a. Turn on main circuit breaker on north wall for Anode power supply (AmRel)
    b. Turn on power to AmRel with front panel switch.
    c. Set voltage limit to 150 V and discharge current limit to 3.5 A. Enter setpoints by holding "Display" button in the upper right corner and turning the voltage and current knobs.
    d. Press the green "Start" button to enable output.
4. **Anode Mass Flow**
    a. Ensure that valves in gas feed system and on gas bottle were opened using a previous procedure (subsection B.12) so that gas flow can reach the thruster.
    b. Start anode mass flow rate at ∼100 sccm.
    c. Thruster should light and be in current control mode with a glow discharge.
5. **Plume Mode**
    a. Increase the discharge current limit slowly (∼0.5 A/s) until the thruster switches to plume mode and the power supply switches to voltage control mode, which should happen at ∼10 A. Continue to increase the current past this point so the thruster and power supply do not jump back and forth between modes. The slow ramp up gives the cathode insert time to self-heat as it supplies more current.
    b. Increase discharge current limit to 25-30 A to account for plasma oscillations. Press the "Display" button to monitor the discharge current limit setting.

6. **Final Settings**
    a. Set the magnets to their final settings.
    b. Set the discharge voltage to the value that will be used for testing. Nominal is 300 V for this thruster. As the discharge voltage is increased the AmRel humming will increase in pitch.
    c. Adjust cathode mass flow rate to maintain a 7% cathode flow fraction (CFF) or other desired CFF of the anode mass flow rate set in the next step. Change the cathode flow rate before the anode flow rate if the anode flow rate will be increased. If the anode flow rate will be decreased from the present setting, change the anode flow rate and then the cathode flow rate. This will put less strain on the cathode as it supplies the current necessary to sustain the discharge.
    d. Adjust the anode mass flow rate to achieve the desired discharge current. Note that: 1 A $\sim$ 1 mg/s $\sim$ 10 sccm. Nominal discharge current for this thruster is 20 A.
    e. If the cathode heater is still on, turn down heater current to 0 A and then turn off heater supply.
    f. Turn off keeper supply. Don't ramp down the current or voltage, just turn the power supply off.

After the thruster has been turned on, the discharge current will rise and fall as water absorbed in the boron nitride channel walls is baked out (outgassed). The thruster should be at steady state in 3 hours after initial ignition. Allow half an hour to reach steady state when moving to substantially different operating points as new regions of the discharge channel will be exposed to the plasma and begin to outgas. After the first day of testing if the chamber remained at vacuum between the end of the first day of tests and the start of the subsequent days of testing, wait 1 hour after lighting the thruster to reach steady state.

Thruster Shut Down Procedure

1. Ground thruster body if thruster body is floating.
2. Ramp voltage down to 0 V.
3. Turn anode flow down to 0 sccm.
4. Turn magnet current all the way down.
5. Turn off flow to cathode.
6. Record the pressure on the high side of the flow controllers as a rough indication of how much xenon is left. The best estimate of the amount of xenon remaining comes from calculating it based on how long the thruster was on and the flow rates used.

APPENDIX C

Videos

C.1 Video: External Cathode Thruster Firing

Instructions: Open this PDF in Adobe Reader or Acrobat. Click image to play the video. Once video is playing, use the controls to adjust playback. Zoom page out until video is clear.

Video C.1: Video of thruster startup with the external cathode. See subsection 3.1.2 for details. See Vid. C.2 below to compare this startup to thruster startup with a standard, centrally-mounted cathode.

C.2 Video: Internal Cathode Thruster Firing

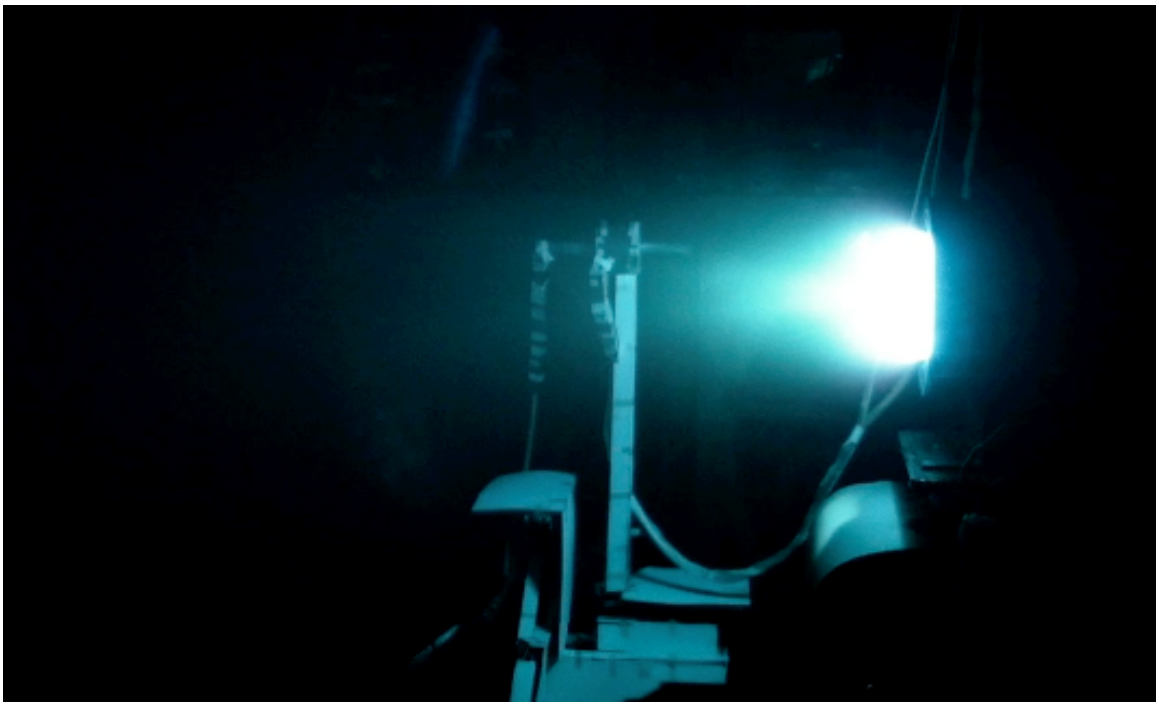

Instructions: Open this PDF in Adobe Reader or Acrobat. Click image to play the video. Once video is playing, use the controls to adjust playback. Zoom page out until video is clear.

Video C.2: Video of thruster startup with the centrally-mounted cathode. See subsection 3.1.2 for details.
Note: The external cathode and mount that are seen in the frame have been moved radially away from the thruster such that this structure and cathode are about a few thruster diameters away from thruster centerline.

APPENDIX D

EEDFs at 150 V

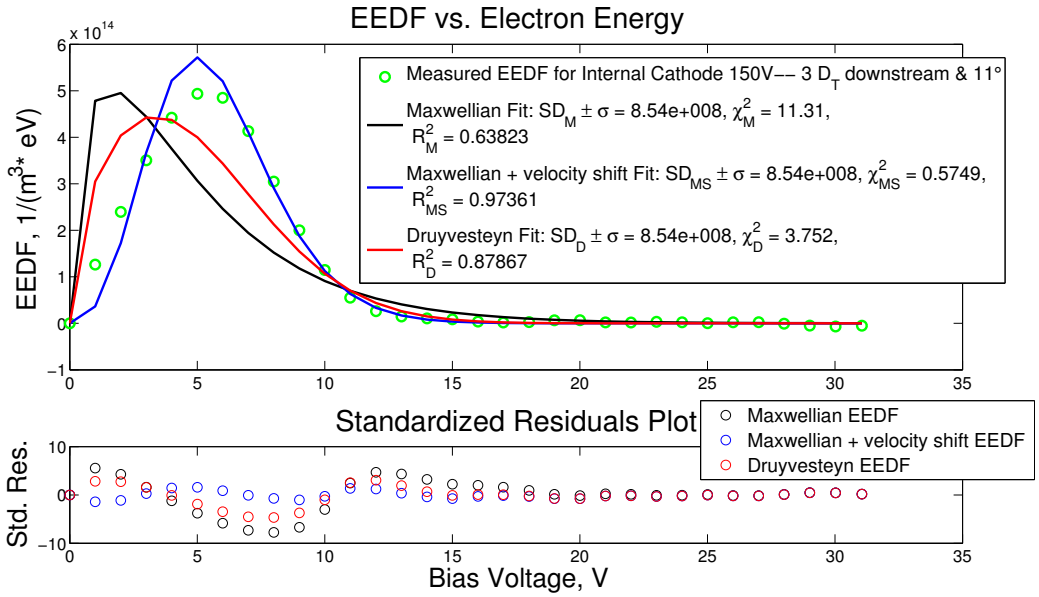

(a)

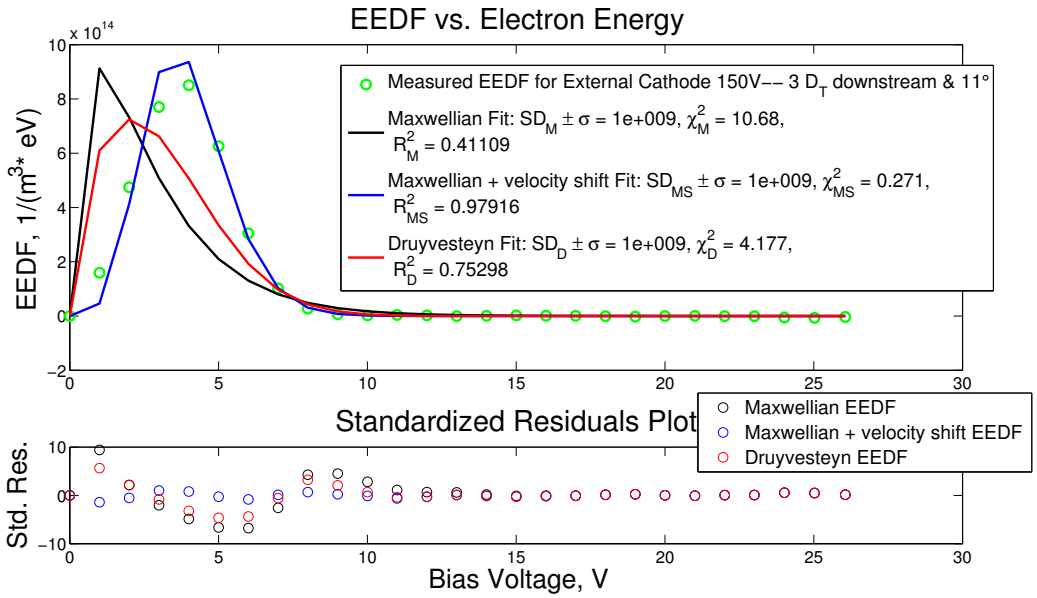

(b)

Figure D.**1:** (a) A plot showing the Maxwellian and Druyvesteyn functions that were fit to the EEDF at the 3 D_T 11° location while running the thruster at 150 V with the internal cathode to determine the form of the distribution. The legend shows each curve fit's corresponding reduced chi-squared (χ^2) and R^2 values, and the average of each point's SD from the fit function. (b) The same as (a) but for running the thruster at 150 V with the external cathode.

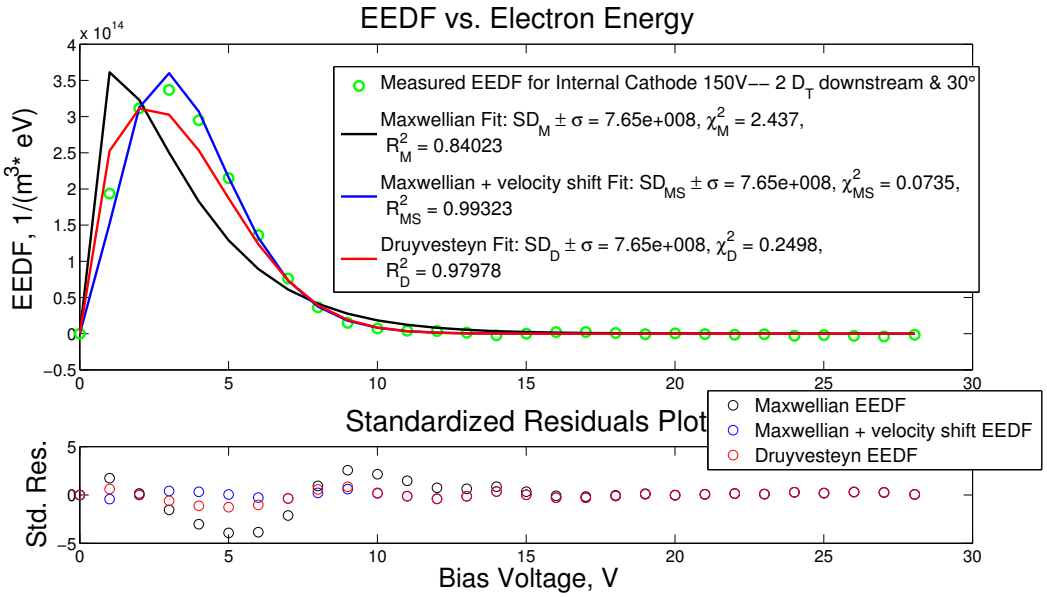

(a)

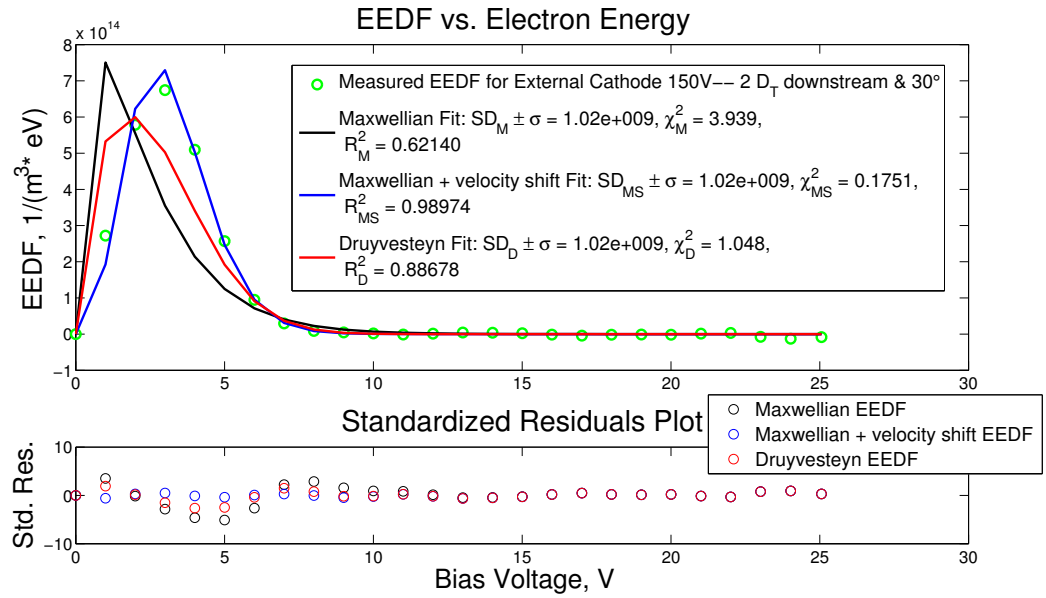

(b)

Figure D.**2:** (a) A plot showing the Maxwellian and Druyvesteyn functions that were fit to the EEDF at the 2 D_T 30° location while running the thruster at 150 V with the internal cathode to determine the form of the distribution. The legend shows each curve fit's corresponding reduced chi-squared (χ^2) and R^2 values, and the average of each point's SD from the fit function. (b) The same as (a) but for running the thruster at 150 V with the external cathode.

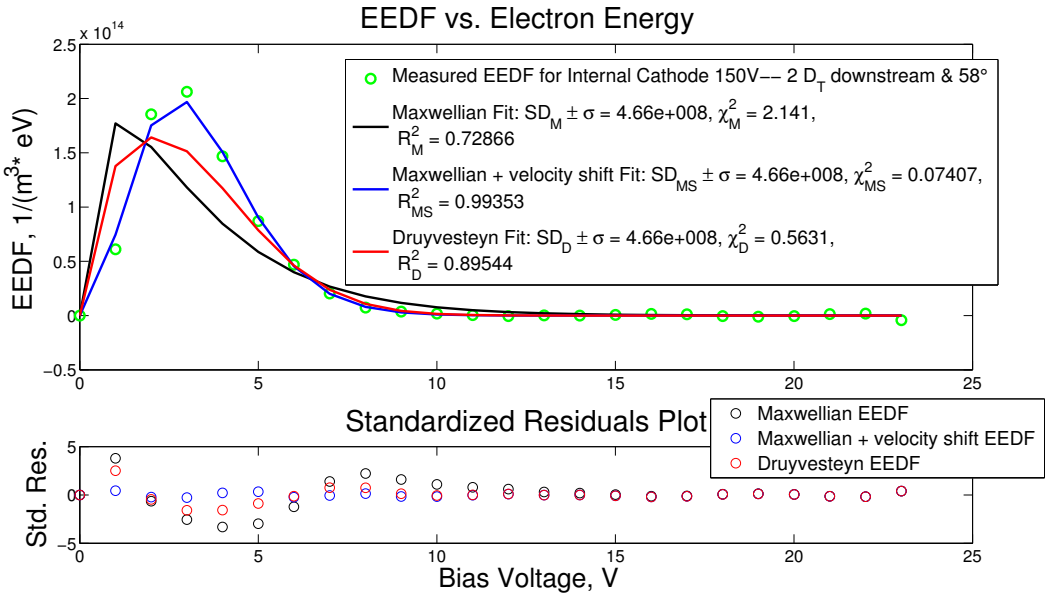

(a)

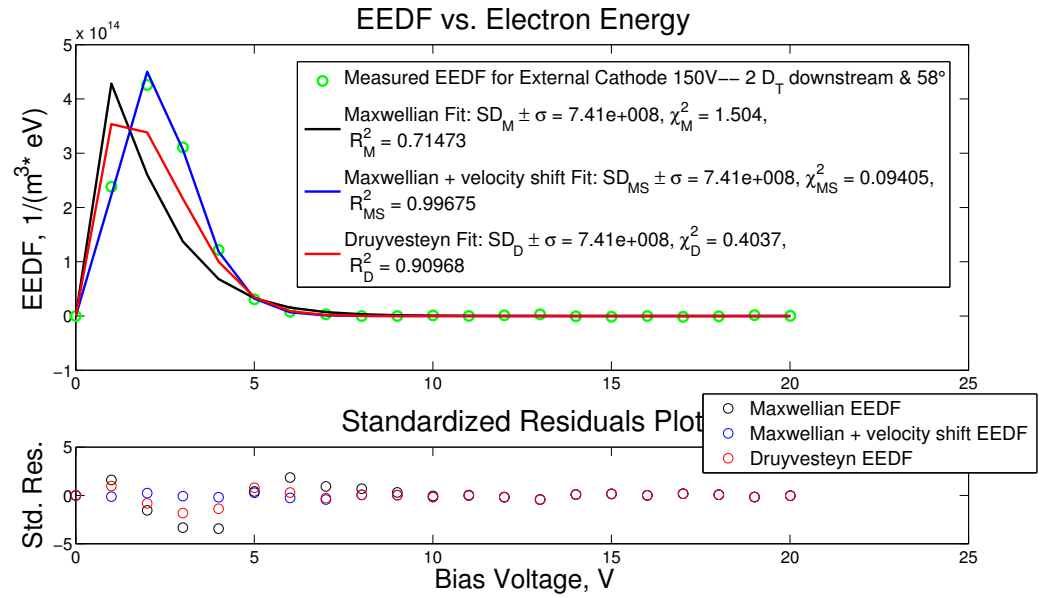

(b)

Figure D.**3:** (a) A plot showing the Maxwellian and Druyvesteyn functions that were fit to the EEDF at the 2 D_T 30° location while running the thruster at 150 V with the internal cathode to determine the form of the distribution. The legend shows each curve fit's corresponding reduced chi-squared (χ^2) and R^2 values, and the average of each point's SD from the fit function. (b) The same as (a) but for running the thruster at 150 V with the external cathode.

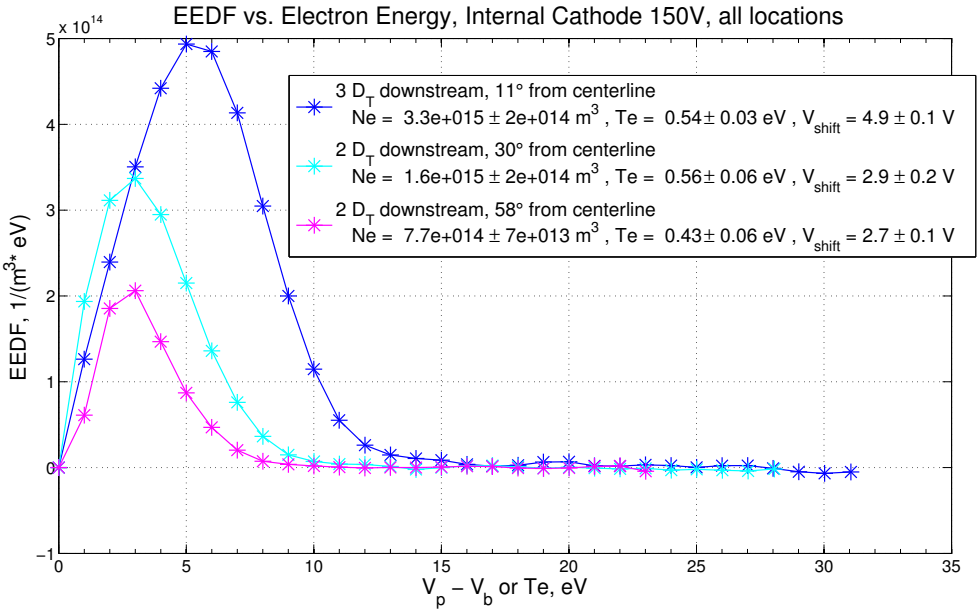

(a)

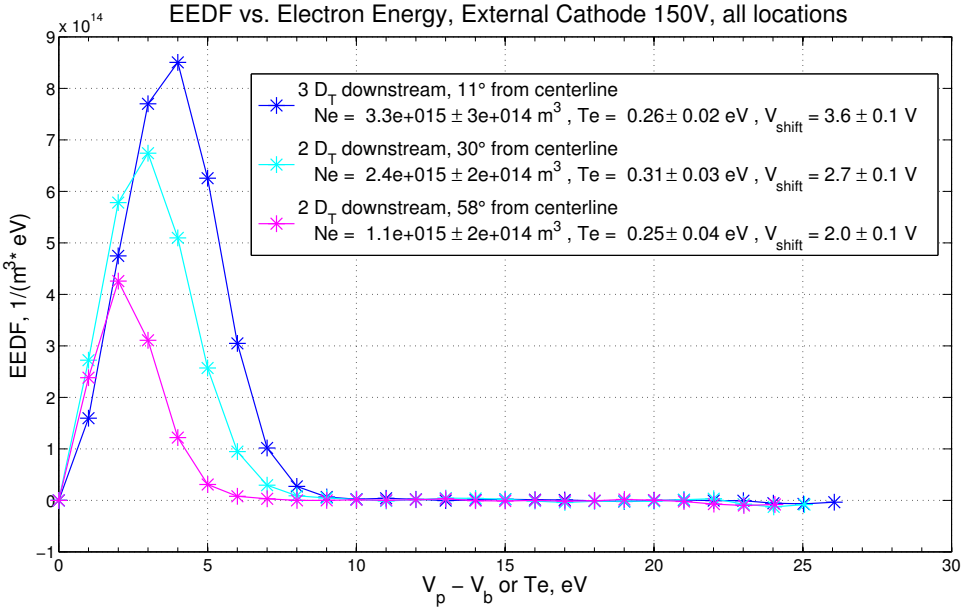

(b)

Figure D.**4:** (a) & (b) Shows the EEDFs from all locations where data was taken on the same graph for each 150 V cathode operating configuration.

BIBLIOGRAPHY

BIBLIOGRAPHY

[1] Johnson, W., "The Rise and Fall of Early War Rockets," *International Journal of Impact Engineering*, Vol. 15, No. 4, Aug. 1994, pp. 365–383.

[2] Johnson, W., "Contents and Commentary on William Moore's a Treatise on the Motion of Rockets and an Essay on Naval Gunnery," *International Journal of Impact Engineering*, Vol. 16, No. 3, Jun. 1995, pp. 499–521.

[3] Kosmodemyansky, A. and Danko, X., *Konstantin Tsiolkovsky His Life and Work*, University Press of the Pacific, Honolulu, Hawaii, Dec. 2000.

[4] Hall, R. and Shayler, D. J., *The Rocket Men: Vostok & Voskhod. The First Soviet Manned Spaceflights*, Springer Science & Business Media, New York, NY, Apr. 2001.

[5] "Konstantin Eduardovich Tsiolkovsky | Biography - Soviet Scientist," URL `http://www.britannica.com/biography/Konstantin-Eduardovich-Tsiolkovsky`.

[6] Peraire, J. and Widnall, S., "Variable Mass Systems: The Rocket Equation," 2008, URL `http://ocw.mit.edu/courses/aeronautics-and-astronautics/16-07-dynamics-fall-2009/lecture-notes/MIT16_07F09_Lec14.pdf`.

[7] Jahn, R. G., *Physics of Electric Propulsion*, Dover Publications, INC., Mineola, NY, 2006.

[8] Halliday, D., Resnick, R., and Walker, J., *Fundamentals of Physics*, Vol. 1, 6th ed., JohnWiley & Sons, Inc., New York, NY, 2001.

[9] Gruntman, M., *Blazing the Trail: The Early History of Spacecraft and Rocketry*, American Institute of Aeronautics and Astronautics, Reston, VA, USA, 2004, URL `http://site.ebrary.com/lib/alltitles/docDetail.action?docID=10516693`.

[10] Wilson, J., "NASA - Space Shuttle - Solid Rocket Boosters," Mar. 2006, URL `http://www.nasa.gov/returntoflight/system/system_SRB.html`.

[11] Turner, M. J. L., *Rocket and Spacecraft Propulsion: Principles, Practice and New Developments*, Springer-Praxis books in astronautical engineering, 3rd ed., Springer, published in association with Praxis Pub, Berlin ; New York, 2009.

[12] Fossum, E. C., King, L. B., and Makela, J., "Mobility Studies of a Pure Electron Plasma in Hall Thruster Fields," 42nd AIAA/ASME/SAE/ASEE Joint Propulsion Conference & Exhibit, AIAA 2006-5173, Sacramento, California, Jul. 2006.

[13] Goebel, D. M. and Katz, I., *Fundamentals of Electric Propulsion: Ion and Hall Thrusters*, JPL Space Science and Technology Series, John Wiley & Sons, 2008.

[14] Lobbia, R. B., *A Time-Resolved Investigation of the Hall Thruster Breathing Mode*, Ph.D. Thesis, Aerospace Engineering Dept., University of Michigan, Ann Arbor, MI, 2010.

[15] Halliday, D., Resnick, R., and Walker, J., *Fundamentals of Physics*, Vol. 2, 6th ed., JohnWiley & Sons, Inc., New York, NY, 2001.

[16] Brown, D. L., *Investigation of Low Discharge Voltage Hall Thruster Characteristics and Evaluation of Loss Mechanisms*, Ph.D. Thesis, Aerospace Engineering Dept., University of Michigan, Ann Arbor, MI, 2009.

[17] Space Systems-Loral, *GOES I-M DataBook*, No. DRL 101-08, GSFC Specification S-480-21A, Contract NAS5-29500 in Revision 1, Aug. 1996.

[18] Grayzeck, E., "SMART-1," Aug. 2014, URL `http://nssdc.gsfc.nasa.gov/nmc/spacecraftDisplay.do?id=2003-043C`.

[19] Choueiri, E. Y., "A Critical History of Electric Propulsion: The First 50 Years (1906-1956)," *Journal of Propulsion and Power*, Vol. 20, No. 2, 2004, pp. 193–203.

[20] Kim, V., Kozubsky, K., Murashko, V., and Semenkin, A., "History of the Hall Thrusters Development in USSR," 30th International Electric Propulsion Conference, IEPC-2007-142, Florence, Italy, Sep. 2007.

[21] Khrabrov, V. A., "Development and Flight Tests of the First Electric Propulsion System in Space," 30th International Electric Propulsion Conference, IEPC-2007-109, Florence, Italy, Sep. 2007.

[22] Bouchoule, A., Boeuf, J.-P., Heron, A., and Duchemin, O., "Physical Investigations and Developments of Hall Plasma Thrusters," *Plasma Physics and Controlled Fusion*, Vol. 46, Dec. 2004, pp. B407–B421.

[23] Grayzeck, E., "STEX NSSDC/COSPAR ID: 1998-055a," Aug. 2014, URL `http://nssdc.gsfc.nasa.gov/nmc/spacecraftDisplay.do?id=1998-055A`.

[24] Szabo, J., Robin, M., Paintal, S., Pote, B., and Hruby, V., "High Density Hall Thruster Propellant Investigations," 48th AIAA/ASME/SAE/ASEE Joint Propulsion Conference & Exhibit, AIAA-2012-3853, Atlanta, Georgia, Aug. 2012.

[25] Grayzeck, E., "TacSat-2 NSSDC/COSPAR ID: 2006-058a," Aug. 2014, URL http://nssdc.gsfc.nasa.gov/nmc/spacecraftSearch.do.

[26] Grayzeck, E., "NASA - NSSDC - Spacecraft - Query Results," Aug. 2014, URL http://nssdc.gsfc.nasa.gov/nmc/spacecraftSearch.do.

[27] Randolph, T. M., "Qualification of Commercial Electric Propulsion Systems for Deep Space Missions," Vol. 271, 30th International Propulsion Conference, IEPC-2007-271, Florence, Italy, Sep. 2007.

[28] Grego, L., "New Quarterly Update to the UCS Satellite Database," Sep. 2013, URL http://allthingsnuclear.org/new-quarterly-update-to-the-ucs-satellite-database/.

[29] Manzella, D. H. and Hack, K., "High-Power Solar Electric Propulsion for Future NASA Missions," 50th AIAA/ASME/SAE/ASEE Joint Propulsion Conference, Propulsion and Energy Forum, AIAA 2014-3718, Cleveland, OH, Jul. 2014.

[30] Rayman, M. D., "The Successful Conclusion of the Deep Space 1 Mission: Important Results Without a Flashy Title," *Space Technology*, Vol. 23, No. 2-3, 2003, pp. 185–196.

[31] Williams, S. N. and Coverstone-Carroll, V., "Mars Missions Using Solar Electric Propulsion," *Journal of Spacecraft and Rockets*, Vol. 37, No. 1, Feb. 2000, pp. 71–77.

[32] Rayman, M. D., Varghese, P., Lehman, D. H., and Livesay, L. L., "Results from the Deep Space 1 Technology Validation Mission," *Acta Astronautica*, Vol. 47, No. 2–9, Jul. 2000, pp. 475–487.

[33] Hofer, R. R., Randolph, T. M., Oh, D. Y., Snyder, J. S., and de Grys, K. H., "Evaluation of a 4.5 kW Commercial Hall Thruster System for NASA Science Missions," 42nd AIAA/ASME/SAE/ASEE Joint Propulsion Conference & Exhibit, AIAA-2006-4469, Sacramento, CA, Jul. 2006.

[34] Manzella, D., "Low Cost Electric Propulsion Thruster for Deep Space Robotic Missions," 2007 NASA Science Technology Conference, University of Maryland, MD, 2007.

[35] NASA, "NASA Technology Roadmaps TA2: In-Space Propulsion Technologies," Jul. 2015, URL http://www.nasa.gov/sites/default/files/atoms/files/2015_nasa_technology_roadmaps_ta_2_in-space_propulsion_final.pdf.

[36] Mercer, C. R., Oleson, S. R., and Drake, B., "A Combined Solar Electric and Storable Chemical Propulsion Vehicle for Piloted Mars Missions," AIAA SPACE Conference and Exposition, AIAA–2013–5492, San Diego, California, Sep. 2013.

[37] Brophy, J., Gershman, R., Strange, N., Landau, D., Merrill, R., and Kerslake, T., "300-kW Solar Electric Propulsion System Configuration for Human Exploration of Near-Earth Asteroids," 47th AIAA/ASME/SAE/ASEE Joint Propulsion Conference & Exhibit, AIAA 2011-5514, San Diego, California, Aug. 2011.

[38] Williams, G. and Crusan, J., "Pioneering Space–the Evolvable Mars Campaign," 2015, URL `http://www.nasa.gov/sites/default/files/files/20150408-NAC-Crusan-EMC-v7a_TAGGED.pdf`.

[39] Oh, D. Y., "Evaluation of Solar Electric Propulsion Technologies for Discovery-Class Missions," *Journal of Spacecraft and Rockets*, Vol. 44, No. 2, 2007, pp. 399–411.

[40] Oh, D. Y., Snyder, J. S., Goebel, D. M., Hofer, R. R., and Randolph, T. M., "Solar Electric Propulsion for Discovery-Class Missions," *Journal of Spacecraft and Rockets*, Vol. 51, No. 6, Nov. 2014, pp. 1822–1835.

[41] DeMaster-Smith, L., Kimbrel, S., Carpenter, C., Overton, S., Myers, R., and King, D., "Solar Electric Propulsion (SEP) Benefits for Near Term Space Exploration," 33rd International Electric Propulsion Conference, IEPC-2013-45, Washington, D.C., Oct. 2013.

[42] Merrill, R. G., Chai, P., and Qu, M., "An Integrated Hybrid Transportation Architecture for Human Mars Expeditions," AIAA SPACE Conference and Exposition, AIAA 2015-4442, Pasadena, California, Sep. 2015.

[43] Hofer, R., Kamhawi, H., Herman, D., Polk, J., Snyder, J. S., Mikellides, I., Huang, W., Myers, J., Yim, J., Williams, G., Ortega, A. L., Jorns, B., Sekerak, M., Griffiths, C., Shastry, R., Haag, T., Verhey, T., Gilliam, B., Katz, I., Goebel, D., Anderson, J. R., Gilland, J., and Clayman, L., "Development Approach and Status of the 12.5 kW HERMeS Hall Thruster for the Solar Electric Propulsion Technology Demonstration Mission," 34th Annual International Electric Propulsion Conference, IEPC-2015-186, Kobe-Hyogo, Japan, Jul. 2015.

[44] Gilland, J., LaPointe, M., Oleson, S., Mercer, C., Pencil, E., and Mason, L., "MW-Class Electric Propulsion System Designs for Mars Cargo Transport," AIAA SPACE 2011 Conference & Exposition, AIAA 2011-7253, Long Beach, California, Sep. 201.

[45] NASA, "2001 Mars Odyssey Arrival," Press Kit, Oct. 2001, URL `http://www.jpl.nasa.gov/news/press_kits/odysseyarrival.pdf`.

[46] Drake, B. G., "Mars Design Reference Architecture 5.0 Study," Dec. 2008, URL `https://www.nasa.gov/pdf/373669main_2008-12-04_Mars_DRA5_Executive_Summary-Presentation.pdf`.

[47] Bérend, N., Moreno, E. C., Ruault, J.-M., and Epenoy, R., "Feasibility Assessment of Rapid Earth–Mars Transfers Using High-Power Electric Propulsion," *Journal of Spacecraft and Rockets*, Vol. 51, No. 3, May 2014, pp. 946–957.

[48] Durante, M. and Cucinotta, F. A., "Physical Basis of Radiation Protection in Space Travel," *Reviews of Modern Physics*, Vol. 83, No. 4, Nov. 2011, pp. 1245–1281.

[49] Cucinotta, F. A., Kim, M.-H. Y., and Ren, L., "Managing Lunar and Mars Mission Radiation Risks Part I: Cancer Risks, Uncertainties, and Shielding Effectiveness," JSC-NASA Internal Report NASA/TP-2005-213164, Jul. 2005, URL `http://emmrem.unh.edu/papers/general/cucinotta.pdf`.

[50] Cucinotta, F. A., "Radiation Risk Acceptability and Limitations," Tech. rep., Dec. 2010, URL `https://three.jsc.nasa.gov/articles/AstronautRadLimitsFC.pdf`.

[51] Cucinotta, F. A., "Review of NASA Approach to Space Radiation Risk Assessments for Mars Exploration," *Health Physics*, Vol. 108, No. 2, Feb. 2015, pp. 131–142.

[52] Cucinotta, F. A., Alp, M., Rowedder, B., and Kim, M.-H. Y., "Safe Days in Space with Acceptable Uncertainty from Space Radiation Exposure," *Life Sciences in Space Research*, Vol. 5, Apr. 2015, pp. 31–38.

[53] Jefferies, S. A., McCleskey, C. M., Nufer, B., Lepsch, R. A., Merrill, R. G., North, D., Martin, J., and Komar, D. R., "Viability of a Reusable In-Space Transportation System," AIAA SPACE 2015 Conference and Exposition, AIAA 2015-4580, Pasadena, California, Sep. 2015.

[54] Hofer, R. R., *Development and Characterization of High-Efficiency, High-Specific Impulse Xenon Hall Thrusters*, Ph.D. Thesis, Aerospace Engineering Dept., University of Michigan, Ann Arbor, MI, 2004.

[55] Reid, B. M., *The Influence of Neutral Flow Rate in the Operation of Hall Thrusters*, Ph.D. Thesis, Aerospace Engineering Dept., University of Michigan, Ann Arbor, MI, 2009.

[56] Shastry, R., Hofer, R. R., Reid, B. M., and Gallimore, A. D., "Method for Analyzing E×B Probe Spectra from Hall Thruster Plumes," *Review of Scientific Instruments*, Vol. 80, No. 6, 2009, p. 063502.

[57] Hofer, R. R., Katz, I., Mikellides, I. G., Goebel, D. M., Jameson, K. K., Sullivan, R. M., and Johnson, L. K., "Efficacy of Electron Mobility Models in Hybrid-PIC Hall Thruster Simulations," 44th AIAA/ASME/SAE/ASEE Joint Propulsion Conference & Exhibit, AIAA 2008-4924, Hartford, CT, Jul. 2008.

[58] Jameson, K. K., *Investigation of Hollow Cathode Effects on Total Thruster Efficiency in a 6 kW Hall Thruster*, Ph.D. Thesis, Aerospace Engineering Dept., University of California, Los Angeles, CA, 2008.

[59] Sekerak, M. J., *Plasma Oscillations and Operational Modes in Hall Effect Thrusters*, Ph.D. Thesis, Aerospace Engineering Dept., University of Michigan, Ann Arbor, MI, 2014.

[60] Smirnov, A., Raitses, Y., and Fisch, N. J., "Electron Cross-Field Transport in a Low Power Cylindrical Hall Thruster," *Physics of Plasmas*, Vol. 11, No. 11, Oct. 2004, pp. 4922–4933.

[61] Choueiri, E. Y., "Plasma Oscillations in Hall Thrusters," *Physics of Plasmas*, Vol. 8, No. 4, 2001, pp. 1411–1426.

[62] "NIST Atomic Ionization Energies Output for Xenon," URL `http://physics.nist.gov/PhysRefData/ASD/ionEnergy.html`.

[63] Saloman, E. B., "Energy Levels and Observed Spectral Lines of Xenon, Xe I through Xe LIV," *Journal of Physical and Chemical Reference Data*, Vol. 33, No. 3, Sep. 2004, pp. 765–921.

[64] Hansen, J. E. and Persson, W., "Revised Analysis of Singly Ionized Xenon, Xe II," *Physica Scripta*, Vol. 36, No. 4, 1987, pp. 602–643.

[65] Gallardo, M., Massone, C. A., Tagliaferri, A. A., Garavaglia, M., and Persson, W., "$5s^2 5p^3 (^4S)$nl Levels of Xe III," *Physica Scripta*, Vol. 19, No. 5-6, 1979, pp. 538–544.

[66] Goebel, D., Jameson, K. K., and Hofer, R. R., "Hall Thruster Cathode Flow Impact on Coupling Voltage and Cathode Life," *Journal of Propulsion and Power*, Vol. 28, No. 2, Mar. 2012, pp. 355–363.

[67] NASA, "Next Space Technologies for Exploration Partnerships (NextSTEP) Broad Agency Announcement," Oct. 2014.

[68] Shabshelowitz, A., Gallimore, A. D., and Peterson, P. Y., "Performance of a Helicon Hall Thruster Operating with Xenon, Argon, and Nitrogen," 48th AIAA/ASME/SAE/ASEE Joint Propulsion Conference & Exhibit, AIAA 2012-4336, Atlanta, Georgia, Aug. 2012.

[69] Florenz, R., Gallimore, A. D., and Peterson, P. Y., "Developmental Status of a 100-kW Class Laboratory Nested Channel Hall Thruster," 32nd International Electric Propulsion Conference, IEPC-2011-246, Wiesbaden, Germany, Sep. 2011.

[70] Liang, R. and Gallimore, A. D., "Constant-Power Performance and Plume Measurements of a Nested-Channel Hall-Effect Thruster," 32nd International Electric Propulsion Conference, IEPC-2011-049, Wiesbaden, Germany, Sep. 2011.

[71] Liang, R. and Gallimore, A. D., "Far-Field Plume Measurements of a Nested-Channel Hall-Effect Thruster," 49th AIAA Aerospace Sciences Meeting including the New Horizons Forum and Aerospace Exposition, AIAA 2011-1016, Orlando, Florida, Jan. 2011.

[72] Liang, R., *The Combination of Two Concentric Discharge Channels into a Nested Hall-Effect Thruster*, Ph.D. Thesis, Aerospace Engineering Dept., University of Michigan, Ann Arbor, MI, 2013.

[73] McDonald, M. S., Liang, R., and Gallimore, A. D., "Practical Application of Wide Bandwidth Floating Emissive Probes and Wavelet Analysis to the X2 Nested Hall Thruster," 33rd International Electric Propulsion Conference, IEPC-2013-352, Washington D.C., Oct. 2013.

[74] Trent, K. R., McDonald, M. S., Lobbia, R. B., and Gallimore, A. D., "Time-resolved Langmuir Probing of a New Lanthanum Hexaboride (LaB6) Hollow Cathode," 32nd International Electric Propulsion Conference, IEPC-2011-245, Wiesbaden, Germany, Sep. 2011.

[75] Hofer, R. R., Goebel, D. M., and Watkins, R. M., "Compact LaB_6 Hollow Cathode for the H6 Hall Thruster," 54th JANNAF Propulsion Meeting, Denver, CO, May 2007.

[76] Mavrodineanu, R., "Hollow Cathode Discharges - Analytical Applications," *National Institute of Standards and Technology*, Vol. 89, No. 2, 1984, pp. 143–185.

[77] Lafferty, J. M., "Boride Cathodes," *Journal of Applied Physics*, Vol. 22, No. 3, 1951, pp. 299–309.

[78] Kim, V., Popov, G., Arkhipov, B., Murashko, V., Gorshkov, O., Koroteyev, A., Garkusha, V., Semenkin, A., and Tverdokhlebov, S., "Electric Propulsion Activity in Russia," 27th International Electric Propulsion Conference, IEPC-01-05, Pasadena, CA, Oct. 2001.

[79] Goebel, D. M., Watkins, R. M., and Jameson, K. K., "LaB6 Hollow Cathodes for Ion and Hall Thrusters," *Journal of Propulsion and Power*, Vol. 23, No. 3, May 2007, pp. 552–558.

[80] Goebel, D. M., Hirooka, Y., and Sketchley, T. A., "Large-Area Lanthanum Hexaboride Electron Emitter," *Review of Scientific Instruments*, Vol. 56, No. 9, 1985, pp. 1717–1722.

[81] Goebel, D. M. and Watkins, R. M., "High Current Hollow Cathodes for High Power Ion and Hall Thrusters," 41st AIAA/ASME/SAE/ASEE Joint Propulsion Conference & Exhibit, AIAA 2005-4239, Tucson, AZ, Jul. 2005.

[82] Goebel, D. M. and Watkins, R. M., "Compact Lanthanum Hexaboride Hollow Cathode," *Review of Scientific Instruments*, Vol. 81, No. 8, 2010, p. 083504.

[83] Lobbia, R. B. and Gallimore, A. D., "A Method of Measuring Transient Plume Properties," 44th AIAA/ASME/SAE/ASEE Joint Propulsion Conference & Exhibit, AIAA-2008-4650, Hartford, CT, Jul. 2008.

[84] Barral, S. and Ahedo, E., "On the Origin of Low Frequency Oscillations in Hall Thrusters," AIP Conference PLASMA 2007: International Conference on Research and Applications of Plasmas, CP993, Greifswald, Germany, Oct. 2007, pp. 439–442.

[85] McDonald, M. S., *Electron Transport in Hall Thrusters*, Ph.D. Thesis, Applied Physics, University of Michigan, Ann Arbor, MI, 2012.

[86] Smirnov, A., Raitses, Y., and Fisch, N. J., "Electron Cross-Field Transport in a Low Power Cylindrical Hall Thruster," *Physics of Plasmas*, Vol. 11, No. 11, Oct. 2004, pp. 4922–4933.

[87] Garrigues, L., Pérez-Luna, J., Lo, J., Hagelaar, G. J. M., Boeuf, J. P., and Mazouffre, S., "Empirical Electron Cross-Field Mobility in a Hall Effect Thruster," *Applied Physics Letters*, Vol. 95, No. 14, Oct. 2009, p. 141501.

[88] McDonald, M. S., Bellant, C. K., Pierre, B. A. S., and Gallimore, A. D., "Measurement of Cross-Field Electron Current in a Hall Thruster Due to Rotating Spoke Instabilities," 47th AIAA/ASME/SAE/ASEE Joint Propulsion Conference & Exhibit, AIAA 2011-5810, San Diego, California, Jul. 2011.

[89] Ellison, C. L., Raitses, Y., and Fisch, N. J., "Cross-Field Electron Transport Induced by a Rotating Spoke in a Cylindrical Hall Thruster," *Physics of Plasmas (1994-present)*, Vol. 19, No. 1, Jan. 2012, p. 013503.

[90] Garrigues, L., Mazouffre, S., and Bourgeois, G., "Computed Versus Measured Ion Velocity Distribution Functions in a Hall Effect Thruster," *Journal of Applied Physics*, Vol. 111, No. 11, Jun. 2012, p. 113301.

[91] Sydorenko, D., Smolyakov, A., Kaganovich, I., and Raitses, Y., "Modification of Electron Velocity Distribution in Bounded Plasmas by Secondary Electron Emission," *IEEE Transactions on Plasma Science*, Vol. 34, No. 3, Jun. 2006, pp. 815–824.

[92] Smirnov, A., Raitses, Y., and Fisch, N., "Controlling the Plasma Flow in the Miniaturized Cylindrical Hall Thruster," *IEEE Transactions on Plasma Science*, Vol. 36, No. 5, Oct. 2008, pp. 1998–2003.

[93] Diamant, K., Pollard, J., Raitses, Y., and Fisch, N., "Low Power Cylindrical Hall Thruster Performance and Plume Properties," 44th AIAA/ASME/SAE/ASEE Joint Propulsion Conference & Exhibit, AIAA 2008-4998, Hartford, CT, Jul. 2008.

[94] Raitses, Y., Smirnov, A., and Fisch, N. J., "Effects of Enhanced Cathode Electron Emission on Hall Thruster Operation," *Physics of Plasmas (1994-present)*, Vol. 16, No. 5, May 2009, p. 057106.

[95] Hong, J. I., Seo, S. H., Kim, S. S., Yoon, N. S., Chang, C. S., and Chang, H. Y., "Electron Temperature Control with Grid Bias in Inductively Coupled Argon Plasma," *Physics of Plasmas*, Vol. 6, No. 3, 1999, p. 1017.

[96] Haas, F. A., Goodyear, A., and Braithwaite, N. S., "Tailoring of Electron Energy Distributions in Low Temperature Plasmas," *Plasma Sources Science and Technology*, Vol. 7, 1998, p. 471.

[97] Haas, F. A. and Braithwaite, N. S. J., "Tailoring of Electron Energy Distributions in Low-Pressure Inductive Discharges," *Applied Physics Letters*, Vol. 74, No. 3, 1999, p. 338.

[98] Fruchtman, A., Fisch, N. J., and Raitses, Y., "Control of the Electric-Field Profile in the Hall Thruster," *Physics of Plasmas (1994-present)*, Vol. 8, No. 3, Mar. 2001, pp. 1048–1056.

[99] Dushman, S., *Scientific Foundations of Vacuum Technique*, Vol. 4, John Wiley & Sons, New York, 1958.

[100] Diamant, K. D., Liang, R., and Corey, R. L., "The Effect of Background Pressure on SPT-100 Hall Thruster Performance," 50th AIAA/ASME/SAE/ASEE Joint Propulsion Conference (JPC), AIAA 2014-3710, Cleveland, OH, Jul. 2014.

[101] Brown, D. L. and Gallimore, A. D., "Investigation of Low Discharge Voltage Hall Thruster Operating Modes and Ionization Processes," 31st International Electric Propulsion Conference, IEPC-2009-114, Ann Arbor, MI, Sep. 2009.

[102] Shabshelowitz, A., *Study of RF Plasma Technology Applied to Air-Breathing Electric Propulsion*, Ph.D. Thesis, Aerospace Engineering Dept., University of Michigan, Ann Arbor, MI, 2013.

[103] Polk, J. E., Pancotti, A., Haag, T., King, S., Walker, M., Blakely, J., and Ziemer, J., "Recommended Practices in Thrust Measurements," 33rd International Electric Propulsion Conference, IEPC-2013-440, Washington, D.C., Oct. 2013.

[104] Linnell, J. A., *An Evaluation of Krypton Propellant in Hall Thrusters*, Ph.D. Thesis, Aerospace Engineering Dept., University of Michigan, Ann Arbor, Michigan, 2007.

[105] Sommers, B. S., Foster, J. E., Davis, C. N., and Viges, E., "Preliminary Characterization of Ion Energy Spectra Acquired from High Current Hollow Cathodes," 33rd International Electric Propulsion Conference, IEPC-2013-437, Washington, D.C., Oct. 2013.

[106] Lemmer, K. M., *Use of a Helicon Source for Development of a Re-Entry Blackout Amelioration System*, Ph.D. Thesis, Aerospace Engineering Dept., University of Michigan, Ann Arbor, MI, 2009.

[107] Shastry, R., *Experimental Characterization of the Near-Wall Region in Hall Thrusters and Its Implications on Performance and Lifetime*, Ph.D. Thesis, Aerospace Engineering Dept., University of Michigan, Ann Arbor, MI, 2011.

[108] Huang, W., Shastry, R., Herman, D., Soulas, G., and Kamhawi, H., "Ion Current Density Study of the NASA-300m and NASA-457m v2 Hall Thrusters," 48th AIAA/ASME/SAE/ASEE Joint Propulsion Conference & Exhibit, AIAA 2012-3870, Atlanta, Georgia, Aug. 2012.

[109] Bellan, P. M., *Fundamentals of Plasma Physics*, Cambridge University Press, New York, NY, Jul. 2008.

[110] Chen, F. F., "Lecture Notes on Langmuir Probe Diagnostics," Jun. 2003.

[111] Lieberman, M. A. and Lichtenberg, A. J., *Principles of Plasma Discharges and Materials Processing*, 2nd ed., John Wiley and Sons, Inc Publication, Hoboken, New Jersey, 2005.

[112] Chen, F. F., "Langmuir Probes in RF Plasma: Surprising Validity of OML Theory," *Plasma Sources Science and Technology*, Vol. 18, No. 3, Aug. 2009, p. 035012.

[113] Godyak, V. A., Piejak, R. B., and Alexandrovich, B. M., "Measurements of Electron Energy Distribution in Low-Pressure RF Discharges," *Plasma Sources Science and Technology*, Vol. 1, 1992, pp. 36–58.

[114] Godyak, V. A., Piejak, R. B., and Alexandrovich, B. M., "Probe Diagnostics of Non-Maxwellian Plasmas," *Journal of Applied Physics*, Vol. 73, No. 8, Apr. 1993, pp. 3657–3663.

[115] Demidov, V. I., Ratynskaia, S. V., and Rypdal, K., "Electric Probes for Plasmas: The Link Between Theory and Instrument," *Review of Scientific Instruments*, Vol. 73, No. 10, Oct. 2002, pp. 3409–3439.

[116] Godyak, V. A. and Demidov, V. I., "Probe Measurements of Electron-Energy Distributions in Plasmas: What Can We Measure and How Can We Achieve Reliable Results?" *Journal of Physics D: Applied Physics*, Vol. 44, No. 26, Jul. 2011, p. 269501.

[117] Hershkowitz, N., "How Langmuir Probes Work, Chapter 3," O. Auciello and D. L. Flamm (eds.), "Plasma Diagnostics: Discharge Parameters and Chemistry," Vol. 1, Academic Press, Inc., San Diego, CA, 1989.

[118] Baierlein, R., *Thermal Physics*, Cambridge University Press, New York, NY, Jul. 1999.

[119] Kittel, C. and Kroemer, H., *Thermal Physics*, 2nd ed., W. H. Freeman and Company, New York, NY, Jan. 1980.

[120] Pu, Y. K., Guo, Z. G., Kang, Z. D., Ma, J., Guan, Z. C., Zhang, G. Y., and Wang, E. G., "Comparative Characterization of High-Density Plasma Reactors Using Emission Spectroscopy from VUV to NIR," *Pure and Applied Chemistry*, Vol. 74, No. 3, 2002, pp. 459–464.

[121] Jovanović, J. V., Basurto, E., Šašić, O., Hernández-Ávila, J. L., Petrović, Z. L., and de Urquijo, J., "Electron Impact Ionization and Transport in Nitrogen–Argon Mixtures," *Journal of Physics D: Applied Physics*, Vol. 42, 2009, p. 045202.

[122] Shastry, R., Gallimore, A. D., and Hofer, R. R., "Near-Wall Plasma Properties and EEDF Measurements of a 6-kW Hall Thruster," 31st International Electric Propulsion Conference, IEPC-2009-133, University of Michigan, Ann Arbor, MI, Sep. 2009.

[123] Hayashi, M., "Determination of Electron-Xenon Total Excitation Cross-Sections, from Threshold to 100 eV, from Experimental Values of Townsend's α," *Journal of Physics D: Applied Physics*, Vol. 16, No. 4, Apr. 1983, pp. 581–589.

[124] Sommerville, J. D. and King, L. B., "Hall-Effect Thruster–Cathode Coupling, Part I: Efficiency Improvements from an Extended Outer Pole," *Journal of Propulsion and Power*, Vol. 27, No. 4, Aug. 2011, pp. 744–753.

[125] Hofer, R., Goebel, D., Mikellides, I., and Katz, I., "Design of a Laboratory Hall Thruster with Magnetically Shielded Channel Walls, Phase II: Experiments," 48th AIAA/ASME/SAE/ASEE Joint Propulsion Conference & Exhibit, AIAA 2012-3788, Atlanta, Georgia, Aug. 2012.

[126] Haas, J. M. and Gallimore, A., "An Investigation of Internal Ion Number Density and Electron Temperature Profiles in a Laboratory-Model Hall Thruster," 36th AIAA/ASME/SAE/ASEE Joint Propulsion Conference & Exhibit, AIAA 00-3422, Huntsville, AL, Jul. 2000.

[127] Goebel, D. M., Jameson, K. K., Katz, I., and Mikellides, I. G., "Energetic Ion Production and Keeper Erosion in Hollow Cathode Discharges," 29th International Electric Propulsion Conference, IEPC-2005-266, Princeton University, Princeton, NJ, Nov. 2005, p. 18.

[128] Goebel, D. M., Jameson, K. K., Katz, I., and Mikellides, I. G., "Potential Fluctuations and Energetic Ion Production in Hollow Cathode Discharges," *Physics of Plasmas*, Vol. 14, No. 10, 2007, p. 103508.

[129] Lyons, L., *Statistics for Nuclear and Particle Physicists*, Cambridge University Press, Cambridge, UK, 1986.

[130] Bevington, P. R. and Robinson, D. K., *Data Reduction and Error Analysis for the Physical Sciences*, 3rd ed., McGraw-Hill, New York, NY, 2003.

[131] Pullins, S., Chiu, Y.-H., Levandier, D., and Dressler, R., "Ion Dynamics in Hall Effect and Ion Thrusters - $Xe^+ + Xe$ Symmetric Charge Transfer," 38th AIAA Aerospace Sciences Meeting & Exhibit, AIAA 2000-0603, Reno, NV, Jan. 2000.

[132] Brieda, L., *Multiscale Modeling of Hall Thrusters*, Ph.D. Thesis, The George Washington University, Washington, D.C., 2012.

[133] Lee, D., Ting, Y. H., Oksuz, L., and Hershkowitz, N., "Measurement of Plasma Potential Fluctuations by Emissive Probes in CF_4 Radio-Frequency Plasma," *Plasma Sources Science and Technology*, Vol. 15, 2006, pp. 873–878.

[134] Domonkos, M. T., *Evaluation of Low-Current Orificed Hollow Cathodes*, Ph.D. Thesis, Aerospace Engineering Dept., University of Michigan, Ann Arbor, MI, 1999.

[135] Paranjpe, A. P., McVittie, J. P., and Self, S. A., "A Tuned Langmuir Probe for Measurements in RF Glow Discharges," *Journal of Applied Physics*, Vol. 67, No. 11, 1990, pp. 6718–6727.

[136] Sudit, I. D. and Woods, R. C., "A Study of the Accuracy of Various Langmuir Probe Theories," *Journal of Applied Physics*, Vol. 76, No. 8, 1994, pp. 4488–4498.

[137] Hutchinson, I. H., *Principles of Plasma Diagnostics*, 2nd ed., Cambridge University Press, New York, 2002.

[138] Behlman, N. J., *Electron Energy Distribution Measurements in the Plume Region of a Low Current Hollow Cathode*, Master's Thesis, Mechanical Engineering Dept., Worcester Polytechnic Institute, Worcester, MA, 2009.

[139] Ramamurthi, B., Economou, D. J., and Kaganovich, I. D., "Effect of Electron Energy Distribution Function on Power Deposition and Plasma Density in an Inductively Coupled Discharge at Very Low Pressures," *Plasma Sources Science and Technology*, Vol. 12, No. 3, Aug. 2003, pp. 302–312.

[140] Godyak, V. A. and Kolobov, V. I., "Effect of Collisionless Heating on Electron Energy Distribution in an Inductively Coupled Plasma," *Physical Review Letters*, Vol. 81, No. 2, Jul. 1998, pp. 369–372.

[141] Godyak, V., "Nonequilibrium EEDF in Gas Discharge Plasmas," *Plasma Science, IEEE Transactions on*, Vol. 34, No. 3, 2006, pp. 755–766.

[142] Foster, J. E., "Intercusp Electron Transport in an NSTAR-Derivative Ion Thruster," *Journal of Propulsion and Power*, Vol. 18, No. 1, Jan. 2002, pp. 213–217.

[143] Gorse, C., De Benedictis, S., Dilecce, G., and Capitelli, M., "Electron Energy Distribution Functions in He/N_2 Mixtures in the Presence of Metastable States," *Spectrochimica Acta Part B: Atomic Spectroscopy*, Vol. 45B, No. 4/5, 1990, pp. 521–525.

[144] Shul, R. J. and Pearton, S. J. (eds.), *Handbook of Advanced Plasma Processing Techniques*, Springer-Verlag, Berlin, Germany, 2000.

[145] Chung, T. H., Lee, Y. W., Joh, H. M., and Song, M. A., "Pressure Dependence of Dissociation Fraction and Optical Emission Characteristics in Low-Pressure Inductively Coupled N_2-Ar Plasmas," *AIP Advances*, Vol. 1, No. 3, 2011, p. 032136.

[146] Goebel, D. M., Jameson, K. K., Katz, I., and Mikellides, I. G., "Potential Fluctuations and Energetic Ion Production in Hollow Cathode Discharges," *Physics of Plasmas*, Vol. 14, No. 10, 2007, p. 103508.

[147] Barral, S. and Ahedo, E., "On the Origin of Low Frequency Oscillations in Hall Thrusters," "AIP Conference Proceedings," Vol. 993, American Institute of Physics, Greifswald, Germany, Oct. 2007, pp. 439–442.

[148] Albarède, L., Mazouffre, S., Bouchoule, A., and Dudeck, M., "Low-Frequency Electron Dynamics in the Near Field of a Hall Effect Thruster," *Physics of Plasmas*, Vol. 13, No. 6, 2006, p. 063505.

[149] Lobbia, R. B. and Gallimore, A. D., "High-Speed Dual Langmuir Probe," *Review of Scientific Instruments*, Vol. 81, No. 7, 2010, p. 073503.

[150] Bai, K. H., Lee, D. S., Chang, H. Y., and Uhm, H. S., "Control and Analysis of Ion Species in N_2 Inductively Coupled Plasma with Inert Gas Mixing," *Applied Physics Letters*, Vol. 80, No. 21, 2002, p. 3907.

[151] Linnell, J. and Gallimore, A., "Internal Langmuir Probe Mapping of a Hall Thruster with Xenon and Krypton Propellant," 42nd AIAA/ASME/SAE/ASEE Joint Propulsion Conference and Exhibit, AIAA-2006-4470, Sacramento, California, Jul. 2006.

[152] Vinodkumar, M., Limbachiya, C., Antony, B., and Joshipura, K. N., "Calculations of Elastic, Ionization and Total Cross Sections for Inert Gases Upon Electron Impact: Threshold to 2 KeV," *Journal of Physics B: Atomic, Molecular and Optical Physics*, Vol. 40, 2007, pp. 3259–3271.

[153] Itikawa, Y., "Cross Sections for Electron Collisions with Nitrogen Molecules," *Journal of Physical and Chemical Reference Data*, Vol. 35, No. 1, 2006, pp. 31–53.

[154] Sucher, J., "Magnetic Dipole Transitions in Atomic and Particle Physics: Ions and Psions," *Reports on Progress in Physics*, Vol. 41, No. 11, 1978, pp. 1781–1838.

[155] Butler, L. R. P., Laqua, K., and Strasheim, A., "Nomenclature, Symbols, Units and Their Usage in Spectrochemical Analysis - V: Radiation Sources (Recommendations 1985)," *Pure and Applied Chemistry*, Vol. 57, No. 10, Jan. 1985, pp. 1453–1490.

[156] Fridman, A. and Kennedy, L. A., *Plasma Physics and Engineering*, Taylor & Francis, New York, NY, 2004.

[157] "NIST Atomic Ionization Energies Output for Krypton," URL `http://physics.nist.gov/PhysRefData/ASD/ionEnergy.html`.

[158] "NIST: Atomic Spectra Database Lines Form," URL `http://physics.nist.gov/PhysRefData/ASD/lines_form.html`.

[159] Hardy, K. A. and Sheldon, J. W., "Metastable Atom Density in Helium, Neon, and Argon Glow Discharges," *Journal of Applied Physics*, Vol. 53, No. 12, Dec. 1982, pp. 8532–8536.

[160] Rapp, D. and Englander-Golden, P., "Total Cross Sections for Ionization and Attachment in Gases by Electron Impact. I. Positive Ionization," *The Journal of Chemical Physics*, Vol. 43, No. 5, Sep. 1965, pp. 1464–1479.

[161] Czerwiec, T. and Graves, D. B., "Mode Transitions in Low Pressure Rare Gas Cylindrical ICP Discharge Studied by Optical Emission Spectroscopy," *Journal of Physics D: Applied Physics*, Vol. 37, No. 20, Oct. 2004, pp. 2827–2840.

[162] Cooper, J., "Plasma Spectroscopy," *Reports on Progress in Physics*, Vol. 29, 1966, pp. 35–130.

[163] Phelps, A. V., "Diffusion, De-excitation, and Three-Body Collision Coefficients for Excited Neon Atoms," *Physical Review*, Vol. 114, No. 4, May 1959, pp. 1011–1025.

[164] Ichikawa, Y. and Teii, S., "Molecular Ion and Metastable Atom Formations and Their Effects on the Electron Temperature in Medium-Pressure Rare-Gas Positive-Column Plasmas," *Journal of Physics D: Applied Physics*, Vol. 13, No. 11, Nov. 1980, pp. 2031–2043.

[165] Salinger, S. N. and Rowe, J. E., "Determination of the Predominant Ionization and Loss Mechanisms for the Low-Voltage Arc Mode in a Neon Plasma Diode," *Journal of Applied Physics*, Vol. 39, No. 9, Aug. 1968, pp. 4299–4307.

[166] Mason, N. J. and Newell, W. R., "Total Cross Sections for Metastable Excitation in the Rare Gases," *Journal of Physics B: Atomic and Molecular Physics*, Vol. 20, No. 6, Mar. 1987, pp. 1357–1377.

[167] Kolokolov, N. B. and Blagoev, A. B., "Ionization and Quenching of Excited Atoms with the Production of Fast Electrons," *Physics-Uspekhi*, Vol. 36, No. 3, 1993, pp. 152–170.

[168] Johnston, M., Fujii, K., Nickel, J., and Trajmar, S., "Ionization of Metastable Neon by Electron Impact," *Journal of Physics B: Atomic, Molecular and Optical Physics*, Vol. 29, No. 3, Feb. 1996, pp. 531–543.

[169] Ton-That, D. and Flannery, M. R., "Cross Sections for Ionization of Metastable Rare-Gas Atoms (Ne^*, Ar^*, Kr^*, Xe^*) and of Metastable $N_2{}^*$, CO^* Molecules by Electron Impact," *Physical Review A*, Vol. 15, No. 2, Feb. 1977, pp. 517–526.

[170] Jung, R. O., Piech, G. A., Keeler, M. L., Boffard, J. B., Anderson, L. W., and Lin, C. C., "Electron-Impact Excitation Cross Sections into $Ne(2p^5 3p)$ Levels for Plasma Applications," *Journal of Applied Physics*, Vol. 109, No. 12, Jun. 2011, pp. 123303–1 –8.

[171] Blessington, J. C., *Measurements of Metastable Atom Density Using Energies and Densities of Energetic "Fast" Electrons Detected in the Electron Energy Distribution Function Associated with the Afterglow Plasma Produced by a Radio Frequency Inductively Coupled Plasma Helium Discharge*, Master's Thesis, Physics Dept., West Virginia University, Morgantown, West Virginia, 2007.

[172] Phelps, A. V., "The Diffusion of Charged Particles in Collisional Plasmas: Free and Ambipolar Diffusion at Low and Moderate Pressures," *Journal of Research of the National Institute of Standards and Technology*, Vol. 95, No. 4, Aug. 1990, pp. 407–431.

[173] Lee, C., Graves, D. B., Lieberman, M. A., and Hess, D. W., "Global Model of Plasma Chemistry in a High Density Oxygen Discharge," *Journal of The Electrochemical Society*, Vol. 141, No. 6, Jun. 1994, pp. 1546–1555.

[174] Malyshev, M. V. and Donnelly, V. M., "Trace Rare Gases Optical Emission Spectroscopy: Nonintrusive Method for Measuring Electron Temperatures in Low-Pressure, Low-Temperature Plasmas," *Physical Review E*, Vol. 60, No. 5, Nov. 1999, pp. 6016–6029.

[175] Hirschfelder, J. O., Curtiss, C. F., and Bird, R. B., *Molecular Theory of Gases and Liquids*, Wiley, New York, NY, 1964.

[176] Biondi, M. A., "Diffusion, De-Excitation, and Ionization Cross Sections for Metastable Atoms. I," *Physical Review*, Vol. 88, No. 3, Nov. 1952, pp. 660–665.

[177] Neynaber, R. H. and Tang, S. Y., "Chemi-Ionization in Collisions of Metastable Neon with Xenon," *The Journal of Chemical Physics*, Vol. 70, No. 9, May 1979, pp. 4272–4276.

[178] West, W. P., Cook, T. B., Dunning, F. B., Rundel, R. D., and Stebbings, R. F., "Chemiionization Involving Rare Gas Metastable Atoms," *The Journal of Chemical Physics*, Vol. 63, No. 3, Aug. 1975, pp. 1237–1242.

[179] Verheijen, M. and Beijerinck, H., "State Selected Total Penning Ionisation Cross Sections for the Systems $Ne^*(^3P_0, {}^3P_2)$ + Ar, Kr, Xe and N_2 in the Energy Range $0.06 < E_0(eV) < 8.0$," *Chemical Physics*, Vol. 102, No. 1–2, Feb. 1986, pp. 255–273.

[180] Neynaber, R. H. and Magnuson, G. D., "Penning and Associative Ionization in the Metastable Neon-Krypton System," *Physical Review A*, Vol. 14, No. 3, Sep. 1976, pp. 961–964.

[181] Mikellides, I. G., Katz, I., Goebel, D. M., and Polk, J. E., "Hollow Cathode Theory and Experiment. II. A Two-Dimensional Theoretical Model of the Emitter Region," *Journal of Applied Physics*, Vol. 98, No. 11, 2005, pp. 113303–1–14.

[182] Sukhorukov, V. L., Petrov, I. D., Schäfer, M., Merkt, F., Ruf, M.-W., and Hotop, H., "Photoionization Dynamics of Excited Ne, Ar, Kr and Xe Atoms Near Threshold," *Journal of Physics B: Atomic, Molecular and Optical Physics*, Vol. 45, No. 9, May 2012, pp. 092001 1–43.

[183] Boffard, J. B., Keeler, M. L., Piech, G. A., Anderson, L. W., and Lin, C. C., "Measurement of Electron-Impact Excitation Cross Sections Out of the Neon $^3P_2$ Metastable Level," *Physical Review A*, Vol. 64, No. 3, Aug. 2001, p. 032708.

[184] Reid, B. M., Shastry, R., Gallimore, A. D., and Hofer, R. R., "Angularly-Resolved ExB Probe Spectra in the Plume of a 6-kW Hall Thruster," 44th AIAA/ASME/SAE/ASEE Joint Propulsion Conference & Exhibit, AIAA 2008-5287, Hartford, CT, Jul. 2008.

[185] Xu, K. G. and Walker, M. L. R., "High-Power, Null-Type, Inverted Pendulum Thrust Stand," *Review of Scientific Instruments*, Vol. 80, No. 5, May 2009, p. 055103.